PERFORMANCE ANALYSIS, DYNAMIC SIMULATION AND CONTROL OF MASS-ACTUATED AIRPLANE

by

SUKRU AKIF ERTURK

Presented to the Faculty of the Graduate School of
The University of Texas at Arlington in Partial Fulfillment
of the Requirements
for the Degree of

DOCTOR OF PHILOSOPHY

THE UNIVERSITY OF TEXAS AT ARLINGTON
August 2016

Copyright © by SUKRU AKIF ERTURK 2016

All Rights Reserved

To my mother Seher, my father Mustafa,
and my sister Sule Busra.

ACKNOWLEDGEMENTS

First of all, I would like to express my deepest appreciation to my supervising professor Dr. Atilla Dogan throughout my doctoral education. With the guidance of his viewpoint, I could comprehend the basics of being an effective and a productive researcher. Also, his wonderful mentoring and experiences widened my horizon about my perspective of being a good academician. I would also like to thank to him for his immense support when I got desperate about building up my dissertation and he motivated me to keep going.

I would like to thank my dissertation committee members, Dr. Kamesh Subbarao, Dr. Dudley Smith, Dr. Brian Huff, and Dr. Donald Wilson, for their valuable comments and suggestions to shape my research in the final form. Their perspectives and evaluations helped me to finalize my dissertation.

I would like to thank the Department of Mechanical and Aerospace Engineering for their financially support throughout my graduate studies.

I would also like to thank my friends in our core Turkish community who are currently pursuing their Masters or Ph.D. degrees at The University of Texas at Arlington for their support and sharing wonderful times with me during my education.

Lastly, I would like to express my sincere appreciation to my parents. Special thanks to my father Mustafa who inspires me with his ideals and guides me to become a decent person in my life, to my mother Seher who supports me endlessly for her patience about me throughout my life, and to my sister Busra who is always my true friend and supporter. I could not have done any of this without them.

August 4, 2016

ABSTRACT

PERFORMANCE ANALYSIS, DYNAMIC SIMULATION AND CONTROL OF MASS-ACTUATED AIRPLANE

SUKRU AKIF ERTURK, Ph.D.

The University of Texas at Arlington, 2016

Supervising Professor: Atilla Dogan

The control of space, aerial and underwater vehicles requires moment generation mechanisms to change their orientation. In addition to or in place of conventional moment generation actuators, internally moving-mass actuation has been proposed and/or used for such vehicles. The primary principle for mass-actuation is to reposition gravitational force to change the associated moment while the secondary effect may come from the inertial force due to the motion of the masses. Recent development/miniaturization in flight control sensor, computing and actuation, and electric motors and expansion of applications for small UAV (Unmanned Aerial Vehicle) offer a potential for implementation of internal mass-actuation in small UAV. The mass-actuation offers various advantages over the conventional mechanisms in airplane flight such as reduced drag and lift loss due to aerodynamic control surface deflections, simplified wing and tail design, improved lift-generation performance of wing, smaller radar signature for stealth aircraft.

This dissertation research investigates the feasibility and benefit of mass-actuation of a small UAV in various flight phases and full missions consisting of all these flight phases and transitions between them. Three different configurations of the same airplane are considered: (1) aero-actuated, conventional airplane with three standard aerodynamic control surfaces, aileron, elevator and rudder, (2) mass-actuated, a mass moving along the fuselage to mainly generate pitching moment, and another mass moving along the wing to generate rolling moment, and (3) mass-rudder actuated, mass-actuation as in case-2 augmented with a rudder. The airplane is an electric powered and has a single propeller at the nose. A full 6-DOF (Degrees of Freedom) nonlinear equations of motion are derived, including the terms modeling inertia forces induced by the motion of the internal masses, and the effect of this internal mass motion on the variation of the center of mass and inertia matrix. The dynamics of the electric motor of the propeller and the servos of the actuators are also modeled. The effect of the propeller on the dynamics of the aircraft is also included. Modeling also includes electric power consumption by the electric motor driving the propeller, and servos of the aerodynamic and mass actuators. An integrated simulation environment is developed that includes all these factors and can be switched between the different configurations defined above.

Trim analyses of all three configurations of the airplane are carried out in all four flight conditions (steady climb, cruise, steady turn, steady descent). Trim analyses consider all the constraints of the control and state variables such as limits on the deflections of the aerodynamic surfaces, position of the mass actuators, battery provided voltage, and angle of attack. These analyses demonstrate the feasibility of flying the airplane with mass-actuation only within varying speed ranges depending on the actuation mechanism. The results also show the benefit of mass-actuation over the conventional aero-actuation in terms of range and endurance especially in cruise flight, as compared to the other two configurations. In the second phase of the research, controllability of the airplane with each actuation mechanisms is determined and compared over the feasible speed range of each trim condition. A new relative controllability metrics is defined and calculated for this purpose. This analysis, based on the linearized model of the aircraft in each trim flight condition, show that the mass-actuation provides full controllability with various degree over the speed ranges. Once the controllability is verified, an LQR-based gain scheduling controller is designed for each aircraft configuration to track commanded climb/descent rate, altitude, airspeed, and turn rate. These controllers are implemented in the integrated simulation environment to simulate various flight profiles including full missions that start with a hand-launch of the airplane, climb to a specified altitude, and cruise at that altitude with various commanded speed, and loiter with commanded left and right turn rates, and descend to land with varying approach speed. These simulations also demonstrate the feasibility potential benefits, and/or limitations of mass actuation.

TABLE OF CONTENTS

Appendix

LIST OF ILLUSTRATIONS

Figure Page

LIST OF TABLES

Table Page

CHAPTER 1

INTRODUCTION

1.1 Motivation

In aviation, standard control surfaces such as aileron, rudder, elevator are used to control the aircraft motion. When the control surfaces are deflected to generate control moments, the airflow around wings and tails is distorted due to the change in camber of the airfoil. Increasing the camber of the airfoil results in drag increase. The motivation is to eliminate drag increase and lift loss caused by deflection of control surfaces by replacing them with internal moving-mass actuators as alternative moment generation mechanisms. Elimination of control surfaces may also help simplify wing and tail design and improve aerodynamic performance of these lift generation surfaces. For example, the ability of generating rolling moment without ailerons may eliminate the adverse yaw due to aileron drag in turns or using internal mass-actuators may protect the controlling of the aircraft motion if any physical impact on control surfaces would happen during flight. Removal of the control surfaces and associated components such as servos, hinges and rods may also reduce the weight of the aircraft. To determine whether the use of moving-mass actuation should be seriously considered, the following questions should first be investigated. (1) Can the removal of the aerodynamic control surfaces bring in benefits significant enough to warrant consideration for alternative trim mechanisms? (2) Can moving-mass actuation generate moments with magnitude and speed large enough to trim and maneuver airplane without adding too much weight and complexity to its flight control system?

1.2 Literature Review

This section presents the literature review of prior studies pertaining to mass-varying dynamical systems. The prior work is categorized in various aspects. First, sources and/or purposes of variation in internal mass distribution are identified; specifically, whether the mass distribution changes inadvertently, or is changed intentionally. It is shown that the mass distribution variation, when done intentionally, is usually employed to control the vehicle motion. The second classification is done in terms of the domain of operation of the vehicle with the mass variation such as in air, on ground, in water, or in space. Another classification is done by the mechanism used to change the mass distribution such as internal mass motion, or internal fuel transfer. In the case of internal mass actuation, the number of masses moved internally and the number of axes they are moved along are other ways of classifying the prior work. Lastly, a classification is done based on the control design methods when the internal mass actuation is used for controlling vehicle motion.

1.2.1 The Effects of Mass Distribution on Vehicle Dynamics and Its Utilization for Control

The effects of variation in internal mass distribution on vehicle dynamics have been investigated in the literature. These research studies can be grouped under two main topics: (i) the mass distribution changes inadvertently and the analysis of the effects of that mass movement in the dynamics requires more accurate dynamic model of the vehicle, and (ii) the mass distribution of the vehicle is intentionally changed by shifting the position of internal masses to generate gravitational moments and/or to change the inertia properties for the purpose of controlling the motion of the vehicle. First, the variation in mass distribution on the vehicle dynamics have been investigated [24, 25, 26, 27, 28, 29, 30, 31, 32, 33, 34, 35]. These papers show that variation of mass distribution in the vehicle affects the system dynamics and stability. Furthermore, designing and locating a passive control device to make prolate spinners stable under thrust is proposed. When mass distribution changes unintentionally, the mass variation is modeled as a pendulum and spin about the minor axis can be made asymptotically stable if the thrust is large enough, the mass variation happens in the back of the center of gravity (c.g.) of the system and the spring is stiff enough [36, 37, 38]. Second, the internal mass distribution is performed intentionally to control the vehicle motion as desired. There are many research efforts focusing on controlling the motion of vehicle by means of internal mass movement. Majority of such efforts is in the area of attitude control [39, 5, 40, 16, 41, 7, 9, 13, 42, 43, 44, 45, 1, 46, 17, 18, 47, 48, 49, 50, 51, 52, 53, 54, 8, 15, 55, 56, 57, 58, 59, 60, 61, 62, 63, 64, 4, 65, 66, 67, 68]. Specifically, Refs. [69, 3, 70, 71, 72, 11, 73] attempt to utilize internal mass motion for roll control. Controlling the stability margin for projectile is also performed with the internal mass motion [74, 10]. Internal moving masses are also used in deconing, or detumbling of spinning spacecraft [75, 14, 76, 77] and nutation damping control [78]. Varying mass distribution is also used for trim control [79, 80, 12, 81, 82, 83, 84, 85, 86, 87, 88, 2, 89, 90, 91, 92, 93]. For underwater vehicles, internal mass motion is used for glide path control [6, 94, 69, 95, 96, 97] and depth control [69, 98]. Trajectory control [99, 72, 100, 101] and orbit control [102] are achieved with the internal mass motion.

1.2.2 Application Areas of Mass-actuation

Moving-mass actuation has been proposed as a control mechanism in many applications in the literature. It is used for (i) endo-atmospheric environment only, (ii) exo-atmospheric environment only, (iii) both endo- and exo-atmospheric environments, and (iv) underwater environment. First, moving-mass control methodology is observed for the applications in the endo-atmospheric environment such as missile [9, 41, 8], projectile [74, 10, 99], re-entry vehicle [13, 70, 71, 72, 80, 79, 12, 83, 42, 11, 43, 44, 45, 101, 48, 73, 63], airship [1], airplane [87, 88, 2, 89, 90, 91, 93, 92], and rotorcraft [5, 3, 64, 4, 65]. Internal moving-mass actuation is an attractive control mechanism for missiles and re-entry vehicles since aerodynamic control surfaces are subject to ablation and erosion due to hypersonic flow. Since Concorde can also fly with the supersonic speed, changing internal mass distribution helps trimming the aircraft in transonic conditions. Second, moving-mass control system is observed for the applications in the exo-atmospheric environment such as missile [7], spacecraft [14, 54, 15, 62, 66], solar sail [17, 84, 85, 18], satellite [39, 49, 50, 86, 51, 52, 102, 78, 53], and space station [75, 77, 55, 56, 76]. Third, controlling with mass-actuation is also observed for the vehicles in both endo- and exo-atmospheric environments such as kinetic warhead [40, 16] and spacecraft [81, 82, 47]. Finally, the moving-mass system is used in the underwater environment for controlling the vehicle [6, 94, 69, 98, 95, 96, 67, 68, 100, 46, 97].

A real flight with mass-actuators for a small unmanned airplane was achieved and presented in Ref. [103] which was built upon the preliminary works of this dissertation. In that study, two lateral masses (one for each wing) moving inside the wings were used. Study showed that airplane have rolling capability in a real flight by using lateral moving-masses without aileron.

1.2.3 Description of Mechanisms for Mass-actuators

Another classification of the literature is done based on the mechanism used to change the internal mass distribution. In the very early stages of aviation, pilots used to change the pose of their body and thus to move the center of mass of the aircraft in order to achieve controlled flight [104, 105]. Other mechanisms implemented later on for changing the mass distribution include internal solid mass-actuator motions, variable buoyancy and fluid transfer. Internal mass-actuation, moving a specific mass within the vehicle to change the center of mass and/or inertia properties, is the most commonly used mechanism for changing internal mass distribution. Internal mass-actuation is mostly done as a linear motion [74, 75, 3, 39, 94, 6, 69, 40, 16, 7, 9, 41, 13, 71, 70, 10, 99, 72, 14, 79, 80, 12, 83, 42, 11, 43, 44, 45, 1, 95, 96, 68, 100, 46, 97, 17, 84, 85, 18, 47, 101, 48, 49, 86, 51, 52, 102, 53, 54, 8, 55, 56, 76, 77, 58, 60, 57, 59, 61, 62, 66, 73, 63]. In some other applications, the internal-mass actuation is done along a circular path [5, 13, 12, 81, 82, 50, 15, 63, 64, 4, 65]. For underwater vehicles, variable buoyancy is one of the mechanisms for changing the inertia properties [69, 94, 6, 98, 95, 96, 97]. By pumping water in or out, the weight of the underwater vehicle is adjusted to keep it at a desired depth. Fluid transfer from one position to another is also implemented as a control mechanism [39, 78, 87, 88, 2, 90, 91, 93, 89, 92]. For example, fuel transfer from a front tank to an aft tank were implemented in Concorde to shift the center of gravity backward when the center of pressure moves backward during the transition from subsonic to supersonic flight [88, 2, 90, 93, 89, 92].

1.2.4 Number of Axes Controlled by Mass-actuators

Internal mass-actuation with different degrees of freedom are used for vehicle control. Generally, mass-actuators are moved along one axis only, two axes, or all three axes. Many applications use one mass-actuator moving along an axis [74, 75, 3, 7, 70, 71, 10, 99, 72, 12, 11, 96, 100, 46, 97, 53, 55, 56, 76, 77, 66, 73]. Refs. [14, 51] move two masses along the same single axis. Alternatively, the direction that one mass is moved along is set within the span of two axes [52, 64, 4, 65] or the mass moves on a rail linearly while the rail can be rotated [13, 63]. Another implementation for 2-axes control has a mass placed at a fixed position on an arm that can be rotated [5]. Most two degrees of freedom mass-actuators have two masses that move along two orthogonal axes [6, 69, 13, 14, 12, 81, 82, 83, 45, 1, 95, 17, 84, 85, 18, 47, 101, 48, 54, 8, 15, 60]. For a satellite, four mass-actuators are proposed for 2-axes control that each axis is controlled by two of them [86]. Three degrees of freedom mass-actuators have three masses that move along three orthogonal axes [40, 16, 9, 79, 80, 42, 43, 44, 102, 58, 57, 59, 62], one mass is moved along a line within the span of three axes [94, 41], or six mass-actuators are used for 3-axes control that each axis is controlled by two of them [39].

1.2.5 Control Design Methods for Mass-actuated Systems

For systems with moving mass-actuation, the positions of the moving masses are used as control variables in various control design methods. Optimal control methods, specifically the linear quadratic regulator techniques, are commonly used [75, 6, 70, 14, 96, 18, 52, 53, 54, 77, 87]. Optimal control with convex optimization [7], extended state observer [71], gain scheduling [72], and integral error [83] are used to improve the closed loop performance. Another commonly used control method is the family of proportional (P), integral (I), and/or derivative (D) controllers. PID controllers [69, 45, 17, 84, 85, 55, 56], PD controllers [40, 16, 98, 100, 86, 65], PI controllers [80, 79], P controllers [64] are designed for controlling the internal mass movement. PID controllers with Neural Network technique [9, 48] and Genetic Algorithm (GA) optimization [101, 48] are also used to improve the performance of the mass-actuated system. Nonlinear control design is another common method for mass-actuated system. Specifically, many different nonlinear control techniques are proposed in the literature such as feedback linearization [94, 40, 13, 63, 99], multi-stepping algorithm [16], sliding mode [74, 42, 43, 46, 8, 63], dynamic inversion [82, 43], trajectory linearization [11], predictive control [44], weighted generalized inverse method [1], back-stepping approach [3, 100, 8], interconnection and damping assignment-passivity based control (IDA-PBC) [15], Lyapunov based [76, 57, 59, 61], and Lie bracket expansion [62]. Robust control techniques [41] are also used for systems with internal mass movement.

1.2.6 Examples of Mass-actuated Systems

In this section, some examples of the mass-actuation as a control mechanism in the literature are presented for illustration.

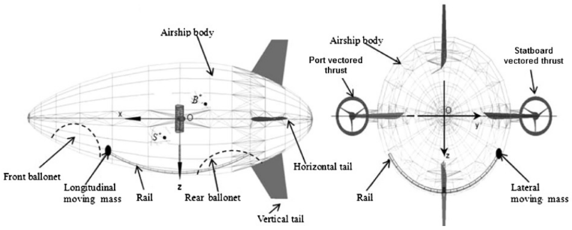

Figure 1.1. Airship with internal mass mechanism [1].

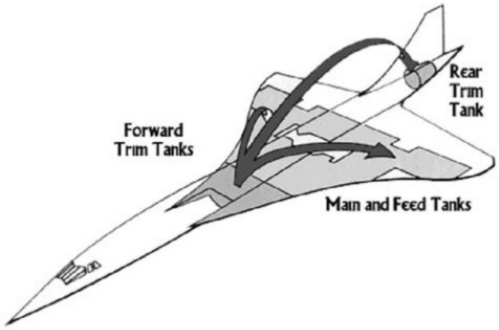

Figure 1.2. Concorde with fuel transfer [2].

Figure 1.1 shows that two mass-actuators are used as a control mechanism for an airship. One of them moves longitudinally and another one moves laterally inside the airship. Fig. 1.2 illustrates the fuel transfer between tanks in Concorde to shift the aircraft center of gravity for trimming the aircraft. Figs. 1.3 and 1.4 show the moving mass mechanism for helicopter to roll. In Fig. 1.3, lateral motion of the mass is considered for controlling while the mass-actuator (specifically battery) can control 2-axes by rotating it. Fig. 1.5 shows the internal mass mechanism for hopping rotochute. The position of mass is fixed at the end of the rod and it gives the

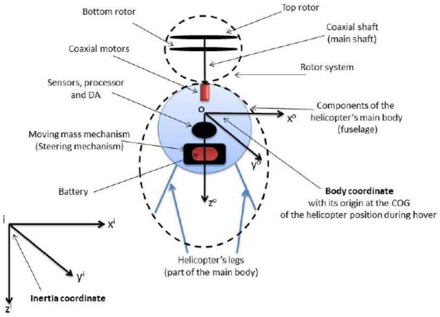

Figure 1.3. Helicopter with internal mass mechanism [3].

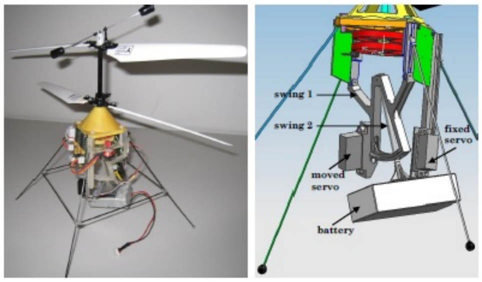

Figure 1.4. Helicopter with internal mass mechanism [4].

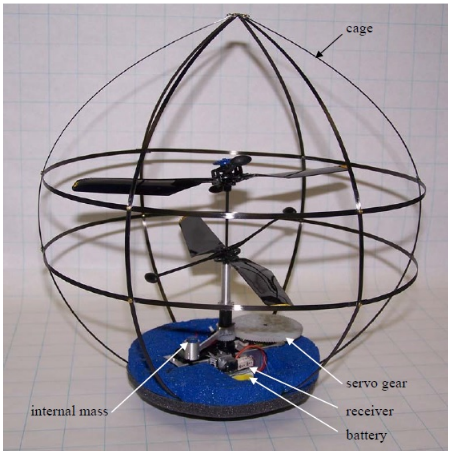

Figure 1.5. Hopping rotochute with internal mass mechanism [5].

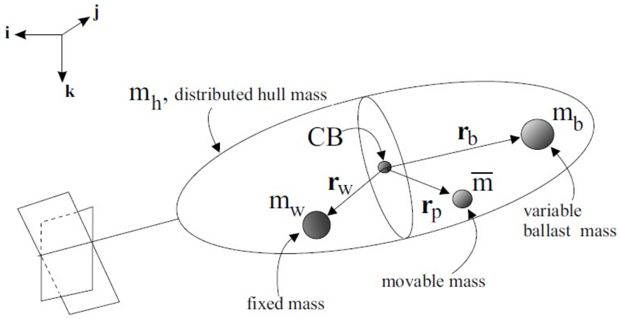

Figure 1.6. Underwater vehicle with internal mass mechanism [6].

direction control by rotating it in the horizontal plane. Fig. 1.6 illustrates the moving mass-actuator and variable ballast mass in an underwater vehicle. Two moving mass-actuators are used to generate pitching and rolling moment while variable ballast mass is used for depth control. Figs. 1.7-1.9 show the mass-actuated systems in missiles. One mass-actuator is used for 1-axis control in Fig. 1.7 while two mass-actuators are used for 2-axes control in Fig. 1.8 and three mass-actuators are used for 3-axes control in Fig. 1.9. Fig. 1.10 shows that one mass-actuator is translated along an axis to change the stability margin during the flight of a projectile. Figs. 1.11-1.14

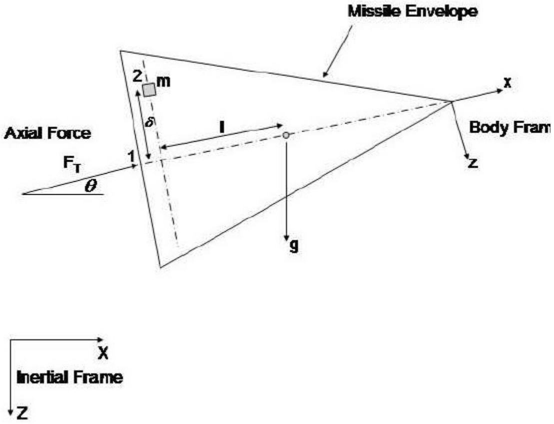

Figure 1.7. Missile with internal mass mechanism [7].

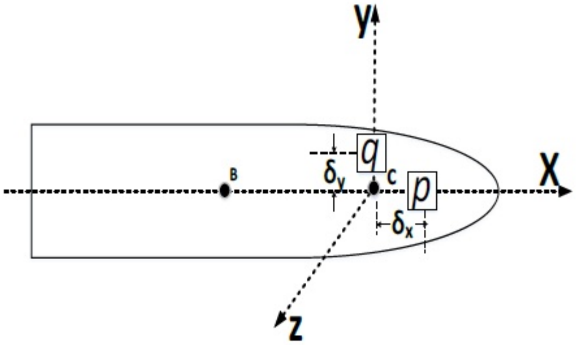

Figure 1.8. Missile with internal mass mechanism [8].

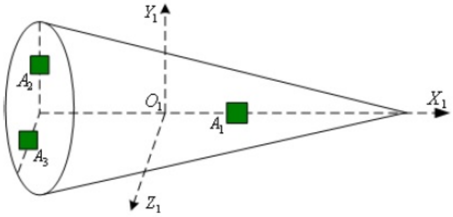

Figure 1.9. Missile with internal mass mechanism [9].

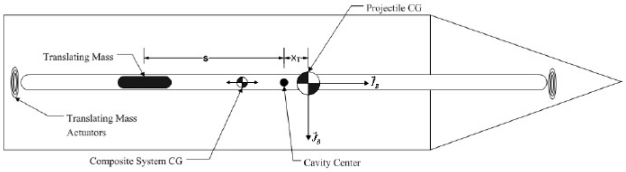

Figure 1.10. Projectile with internal mass mechanism [10].

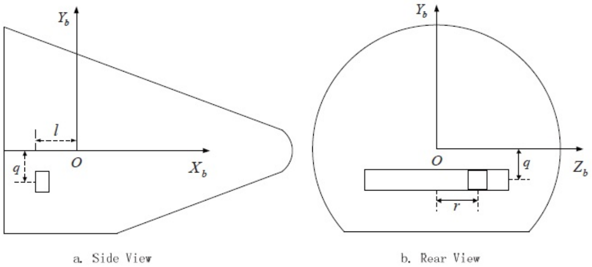

a. Side View

b. Rear View

Figure 1.11. Re-entry vehicle with internal mass mechanism [11].

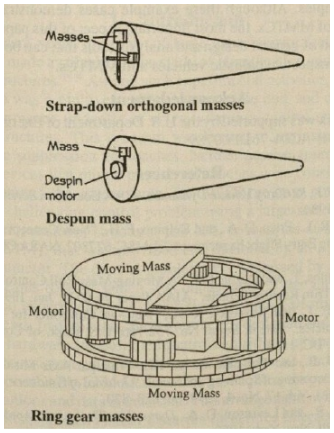

Figure 1.12. Re-entry vehicle with internal mass mechanism [12].

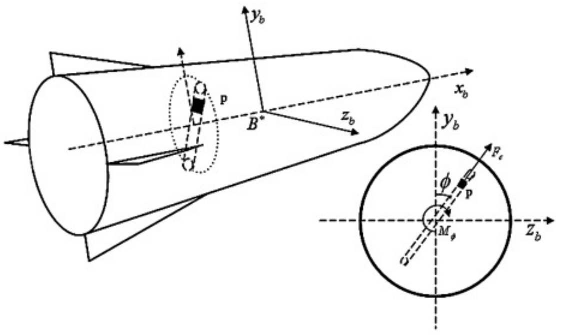

Figure 1.13. Re-entry vehicle with internal mass mechanism [13].

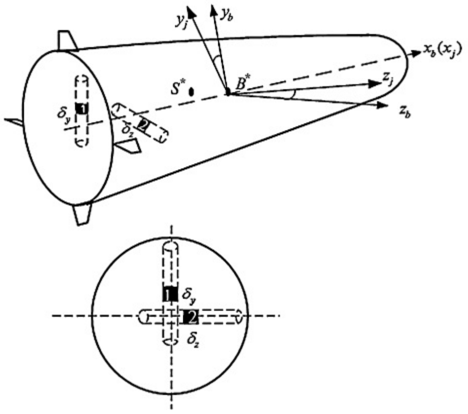

Figure 1.14. Re-entry vehicle with internal mass mechanism [13].

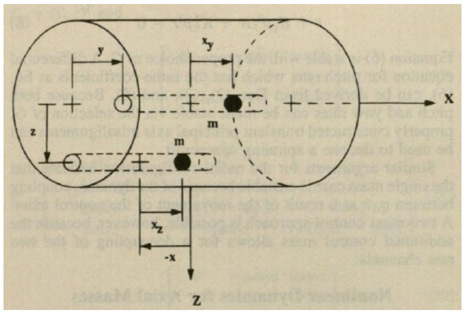

Figure 1.15. Spacecraft with internal mass mechanism [14].

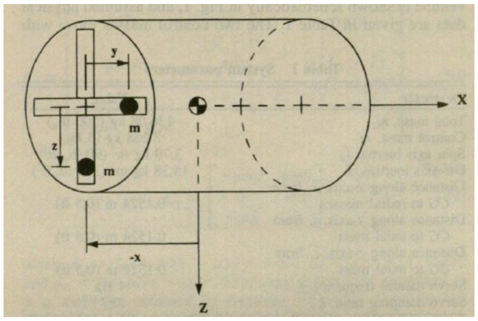

Figure 1.16. Spacecraft with internal mass mechanism [14].

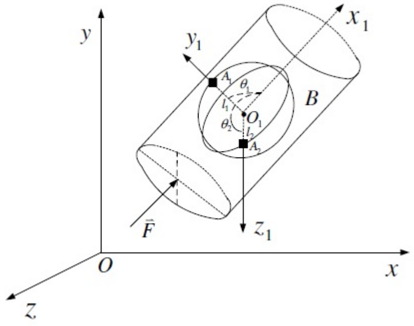

Figure 1.17. Spacecraft with internal mass mechanism [15].

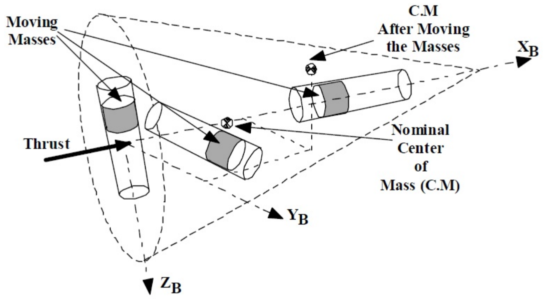

Figure 1.18. Warhead with internal mass mechanism [16].

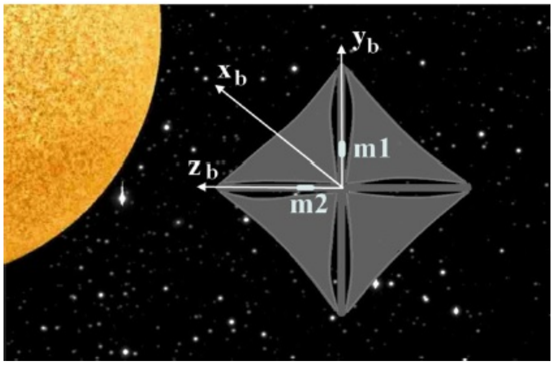

Figure 1.19. Solar Sail with internal mass mechanism [17].

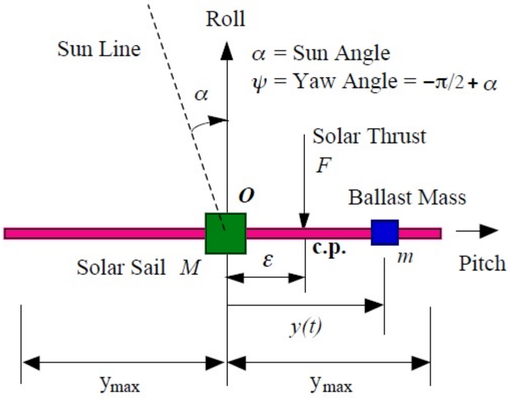

Figure 1.20. Solar Sail with internal mass mechanism [18].

show the mass-actuators in re-entry vehicles. In Fig. 1.11, 1-axis is controlled by one-mass actuator. Fig. 1.12 proposes that one mass-actuator is rotated by despin motor or two mass-actuators are placed orthogonally and move linearly for 2-axes control. Similarly, one mass-actuator moves radially on a rod while the rod can rotate in Fig. 1.13 and two orthogonal mass-actuators move linearly in 1.14 for 2-axes control. Figs. 1.15-1.17 show the moving mass-actuator mechanism for spacecraft. Two mass-actuators move on the same axis in Fig. 1.15 and are orthogonally placed for 2-axes control in Fig. 1.16. Fig. 1.18 shows that three mass-actuators control the 3-axes for a kinetic warhead. Figs. 1.19-1.20 show the internal mass-actuator mechanism for controlling the motion of a solar sail.

1.3 Problem Statement

The literature review shows that moving mass-actuators are used in several application areas for control purpose. However, controlling with mass-actuation of a small unmanned airplane has not been attempted. This research aims to investigate the feasibility of using mass actuation for controlling of a small unmanned airplane. Moving mass-actuators are considered as an alternative control mechanism that generates gravitational moments by moving them inside the airplane as control moments instead of moments produced by aerodynamic control surfaces. In order to implement the mass-actuators to control the airplane motion, some of questions should be answered. (1) Can moving mass-actuators generate the control moments large enough for different trim flight conditions? (2) If that is possible, do the moving mass-actuators provide full controllability and can they be used as a control mechanism? (3) If the aircraft is completely controllable, is there any control design possible with mass-actuators to provide performance at the level comparable with aerodynamic control surfaces even in open-loop unstable flight conditions? (4) How does the motion of the mass actuators affect the airplane dynamics and control since they move inside the airplane and change the inertia properties during the flight?

1.4 Original Contributions

Mass-actuation mechanism has been used in many different application areas. In this research, moving mass-actuators are investigated the first time for a small unmanned airplane as an alternative control mechanism instead of standard control surfaces. Two moving mass-actuators are considered for control purpose in this research: (i) one is moved longitudinally along the body x-axis to generate pitching moment, and (ii) the other is moved laterally along the wings to generate rolling moment.

First, trim analyses for the flight modes including cruise, steady-state turn, ascending and descending are investigated to see if the mass-actuators are capable of generating gravitational moments comparable to those generated by elevator and aileron. During the trim analyses, physical limitations of mass-actuators are considered since they move inside the aircraft. It is shown that all the flight modes are possible with mass-actuators within the feasible trim speed ranges. On the other hand, since there is no alternative mechanism for rudder, it is observed that flight modes are possible only with non-zero sideslip angle. If rudder is used in addition to mass-actuators, it is still possible to fly with zero sideslip angle. After all the trim analyses are done, a benefit of eliminating aerodynamic control surface is obtained in terms of endurance and range increase.

Second, controllability of the airplane with mass-actuation is investigated. Trim results showed that if mass-actuators are placed at their trim conditions, gravitational moments generated by them can be used as controlling the aircraft motion. If a specific maneuver is desired such as changing the flight from cruise to turn, mass-actuators should be moved to new positions. This requires the analysis of controllability with mass-actuators. To investigate the controllability of mass-actuated airplane, equations of motions are linearized around the trim states that are obtained from trim analyses for all flight modes within feasible trim speed ranges. Further, a novel method is implemented to quantify the level of controllability of the actuators. This method is built upon based on the Popov-Belevitch-Hautus (PBH) eigenvector test for controllability. Analysis showed that airplane with mass-actuators is controllable for feasible speeds.

Third, stability analysis and control design for the airplane with mass-actuation are investigated. State-space matrices obtained from linearization in stability analysis showed that some of feasible trim speeds may not give stable flight for the airplane. Thus, a feedback controller should be designed and implemented to stabilize the airplane in all feasible trim speeds and fly the aircraft along any other desired trajectory. An LQR-based feedback controller with integral terms is designed to fly the airplane at commanded altitude or rate of ascent/descent, airspeed and turn rate. In the simulation with controller, dynamics of the mass-actuators and the effect of the motion of the mass-actuators on aircraft dynamics are considered. Simulation results showed that mass-actuated airplane can successfully follow altitude or rate of ascent/descent, airspeed and turn rate commands within feasible flight conditions.

1.5 Organization of the Dissertation

The dissertation is organized as follows. Chapter 2 presents the equations of motion and subsystem models such as propulsion and actuator systems. Further, applied forces and moments are introduced. Specifications of the airplane and its subsystems used in the dissertation are also presented. In Chapter 3, the effects of propeller and actuators on aircraft response and performances are discussed. Chapter 4 presents all the trim results of flight modes such as cruise, steady-state turn and ascending/descending. Moreover, the effects of different altitudes and the weights of mass-actuators are discussed. In Chapter 5, linearization of equations of motions is presented. Further, controllability analysis and quality of controllability for airplanes with mass-actuation are described. That discussion is followed by control design procedures in the chapter. Discussions about dynamic simulation and the aircraft performances are presented in Chapter 6. Finally, conclusions and future work are presented in Chapter 7.

CHAPTER 2

AIRCRAFT AND SUBSYSTEM MODELING

This chapter presents the details of aircraft and subsystem modeling and simulation. The equations of motion for an aircraft with varying mass and inertia properties are first introduced. An electric-motor and propeller based propulsion and power system is explained. A modeling of the actuator dynamics is also given. All sources of applied forces and moments are also detailed. The chapter ends with numerical values aircraft and subsystem parameters of a small RC airplane, used in simulations.

2.1 Equations of Motions

Since the problem studied here requires movement of masses within airplane, standard set of equations of motion assuming fixed center of mass and fixed inertia properties cannot be used. Ref. [106] presents equations of motion of an aircraft with varying mass/inertia properties relative to a non-inertial reference frame in the presence of wind. These equations are applied to the dynamics of receiver aircraft in aerial refueling by representing the fuel in each fuel tank with moving and varying mass and by considering the tanker's body frame as the non-inertial reference frame. Further, the origin of the body frame of the receiver is set to be at a geometrically fixed position as the center of mass moves during fuel transfer. Those equations in Ref. [106] are obviously more general than the requirements of the problem of this study. Therefore, the equations of motion required for this problem are easily obtained by simplifying the equations in Ref. [106]. In the problem considered here, mass distribution of the aircraft will change due to moving-mass actuation while the total mass will stay constant. Thus, in the equations of Ref. [106], $\dot{m}$ and $\dot{m}_j$ representing mass transfer into the aircraft and into the jth fuel tank, respectively, are set to zero. Ref. [106] considers m_j, fuel in the jth fuel tank, as time-varying and moving mass in the aircraft. For this study, m_j will represent the constant mass of each moving-mass actuator. In Ref. [106], the center of mass of the rigid aircraft, excluding the fuel in transition and in fuel tanks, has a position ρ_{CM} relative to the origin of the body frame of the receiver. In this study, the origin of the body frame is set to be at the center of mass of the aircraft, excluding the moving-mass actuators, which means $\rho_{CM} = 0$. In Ref. [106] the equations are written relative to the body frame of the tanker aircraft, a non-inertial frame. In this study, the equations are written relative to an inertial frame. This is achieved by setting the translational and rotational velocity and accelerations of the tanker's body frame to zero, which makes the tanker's body frame an inertial frame. This procedure leads to a set of 12 equations of motion for the translational and rotational kinetics and kinematics of an aircraft with moving-mass actuators.

2.1.1 Translational Kinematics

The translational kinematic equation written in matrix form with respect to the non-inertial tanker frame is [106]

$$\dot{\xi} = \mathbf{R}^{\mathbf{T}}_{\mathbf{B_R B_T}} \mathbf{R}_{\mathbf{B_R W_R}} U + W_I - \mathbf{R}_{\mathbf{B_T I}} \dot{r}_{B_T} + \mathbf{S}(\omega_{\mathbf{B_T}}) \xi \tag{2.1}$$

The frame of the tanker is considered to be the inertial frame. Inertial frame is defined where origin is arbitrary and fixed relative to the surface of the Earth, x-axis is positive in the direction of local north, y-axis is positive in the direction of local east and z-axis is positive towards the center of the Earth. As a result, since the inertial frame does not move and rotate, Eq. (2.1) is simplified to be

$$\dot{\xi} = \mathbf{R}^{\mathbf{T}}_{\mathbf{B_R I}} \mathbf{R}_{\mathbf{B_R W_R}} U + W_I \tag{2.2}$$

where ξ is the position of the airplane (x, y, z) relative to the inertial frame, $\mathbf{R}_{\mathbf{B_R B_T}}$ is the rotation matrix between receiver frame and tanker frame, $\mathbf{R}_{\mathbf{B_R W_R}}$ is the rotation matrix between receiver frame and wind frame, $\mathbf{R}_{\mathbf{B_R I}}$ is the rotation matrix between receiver frame and inertial frame, $\mathbf{R}_{\mathbf{B_T I}}$ is the rotation matrix between tanker frame and inertial frame, U is translational velocity of the aircraft relative to the air in wind frame, W_I is the velocity of the air relative to the inertial frame, r_{B_T} is the position of tanker frame with respect to inertial frame and $\mathbf{S}(\omega_{\mathbf{B_T}})$ is the skew symmetric matrix of the rotational velocities of the tanker.

2.1.2 Rotational Kinematics

Rotational kinematics in Ref. [106] is written in terms of Euler angles, (ψ, θ, ϕ), which are relative to the tanker's body frame. In this study, Euler angles are relative to the inertial frame since the body frame becomes the inertial frame. Therefore, standard rotational kinematics in terms of Euler angles is used in this study.

$$\dot{\psi} = (q \sin\phi + r \cos\phi) \sec\theta \tag{2.3}$$

$$\dot{\theta} = q \cos\phi - r \sin\phi \tag{2.4}$$

$$\dot{\phi} = p + q \sin\phi \tan\theta + r \cos\phi \tan\theta \tag{2.5}$$

where p, q, r are angular velocities in body frame.

2.1.3 Translational Dynamics

With the simplifications stated above, the translational dynamics equations in Ref. [106] are reduced to

$$\begin{aligned}\dot{\chi} = \epsilon_R^{-1}\left(\mathbf{S}(\omega_{\mathbf{B_R I}})\mathbf{R}_{\mathbf{B_R W_R}}U - \mathbf{R}_{\mathbf{B_R I}}\dot{W}_I\right) + \frac{1}{m_T}\epsilon_R^{-1}\mathbf{R}_{\mathbf{B_R I}}F \\ - \frac{1}{m_T}\epsilon_R^{-1}\sum_{j=1}^{k}\left(m_j\left[\ddot{\rho}_{m_j} + \mathbf{S}(\omega_{\mathbf{B_R I}})\left(\mathbf{S}(\omega_{\mathbf{B_R I}})\rho_{m_j} - 2\dot{\rho}_{m_j}\right) + \mathbf{S}(\rho_{\mathbf{m_j}})\dot{\omega}_{B_R I}\right]\right)\end{aligned} \tag{2.6}$$

where

$$\chi = \begin{bmatrix} V & \beta & \alpha \end{bmatrix}^T \tag{2.7}$$

$$\epsilon_R = \begin{bmatrix} \cos\beta\cos\alpha & -V\sin\beta\cos\alpha & -V\cos\beta\sin\alpha \\ \sin\beta & V\cos\beta & 0 \\ \cos\beta\sin\alpha & -V\sin\beta\sin\alpha & V\cos\beta\cos\alpha \end{bmatrix} \tag{2.8}$$

$\mathbf{S}(\omega_{\mathbf{B_R I}})$ is the skew symmetric matrix of the rotational velocities in body frame, F is external forces in inertial frame, m_T is total mass of the aircraft, m_j is mass of each mass-actuator. Note that ρ_{m_j}, $\dot{\rho}_{m_j}$ and $\ddot{\rho}_{m_j}$ represent position, velocity and acceleration, respectively, of moving-mass actuator m_j relative to the body frame.

2.1.4 Rotational Dynamics

Similarly, with the simplifications stated above, the rotational dynamics equations in Ref. [106] are reduced to

$$\begin{aligned}
\dot{\omega}_{B_RI} = {} & \underline{\mathbf{I_t}}^{\mathbf{-1}} M_{B_R} + \underline{\mathbf{I_t}}^{\mathbf{-1}} \mathbf{S}(\omega_{\mathbf{B_RI}}) \underline{\mathbf{I_M}} \omega_{B_RI} \\
& + \underline{\mathbf{I_t}}^{\mathbf{-1}} \sum_{j=1}^{k} \mathbf{S}(\rho_{\mathbf{m_j}}) m_j \mathbf{R_{B_RI}} \dot{W}_I \\
& + \underline{\mathbf{I_t}}^{\mathbf{-1}} \sum_{j=1}^{k} \mathbf{S}(\rho_{\mathbf{m_j}}) m_j \left[(\omega_{B_RI}^T) \rho_{m_j} (\omega_{B_RI}) + \ddot{\rho}_{m_j} \right] \\
& + \underline{\mathbf{I_t}}^{\mathbf{-1}} \sum_{j=1}^{k} \mathbf{S}(\rho_{\mathbf{m_j}}) m_j \left[- \mathbf{S}(\omega_{\mathbf{B_RI}}) (\mathbf{R_{B_RW_R}} U) + \epsilon_R \dot{\chi}_R \right] \\
& - 2 \underline{\mathbf{I_t}}^{\mathbf{-1}} \sum_{j=1}^{k} m_j \left[(\rho_{m_j}^T \dot{\rho}_{m_j}) I_{3X3} - \dot{\rho}_{m_j} \rho_{m_j}^T \right] \omega_{B_RI}
\end{aligned} \tag{2.9}$$

where

$$\omega_{B_RI} = \begin{bmatrix} p & q & r \end{bmatrix}^T \tag{2.10}$$

M_{B_R} is external moments in body frame, $\underline{\mathbf{I_t}}$ is total inertia matrix of the entire system, $\underline{\mathbf{I_M}}$ is the inertia matrix without mass-actuation.

2.2 Propulsion System Model

The propulsion system consists of an electric motor powered by a battery and driving a propeller. The propulsion model includes a set of typical DC Motor equations [107, 108, 109, 110] as

$$\dot{\imath}_m = \frac{1}{L} \left[-R\imath_m - k_e \omega_m + \mathcal{V}_s \right] \tag{2.11}$$

$$\dot{\omega}_m = \frac{1}{J_p + J_m} \left[k_T \imath_m - k_f \omega_m - \tau_m \right] \tag{2.12}$$

where $\imath_m$ is current the motor draws, ω_m is rotational speed of the motor, R is phase resistance the motor, L is phase inductance the motor, k_e is electrical constant of the motor, k_f is friction constant of the motor, k_T is torque constant of the motor, J_p is propeller inertia, J_m is motor inertia, and $\mathcal{V}_s$ is supplied voltage from the battery.

Assuming a linear relation between the throttle setting and the supplied voltage, throttle input formulated as the ratio to the maximum voltage supplied by the battery as

$$\delta_T = \frac{\mathcal{V}_s}{\mathcal{V}_{max}} \tag{2.13}$$

The relation between the propeller and motor speeds, ω_p and ω_m, and the propeller and motor torques, τ_p and τ_m, depends on the mechanism used to connect the propeller to the motor shaft. If the propeller is connected directly to the motor shaft, the respective propeller and motor quantities will be the same. If there is a gear/pulley mechanism between the propeller and the motor, the relation will be based on the gear/pulley ratio. The torque required to spin the propeller at a given speed ω_p while the airplane moves with airspeed V is formulated as lookup tables

$$\tau_p = f(\omega_p, V) \tag{2.14}$$

In this work, x-component of the direct torque in Eq. (2.14) is considered as the torque required to spin the propeller only. Similarly, the thrust generated by the propeller when spinning at ω_p while aircraft moving with airspeed V is formulated as lookup tables

$$T_p = f(\omega_p, V) \tag{2.15}$$

2.3 Actuator System Model

In this study, same servo dynamics is used for both aero- and mass-actuators. Simulink diagrams for actuator dynamics are shown in Figs. 2.1-2.3. For aero-actuators, commanded control inputs will be the deflections of aerodynamic control surfaces (aileron, elevator, rudder) and load torque will be the hinge torque due to aerodynamic forces on control surfaces. For mass-actuators, commanded control inputs will be the positions of mass-actuators (longitudinal-mass and lateral-mass) and load torque will be the torque due to gravitational forces generated by mass-actuators and forces required to move or accelerate the mass-actuators.

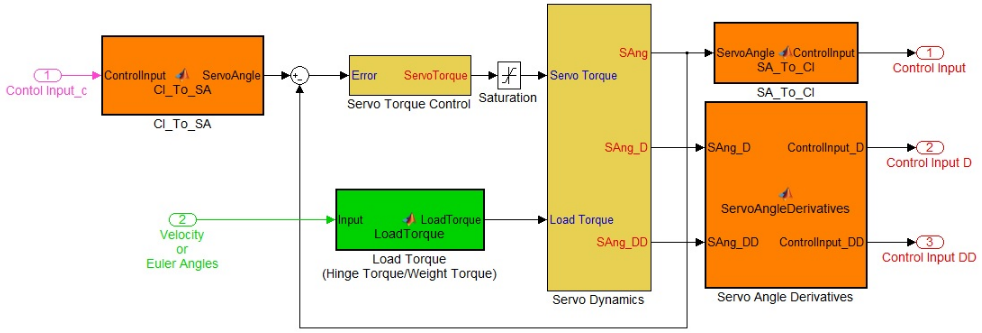

Figure 2.1. Simulink diagram for actuator dynamics.

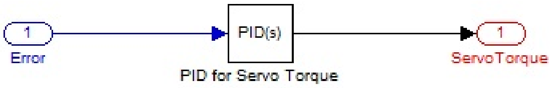

Figure 2.2. Subsystem for servo torque control.

Figure 2.1 shows the servo dynamics for aero- or mass-actuation including the saturation of servo torque and load torque on the servo. In the first part of the subsystem, applied torque is calculated to rotate the servo as commanded and PID controller is designed to control the servo torque as shown in Fig. 2.2. In the second part of the subsystem, position, velocity and acceleration of the servo angle are calculated based on the servo torque subjected to external load such as hinge torque

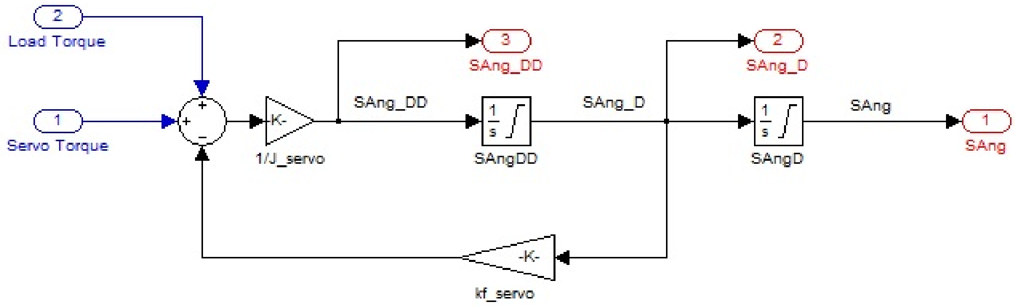

Figure 2.3. Subsystem for servo dynamics.

or torque due to weight of the mass-actuators. In this calculation, two saturation blocks are included to represent the position and rate limits of the servo angle as shown in Fig. 2.3. Between the two subsystems, saturation of the servo torque is also considered. Servo dynamics used in Simulink diagram is defined as

$$\ddot{\theta}_{servo} = \frac{1}{J_{act}}\left(\tau_{servo} + \tau_{load} - k_{f_{act}}\dot{\theta}_{servo}\right) \tag{2.16}$$

where θ_{servo} is the servo angle, J_{act} is the inertia of the actuator system and $k_{f_{act}}$ is the friction of the actuator system. For aerodynamic control surfaces, relationship between the control surface deflection and the servo angle is defined as [111]

$$\frac{\tan\delta_{CS}}{\tan\theta_{servo}} = \frac{r_{CS}}{r_{servo}} \tag{2.17}$$

where $\tan\delta_{CS}$ is the control surface deflection, r_{CS} is the control surface arm and r_{servo} is the servo arm for the aero-actuation system. Relationships of the position, velocity and acceleration between the mass-actuator and the servo angle are defined as

$$\rho_{m_j} = r_{pulley}\theta_{servo} \tag{2.18}$$

$$\dot{\rho}_{m_j} = r_{pulley}\dot{\theta}_{servo} \tag{2.19}$$

$$\ddot{\rho}_{m_j} = r_{pulley}\ddot{\theta}_{servo} \tag{2.20}$$

where r_{pulley} represents the radius of the pulley placed on the servo for the mass-actuator system. Hinge torque due to aerodynamic forces on control surfaces are obtained and modified from Ref. [111]. It can be defined as

$$\tau_{hinge} = \left(\frac{1}{2}\rho_{air}V^2\right)(c_{CS}L_{CS})\left(\frac{c_{CS}\sin\delta_{CS}}{2}\right) \tag{2.21}$$

where c_{CS} and L_{CS} are the chord length and span of control surfaces, respectively. Relationship between hinge torque and load torque on servo depends on the ratio between control surface arm and servo arm. It can be defined as

$$\tau_{load} = \tau_{hinge}\frac{r_{servo}}{r_{CS}} \tag{2.22}$$

Load torque on the servo due to gravitational forces generated by mass-actuators can be found as

$$\tau_{load} = G_{m_j} r_{pulley} \tag{2.23}$$

where

$$G_{m_j} = \mathbf{R_{B_R I}}\begin{bmatrix} 0 \\ 0 \\ m_j g \end{bmatrix} \tag{2.24}$$

where g is acceleration of gravity. If the mass-actuator can only move along 1-axis, the load torque is found by using the respective component of gravitational forces in Eq. (2.23).

Required servo current, $\imath_s$, to control the actuator depends on the torque that is applied due to load on the servo and can be calculated as

$$\imath_s = \imath_{nl} + \left(\frac{\imath_{st} - \imath_{nl}}{\tau_{servo_{max}}}\right)\tau_{servo} \tag{2.25}$$

where $\tau_{servo_{max}}$ is the maximum (stall) torque that the servo can produce, $\imath_{nl}$ is the current that the servo is required with no load condition and $\imath_{st}$ is the maximum current that occurs when the maximum torque is reached.

2.4 Endurance and Range

This section presents the procedure followed to compute the endurance and range based on propulsion and actuator systems for an airplane with propeller driven by an electric motor powered from a battery set. This is to quantify the performance of internal mass actuation as compared to conventional control surfaces in terms of endurance and range, which directly depend on battery life.

Battery capacity, C_b, is defined as the time integral of the current flow out of the battery from the beginning of the current flow ($t = 0$) to a time when it reaches a specified cut-off voltage, and can be expressed as [112]

$$C_b = \int_{\Delta_t} \imath \, dt \tag{2.26}$$

Hence, endurance can be calculated as

$$E = \frac{C_b}{\imath_T} \tag{2.27}$$

where the current, $\imath_T$, is defined as the sum of motor and servo current drawn from a battery

$$\imath_T = \imath_m + \imath_s \tag{2.28}$$

Range is calculated from the endurance

$$R = E\,V \tag{2.29}$$

2.5 Applied Forces and Moments

The aircraft with mass-actuation and the aircraft with aero-actuation are identical in every aspect except the control mechanism. Thus, the same aerodynamic model is used for both aircraft. For the mass-actuated aircraft, the terms associated with aerodynamic control surfaces are set to zero except rudder in the cases when the mass-actuation is augmented with rudder. The aerodynamic forces and moments are calculated as

$$X = C_X Q S \tag{2.30}$$

$$Y = C_Y Q S \tag{2.31}$$

$$Z = C_Z Q S \tag{2.32}$$

$$\mathcal{L} = C_l Q S b \tag{2.33}$$

$$\mathcal{M} = C_m Q S c \tag{2.34}$$

$$\mathcal{N} = C_n Q S b \tag{2.35}$$

where S is wing area, b is wing span, c is chord length of the wing and Q is dynamic pressure and defined as

$$Q = \frac{1}{2}\rho_{air} V^2 \tag{2.36}$$

where ρ_{air} is air density.

The components of the gravitational forces in the body frame, due to the aircraft mass and moving-mass actuators, are

$$\begin{bmatrix} G_x \\ G_y \\ G_z \end{bmatrix} = \mathbf{R_{B_R I}} \begin{bmatrix} 0 \\ 0 \\ m_T g \end{bmatrix} \tag{2.37}$$

where

$$m_T = M + \sum_{j=1}^{k} m_j \tag{2.38}$$

However, the moving mass-actuators produce both gravitational forces and moments. In fact, the gravitational moment by the moving mass-actuators is the mechanism for alternative moment-generation. The components in the body frame of the gravitational moments due to the moving mass-actuators are

$$\begin{bmatrix} \mathcal{L}_{mass} \\ \mathcal{M}_{mass} \\ \mathcal{N}_{mass} \end{bmatrix} = -\sum_{j=1}^{k} S(\rho_{m_j})\mathbf{R_{B_R I}} \begin{bmatrix} 0 \\ 0 \\ m_j g \end{bmatrix} \tag{2.39}$$

where $\mathbf{S}(\rho_{\mathbf{m_j}})$ is the skew-symmetric matrix of the representation of the position of the jth moving mass, which is written in body frame, as

$$\rho_{m_j} = \begin{bmatrix} \rho_{m_{jx}} & \rho_{m_{jy}} & \rho_{m_{jz}} \end{bmatrix}^T \tag{2.40}$$

To calculate components of the thrust generated by the propeller and the torque required to turn the propeller, two frames associated with the propeller are defined. First, propeller frame is defined where the x-axis of the propeller frame is always normal to the propeller disk and denoted as $[\underline{\mathbf{p}}]$. Flow frame, which is similar to wind frame, is defined where the x-axis of flow frame is always along with the velocity vector, $\underline{V_p}$, and the z-axis of flow frame is always on x_p-z_p plane of the propeller frame and it is denoted as $[\underline{\mathbf{f}}]$. Propeller and flow frame are shown in Fig. 2.4.

Flow angle is defined between x-axes of propeller frame and flow frame. Using the cosine theorem in terms of velocity components in propeller frame

$$\delta_p = \cos^{-1}\left(\frac{u_p}{V_p}\right) \tag{2.41}$$

where

$$V_p = \sqrt{u_p^2 + v_p^2 + w_p^2} \tag{2.42}$$

Substituting Eq. (2.42) into Eq. (2.41), the flow angle is found to be

$$\delta_p = \cos^{-1}\left(\cos\alpha_p \cos\beta_p\right) \tag{2.43}$$

where α_p is angle of attack of $\underline{V_p}$ and β_p is sideslip angle of $\underline{V_p}$ in propeller frame.

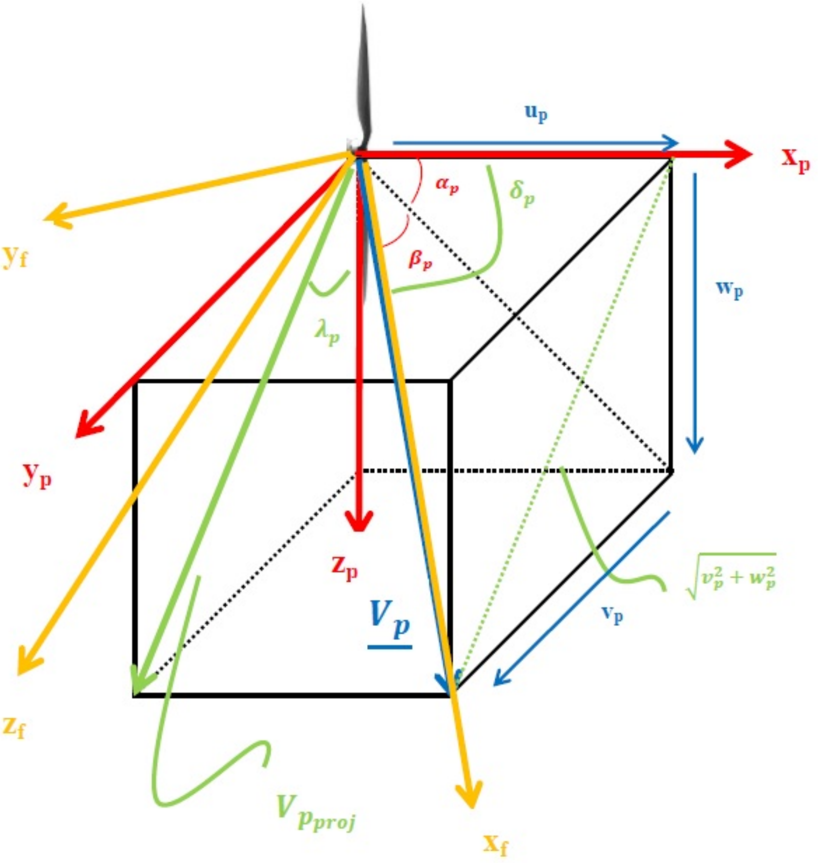

Figure 2.4. Propeller and flow frame.

Projection of the velocity vector $\underline{V_p}$ on y_p-z_p plane of the propeller frame is shown in Fig. 2.5 to find the components of normal force, P_N, and the moment, N_P, on propeller disk. Projection angle, λ_p, is defined between z-axis of propeller frame and the projection of the velocity vector of the propeller, $\underline{V_p}$. The normal force, P_N, which is normal to x_p, on y_p-z_p plane is always along the projection of $\underline{V_p}$, i.e. if there is only angle of attack in the flow, projection of $\underline{V_p}$ will along with z_p or if there is only sideslip angle in the flow, projection of $\underline{V_p}$ will along with y_p. Hence, projection angle, λ_p, can be found as

$$\tan \lambda_p = \frac{v_p}{w_p} = \frac{V_p \sin \beta_p}{V_p \cos \beta_p \sin \alpha_p} \tag{2.44}$$

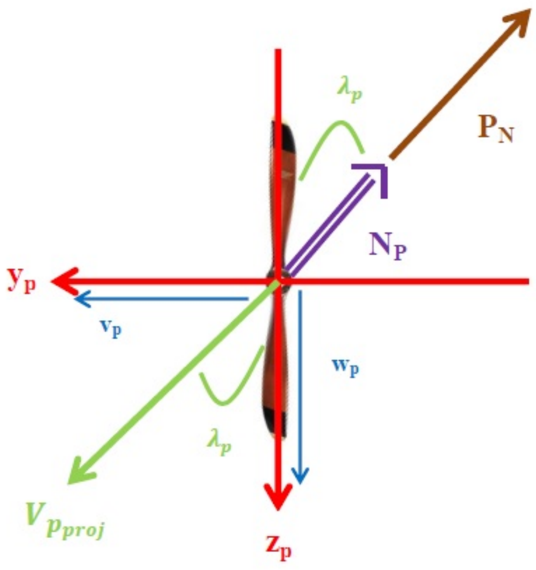

Figure 2.5. Projection of the velocity vector and y_p-z_p plane of the propeller frame.

By manipulating Eq. (2.44), λ_p is found to be

$$\lambda_p = \tan^{-1} \frac{\sin \beta_p}{\cos \beta_p \sin \alpha_p} \tag{2.45}$$

Hence, the components of the normal force, P_N, in the propeller frame are

$$\begin{bmatrix} T_{p_x} \\ T_{p_y} \\ T_{p_z} \end{bmatrix} = \begin{bmatrix} 0 \\ -P_N \sin \lambda_p \\ -P_N \cos \lambda_p \end{bmatrix} \tag{2.46}$$

and the components of the moment, N_P, in the propeller frame are

$$\begin{bmatrix} \tau_{p_x} \\ \tau_{p_y} \\ \tau_{p_z} \end{bmatrix} = \begin{bmatrix} 0 \\ -N_P \sin \lambda_p \\ -N_P \cos \lambda_p \end{bmatrix} \tag{2.47}$$

Thrust generated by the propeller and the torque required to turn the propeller depend on the propeller speed and the aircraft speed. The coefficients of thrust and propeller torque are available as lookup tables and they can be defined in terms of propeller speed, ω_p, and the aircraft speed, V, as the functions of these parameters.

$$C_T = f(\omega_p, V) \tag{2.48}$$

$$C_Q = f(\omega_p, V) \tag{2.49}$$

Hence, thrust generated by propeller and torque required to turn the propeller can be calculated in propeller frame as

$$T_{p_x} = \rho n^2 D_p^4 C_T \tag{2.50}$$

$$\tau_{p_x} = \rho n^2 D_p^5 C_Q \tag{2.51}$$

In addition to thrust and torque generated by propeller, a number of other factors are effective on propeller orientation relative to the velocity vector $\underline{V_p}$ for any general motion of the airplane such as propeller aerodynamics with different angle of attack and/or sideslip angles and gyroscopic effects. If the flow is not axial to the propeller as shown in Fig. 2.4, i.e. propeller has the angle of attack to the flow, there are a normal force, P_N, and a moment (P-factor), N_P, generated on the propeller disk plane due to aerodynamic angles [113, 114]. Ref. [113, 114] studied only the normal force and the moment due to angle of attack. In this study, sideslip angle is also considered in addition to angle of attack and the normal force and the moment on the propeller disk are obtained by modifying the studies in Ref. [113, 114]. Hence, the flow angle, δ_p, in Eq. 2.43 is defined by combining the propeller angle of attack, α_p, and sideslip angle, β_p, in propeller frame. The normal force, P_N, and the moment,

N_P, on the propeller disk based on flow angle can be found by modifying the equation in Ref. [113, 114] as

$$P_N = \frac{\sigma Q A_p}{2} \left\{ \overline{C_{l_p}} + \frac{aJ}{2\pi} \ln \left[1 + \left(\frac{\pi}{J} \right)^2 \right] + \frac{\pi}{J} C_{d_p} \right\} \delta_p \tag{2.52}$$

$$N_P = \frac{\sigma Q A_p R_p}{2} \left\{ \left(\frac{2\pi}{3J} \right) \overline{C_{l_p}} + \frac{a}{2} \left[1 - \left(\frac{J}{\pi} \right)^2 \ln \left(1 + \left(\frac{\pi}{J} \right)^2 \right) \right] - \frac{\pi}{J} C_{d_p} \right\} \delta_p \tag{2.53}$$

where

$$\overline{C_{l_p}} = \left(\frac{3J}{2\pi} \right) \left[\frac{2}{\sigma Q A_p} \frac{J}{\pi} T_{p_x} + C_{d_p} \right] \tag{2.54}$$

and

$$J = \frac{u_p}{n D_p} \tag{2.55}$$

where σ is the ratio of propeller blade area to propeller disk area, Q is dynamic pressure, A_p is propeller disk area, R_p is radius of propeller, D_p is diameter of propeller, J is advance ratio, n is revolution per second of propeller, a is airfoil lift curve slope, $\overline{C_{l_p}}$ is lift coefficient of the propeller, C_{d_p} is drag coefficient of the propeller, T_{p_x} is the x-component of the thrust in propeller frame.

Finally, thrust and moment components in propeller frame are obtained by combining the forces and moments on the propeller disk from Eqs. (2.46)-(2.47) and the thrust produced by propeller and the direct torque required to turn the propeller from Eqs. (2.50)-(2.51).

$$T_p = \begin{bmatrix} T_{p_x} & T_{p_y} & T_{p_z} \end{bmatrix}^T \tag{2.56}$$

$$\tau_p = \begin{bmatrix} \tau_{p_x} & \tau_{p_y} & \tau_{p_z} \end{bmatrix}^T \tag{2.57}$$

In some situations, alignment of thrust line with respect to the origin of the body frame of the airplane is desired by placing the propeller above/below the origin of the body frame of the airplane or inclining the thrust line with some angles to the body frame of the airplane. If the inclining of the propeller is performed, rotational matrix from body frame to propeller frame is defined as

$$\mathbf{R_{PB}} = \begin{bmatrix} \cos\theta_p \cos\psi_p & \cos\theta_p \sin\psi_p & -\sin\theta_p \\ -\sin\psi_p & \cos\psi_p & 0 \\ \sin\theta_p \cos\psi_p & \sin\theta_p \sin\psi_p & \cos\theta_p \end{bmatrix} \tag{2.58}$$

where ψ_p is the rotation angle around the body z-axis and θ_p is the rotation angle around the body y-axis. Hence, the forces produced by propeller and the normal forces on y_p-z_p plane of the propeller frame due to aerodynamic effects of the flow angle are written in body frame as

$$\begin{bmatrix} T_x \\ T_y \\ T_z \end{bmatrix} = \mathbf{R_{PB}}^T \begin{bmatrix} T_{p_x} \\ T_{p_y} \\ T_{p_z} \end{bmatrix} \tag{2.59}$$

Similarly, the moments on y_p-z_p plane of the propeller frame due to aerodynamic effect of the propeller and the moments generated by the thrust components from Eq. (2.59) are written in body frame as

$$\tau_{aero} = \mathbf{R_{PB}}^T \begin{bmatrix} 0 \\ \tau_{p_y} \\ \tau_{p_z} \end{bmatrix} + \left\{ -\mathbf{S}(\mathbf{r_{pcg}}) \begin{bmatrix} T_x \\ T_y \\ T_z \end{bmatrix} \right\} \tag{2.60}$$

where $\mathbf{S}(\mathbf{r_{pcg}})$ represents the skew symmetric matrix of the position vector of the propeller with respect to the origin of the body frame of the airplane. Further, direct torque required to turn the propeller can be written in body frame as

$$\tau_{DT} = \mathbf{R_{PB}}^T \begin{bmatrix} \tau_{p_x} \\ 0 \\ 0 \end{bmatrix} \tag{2.61}$$

Furthermore, gyroscopic effect due to acceleration of propeller speed and pitch, roll or yaw change of the airplane is defined in body frame as [115]

$$\tau_{gyro} = \begin{bmatrix} -\cos\psi_p \cos\theta_p \\ -\sin\psi_p \cos\theta_p \\ \sin\theta_p \end{bmatrix} J_p\dot{\omega}_p + \begin{bmatrix} r\sin\psi_p\cos\theta_p + q\sin\theta_p \\ -r\cos\psi_p\cos\theta_p - p\sin\theta_p \\ -p\sin\psi_p\cos\theta_p + q\cos\psi_p\cos\theta_p \end{bmatrix} J_p\omega_p \quad (2.62)$$

where J_p represents the propeller inertia. Finally, total moments due to propeller effect in body frame can be written as

$$\begin{bmatrix} \mathcal{L}_{prop} \\ \mathcal{M}_{prop} \\ \mathcal{N}_{prop} \end{bmatrix} = \tau_{DT} + \tau_{aero} + \tau_{gyro} \quad (2.63)$$

The components of thrust and propeller torque are included in the final form of the applied force and moment expressions and the final forms are

$$F_{B_R} = \begin{bmatrix} T_x + X + G_x \\ T_y + Y + G_y \\ T_z + Z + G_z \end{bmatrix} \quad (2.64)$$

$$M_{B_R} = \begin{bmatrix} \mathcal{L}_{prop} + \mathcal{L} + \mathcal{L}_{mass} \\ \mathcal{M}_{prop} + \mathcal{M} + \mathcal{M}_{mass} \\ \mathcal{N}_{prop} + \mathcal{N} + \mathcal{N}_{mass} \end{bmatrix} \quad (2.65)$$

2.6 Specifications of the Airplane Analyzed

This section presents the specifics of the airplane model used in this dissertation. The airplane model parameters are chosen to represent an electric-powered RC airplane, UltraStick 25E (see Fig. 2.6). This aircraft has symmetric airfoil wings and all three conventional control surfaces. In Table 2.1, geometric parameters of the aircraft is tabulated. The aerodynamic model and the geometry of the airplane are obtained from Ref. [20]. Aerodynamic model was originally developed by Ref. [116] through wind tunnel and flight tests including the propeller effect. Ref. [20] further tuned the aerodynamic coefficients based on two RC pilots' perceptions of how much the flight simulator were felt like actual flight of the airplane.

Figure 2.6. RC Airplane UltraStick 25E [19].

Table 2.1. Geometric parameters for UltraStick 25E [20]

Description	**Value**	**Unit**
Wing Area, S	0.32	m^2
Overall Length	1.05	m
Wing Span, b	1.2	m
Wing Chord, c	0.3	m
Total Weight, m_T	1.9	kg

The lift and drag coefficients are

$$C_L = C_{L_0} + C_{L_\alpha}\alpha + C_{L_{\delta_e}}\delta_e + \frac{c}{2V}(C_{L_q}q + C_{L_{\dot\alpha}}\dot\alpha) \tag{2.66}$$

$$C_D = C_{D_{\delta_e}}\delta_e + C_{D_{\delta_r}}\delta_r + C_{D_{\delta_a}}\delta_a + K_2(\beta)\alpha^2 + K_1(\beta)\alpha + K_0(\beta) \tag{2.67}$$

where the last three terms of C_D expression are added to model the contribution of sideslip angle on drag. The coefficients K_2, K_1 and K_0 are second order polynomials of β and determined based on experimental data of a micro air vehicle [117].

Aerodynamic forces and moments coefficients in the body frame are

$$C_X = C_L \sin\alpha - C_D \cos\alpha \tag{2.68}$$

$$C_Y = C_{Y_\beta}\beta + C_{Y_{\delta_r}}\delta_r + \frac{b}{2V}(C_{y_p}p + C_{y_r}r) \tag{2.69}$$

$$C_Z = -C_L \cos\alpha - C_D \sin\alpha \tag{2.70}$$

$$C_l = C_{l_\beta}\beta + C_{l_{\delta_a}}\delta_a + C_{l_{\delta_r}}\delta_r + \frac{b}{2V}(C_{l_p}p + C_{l_r}r) \tag{2.71}$$

$$C_m = C_{m_0} + C_{m_\alpha}\alpha + C_{m_{\delta_e}}\delta_e + \frac{c}{2V}(C_{m_q}q + C_{m_{\dot\alpha}}\dot\alpha) \tag{2.72}$$

$$C_n = C_{n_\beta}\beta + C_{n_{\delta_a}}\delta_a + C_{n_{\delta_r}}\delta_r + \frac{b}{2V}(C_{n_p}p + C_{n_r}r) \tag{2.73}$$

where δ_a is aileron deflection, δ_e is elevator deflection and δ_r is rudder deflection.

For the electric motor, E-Flite Power 25 BL Outrunner Motor [21] is chosen as a reference. The characteristics of the motor are tabulated in Table 2.2. Some of the parameters that are not provided by the manufacturer are obtained from a similar electric motor with similar physical characteristics. k_e, k_T, L, and J_m are provided in Ref. [118] for that motor. k_f is obtained from the nominal and no load condition of Eq. (2.12) at idle current, $\imath_0$. Thunder Power 4400mAh 3S2P 11.1V Li-Po is used for power supply to the propulsion system. The characteristics of the battery are tabulated in Table 2.3.

The propeller is directly connected to the motor shaft, and thus the propeller speed is equal to the motor speed, and the torque acting on the motor is the same

Table 2.2. E-Flite Power 25 BL Outrunner Motor [21]

Description	**Value**	**Unit**
k_v	870	RPM/V
k_T	0.011	Nm/A
k_e	0.011	$V/(rad/s)$
k_f	2.8915×10^{-5}	$Nm/(rad/s)$
R	0.03	Ω
L	0.33×10^{-3}	H
J_m	1.836×10^{-6}	Kgm^2
Weight	190	g
$\imath_0$	$2.4(@10V)$	A

Table 2.3. Thunder Power 4400mAh 3S2P 11.1V ProLite + Power 25C LiPo [22]

Description	**Value**	**Unit**
Capacity, C_b	4400	mAh
Volt, $\mathcal{V}_{max}$	11.1	V
Configuration	$3S2P$	
Weight	306	g
Max Cont. Discharge	25	C

as the torque required by the propeller. Propeller torque, τ_p, is calculated based on APC 12 x 8E propeller data [119] by using a lookup table for given airspeed, V, and propeller angular speed, ω_p. Thrust generated by the propeller is also calculated from the same propeller data for aircraft speed, V, and propeller angular speed, ω_p. Figures 2.7 and 2.8 visualize propeller data in terms of the thrust and torque versus aircraft airspeed for various propeller speeds in RPM.

In this study, servo dynamics is considered for aero-actuation to deflect the control surfaces and mass-actuation to move the masses. PID controllers are also designed for both systems to track the commanded control inputs. Hence, PID and servo dynamics parameters of both aero- and mass-actuated systems are tuned to obtain reasonable performance. In Ref. [20], actuation delay for control surfaces is

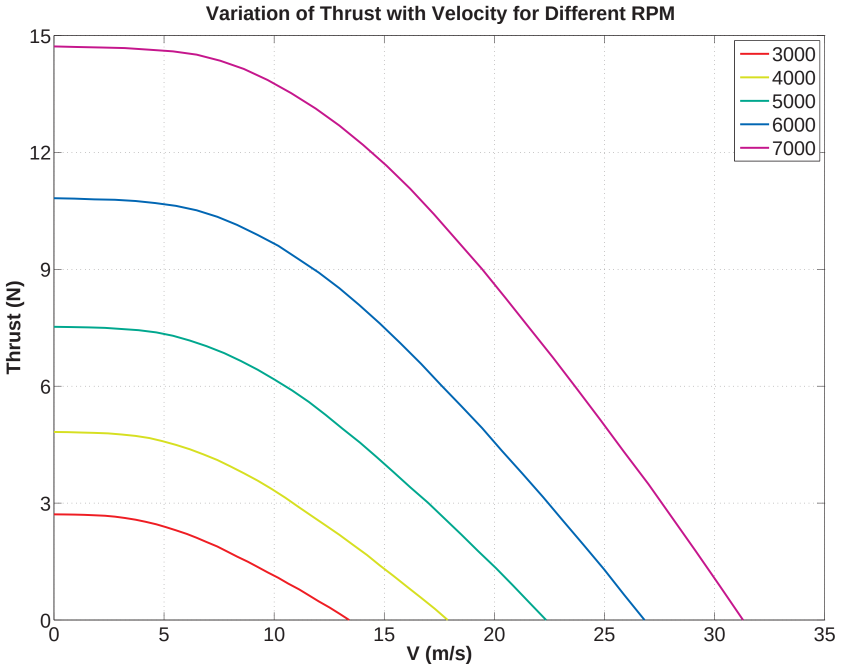

Figure 2.7. Variation of thrust with respect to velocity for different RPM.

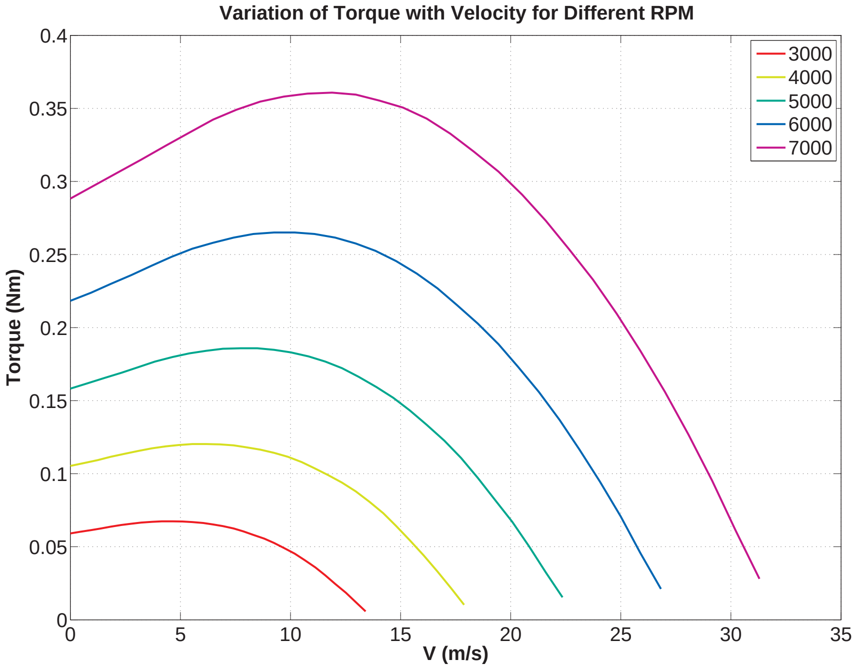

Figure 2.8. Variation of torque with respect to velocity for different RPM.

given as 22 milliseconds. During the parameter tuning for servo dynamics, one degree rotation is considered with the delay of 22 milliseconds approximately.

Table 2.4. Physical constraints of control inputs and propeller speed

Limitations	**Units**
$-20 \leq \delta_e \leq 20$	deg
$-23 \leq \delta_a \leq 23$	deg
$-25 \leq \delta_r \leq 25$	deg
$-0.7 \leq \rho_{m_{1_x}} \leq 0.35$	m
$-0.6 \leq \rho_{m_{2_y}} \leq 0.6$	m
$0 \leq \omega_p \leq 9657$	RPM

Table 2.5. Control surface dimensions

Control Surface	**Chord (m)**	**Length (m)**
Aileron	0.05	0.85
Elevator	0.1	0.4
Rudder	0.1	0.2

Table 2.6. HS-5085MG Premium Metal Gear Micro Servo [23]

Description	**Value**	**Units**
Operating Voltage	4.8	V
Operating Speed	0.17	$s/60^\circ$
Stall Torque	0.353	Nm
No Load Current	0.23	A
Stall Current	1.7	A
Weight	21.83	$grams$

In the simulation, physical constraints of the control inputs such as maximum/minimum deflections or positions and rate limit of the servos are considered. Maximum propeller speed that the electric motor can produce from the maximum supplied voltage available is also considered. Constraints are tabulated in Table 2.4. Physical constraints of the aero-actuators are provided in Ref. [20]. The limitations of the mass-actuators are the physical limitations of the airplane since they are moving inside the fuselage or along the wing as showed in Table 2.1. Control surface dimensions are required to calculate the hinge torque for each control surfaces. These information are not provided by the manufacturer directly. Hence, approximate numbers are obtained by scaling the overall aircraft dimensions and these numbers are tabulated in Table 2.5. Characteristics of the servo used for both aero- and mass-actuated systems are tabulated in Table 2.6. Maximum/minimum rotations of the servo is adjusted by the maximum/minimum deflections or positions of the actuators. For the mass-actuation, multiple turn is required if the same servo is used. The servo can be modified to perform continuous rotation. In the literature, it is observed that encoders are designed to obtain the position feedback for the modified servos. There are also continuous rotation servos with position feedback using a potentiometer available in the market. However, same servo is used for both actuation systems for comparison in this study. The ratio between the servo arm and control surface arm, $\frac{r_{servo}}{r_{CS}}$, is selected as 0.5 for each control surfaces. The radius of the pulley, r_{pulley}, is selected as 0.0254 m or 1 $inch$.

In this work, the weight of the longitudinal mass-actuator is chosen as 0.3 kg, which is comparably the same with the battery weight as shown in Table 2.3 if the battery is to be desired as the part of the mass-actuation. Further, the weight of the lateral mass-actuator is chosen as 0.1 kg. The total weight of the aircraft is 1.9 kg as shown in Table 2.1 and the ratio between the weight of the mass-actuators and the total weight of the airplane is 20% approximately. The weights of mass-actuators chosen here are the nominal values for this work. On the other hand, different weights of mass-actuators are also implemented to understand the effect of the mass-actuators on aircraft trim in Section 4.6.

This work is done for the same airplane with three different control configurations: (1) standard aerodynamic control surfaces (aero-actuated airplane), (2) mass-actuation augmented with rudder (mass-rudder-actuated airplane), and (3) only mass-actuation (mass-actuated airplane). The aircraft with the first configuration is called “aero-actuated” and denoted as “A-A” aircraft. The aircraft with the second configuration is called “mass-rudder-actuated” and denoted as “MRA” aircraft. The one with the third configuration is called “mass-actuated” and denoted as “M-A” aircraft.

2.7 Summary of the Chapter

In this chapter, equations of motions were presented including the effect of mass-actuation on dynamics. Propulsion system model and actuator system model were detailed. For actuator system model, it was assumed that same servo dynamics was used for both aero- and mass-actuation. Endurance and range equations were introduced to show the benefit of using mass-actuation. Applied forces and moments were presented. Since the aircraft with aero-actuation and mass-actuation were identical in every aspect except the control mechanism, the same aerodynamic model was used for both aircraft. The effects of propeller on aircraft dynamics were discussed and equations were presented. Finally, specifications of the airplane used in this work were presented.

CHAPTER 3

PROPELLER AND ACTUATOR EFFECTS ON AIRCRAFT RESPONSE & PERFORMANCE

In this chapter, propeller and actuator effects on aircraft response and performance are introduced. First, different sources of propeller effect on aircraft performance is shown. Second, the effect of placement and alignment of the propeller is discussed. Finally, actuator effect on aircraft performance is shown and comparison between aero- and mass-actuation is discussed.

3.1 Propeller Effect on Aircraft Performance

In this section, propeller effect on aircraft performance is discussed. For small unmanned air vehicle, the effect of propeller may not be ignored. Further, the placement or alignment of propeller with respect to the origin of the body frame of the aircraft may change the performance.

3.1.1 Different Sources of Propeller Effect

In this subsection, the effect of different sources of propeller on aircraft performance is shown. Propeller direct torque, propeller aerodynamic torque and gyroscopic torque are defined as the different sources of propeller effect in Eq. (2.63). Results of these sources are shown on the endurance performance for cruise and steady-state turn and reasons are explained. Since the M-A aircraft is more affected by propeller due to lack of rudder and the effects are more visible, discussions are done for this aircraft only. Further, "No Propeller" case is defined to show the importance of propeller on aircraft performance and the propeller effect is not included in Eq. (2.65). Results of the effect of different propeller sources for cruise and steady-state turn are shown in Figs. 3.1-3.9. In these figures, "NP" represents the results with no propeller effect, "DT only" represents the propeller direct torque only in the aircraft dynamics, "DT + Aero" represents the propeller aerodynamic effect in addition to propeller direct torque and "Full" represents all the propeller effect sources defined in Eq. (2.63).

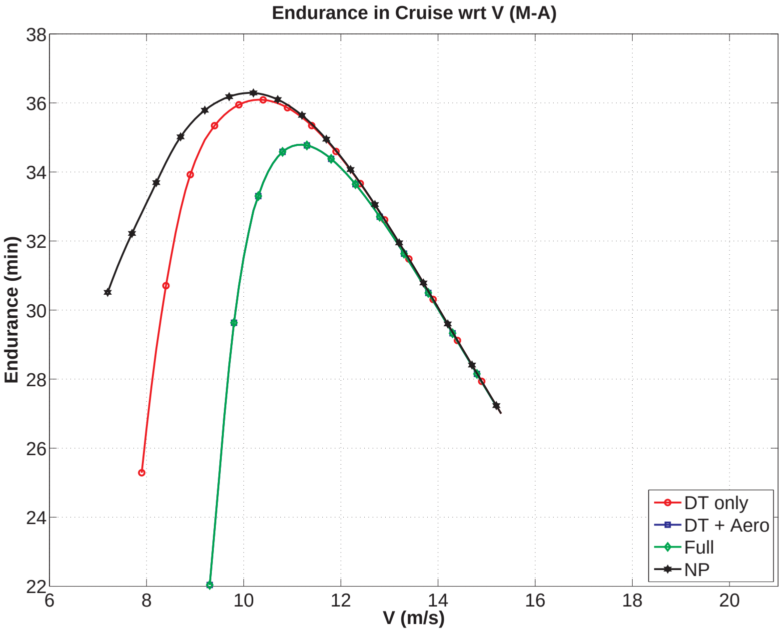

Figure 3.1. Different sources effect on endurance with respect to V in cruise.

It is obvious from Fig. 3.1 that the endurance of the aircraft decreases due to propeller effect. This is due to fact that higher thrust is required with propeller effect as shown in Fig. 3.2. Any of propeller effect is important on aircraft performance since some sideslip angle is required especially in lower speed ranges even in cruise flight as seen in Fig. 3.3 and that increases the required thrust. Furthermore, if the

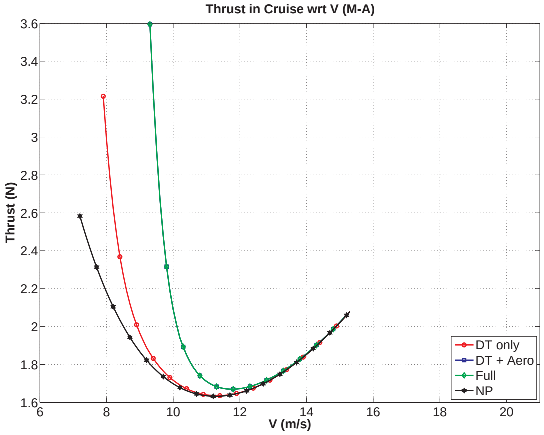

Figure 3.2. Different sources effect on thrust with respect to V in cruise.

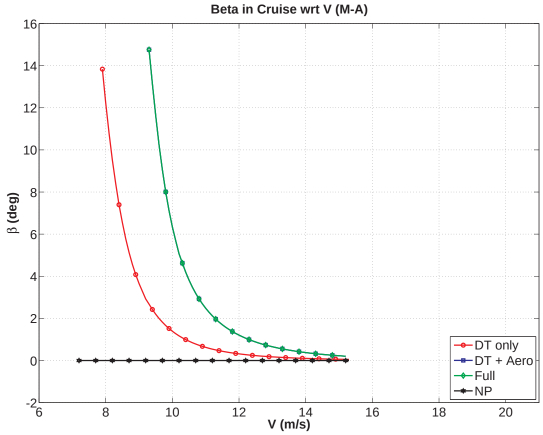

Figure 3.3. Different sources effect on sideslip with respect to V in cruise.

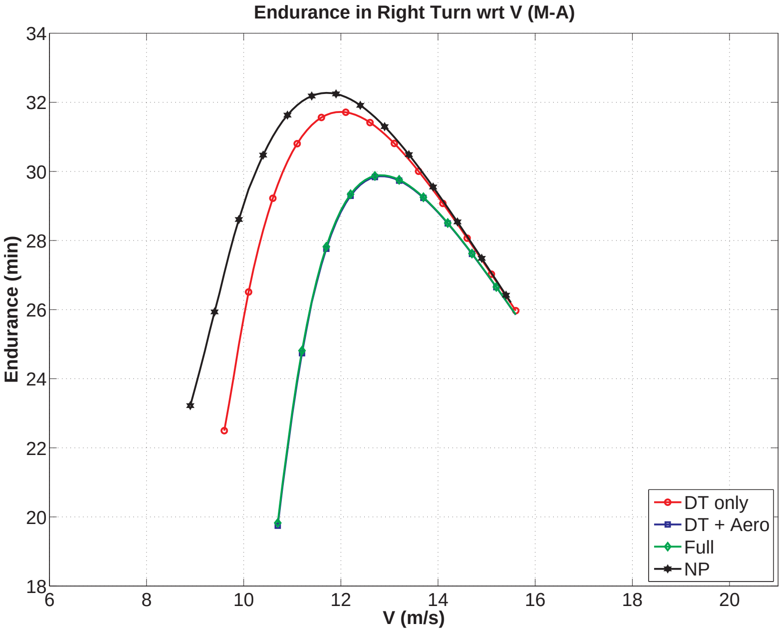

Figure 3.4. Different sources effect on endurance with respect to V in right turn.

comparison between "DT only" and "DT + Aero" is done, it can be seen that propeller aerodynamics affects the aircraft performance since higher sideslip is required as shown in 3.3. Thus, endurance decreases. Since this is cruise trim, gyroscopic effect can not be seen.

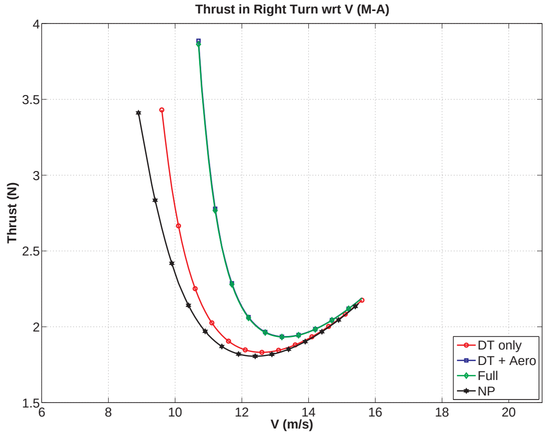

Figure 3.5. Different sources effect on thrust with respect to V in right turn.

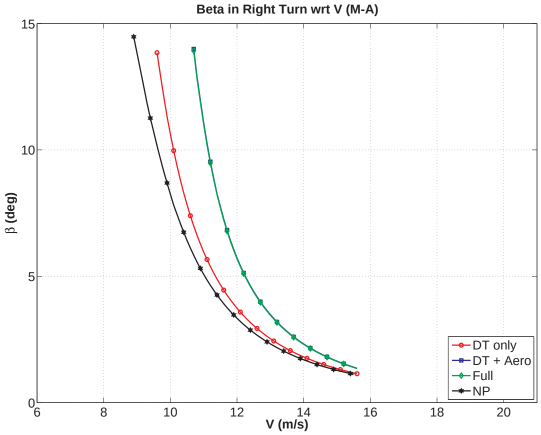

Figure 3.6. Different sources effect on sideslip with respect to V in right turn.

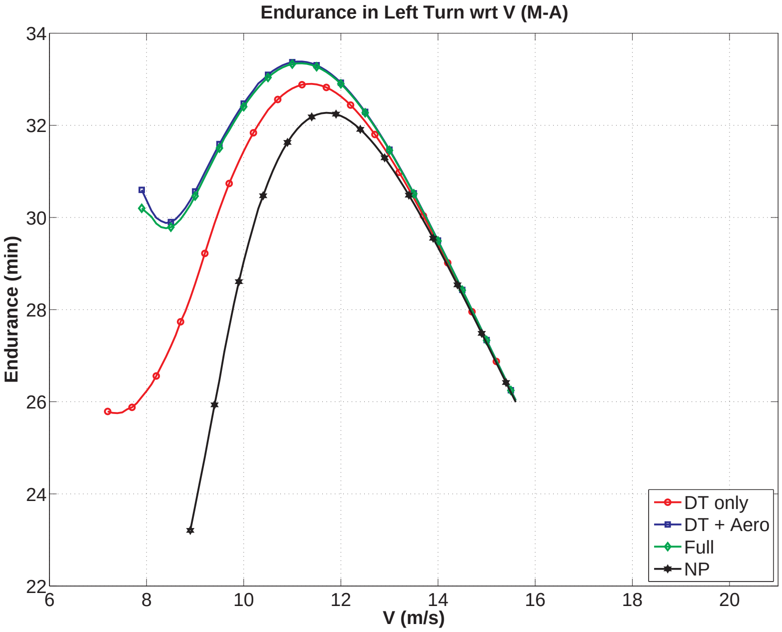

Figure 3.7. Different sources effect on endurance with respect to V in left turn.

Similar to cruise flight, propeller effect decreases endurance for right turn as shown in Fig. 3.4 and increases the required thrust as shown in Fig. 3.5 due to requirement of higher sideslip angle at the same speed as can be seen in Fig. 3.6.

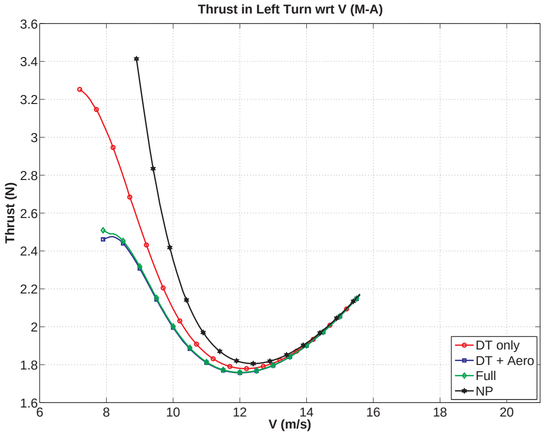

Figure 3.8. Different sources effect on thrust with respect to V in left turn.

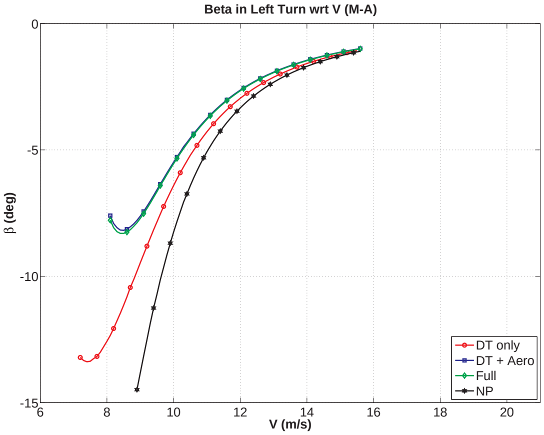

Figure 3.9. Different sources effect on sideslip with respect to V in left turn.

Moreover, gyroscopic effect can be also seen in Figs. 3.4-3.6. It can be said that the gyroscopic effect is not important as compared to the other propeller sources.

Results of left turn performance are shown in Figs. 3.7-3.9. Since the propeller turns clockwise, the performance of left turn differs from the right turn. The required thrust decreases and the endurance increases as shown in Figs. 3.7-3.8 due to the requirement of sideslip angle decreases as shown in Fig. 3.9. Similar to the other flight conditions, the effects of propeller direct torque and propeller aerodynamics are considerable while the gyroscopic effect can be ignored as compared to the others.

3.1.2 Propeller Alignment Effect

Previous subsection showed the effect of propeller on aircraft performance. In this subsection, the effects of propeller alignment and placement are shown with propeller effect. First, propeller is inclined with some angles in four directions while the position vector of the propeller is along with the origin of the body x-axis of the airplane. Second, the vertical position of the propeller is placed above and below of the origin of the body frame of of the airplane.

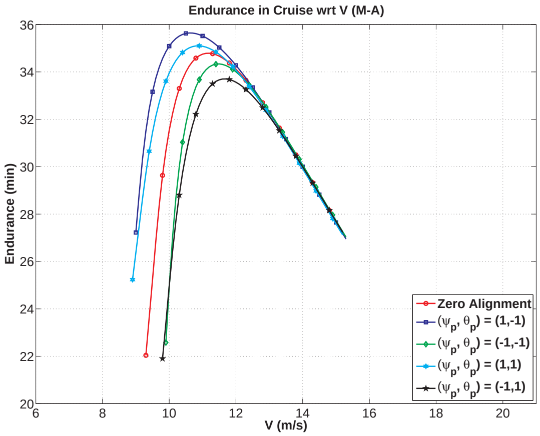

Figure 3.10. Alignment effect on endurance with respect to V in cruise.

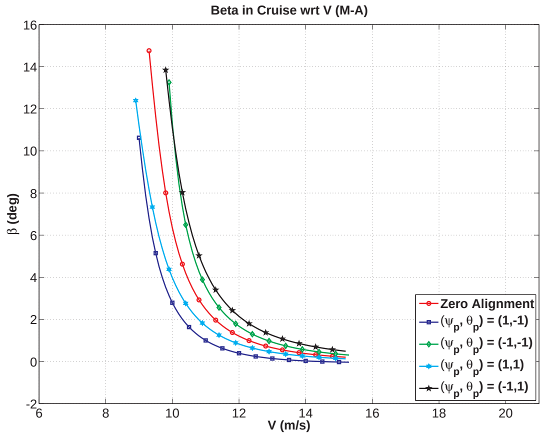

Figure 3.11. Alignment effect on sideslip with respect to V in cruise.

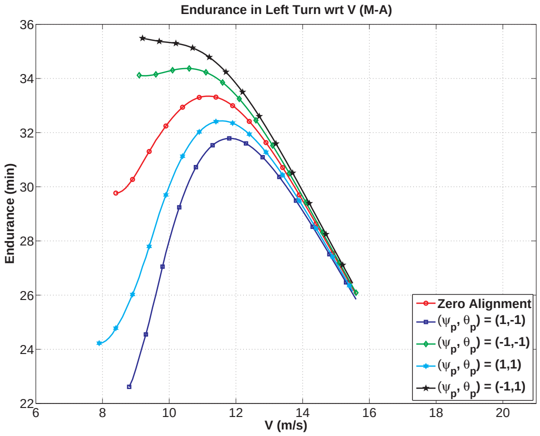

Figure 3.12. Alignment effect on endurance with respect to V in left turn.

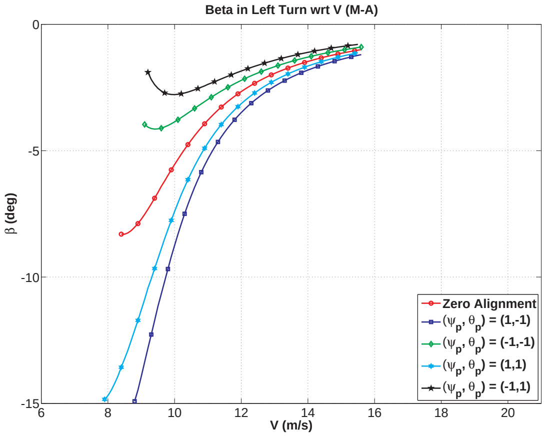

Figure 3.13. Alignment effect on sideslip with respect to V in left turn.

Figures 3.10-3.13 show the results of propeller alignment in four directions with 1 degree for cruise and steady-state left turn flight conditions only since right turn has the similar discussions with cruise results. The most important observation is that alignment of the propeller with right angle increases the endurance as shown in Fig. 3.10 due to requirement of sideslip angle can be reduced, which is shown in Fig. 3.11, especially on the lower speed ranges at the same speed. On the other hand, alignment of the propeller with left angle decreases endurance since it causes higher sideslip angle requirement. Further, results showed that alignment with down angle also reduces the sideslip angle while alignment with up angle increases. Since the results for steady-state right turn are similar to cruise, results are not shown here and discussions for cruise are valid for right turn. For the steady-state left turn, results are in opposition. Alignment of the propeller with left angle increases endurance as shown in Fig. 3.12 and decreases the requirement of sideslip angle as shown in Fig. 3.13 for left turn. On the other hand, some right angle increases the sideslip angle and decreases the endurance at the same speed. In this work, alignment with right and down angles will be chosen since it is useful for cruise flight of the M-A airplane. If loiter is required, right turn can be used since results are similar to cruise condition.

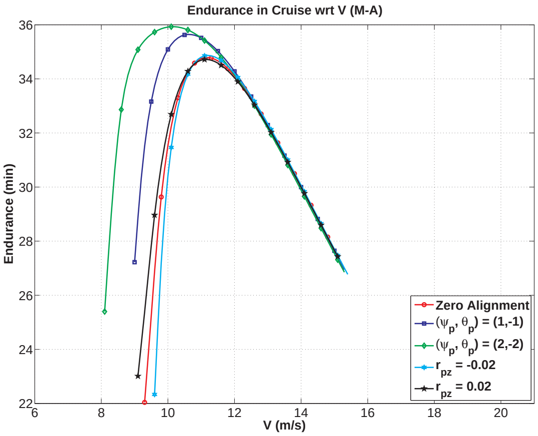

Figure 3.14. Placement effect on endurance with respect to V in cruise.

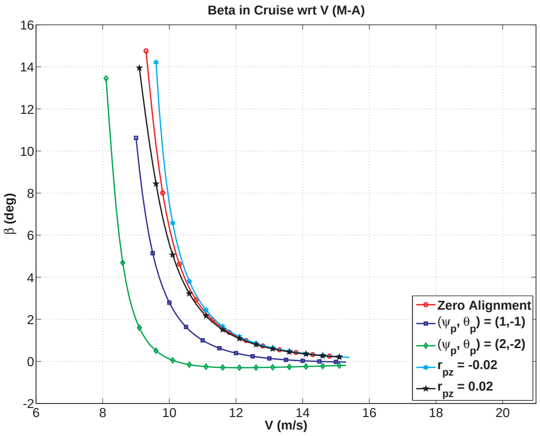

Figure 3.15. Placement effect on sideslip with respect to V in cruise.

Figures 3.14-3.17 show the comparison results for placement of propeller with respect to the origin of the body frame of the airplane (2 cm above or below the origin) and two different configurations of the propeller alignment with right and down angles (the first one has 1 degree and the second one has 2 degrees). The first observation is about placement of the propeller. Figs. 3.14-3.15 show that the placement of the

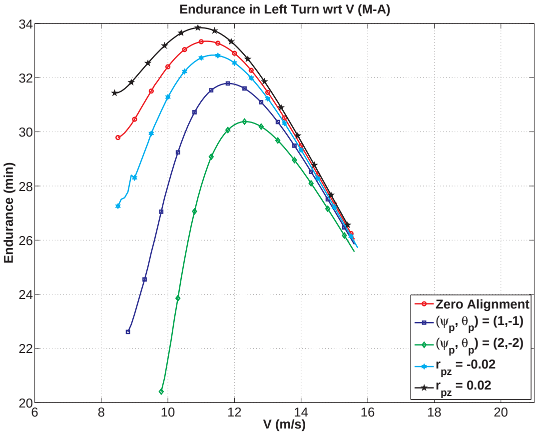

Figure 3.16. Placement effect on endurance with respect to V in left turn.

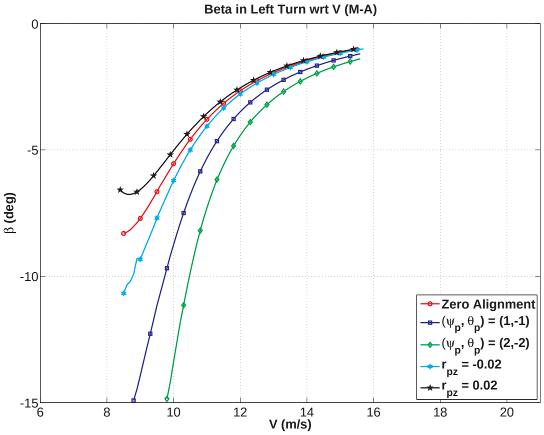

Figure 3.17. Placement effect on sideslip with respect to V in left turn.

propeller gives slightly different results in lower speed ranges and similar results in higher speed ranges as compared to zero alignment of the propeller for cruise flight. On the other hand, alignment of propeller with down and right angles show higher benefit in terms of endurance since the requirement of sideslip angle can be reduced considerably as shown in 3.15. Furthermore, increasing the right and down angles also increases the endurance due to decrease in sideslip. Similar to previous case, steady-state right turn results are very close to cruise. Hence, same discussion is valid. On the other hand, it is the opposite for steady-state left turn. As explained before, alignment with right and down angles of 2 degrees will be chosen for the rest of the work for all aircraft configuration since the handicap of higher sideslip angle in lower speed ranges for cruise flight can be eliminated due to propeller effect.

3.2 Actuator Effect on Aircraft Performance

In this section, the effect of actuator by considering the electric power used by the actuator servos on aircraft endurance is discussed for all aircraft configurations in cruise flight as an example. Furthermore, comparison between aero- and mass-actuation is shown. Finally, the performance of actuators in dynamic simulation is shown.

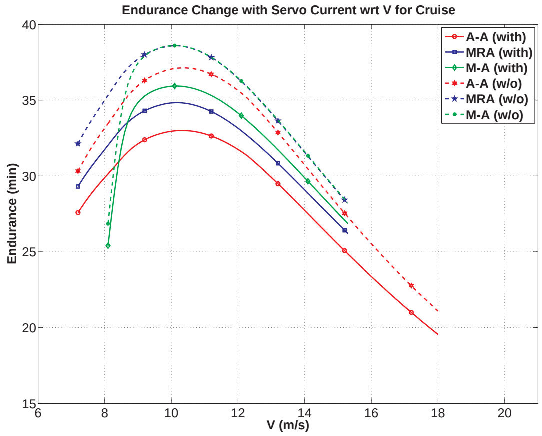

Figure 3.18. Actuator effect on endurance with respect to V in cruise.

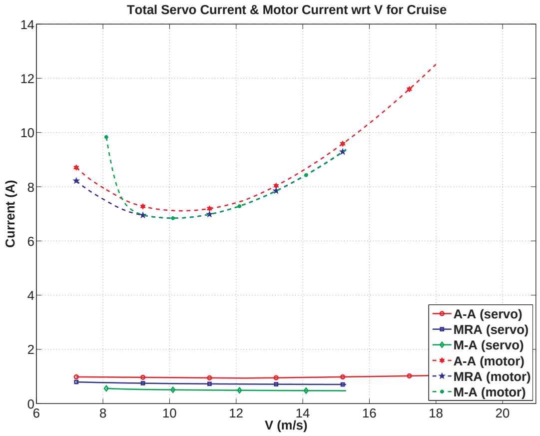

Figure 3.19. Variation of servo and motor current with respect to V in cruise.

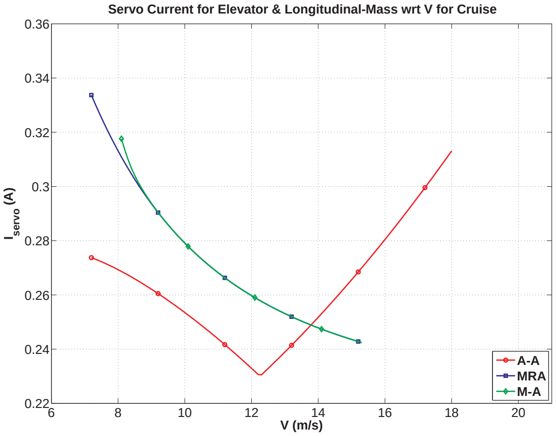

Figure 3.20. Variation of servo current of elevator and long-mass with V in cruise.

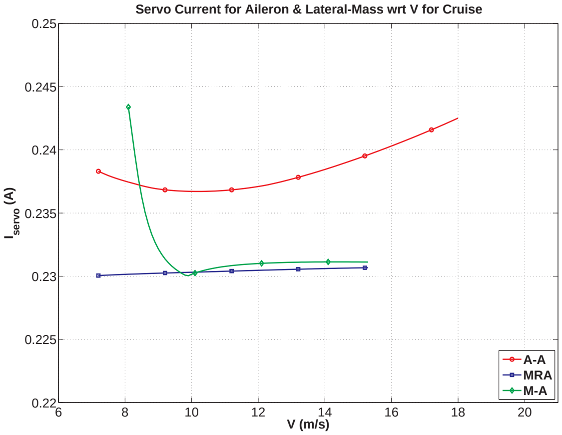

Figure 3.21. Variation of servo current of aileron and lat-mass with V in cruise.

Figures 3.18 shows the endurance results for all aircraft configurations. As expected, including the servo current decreases the endurance for all aircraft and it should be considered in the endurance calculation. On the other hand, the electric motor requires about ten times higher current as compared to the servos in terms of magnitude as shown in Fig. 3.19. Furthermore, aero-actuation requires slightly higher current since A-A airplane uses 4 servos (2 for aileron, 1 for elevator, 1 for rudder) while MRA airplane uses 3 servos (1 for longitudinal-mass, 1 for lateral-mass, 1 for rudder) and M-A airplane uses 2 servos (1 for longitudinal-mass, 1 for lateral-mass) to control the aircraft.

Servo current for aero- and mass-actuation vary with different parameters. These are length of servo and control moment arms for aero-actuation and the weight of the mass-actuators and the pulley radius for mass-actuation as discussed in Section 2.3. Fig. 3.20 shows the comparison of the required current for the same servo between elevator and longitudinal-mass for specified parameters in Section 2.6. Longitudinal-mass requires slightly higher current than the elevator. When the speed increases, servo current decreases for mass-actuation since pitch/angle of attack decreases with increasing speed as shown in Fig. 4.27. For the aero-actuation, servo current decreases with increasing speed until mid-range and increases with increasing speed since higher deflection leads to higher current requirement as shown in Fig. 4.28. When the current drawn for elevator is minimum, the elevator deflection is zero. Similarly, Fig. 3.21 shows the comparison of the required current for the same servo between aileron (1-servo) and lateral-mass for the same parameters. For mid and higher feasible speed range, aileron requires more current for rolling control of the airplane despite of the aileron deflection decreases as shown in Fig. 4.29 since the aircraft speed increases. Furthermore, current required for lateral-mass is higher for M-A airplane than MRA airplane in low speeds. This is due to the fact that M-A airplane has the high trim value of bank angle as shown in Fig. 4.30. When the speed increases, bank angle decreases for M-A airplane. Hence, the currents for lateral-mass for both aircraft are similar since bank angles for both aircraft are similar.

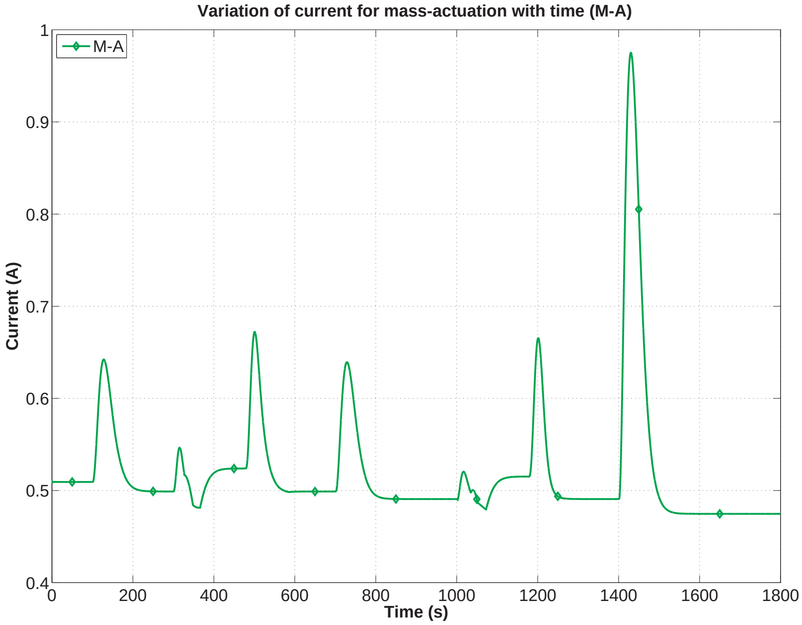

Figure 3.22. Variation of current for mass-actuation with time in mission-1.

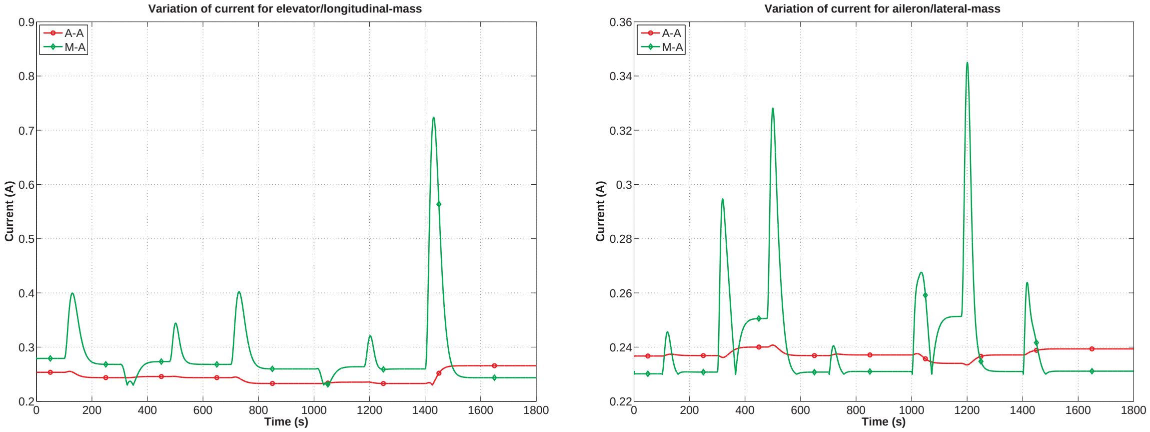

Figure 3.23. Variation of servo current of elevator and lon-mass with time in mission-1.

Figure 3.24. Variation of servo current of aileron and lat-mass with time in mission-1.

Variation of current that the mass-actuation requires for M-A aircraft detailed in the dynamic simulation in Chapter 6.1 is shown in Fig. 3.22. It can be seen that when the flight modes are changed between cruise and turn (between 300-550 s and 1000-1250 s in the figure) and when the speed change is commanded (between 100-200 s, 650-800 s and 1400-1550 s in the figure), current the servo needed to move the mass-actuators are increasing. Especially between 1400-1550 s, current the servo drawn is the highest since speed is commanded from 12 m/s to 15 m/s while the others are only commanded for 1 m/s increase. Since the servo rotates faster to track the commanded speed due to having a smaller radius of the pulley, the current that servo drawn is the highest during that period. After the transitions are complete, servos for the mass-actuators require less current, which is the nominal current for the mission defined. Fig. 3.23 shows the variation of current for longitudinal mass-actuator and elevator and Fig. 3.24 shows the variation of current for lateral mass-actuator and aileron. When the aircraft are in nominal conditions, currents the servos required are close to each other and that confirms the results depicted in Figs. 3.20-3.21. On the other hand, mass-actuators require higher current during the transitions between the flight modes and speed changes while aero-actuation does not require that much current as compared to the mass-actuation. This is due to the fact that the servo for mass-actuation is assumed to be have the capability of multiple turns and that causes to faster turns to track the commanded input. Increasing the radius of pulley on the servo for mass-actuation can decrease the higher requirement of current during transitions. However, that increases the current for nominal flights due to increasing the load torque for mass-actuation in Eq. (2.23). In this study, nominal flight conditions are preferential due to flight missions defined. Hence, the parameters of actuators are selected based on the nominal flight conditions.

3.3 Summary of the Chapter

In this chapter, the effects of propeller and actuator on aircraft response and performance were presented. Firstly, different sources of propeller effects were investigated. The analysis showed that direct torque and aerodynamic effect of the propeller should be considered while gyroscopic effect can be ignorable for M-A airplane since it has the high trim value of sideslip angle for low speeds. When the speed increases, trim value of sideslip angle decreases. Hence, propeller effect on aircraft performances disappeared. Other two aircraft configurations did not show remarkable differences with propeller effect since they had rudder to compensate the sideslip angle. Secondly, the effects of propeller alignment were investigated. Results showed that alignment of the propeller with right and down angles with respect to origin decreases the requirement of high sideslip angle and required thrust and increases the endurance since propeller turns clockwise. Additionally, it was observed that increasing the angles decreases the sideslip angle at the same trim speed and increases the endurance. Results also showed that the placement of the propeller with some distances with respect to origin of the body of the airplane does not show significant changes as compared to having right and down angles. Finally, the effects of actuators on aircraft performance were investigated. It was observed that including the power usage of actuators decreases the endurance of the airplane because of the servo requires the power to keep the desired deflection for aero-action or the position for mass-actuation at the nominal conditions. Results also showed that mass-actuation requires higher current in transitions of the flight while aero-actuation does not require. However, it was observed that the required current drawn from the battery for both actuation systems are similar at the nominal conditions.

CHAPTER 4

TRIM ANALYSES

This chapter presents the trim analyses in cruise, steady-state turn and ascending/descending trim conditions for the aircraft configurations introduced in Chapter 2.6. First, the formulation and solution method is presented for the trim. Results of cruise, steady-state turn and ascending/descending are presented and discussed. Then, the effects of different altitudes on aircraft trim are presented for the M-A aircraft. Finally, the effect of different weights of mass-actuators are investigated for the M-A aircraft. Results are presented and discussed.

4.1 Formulation and Solution

As depicted in Fig. 4.1, two moving masses constitute the mass-actuation mechanism. Specifically, m_1 moves along x-axis within the fuselage to generate pitching moment and m_2 moves laterally within the wings to generate mainly rolling moment. Depending on the aircraft configuration analyzed, pitching and rolling moments are produced by longitudinally and laterally moving-mass actuators for mass-actuation or by elevator and aileron for aero-actuation.

In a trim condition, the aircraft flies with constant translational and angular velocity components in body frame, which implies that $\dot{V} = \dot{\beta} = \dot{\alpha} = 0$, and $\dot{p} = \dot{q} = \dot{r} = 0$. In a trim flight of the mass-actuated aircraft configurations, the positions of the mass actuators are fixed in the body frame, i.e., $\ddot{\rho}_{m_j} = \dot{\rho}_{m_j} = 0$. Further, wind

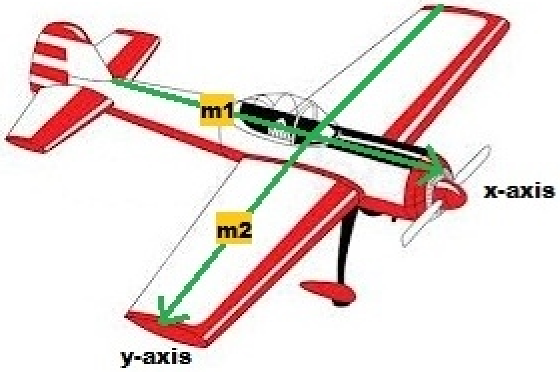

Figure 4.1. Placement of the longitudinal and lateral moving-mass actuators.

components are not considered in the trim. Under these conditions, the translational dynamics in Eq. (2.6) leads to

$$\begin{bmatrix} f_{TD1} \\ f_{TD2} \\ f_{TD3} \end{bmatrix} = (m_T)\left(\begin{bmatrix} 0 & r & -q \\ -r & 0 & p \\ q & -p & 0 \end{bmatrix}\begin{bmatrix} V\cos\beta\cos\alpha \\ V\sin\beta \\ V\cos\beta\sin\alpha \end{bmatrix}\right) + \begin{bmatrix} T_x + X - (m_T)g\sin\theta \\ T_y + Y + (m_T)g\sin\phi\cos\theta \\ T_z + Z + (m_T)g\cos\phi\cos\theta \end{bmatrix}$$
$$-\sum_{j=1}^{k}\left(m_j\begin{bmatrix} 0 & r & -q \\ -r & 0 & p \\ q & -p & 0 \end{bmatrix}\left(\begin{bmatrix} 0 & r & -q \\ -r & 0 & p \\ q & -p & 0 \end{bmatrix}\begin{bmatrix} \rho_{m_{j_x}} \\ \rho_{m_{j_y}} \\ \rho_{m_{j_z}} \end{bmatrix}\right)\right) \tag{4.1}$$

Similarly, the rotational dynamics in Eq. (2.9) for the trim condition defined above is reduced to

$$
\begin{aligned}
\begin{bmatrix} f_{RD1} \\ f_{RD2} \\ f_{RD3} \end{bmatrix} &= \begin{bmatrix} \mathcal{L}_{prop} + \mathcal{L} + \mathcal{L}_{mass} \\ \mathcal{M}_{prop} + \mathcal{M} + \mathcal{M}_{mass} \\ \mathcal{N}_{prop} + \mathcal{N} + \mathcal{N}_{mass} \end{bmatrix} + \begin{bmatrix} 0 & r & -q \\ -r & 0 & p \\ q & -p & 0 \end{bmatrix} \begin{bmatrix} I_{xx} & 0 & -I_{xz} \\ 0 & I_{yy} & 0 \\ -I_{xz} & 0 & I_{zz} \end{bmatrix} \begin{bmatrix} p \\ q \\ r \end{bmatrix} \\
&+ \sum_{j=1}^{k} \left(\begin{bmatrix} 0 & \rho_{m_{jz}} & -\rho_{m_{jy}} \\ -\rho_{m_{jz}} & 0 & \rho_{m_{jx}} \\ \rho_{m_{jy}} & -\rho_{m_{jx}} & 0 \end{bmatrix} m_j \left(\begin{bmatrix} p & q & r \end{bmatrix} \begin{bmatrix} \rho_{m_{jx}} \\ \rho_{m_{jy}} \\ \rho_{m_{jz}} \end{bmatrix} \right) \begin{bmatrix} p \\ q \\ r \end{bmatrix} \right) \\
&+ \sum_{j=1}^{k} \left[\begin{bmatrix} 0 & \rho_{m_{jz}} & -\rho_{m_{jy}} \\ -\rho_{m_{jz}} & 0 & \rho_{m_{jx}} \\ \rho_{m_{jy}} & -\rho_{m_{jx}} & 0 \end{bmatrix} m_j \right] \left(- \begin{bmatrix} 0 & r & -q \\ -r & 0 & p \\ q & -p & 0 \end{bmatrix} \begin{bmatrix} V \cos\beta \cos\alpha \\ V \sin\beta \\ V \cos\beta \sin\alpha \end{bmatrix} \right)
\end{aligned} \tag{4.2}
$$

where it should be noted that propeller torque components are included in the first term of the equation. In the cases when propeller effect is ignored, all components of propulsive moments are set to zero.

Further, when θ and ϕ are considered to be constant, the rotational kinematics equations in Eqs. (2.3)-(2.5) leads to

$$\phi = \tan^{-1}\left(\frac{q}{r}\right) \tag{4.3}$$

$$\dot{\psi} = \frac{r}{\cos\phi\cos\theta} = \frac{q}{\sin\phi\cos\theta} \tag{4.4}$$

$$p = -r\frac{\tan\theta}{\cos\phi} = -q\frac{\tan\theta}{\sin\phi} \tag{4.5}$$

By manipulating Eqs. (4.3)-(4.5), p, q and r are written in terms of $\dot{\psi}$, ϕ and θ as

$$p = -\dot{\psi}\sin\theta \tag{4.6}$$

$$q = \dot{\psi}\sin\phi\cos\theta \tag{4.7}$$

$$r = \dot{\psi}\cos\phi\cos\theta \tag{4.8}$$

In addition to θ and ϕ being constant in any trim condition, ψ is also constant in a cruise or ascent/descent condition, which, through Eqs. (4.6)-(4.8), implies that angular velocity components p, q and r are all zero.

Another requirement set for cruise and steady-state turn trim is to fly at constant altitude, i.e., $\dot{z} = 0$, which implies, from the third equation of the translation kinematics in Eq. (2.2), that

$$f_{TK3} = V[-\cos\beta\cos\alpha\sin\theta + \sin\beta\sin\phi\cos\theta + \cos\beta\sin\alpha\cos\phi\cos\theta] \tag{4.9}$$

which lead to an expression for θ in terms of β, ϕ and α as

$$\tan\theta = \frac{\tan\beta\sin\phi}{\cos\alpha} + \tan\alpha\cos\phi \tag{4.10}$$

The requirement of constant ascent or descent flight implies

$$f_{TK3} = -R/C \tag{4.11}$$

where the rate of ascent/descent is defined as

$$R/C = V\sin\gamma \tag{4.12}$$

R/C is positive for ascending and negative for descending. Further, ascent/descent angle, γ, can be found as

$$\gamma = \sin^{-1}\left(-\frac{\dot{z}}{V}\right) \tag{4.13}$$

Including propeller effect in the trim analysis couples the longitudinal and lateral motion even in the cruise flight. One of the implications of this coupling is that $\dot{y} \neq 0$ in general. Since different aircraft types are compared with and without propeller effect included, $\dot{y} = 0$ condition is imposed to have the same nominal trajectory in all cases for cruise, ascending and descending flight. Thus, the second equation of the translational kinematics in Eq. (2.2) implies

$$\begin{aligned} f_{TK2} = {} & V\cos\beta\cos\alpha\cos\theta\sin\psi \\ & + V\sin\beta(\cos\phi\cos\psi + \sin\phi\sin\theta\sin\psi) \\ & + V\cos\beta\sin\alpha(-\sin\phi\cos\psi + \cos\phi\sin\theta\sin\psi) \end{aligned} \tag{4.14}$$

which is solved along with Eqs. (4.1) and (4.2) for cruise and ascent/descent trim analysis.

Nominal value of throttle input, δ_T, in a trim flight, can be found from the steady-state condition of the DC-motor equations in Eqs. (2.11) and (2.12), i.e., when $\mathrm{i}_m = \dot{\omega}_m = 0$. Under this steady-state condition, Eq. (2.12) is solved for the nominal value of the current as

$$\imath_m = \frac{\tau_{p_x} + k_f\omega_m}{k_T} \tag{4.15}$$

Similarly, Eq. (2.11) is solved for the nominal value of the supplied voltage as

$$\mathcal{V}_s = R\imath_m + k_e\omega_m \tag{4.16}$$

which is substituted into Eq. (2.13) to calculate the nominal value of the throttle input.

To determine the nominal values of the state and control variables in a trim flight, a set of nonlinear algebraic equations obtained from the differential equations at the steady-state conditions should be solved. For cruise conditions, the algebraic equations to be solved are Eqs. (4.1)-(4.2) and Eq. (4.14). For steady turn, Eqs. (4.1) and (4.2) should be solved. For ascending/descending, Eqs. (4.1)-(4.2), (4.11) and (4.14) should be solved. In solving these equations, the physical constraints on δ_e, δ_a, δ_r, $\rho_{m_{1_x}}$, $\rho_{m_{2_y}}$, ω_p as showed in Table 2.4 and modeling constraints on α, β, ψ,

θ, ϕ as listed in Table 4.1 should be considered. Solutions of the nonlinear algebraic equations are carried out using MATLAB's $fmincon$ command. In this approach, the trim analysis is formulated as an optimization problem based on a quadratic cost function of the six, seven or eight equations with the constraints tabulated in Table 2.4 and 4.1 for cruise trim

$$J = f_{TD1}^2 + f_{TD2}^2 + f_{TD3}^2 + f_{RD1}^2 + f_{RD2}^2 + f_{RD3}^2 + f_{TK2}^2 \tag{4.17}$$

for steady-state turn trim

$$J = f_{TD1}^2 + f_{TD2}^2 + f_{TD3}^2 + f_{RD1}^2 + f_{RD2}^2 + f_{RD3}^2 \tag{4.18}$$

and for ascending/descending trim

$$J = f_{TD1}^2 + f_{TD2}^2 + f_{TD3}^2 + f_{RD1}^2 + f_{RD2}^2 + f_{RD3}^2 + f_{TK2}^2 + (f_{TK3} + R/C)^2 \tag{4.19}$$

This approach has the advantage of accounting for the specified constraints in the solution. The solutions are feasible when the minimum value of the cost function is zero.

Table 4.1. Modeling constraints of parameters

Limitations	**Units**
$\lvert\alpha\rvert \leq 20$	deg
$\lvert\beta\rvert \leq 15$	deg
$\lvert\psi\rvert \leq 15$	deg
$\lvert\theta\rvert \leq 90$	deg
$\lvert\phi\rvert \leq 60$	deg
$V \leq 18$	m/s

4.2 Results of Cruise Flight Trim Analysis

For the trim analysis of any of the three aircraft configurations (A-A, MRA, and M-A), described in Chapter 2.6, seven nonlinear algebraic equations in Eqs. (4.1), (4.2), and (4.14) should be solved. The variables these equations are solved for are different depending on the aircraft configuration.

For the trim analysis of the A-A aircraft, there are 21 unknowns in the seven equations: ω_p, V, α, β, p, q, r, ψ, θ, ϕ, m_1, m_2, $\rho_{m_{1_x}}$, $\rho_{m_{1_y}}$, $\rho_{m_{1_z}}$, $\rho_{m_{2_x}}$, $\rho_{m_{2_y}}$, $\rho_{m_{2_z}}$, δ_e, δ_a and δ_r. To solve these equations, the number of unknowns should be reduced to seven, which means the remaining ones should be specified. Since the A-A aircraft has aero-actuation only, all the positions of mass-actuators are set to zero, which implies $\rho_{m_{1_x}} = \rho_{m_{1_y}} = \rho_{m_{1_z}} = \rho_{m_{2_x}} = \rho_{m_{2_y}} = \rho_{m_{2_z}} = 0$. Further, masses of mass-actuators can be considered as part of the rigid body, and thus m_1, m_2 are also set to zero. This reduces the number of unknowns to nine: V, ω_p, α, β, ψ, ϕ, δ_e, δ_a, and δ_r. To reduce the number of unknowns to seven, two of nine unknowns should be specified. Two variables to specify are selected to be airspeed V and one of β, ψ, or ϕ. By specifying each of β, ψ, and ϕ in three separate cases, the seven equations are solved for the seven unknowns for cruise analysis of A-A aircraft.

Trim analysis of the MRA aircraft also requires the solution of 7 equations with the same 21 unknowns: ω_p, V, α, β, p, q, r, ψ, θ, ϕ, m_1, m_2, $\rho_{m_{1_x}}$, $\rho_{m_{1_y}}$, $\rho_{m_{1_z}}$, $\rho_{m_{2_x}}$, $\rho_{m_{2_y}}$, $\rho_{m_{2_z}}$, δ_e, δ_a and δ_r. Since the MRA aircraft has mass-actuation augmented with rudder, only elevator and aileron deflections are set to zero, which implies $\delta_e = \delta_a = 0$. Furthermore, to simplify the analysis for the MRA aircraft, y and z positions of longitudinal moving-mass are set to zero, $\rho_{m_{1_y}} = 0$, $\rho_{m_{1_z}} = 0$. Also, there assumed to be no motion in x and z directions for the lateral moving-mass, $\rho_{m_{2_x}} = 0$, $\rho_{m_{2_z}} = 0$. Masses of mass-actuators, m_1 and m_2, should be specified to generate pitching and rolling moments. Hence, the MRA aircraft has 9 unknowns left with 7 equations: V, ω_p, α, β, ψ, ϕ, $\rho_{m_{1_x}}$, $\rho_{m_{2_y}}$, and δ_r. Similar to the A-A aircraft, two of nine unknowns should be specified. With V specified, each of the three possible cases is analyzed by setting one of β, ψ, or ϕ to zero.

Similarly, trim analysis of the M-A aircraft requires solving 7 equations with 21 unknowns: ω_p, V, α, β, p, q, r, ψ, θ, ϕ, m_1, m_2, $\rho_{m_{1_x}}$, $\rho_{m_{1_y}}$, $\rho_{m_{1_z}}$, $\rho_{m_{2_x}}$, $\rho_{m_{2_y}}$, $\rho_{m_{2_z}}$, δ_e, δ_a and δ_r. Since the M-A aircraft has mass-actuation only, all control surface deflections are set to zero, $\delta_e = \delta_a = \delta_r = 0$. Similar to the MRA aircraft, y and z positions of longitudinal mass-actuator, and x and z positions of lateral mass-actuator are set to zero for simplification, i.e., $\rho_{m_{1_y}} = \rho_{m_{1_z}} = \rho_{m_{2_x}} = \rho_{m_{2_z}} = 0$. In addition, masses of mass-actuators, m_1 and m_2, are set. Hence, the M-A aircraft has 8 unknowns left with 7 equations: V, ω_p, α, β, ψ, ϕ, $\rho_{m_{1_x}}$, and $\rho_{m_{2_y}}$. For specified V, number of unknowns will be 7 and trim analysis of the M-A aircraft is carried out with 7 unknowns left. Note that, unlike A-A and MRA aircraft, in the case of M-A aircraft, none of β, ψ, or ϕ can be specified to zero, which means they may all take non-zero trim values.

Results are discussed in three subsections. In the first subsection, feasible trim analyses for the A-A aircraft are presented for three different cases. This is followed by a similar discussion for the MRA aircraft. The last section presents a comparison of the best cases of the A-A and the MRA aircraft with the M-A aircraft.

4.2.1 Trim Analysis of Aero-Actuated Airplane

Three different trim cases are carried out, in each of which one of β, ψ, or ϕ is specified to be zero and thus the others are allowed to be non zero to satisfy the trim condition.

Figure 4.2 shows that the zero-bank case requires the highest thrust among the three cases while the zero-yaw case is slightly higher than zero-sideslip case. Fig. 4.3

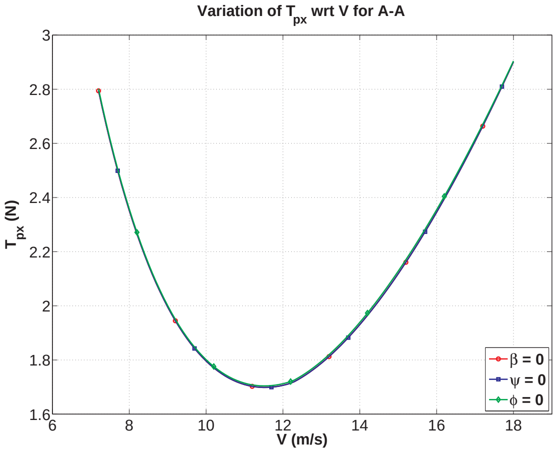

Figure 4.2. Required thrust variation with speed in cruise for A-A aircraft.

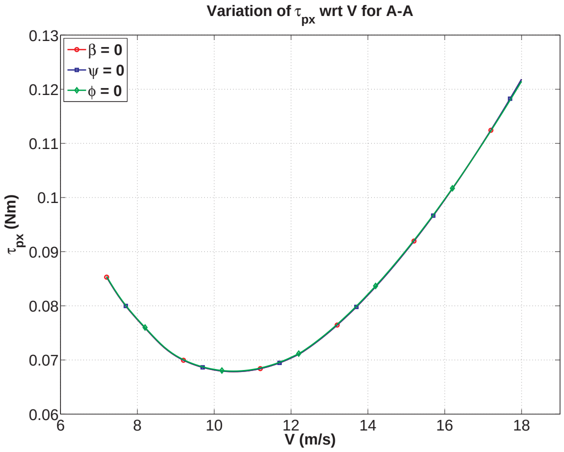

Figure 4.3. Required torque variation with speed in cruise for A-A aircraft.

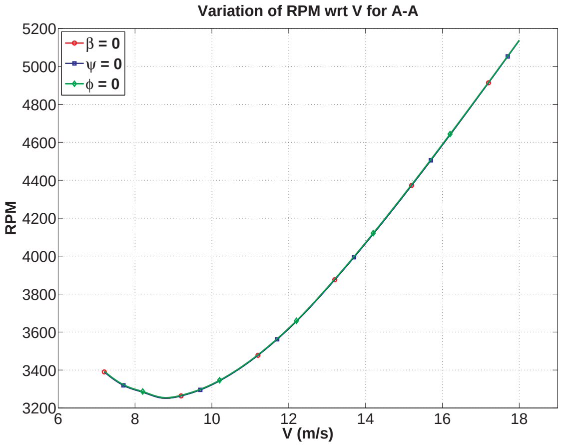

Figure 4.4. RPM variation with speed in cruise for A-A aircraft.

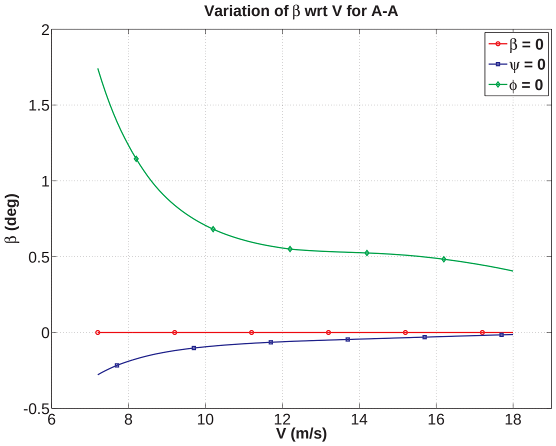

Figure 4.5. Sideslip angle variation with speed in cruise for A-A aircraft.

shows a similar trend in propeller torque required. Thus, the variation of propeller angular speed (Fig. 4.4) is the highest for zero-bank case to generate thrust at the same speed.

The most important observation among all three cases that A-A aircraft have non zero sideslip, bank or yaw angles shown in Figures 4.5-4.7. This means the A-A aircraft should have non zero rudder and aileron deflections to compensate for the

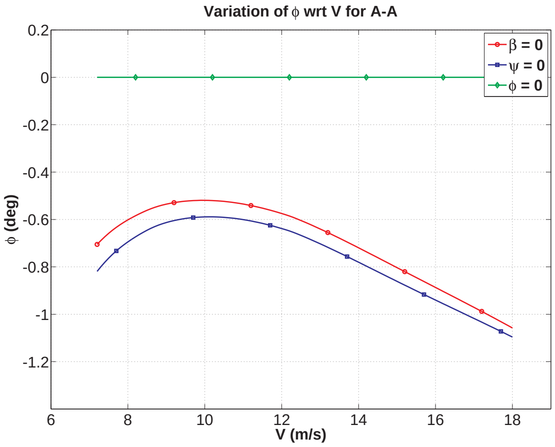

Figure 4.6. Bank angle variation with speed in cruise for A-A aircraft.

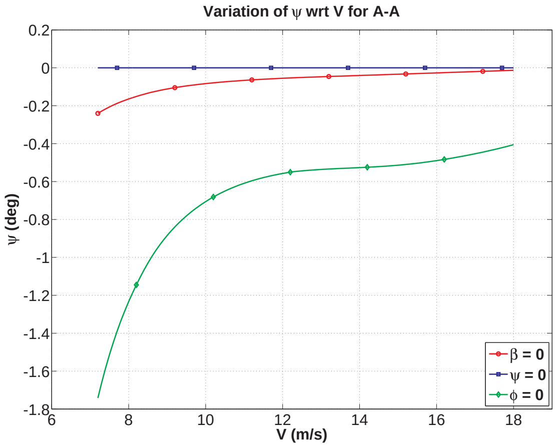

Figure 4.7. Yaw angle variation with speed in cruise for A-A aircraft.

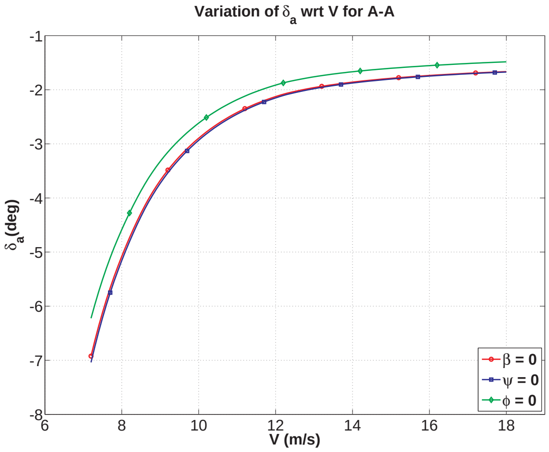

Figure 4.8. Aileron variation with speed in cruise for A-A aircraft.

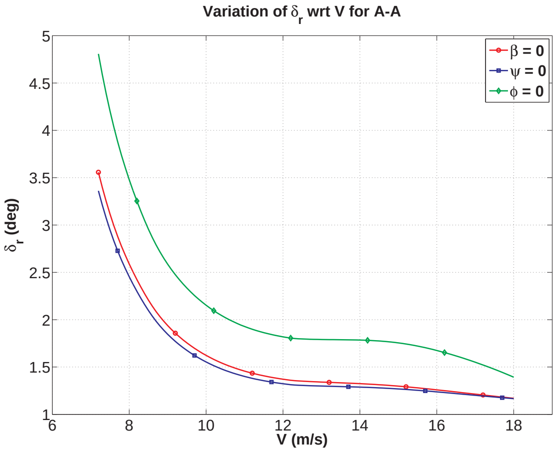

Figure 4.9. Rudder variation with speed in cruise for A-A aircraft.

induced moment even if the aircraft flies in cruise as can be seen in Figs. 4.8 and 4.9. That leads to the zero-bank case requires the highest thrust (Fig. 4.2) since the total deflections of aileron and rudder and required sideslip angle are the highest at the same nominal speed among all three cases. Fig. 4.10 shows that elevator deflections for all cases seem to have no visible differences between each other since all cases require similar angle of attack as it can be seen in Fig. 4.11.

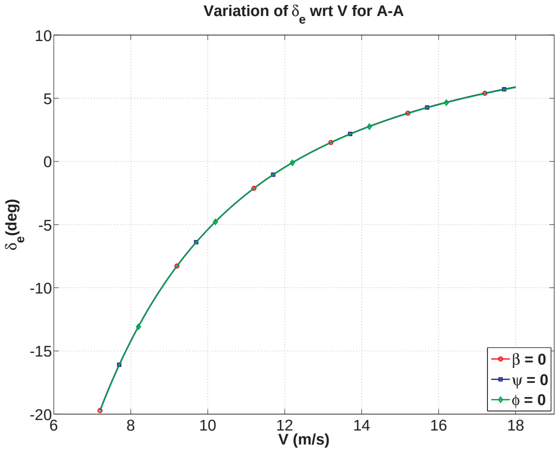

Figure 4.10. Elevator variation with speed in cruise for A-A aircraft.

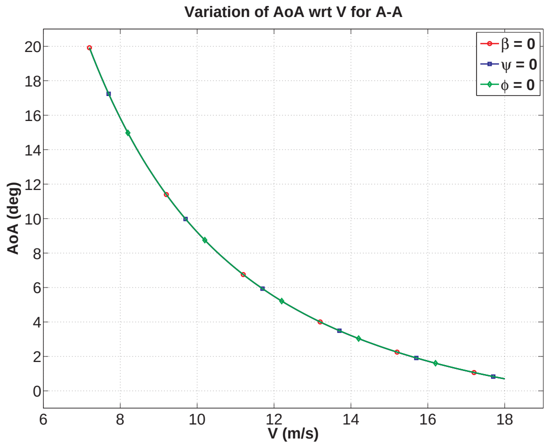

Figure 4.11. Angle of attack variation with speed in cruise for A-A aircraft.

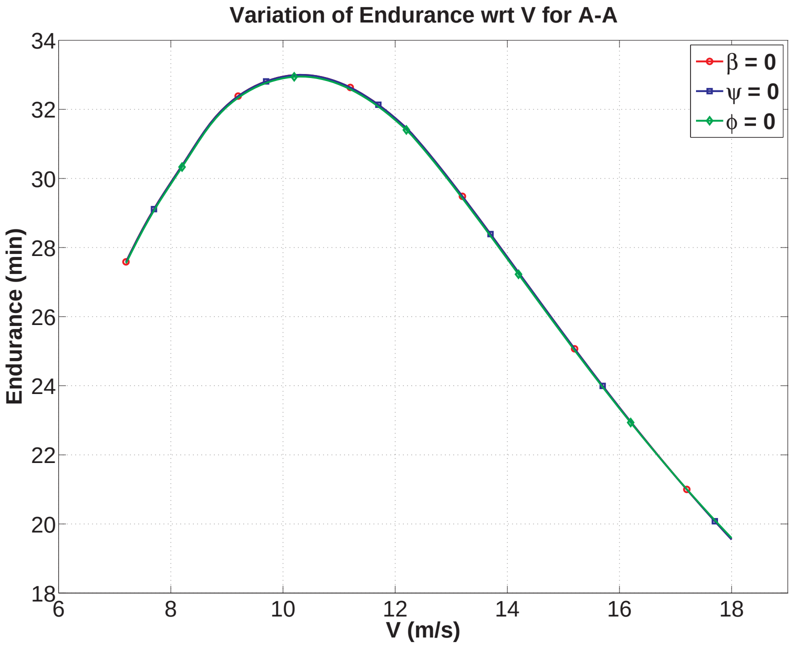

Figure 4.12. Endurance variation with speed in cruise for A-A aircraft.

Figure 4.12 shows the endurance variation for all cases in terms of minutes. As explained earlier, aileron and rudder deflections are required due to non zero sideslip, bank or yaw angles and that leads to shorter endurance in cruise. This is due to the fact that greater control surface deflections results in higher drag and this in turn requires more thrust, as indicated in Eq. (2.67). In the cases of non zero sideslip angle, endurance and thrust are also affected by the existence of sideslip angle since its effect is considered in the drag expression in Eq. (2.67).

4.2.2 Trim Analysis of Mass-Actuated Airplane Augmented With Rudder

Similar to the A-A aircraft, trim conditions of three different cases, in each of which one of β, ψ, or ϕ is specified to be zero, are compared for the MRA aircraft.

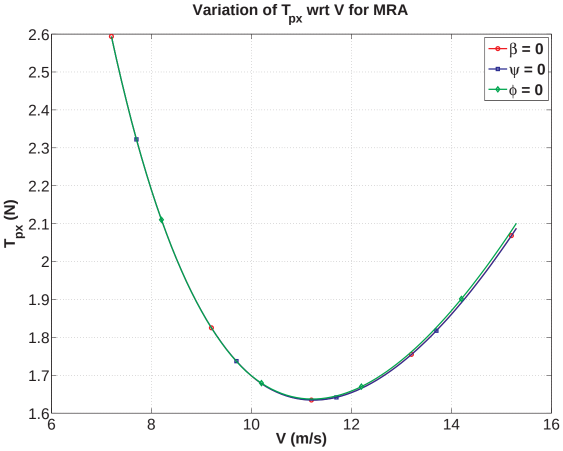

Figure 4.13. Required thrust variation with speed in cruise for MRA aircraft.

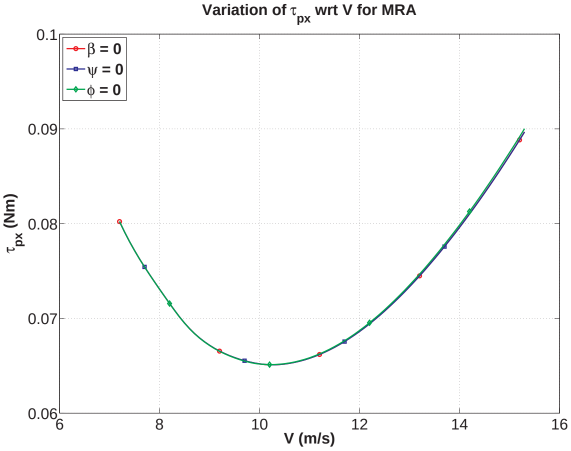

Figure 4.14. Required torque variation with speed in cruise for MRA aircraft.

Figures 4.13-4.15 show the variation of required thrust, required torque and propeller angular speed for all cases. It is observed from these figures that all three cases show similar trends for lower speeds. On the other hand, the zero-bank case needs slightly higher thrust for higher speeds. Thus higher propeller torque and angular speed are required. The zero-yaw and the zero-sideslip cases show similar variation throughout the feasible speed range.

Similar to the A-A aircraft, the MRA aircraft also have non zero β, ψ, or ϕ as shown in Figs. 4.16-4.18. Thus, lateral-mass actuator (Fig. 4.19) and rudder

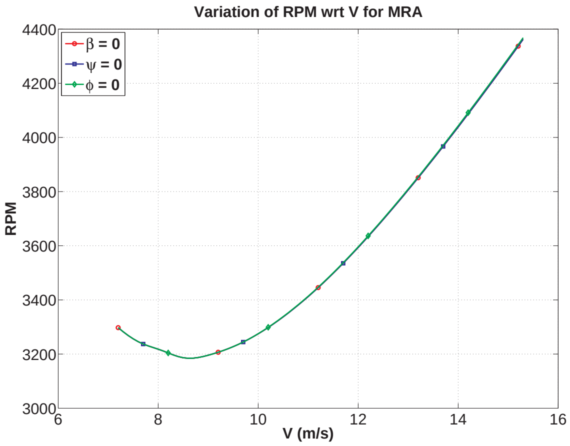

Figure 4.15. RPM variation with speed in cruise for MRA aircraft.

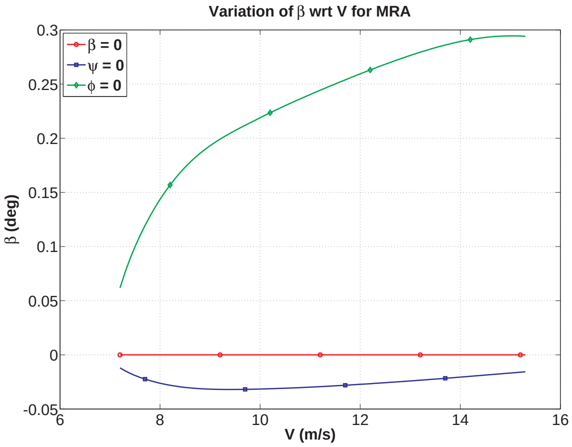

Figure 4.16. Sideslip angle variation with speed in cruise for MRA aircraft.

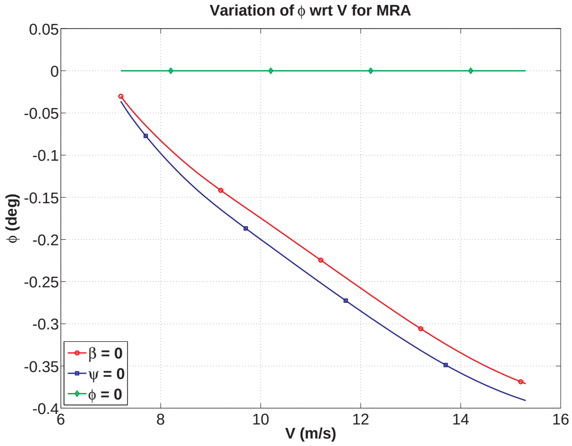

Figure 4.17. Bank angle variation with speed in cruise for MRA aircraft.

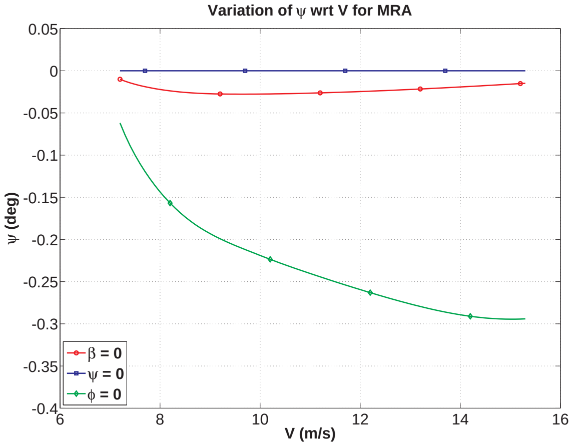

Figure 4.18. Yaw angle variation with speed in cruise for MRA aircraft.

(Fig. 4.20) are required to compensate them in cruise flight. Moreover, since the zero-bank case requires higher rudder deflection and higher sideslip angle for higher speeds, required thrust is the highest for this case as shown in Fig. 4.13. Since the trend of angle of attack is similar for all three cases shown in Fig. 4.22, variations of longitudinal-mass positions are also similar in Fig. 4.21 same as the A-A aircraft.

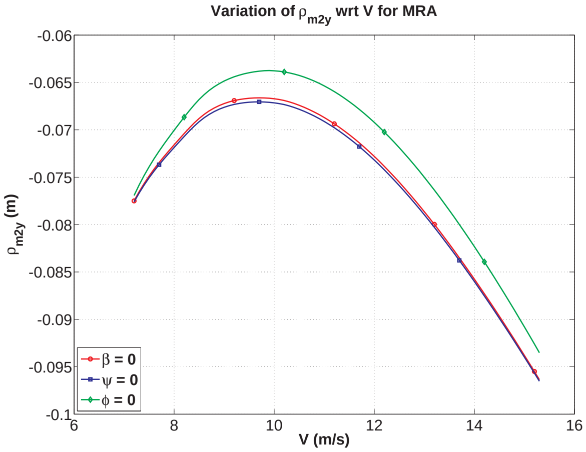

Figure 4.19. $\rho_{m_{2_y}}$ variation with speed in cruise for MRA aircraft.

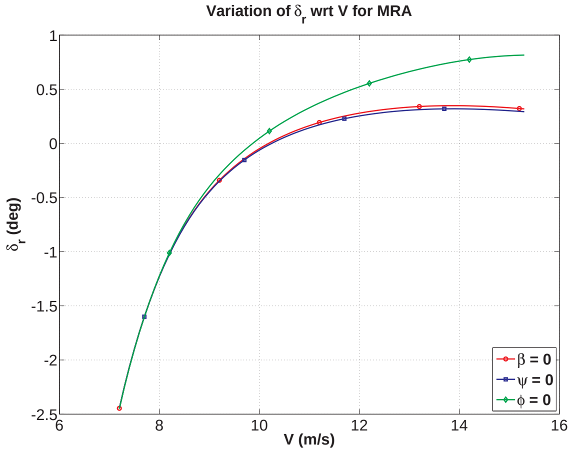

Figure 4.20. Rudder variation with speed in cruise for MRA aircraft.

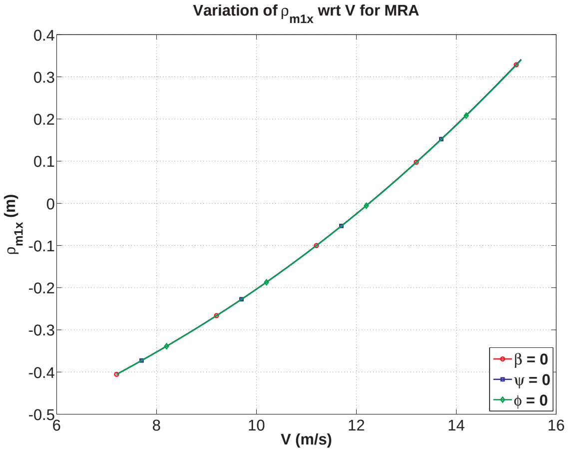

Figure 4.21. $\rho_{m_{1_x}}$ variation with speed in cruise for MRA aircraft.

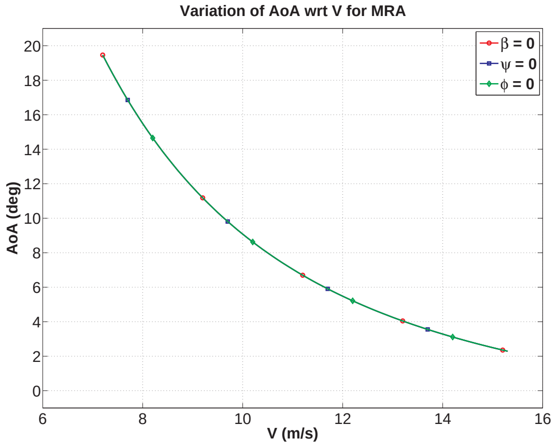

Figure 4.22. Angle of attack variation with speed in cruise for MRA aircraft.

Figure 4.23 shows the endurance for each case in terms of minutes. As explained earlier, the zero-bank case gives slightly lower endurance for higher speeds while the zero-yaw and the zero-sideslip cases give the same endurance.

4.2.3 Comparison of Mass-Actuated Airplane Trim with Aero-Actuated Airplanes

In this section, trim analysis of M-A airplane is performed and the results are compared with those of the best cases of the aircraft with A-A and MRA airplanes.

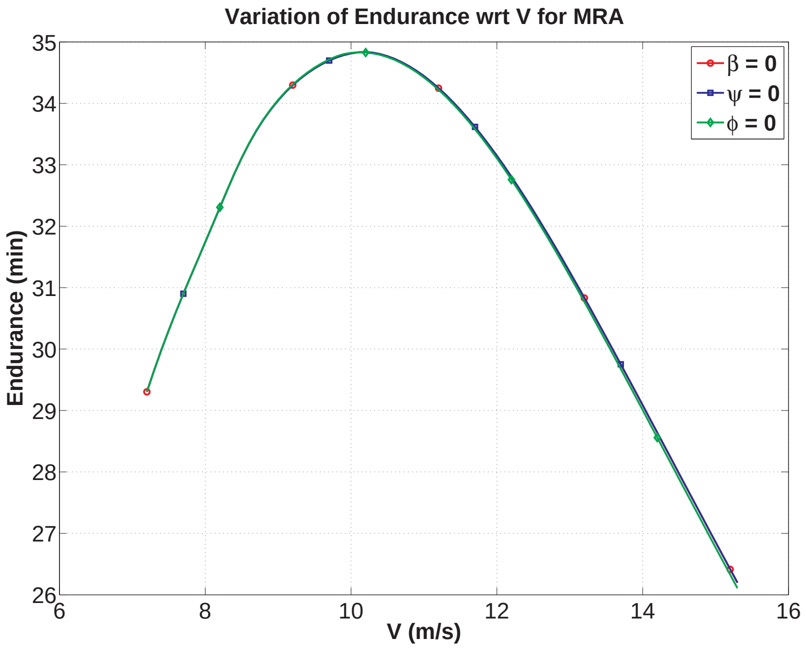

Figure 4.23. Endurance variation with speed in cruise for MRA aircraft.

The best case is defined as the one, among the cases with propeller effect, that has the minimum thrust required throughout the whole feasible speed range. Hence, zero sideslip angle cases are selected as the best case for the A-A and the MRA aircraft and compared with the trim results of the M-A airplane. The comparisons of the three aircraft configurations should demonstrate the effect of the moment generation mechanism on the trim results.

Figure 4.24 shows the required thrust variation over each respective cruise speed range. The required thrust for any cruise speed is lower with the MRA aircraft as compared to the A-A aircraft. M-A aircraft has lower thrust requirement for speeds higher than about 8.5 m/s and almost the same as MRA aircraft for speeds higher than 10 m/s. The lowest required thrust among all three cases considered is achieved at the speed of about 11 m/s by M-A and MRA cases. This indicates the benefit of using mass-actuation instead of elevator and aileron. A comparison of M-A and MRA

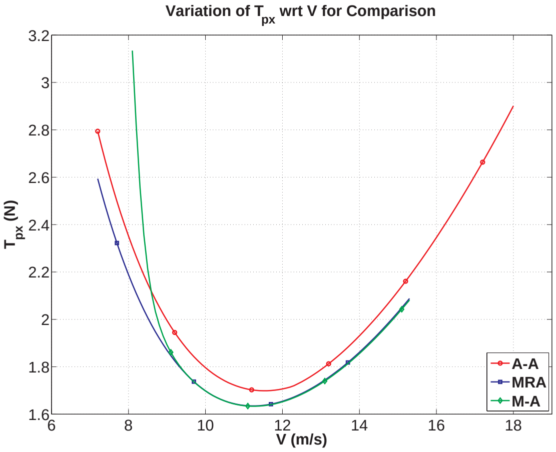

Figure 4.24. Required thrust variation with speed in cruise.

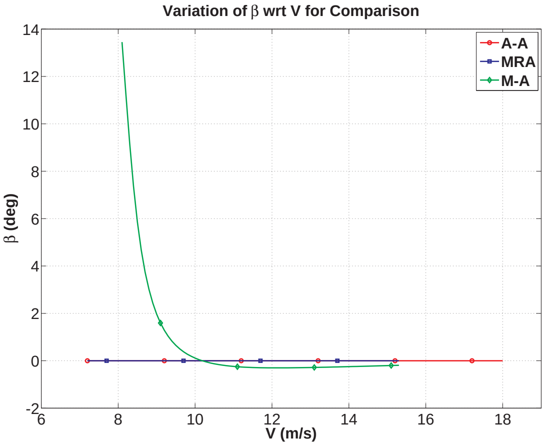

Figure 4.25. Sideslip angle variation with speed in cruise.

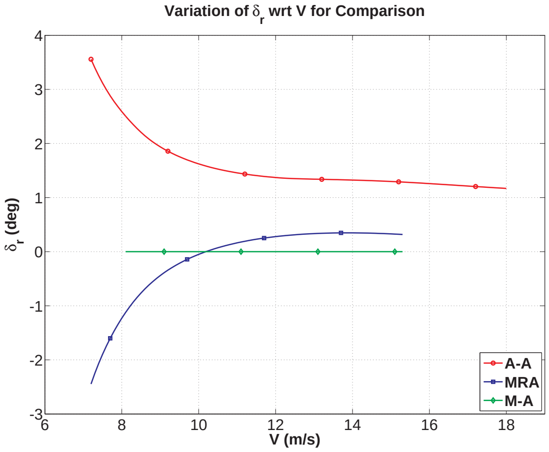

Figure 4.26. Rudder variation with speed in cruise.

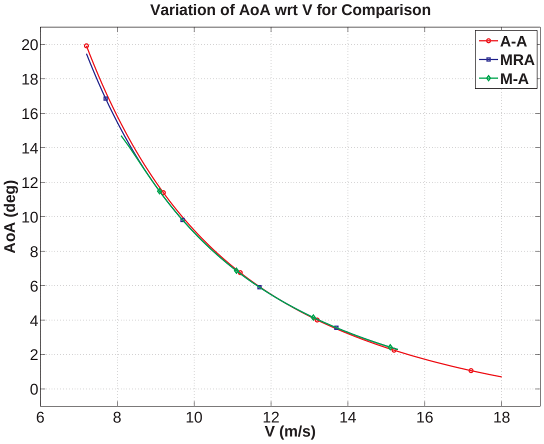

Figure 4.27. Angle of attack variation with speed in cruise.

aircraft cases can reveal the effect of rudder use. M-A aircraft has no yawing moment generation mechanism, which leads to cruise flight with sideslip angle because of the propeller effect. The MRA aircraft, on the other hand, uses rudder along with the mass-actuation. Fig. 4.25 shows that M-A aircraft flies with sideslip and Fig. 4.26 shows that MRA aircraft flies with rudder at low speeds. Another look at Fig. 4.24 shows that flying with sideslip is more costly as the required thrust is higher for M-

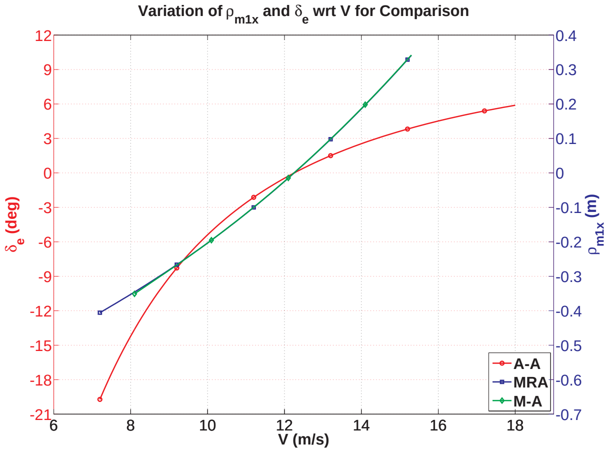

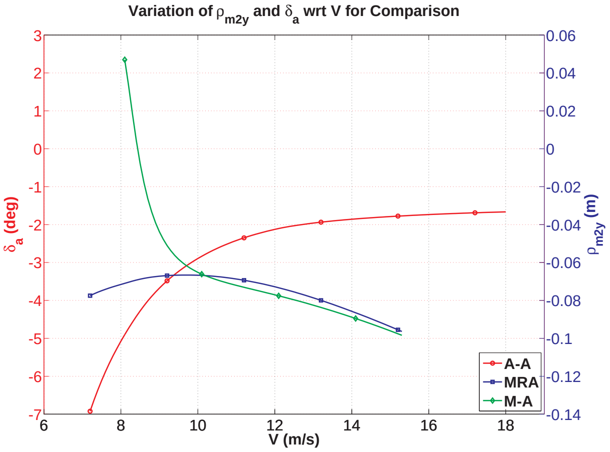

Figure 4.28. Position of longitudinal-mass and elevator variation with speed in cruise.

Figure 4.29. Position of lateral-mass and aileron variation with speed in cruise.

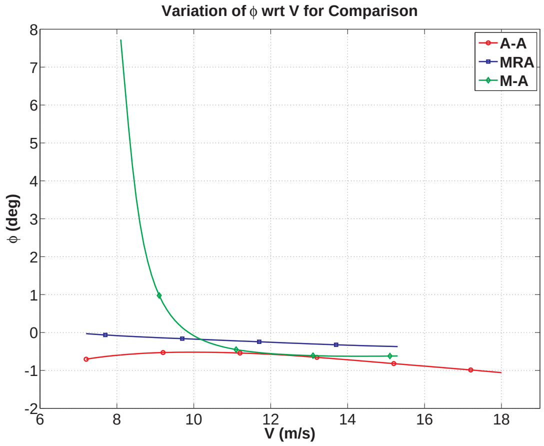

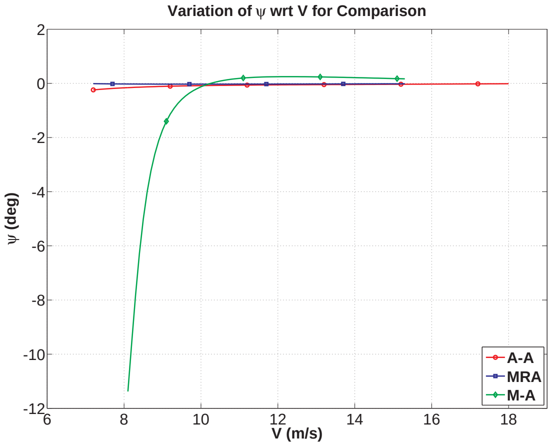

Figure 4.30. Bank angle variation with speed in cruise.

Figure 4.31. Yaw angle variation with speed in cruise.

A aircraft in low speed region. With increasing speed, Fig. 4.25 shows decreasing sideslip with the M-A aircraft. As sideslip decreases with increasing speed, Fig. 4.24 shows that the required thrust for M-A aircraft decreases that of the MRA aircraft. This implies that mass-actuation, even without rudder augmentation, can enable the cruise flight with minimum required thrust.

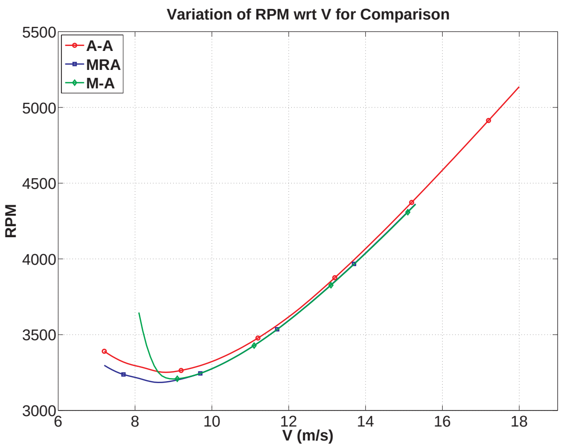

Figure 4.32. RPM variation with speed in cruise.

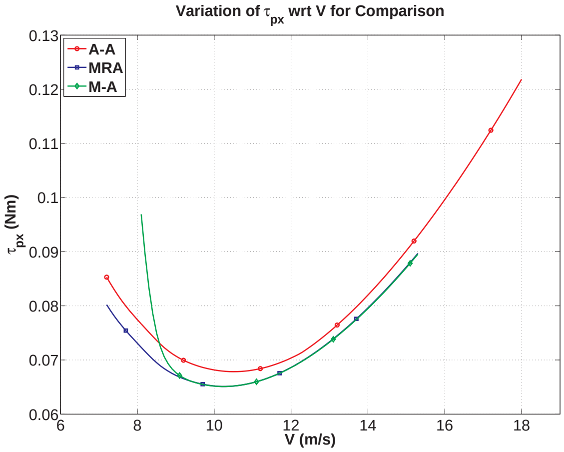

Figure 4.33. Required torque variation with speed in cruise.

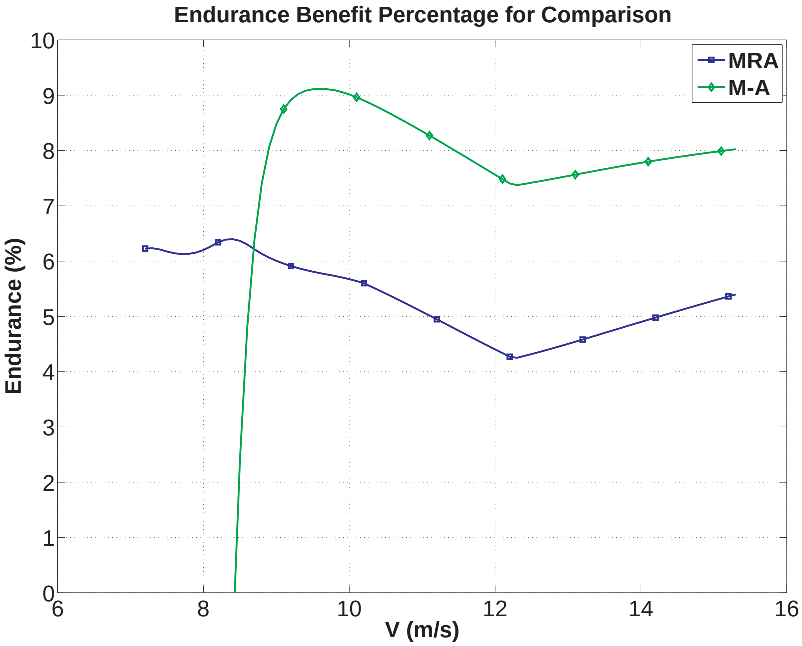

Figure 4.34. Percent increase in endurance as compared to that of A-A aircraft.

Trim results of each aircraft configuration in Figs. 4.24-4.34 are plotted within the respective feasible speed range. The lower and upper limits of the feasible speed ranges are different for each aircraft configuration. This is because the first variable to reach its upper or lower limit (see Tables 2.4 and 4.1) changes depending on the aircraft configuration. The A-A aircraft has the largest feasible speed range, especially towards the upper limit, i.e. higher speeds. As shown in Fig. 4.27, the angle of attack varies similarly for all aircraft configurations since they all have the same aerodynamics; angle of attack increases with decreasing cruise speed. The A-A aircraft speed range is lower bounded at 7 m/s by the angle of attack reaching its maximum limit of 20 deg as seen in Fig. 4.27. The speed range of the A-A aircraft is upper bounded at 18 m/s, as set in Table 4.1. The M-A aircraft speed range is lower bounded by the maximum sideslip angle set at 15 deg as shown in Fig. 4.25. The MRA aircraft speed is lower bounded by the maximum angle of attack set at 20 deg. The upper speed limit for both MRA and M-A aircraft is set at about 15 m/s by the most forward position of the longitudinal moving mass, as shown in Fig. 4.28. This analysis indicates that aero-actuation, specifically elevator, enables higher cruise speed. If high speed cruise is desired with the mass-actuation, a heavier longitudinal moving mass needs to be used.

Figure 4.28 shows elevator deflection variation for A-A aircraft, and longitudinal moving-mass positions for M-A and MRA aircraft configurations. The longitudinal mass starts behind the origin of the body frame (center of mass of the aircraft, excluding the moving masses) at low cruise speed, and moves forward towards the nose as speed increases. The moving-mass moves ahead of the origin of the body frame at the same speed when the elevator deflection for A-A aircraft changes sign from negative deflection to positive deflection. The moving-mass position variations for M-A and MRA aircraft are similar. In both aircraft configurations, the longitudinal-mass moves to its most forward position at cruise speed of 15 m/s, as stated earlier, while the elevator deflection for the A-A aircraft is still small relative to its maximum limit, and its increase slows down. This is why the A-A aircraft can fly faster than the M-A and MRA aircraft.

Figure 4.29 shows the aileron deflection for A-A and lateral moving-mass position for M-A and MRA aircraft. The lateral-mass placement for M-A and MRA aircraft, and aileron deflection for A-A are needed to compensate for the propeller effect. The M-A and MRA aircraft have different lateral-mass position variation especially at low cruise speed because M-A aircraft needs to fly with high sideslip and bank angles while the MRA aircraft uses rudder to keep these angles small. Since the sideslip and bank angles trim values decreases to zero with increasing speed, the lateral-mass positions converges to each other at higher speeds.

As stated earlier, A-A and MRA aircraft are trimmed with zero sideslip angle (Fig. 4.25) while bank (Fig. 4.30) and yaw angles (Fig. 4.31) vary with cruise speed. The M-A aircraft, on the other hand, has all three angles varying with cruise speed. Figs. 4.25, 4.30, and 4.31 show that the M-A aircraft cruises with non-zero sideslip, bank and yaw angles because of the induced propeller effect. These angles are about 10 deg at low speed and decrease toward zero as the cruise speed increases. The A-A and MRA aircraft can set one of these three angles to zero because they have the rudder as an additional control variable and, as a result, the bank and yaw angles remain very small throughout the speed range.

Figure 4.32 shows the propeller RPM variation with cruise speed and Fig. 4.33 shows the variation of torque required to spin the propeller at the corresponding RPM while the aircraft flies at a given cruise speed, based on the propeller characteristics formulated in Eq. (2.51) and illustrated in Fig. 2.8. The MRA aircraft has the lowest required propeller torque throughout the whole speed range. The M-A aircraft propeller torque is the highest at low speeds, decreases as speed increases relative to those of the other aircraft configurations, drops lower than that of the A-A beyond the speed of about 8.5 m/s, and converges down to that of the MRA at speeds higher than 9 m/s. The relations formulated in Eqs. (2.26)-(2.28) are used to calculate the endurance of the aircraft. Fig. 4.34 shows the percent endurance increase with M-A and MRA aircraft relative to that of A-A aircraft. The MRA aircraft has endurance benefit throughout its entire speed range while the M-A aircraft has endurance benefit at speeds higher than about 8.5 m/s. Speeds from 8.5 m/s till 9.5 m/s, the endurance benefit of the MRA aircraft drops while the M-A aircraft increases. At speeds higher than 9.5 m/s, the M-A aircraft has more endurance benefit than that of the MRA aircraft. This analysis demonstrates the advantage of using mass-actuation instead of aerodynamic control surfaces in terms of higher endurance in the same cruise conditions.

4.3 Results of Steady-State Turn Trim Analysis

In this section, results of steady-state turn are presented. Preliminary studies [120, 121] for steady-state turn were performed when propeller effect is ignored during the trim analysis. Results and discussions can be found in Appendix A. Since the propeller affects the turn, nominal conditions for right and left turn are not the same. Mainly, three different aircraft are investigated as explained in Chapter 2.6. All three aircraft are compared between each other to see the differences in the trim with different turn rates. Furthermore, right and left turns are compared for each aircraft to show the propeller effect. In the figures, continuous lines represent right turns and dashed lines represent left turns.

For the trim analysis of A-A aircraft, there are 21 unknowns in the six equations: ω_p, V, α, β, p, q, r, $\dot{\psi}$, θ, ϕ, m_1, m_2, $\rho_{m_{1_x}}$, $\rho_{m_{1_y}}$, $\rho_{m_{1_z}}$, $\rho_{m_{2_x}}$, $\rho_{m_{2_y}}$, $\rho_{m_{2_z}}$, δ_e, δ_a and δ_r. To solve these equations, the number of unknowns should be reduced to six, which means the remaining ones should be specified. Since the A-A aircraft has aero-actuation only, all the positions of mass-actuators are set to zero, which implies $\rho_{m_{1_x}} = \rho_{m_{1_y}} = \rho_{m_{1_z}} = \rho_{m_{2_x}} = \rho_{m_{2_y}} = \rho_{m_{2_z}} = 0$. Further, masses of mass-actuators can be considered as part of the rigid body, and thus m_1, m_2 are also set to zero. This reduces the number of unknowns to nine: V, ω_p, α, β, $\dot{\psi}$, ϕ, δ_e, δ_a, and δ_r. To reduce the number of unknowns to six, three of nine unknowns should be specified. For the A-A aircraft, turn with zero sideslip is desired. Hence, β is set to zero. Specifying V and $\dot{\psi}$ reduces the number of unknowns to six: ω_p, α, ϕ, δ_e, δ_a, and δ_r.

Trim analysis of MRA aircraft also requires the solution of six equations with the same 21 unknowns: ω_p, V, α, β, p, q, r, $\dot{\psi}$, θ, ϕ, m_1, m_2, $\rho_{m_{1_x}}$, $\rho_{m_{1_y}}$, $\rho_{m_{1_z}}$, $\rho_{m_{2_x}}$, $\rho_{m_{2_y}}$, $\rho_{m_{2_z}}$, δ_e, δ_a and δ_r. Since the MRA aircraft has mass-actuation augmented with rudder, only elevator and aileron deflections are set to zero, which implies $\delta_e = \delta_a = 0$. Furthermore, to simplify the analysis for the MRA aircraft, y and z positions of longitudinal moving-mass are set to zero, $\rho_{m_{1_y}} = 0$, $\rho_{m_{1_z}} = 0$. Also, there assumed to be no motion in x and z directions for the lateral moving-mass, $\rho_{m_{2_x}} = 0$, $\rho_{m_{2_z}} = 0$. Masses of mass-actuators, m_1 and m_2, should be specified to generate pitching and rolling moments. Hence, the MRA aircraft has 9 unknowns left with 6 equations: V, ω_p, α, β, $\dot{\psi}$, ϕ, $\rho_{m_{1_x}}$, $\rho_{m_{2_y}}$, and δ_r. Similar to the A-A aircraft, turn with zero sideslip is desired, which means $\beta = 0$. With V and $\dot{\psi}$ specified, the number of unknowns reduces to six: ω_p, α, ϕ, $\rho_{m_{1_x}}$, $\rho_{m_{2_y}}$, and δ_r.

Similarly, trim analysis of the M-A aircraft requires solving 6 equations with 21 unknowns: ω_p, V, α, β, p, q, r, $\dot{\psi}$, θ, ϕ, m_1, m_2, $\rho_{m_{1_x}}$, $\rho_{m_{1_y}}$, $\rho_{m_{1_z}}$, $\rho_{m_{2_x}}$, $\rho_{m_{2_y}}$, $\rho_{m_{2_z}}$, δ_e, δ_a and δ_r. Since the M-A aircraft has mass-actuation only, all control surface deflections are set to zero, $\delta_e = \delta_a = \delta_r = 0$. Similar to the MRA aircraft, y and z positions of longitudinal mass-actuator, and x and z positions of lateral mass-actuator are set to zero for simplification, i.e., $\rho_{m_{1_y}} = \rho_{m_{1_z}} = \rho_{m_{2_x}} = \rho_{m_{2_z}} = 0$. In addition, masses of mass-actuators, m_1 and m_2, are set. Hence, the M-A aircraft has 8 unknowns left with 6 equations: V, ω_p, α, β, $\dot{\psi}$, ϕ, $\rho_{m_{1_x}}$, and $\rho_{m_{2_y}}$. For specified V

and $\dot{\psi}$, number of unknowns will be six: ω_p, α, ϕ, $\rho_{m_{1_x}}$, $\rho_{m_{2_y}}$, and β, which implies that the M-A aircraft will turn with some sideslip angle.

Figures 4.35-4.36 show the variations of required thrust for two different turn rates. For low speed ranges, MRA aircraft requires the lowest thrust while M-A aircraft requires the highest thrust in both turn rates. Since M-A aircraft turns with some sideslip angle as shown in Figs. 4.37-4.38, more thrust is required to compensate drag increase due to higher sideslip angle. With increasing speed, sideslip angle decreases. That results in the drag decrease for mass-actuation. Thus, M-A aircraft requires slightly less thrust while A-A aircraft requires the highest thrust for higher speeds. For whole feasible speed ranges, MRA aircraft requires less thrust than the A-A aircraft in both turn rates. Since aileron and elevator deflections are needed for A-A aircraft as shown in Figs. 4.39-4.42, more thrust is required to compensate drag increase due to control surface deflections.

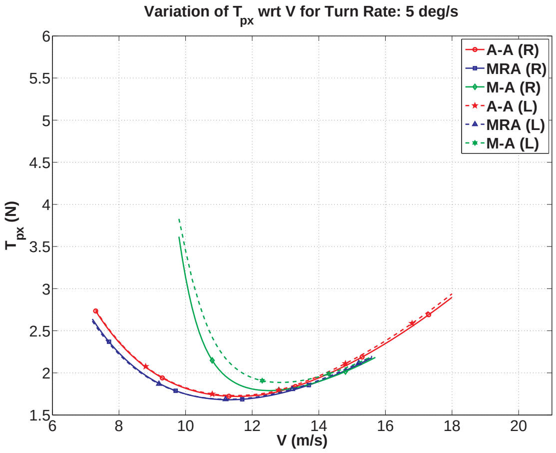

Figure 4.35. Required thrust variation with speed for $\dot{\psi} = 5$ deg/s.

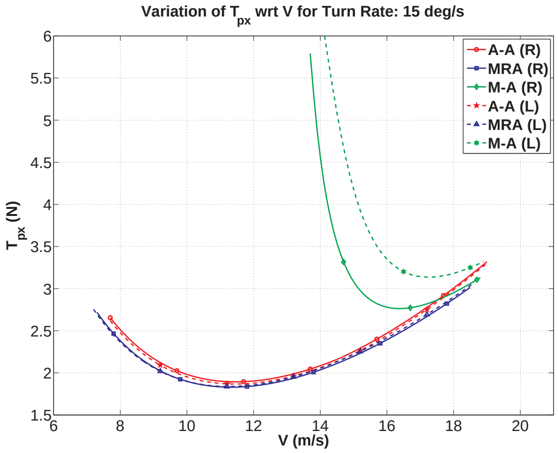

Figure 4.36. Required thrust variation with speed for $\dot{\psi} = 15$ deg/s.

For sharper turns, all aircraft need higher thrust since sideslip angles or higher control surface deflections are required as shown in Figs. 4.37-4.38 and Figs. 4.39-

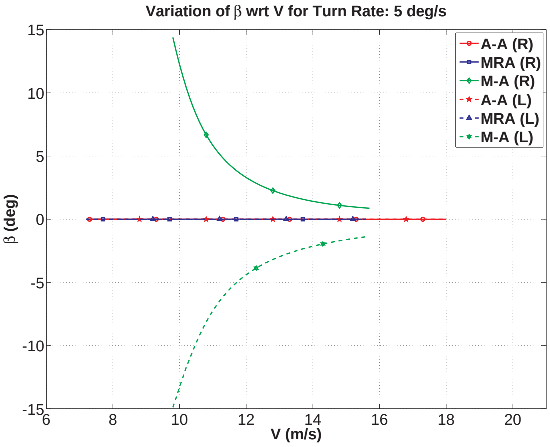

Figure 4.37. Sideslip angle variation with speed for $\dot{\psi} = 5$ deg/s.

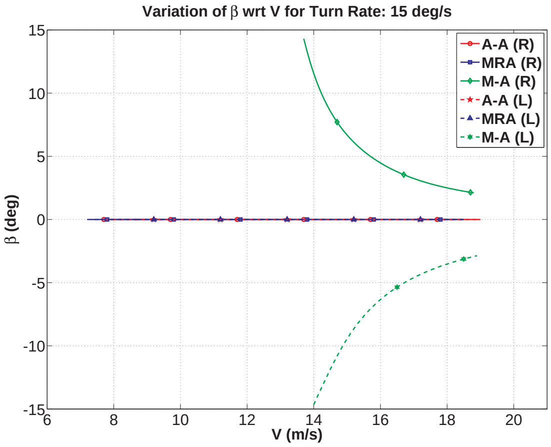

Figure 4.38. Sideslip angle variation with speed for $\dot{\psi} = 15$ deg/s.

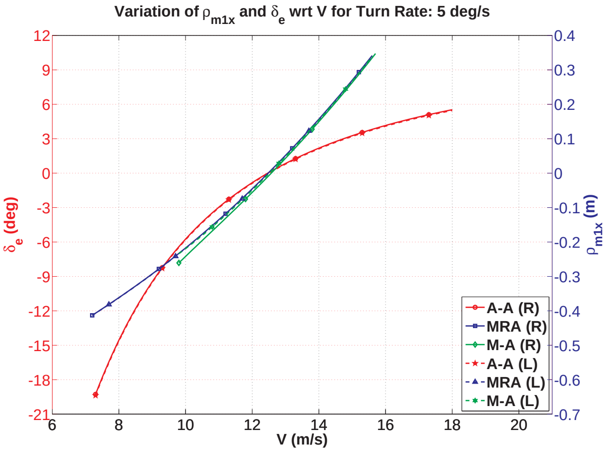

Figure 4.39. Position of long-mass and elevator variation with speed for $\dot{\psi} = 5$ deg/s.

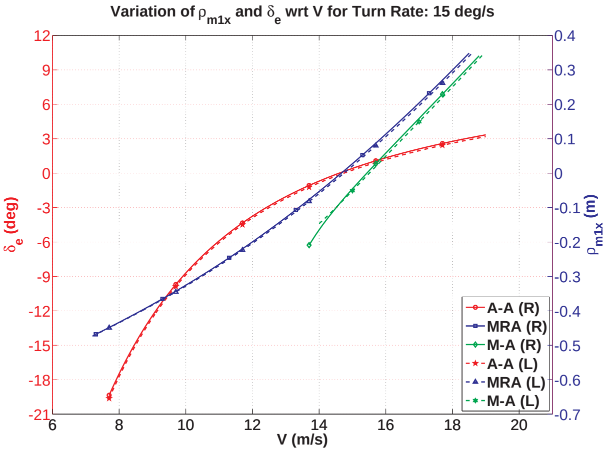

Figure 4.40. Position of long-mass and elevator variation with speed for $\dot{\psi} = 15$ deg/s.

4.44. On the other hand, thrust increase for M-A aircraft is greater than the others for sharper turn as shown in Fig. 4.36. This is due to the fact that sideslip in sharper turn is higher than sideslip in shallower turn for the same speed as shown in Figs. 4.37-4.38. Higher sideslip with the same speed results in higher drag increase as indicated in Eq. (2.67). Further, feasible speed range in shallower turn for M-A aircraft is between 9-16 m/s while it is between 13-19 m/s in sharper turn. Since the sideslip

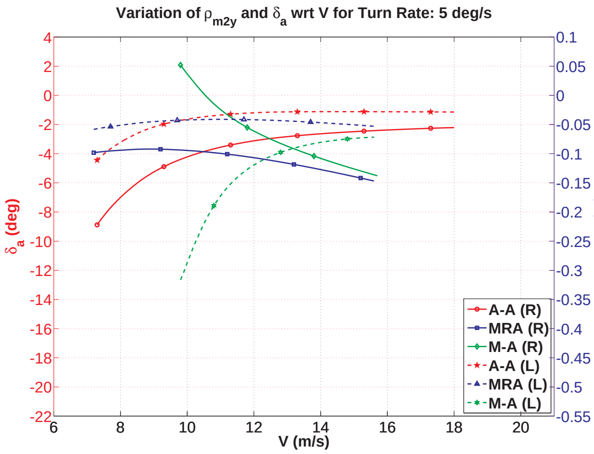

Figure 4.41. Position of lat-mass and aileron variation with speed for $\dot{\psi} = 5$ deg/s.

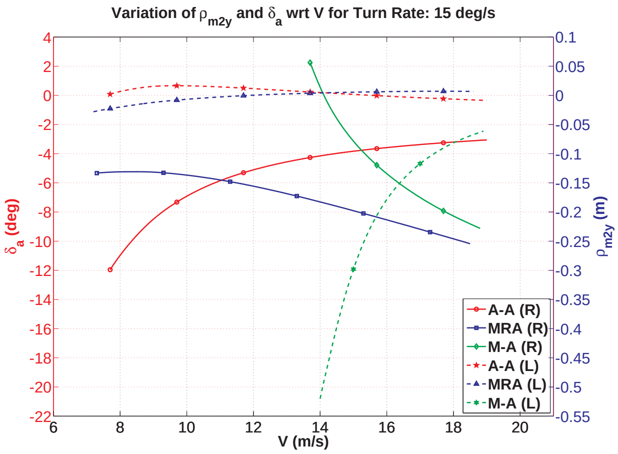

Figure 4.42. Position of lat-mass and aileron variation with speed for $\dot{\psi} = 15$ deg/s.

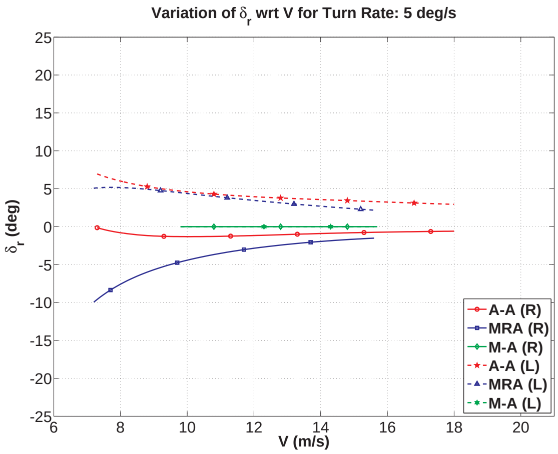

Figure 4.43. Rudder variation with speed for $\dot{\psi} = 5$ deg/s.

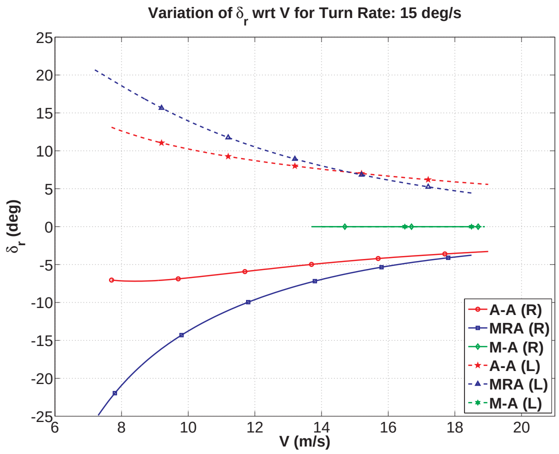

Figure 4.44. Rudder variation with speed for $\dot{\psi} = 15$ deg/s.

angle on M-A aircraft is restricted by model as discussed in the previous section, that affects the limitations of lower speed for M-A aircraft. Hence, the requirement of higher sideslip angle for sharper turn is observed for the same speed. Moreover, sharper turn for all aircraft needs higher bank angles than shallower turns as shown in Figs. 4.45-4.46 since more aileron deflections or lateral-mass positions and more rudder deflections are used as shown in Figs. 4.41-4.44.

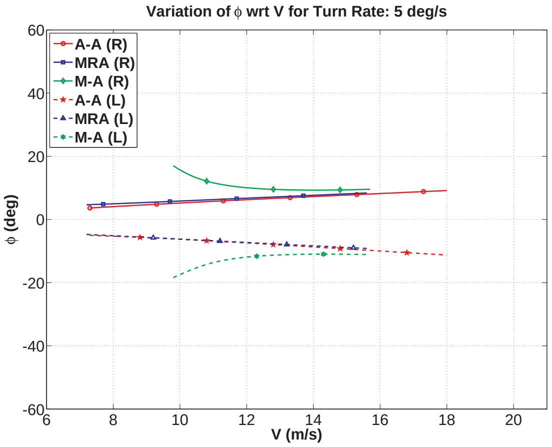

Figure 4.45. Bank angle variation with speed for $\dot{\psi} = 5$ deg/s.

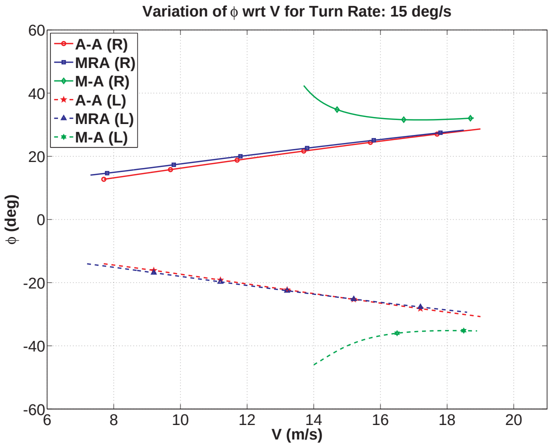

Figure 4.46. Bank angle variation with speed for $\dot{\psi} = 15$ deg/s.

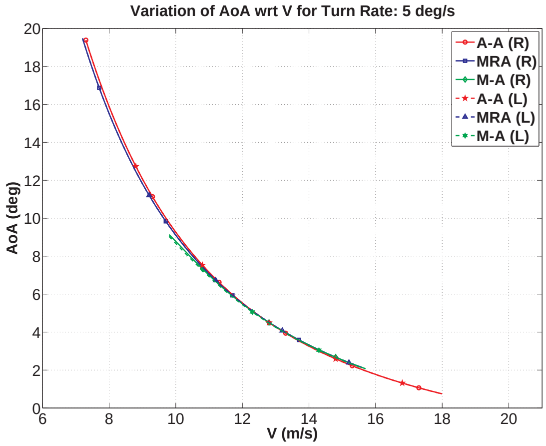

Figure 4.47. Angle of attack variation with speed for $\dot{\psi} = 5$ deg/s.

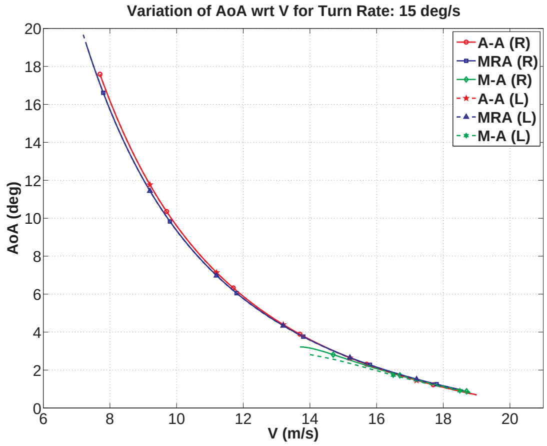

Figure 4.48. Angle of attack variation with speed for $\dot{\psi} = 15$ deg/s.

Since the direction of the propeller rotation affects the turn, left and right turns are performed for all aircraft tho show the difference. In Figs. 4.35-4.36, it can be seen that left turn requires higher thrust than right turn for M-A aircraft since higher sideslip requires at the same speed in shallower and sharp turns. This is due to fact that the orientation selected in Chapter 3 to reduce the sideslip handicap in cruise. For MRA aircraft, right turn requires slightly higher thrust at lower speeds while

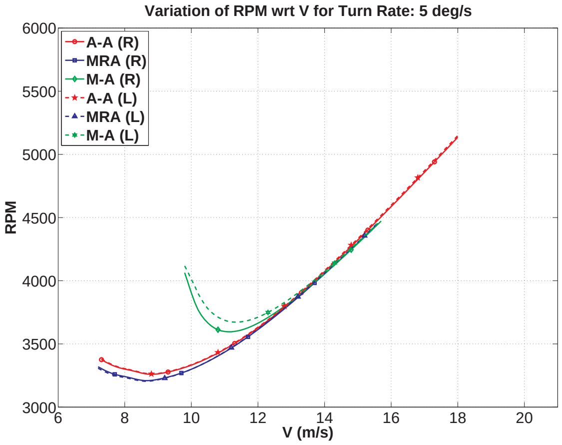

Figure 4.49. RPM variation with speed for $\dot{\psi} = 5$ deg/s.

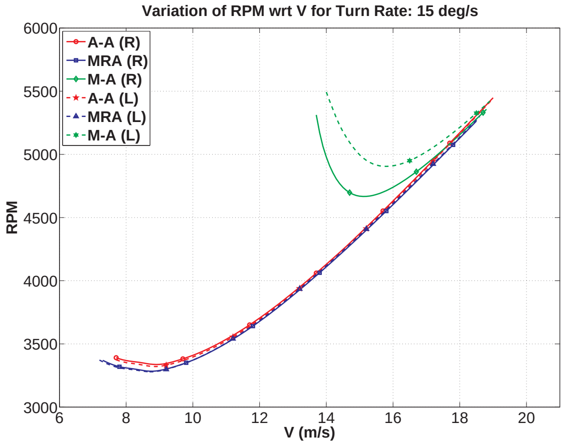

Figure 4.50. RPM variation with speed for $\dot{\psi} = 15$ deg/s.

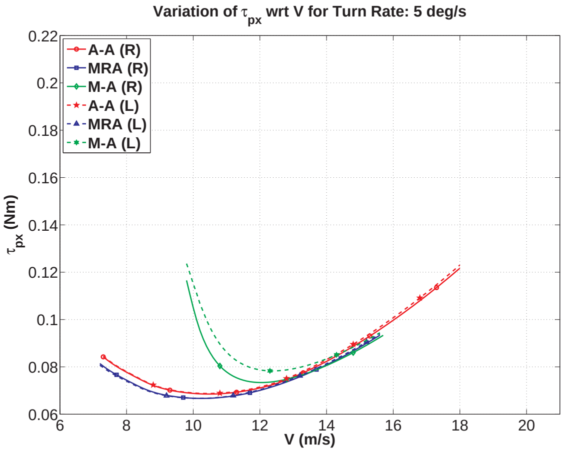

Figure 4.51. Required torque variation with speed for $\dot{\psi} = 5$ deg/s.

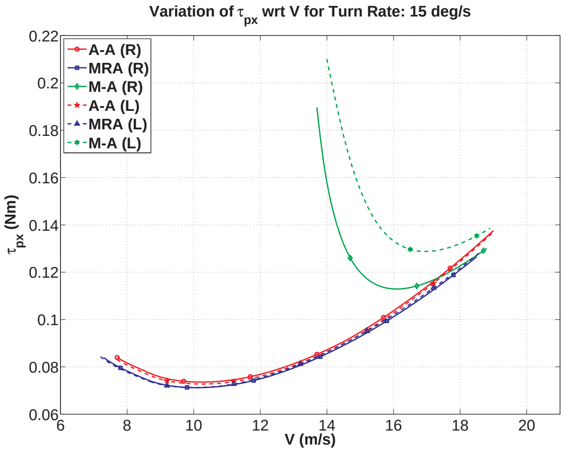

Figure 4.52. Required torque variation with speed for $\dot{\psi} = 15$ deg/s.

left turn requires slightly higher thrust at higher speeds in both turn rates. That is because of the requirement of higher rudder deflection (Figs. 4.43-4.44) for low speeds in right turn and for high speeds in left turn. For A-A aircraft, left turn requires slightly higher thrust in shallower turn while right turn requires slightly higher thrust in sharper turn since the total deflections of aileron and rudder change with the turn rate. Hence, all the states such as bank angle as shown in 4.45-4.46

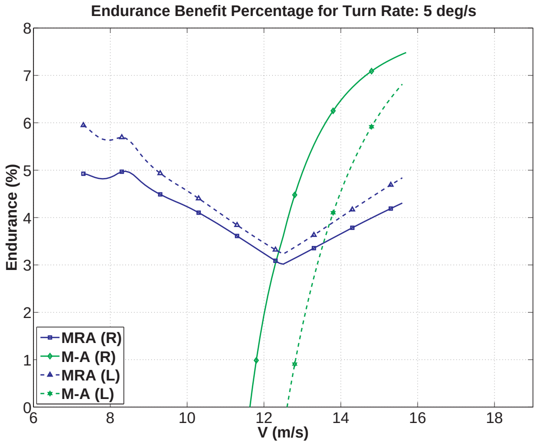

Figure 4.53. Percent increase in endurance as compared to that of A-A aircraft for $\dot{\psi} = 5$ deg/s.

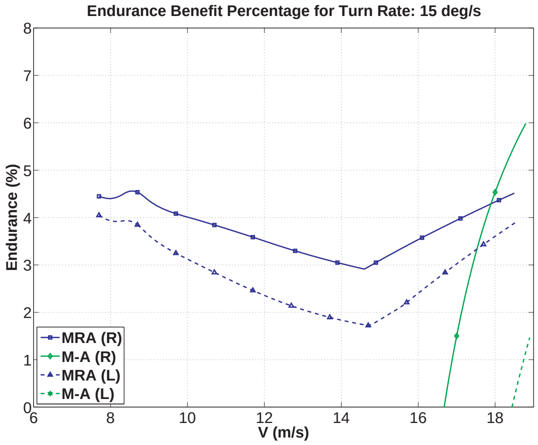

Figure 4.54. Percent increase in endurance as compared to that of A-A aircraft for $\dot{\psi} = 15$ deg/s.

with the same turn rate will not be the same in terms of magnitude for the same speed.

Elevator deflections or positions of longitudinal-mass seem to have slight differences between left and right turns as shown in Figs. 4.39-4.40. This is due to the fact that similar angle of attack is required for both turns as shown in Figs. 4.47-4.48.

Figures 4.49-4.50 show the variation of propeller angular speed. Since required thrust is the function of propeller angular speed as indicated in Eq. (2.50), similar discussion done for thrust is valid. For propeller angular speed, higher needs more torque and lower needs less torque as shown in Figs. 4.51-4.52.

Figures 4.53-4.54 shows the endurance benefit of mass-actuation compared to aero-actuation. For the M-A aircraft, the benefit can be obtained for mid and higher speeds ranges in shallower turn and for higher speed ranges in sharper turn since the M-A aircraft flies with higher sideslip angle at low speed, which increases drag along with sideslip angle. On the other hand, the highest benefit can be observed for the MRA aircraft in the lower speed ranges in both turn rates while the highest benefit for higher speed is observed for the M-A aircraft in shallower turn. Further, right turn gives higher benefit for M-A aircraft than the left turn. This is due to the fact that the required thrust is higher in left turn for M-A aircraft, as explained earlier. Similarly, higher the thrust means lower the endurance for MRA aircraft.

4.4 Results of Ascending and Descending Trim Analyses

In this section, results of ascending and descending trim are presented. As described in Chapter 4.1, eight nonlinear equations in Eqs. (4.1)-(4.2), (4.11) and (4.14) should be solved. Similar to cruise and steady-state turn, the performance of the three aircraft configurations are compared. Ascent/descent angle, γ, can be found from Eq. (4.13) for all aircraft.

For the trim analysis of the A-A aircraft, there are 23 unknowns in the eight equations: ω_p, V, α, β, p, q, r, ψ, θ, ϕ, γ, R/C, m_1, m_2, $\rho_{m_{1_x}}$, $\rho_{m_{1_y}}$, $\rho_{m_{1_z}}$, $\rho_{m_{2_x}}$, $\rho_{m_{2_y}}$, $\rho_{m_{2_z}}$, δ_e, δ_a and δ_r. Same assumptions for the A-A aircraft in cruise trim are considered to reduce the number of unknowns. This reduces the number of unknowns to eleven: V, R/C, ω_p, α, β, ψ, θ, ϕ, δ_e, δ_a, and δ_r. To reduce the number of unknowns to eight, three of eleven unknowns should be specified. Two variables to specify are selected to be airspeed, V, and rate of ascent/descent, R/C. Additionally, sideslip is set to zero, $\beta = 0$.

Trim analysis of the MRA aircraft also requires the solution of eight equations with the same 23 unknowns: ω_p, V, α, β, p, q, r, ψ, θ, ϕ, γ, R/C, m_1, m_2, $\rho_{m_{1_x}}$, $\rho_{m_{1_y}}$, $\rho_{m_{1_z}}$, $\rho_{m_{2_x}}$, $\rho_{m_{2_y}}$, $\rho_{m_{2_z}}$, δ_e, δ_a and δ_r. Same assumptions for the MRA aircraft in cruise trim are considered. Hence, the MRA aircraft has eleven unknowns left with eight equations: V, R/C, ω_p, α, β, ψ, θ, ϕ, $\rho_{m_{1_x}}$, $\rho_{m_{2_y}}$, and δ_r. Similar to the A-A aircraft, three of eleven unknowns should be specified. With V and R/C specified, ascending/descending trim can be found when the sideslip is set to zero, $\beta = 0$.

Similarly, trim analysis of the M-A aircraft requires solving eight equations with 23 unknowns: ω_p, V, α, β, p, q, r, ψ, θ, ϕ, γ, R/C, m_1, m_2, $\rho_{m_{1_x}}$, $\rho_{m_{1_y}}$, $\rho_{m_{1_z}}$, $\rho_{m_{2_x}}$, $\rho_{m_{2_y}}$, $\rho_{m_{2_z}}$, δ_e, δ_a and δ_r. Same assumptions for the M-A aircraft in cruise trim are taken into account. Hence, the M-A aircraft has ten unknowns left with eight equations: V, R/C, ω_p, α, β, ψ, θ, ϕ, $\rho_{m_{1_x}}$, and $\rho_{m_{2_y}}$. For specified V and R/C, number of unknowns will be eight and trim analysis of the M-A aircraft is carried out with eight unknowns left. Similar to cruise trim, the M-A aircraft has non-zero β.

Results are discussed in two subsections. In the first subsection, feasible trim analysis for ascending are presented. This is followed by a similar discussion for descending. Moreover, the performances of three aircraft configurations are compared.

4.4.1 Trim Analysis of Ascending Flight

In this section, results of ascending flight are presented. Figs. 4.55-4.56 show the throttle input and climb angle variation with different rates of climb for the A-A aircraft. As can be seen in Fig. 4.55, the maximum rate of climb is obtained about 13 m/s as this climb rate requires almost the maximum throttle setting within the entire very small feasible speed range. In other words, the feasible speed range will vanish with any higher climb rate. Further, increasing the rate of climb increases the climb angle in Fig. 4.56.

Figures 4.57-4.58 show the positions of mass-actuators and 4.59-4.60 show the throttle input and climb angle variation with different rates of climb for the M-A aircraft. In contrast to A-A aircraft, the maximum rate of climb is limited due to the saturations of the positions of mass-actuators in Figs. 4.57-4.58 and obtained about 9.5 m/s even though the maximum throttle is not implemented in Fig. 4.59. Due to the physical limitations of mass-actuators in M-A aircraft, the climb rate achieved with M-A aircraft is lower than that of A-A aircraft especially in the high speed

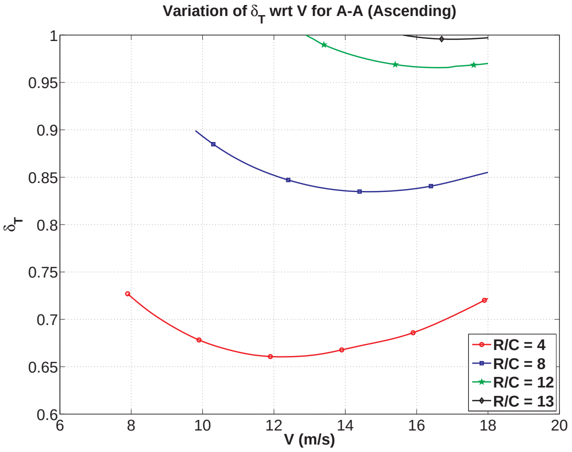

Figure 4.55. Throttle input variation with speed for A-A aircraft.

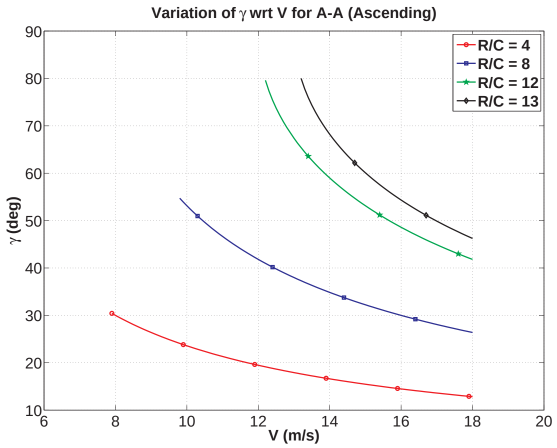

Figure 4.56. Climb angle variation with speed for A-A aircraft.

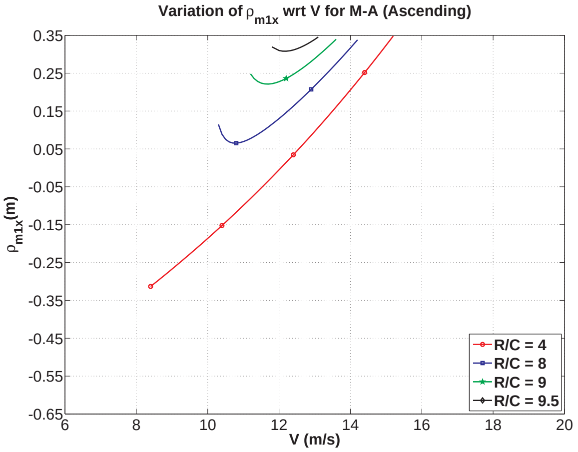

Figure 4.57. $\rho_{m_{1_x}}$ variation with speed for M-A aircraft.

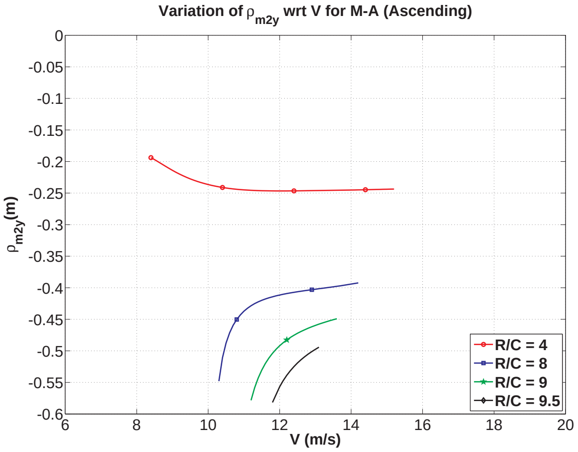

Figure 4.58. $\rho_{m_{2_y}}$ variation with speed for M-A aircraft.

region. Similar to the A-A aircraft, higher climb angle can be obtained by increasing the rate of climb in Fig. 4.60. Since the MRA aircraft has the similar results with the M-A aircraft, same discussions are valid for the MRA aircraft.

The performances of three aircraft configurations are compared for ascending (or climbing) flight when the rate of climb (or rate of ascent), R/C, is set to 4 m/s. Fig. 4.61 shows the variation of required thrust for ascending. The M-A aircraft

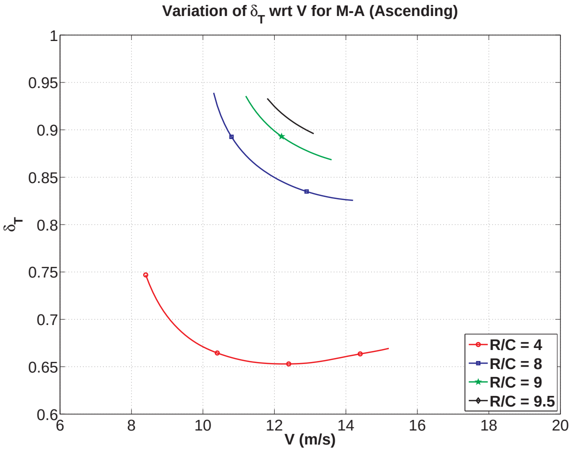

Figure 4.59. Throttle input variation with speed for M-A aircraft.

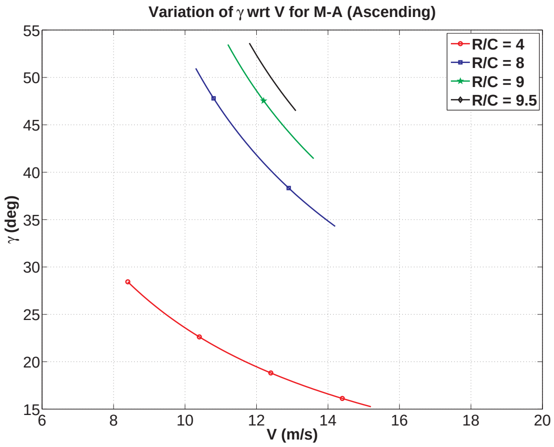

Figure 4.60. Climb angle variation with speed for M-A aircraft.

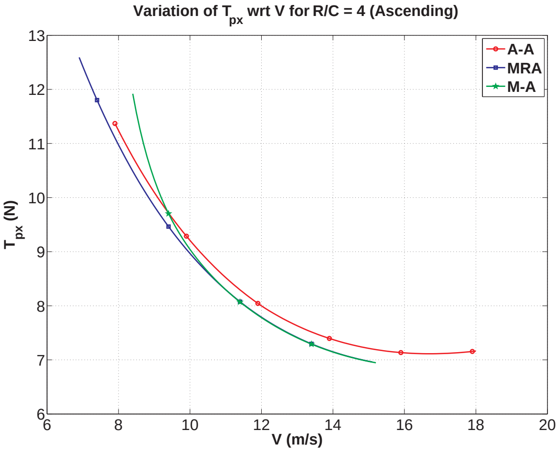

Figure 4.61. Required thrust variation with speed in ascending.

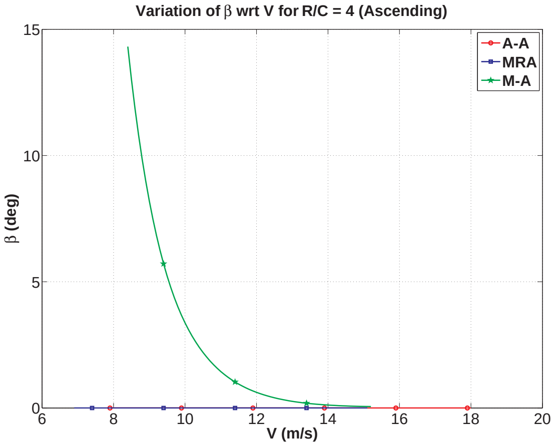

Figure 4.62. Sideslip angle variation with speed in ascending.

requires the highest thrust in lower speeds due to the requirement of higher sideslip angle in Fig. 4.62. On the other hand, the M-A aircraft requires the lowest thrust in higher speeds as the sideslip requirement decreases. Moreover, the MRA aircraft requires the lower thrust than the A-A aircraft for whole feasible speed.

Figures 4.63-4.65 show the variations of $\rho_{m_{2y}}$ & δ_a, δ_e and $\rho_{m_{1x}}$ & δ_e with speed. The minimum speed for the A-A aircraft is limited due to the saturation of minimum

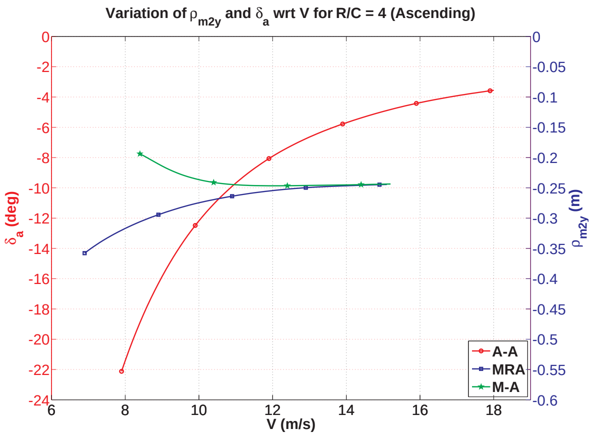

Figure 4.63. ρ_{m2_y} and δ_a variation with speed in ascending.

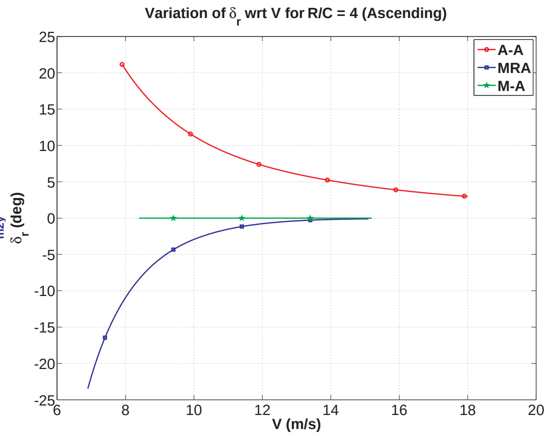

Figure 4.64. δ_r variation with speed in ascending.

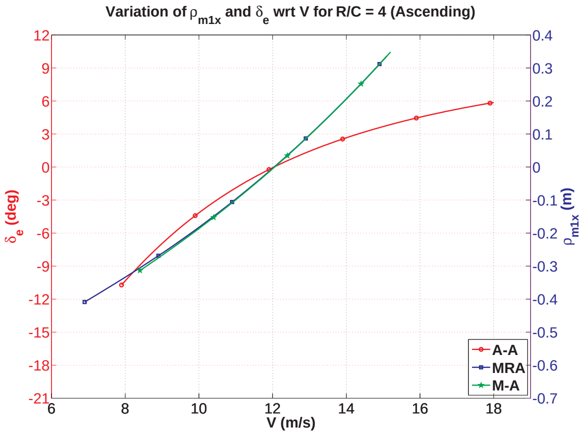

Figure 4.65. ρ_{m1_x} and δ_e variation with speed in ascending.

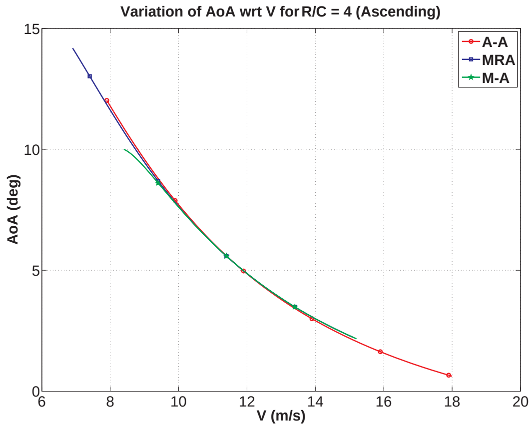

Figure 4.66. Angle of attack variation with speed in ascending.

aileron deflection in Fig. 4.63. On the other hand, the minimum speed for the MRA aircraft is limited due to the saturation of minimum rudder deflection in Fig. 4.64. Hence, the MRA aircraft can climb with slower speed than the A-A aircraft. The upper feasible speed for the MRA and the M-A aircraft is due to the saturation of maximum positions in Fig. 4.65 while the maximum limit for the A-A aircraft is restricted since the simulation is stopped at 18 m/s.

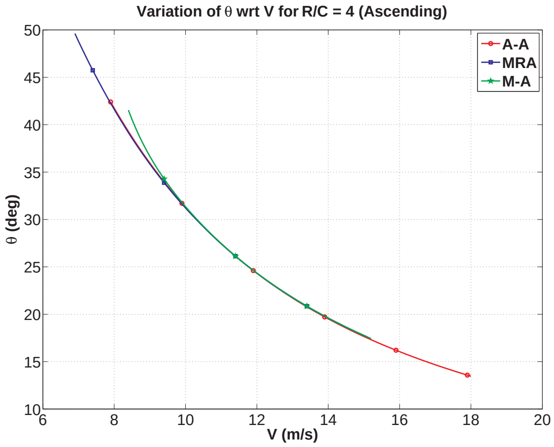

Figure 4.67. Pitch angle variation with speed in ascending.

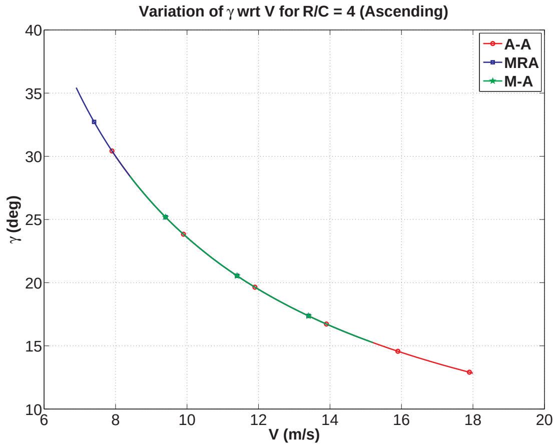

Figure 4.68. Climb angle variation with speed in ascending.

Figures 4.66-4.68 show the variations of angle of attack, pitch angle and climb angle with speed. As can be seen in these figures, all three aircraft have the similar values with the same rate of climb at the same flight speed. Hence, the same mission can be achieved for all aircraft if the same climb angle is desired.

4.4.2 Trim Analysis of Descending Flight

In this section, results of descending flight are presented. In this work, thrust and torque coefficients are calculated based on lookup tables obtained from Ref. [119]. In the lookup tables published by the manufacturer, the performance of propeller data are presented for advance ratios between $0 - 0.88$ and the coefficients are zero when the advance ratio, J, is 0.88. Fig. 4.69 shows the variation of advance ratio with different rates of descent for the A-A aircraft. As can be seen, when the rate of descent increases, advance ratio increases for the propeller. Since the maximum advance ratio available from Ref. [119] is reached, the feasible maximum rate of descent is obtained about 3 m/s in the higher speed region for the A-A aircraft. In Fig. 4.70, when the rate of descent increases, descent angle, γ, increases.

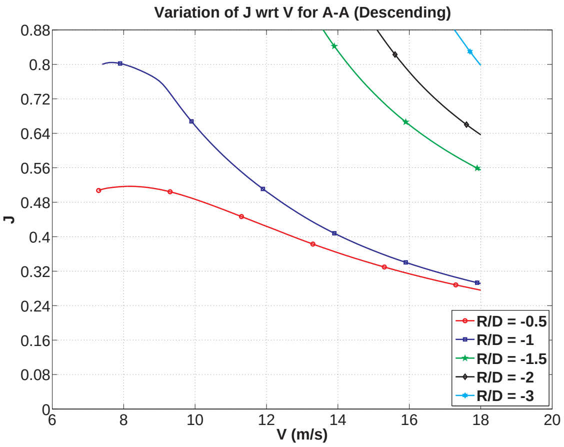

Figure 4.69. Advance ratio variation with speed for A-A aircraft.

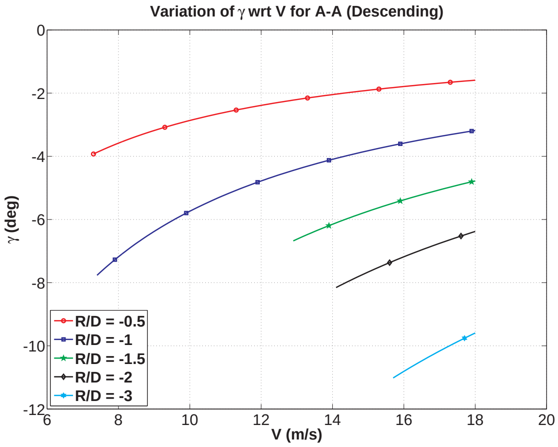

Figure 4.70. Descent angle variation with speed for A-A aircraft.

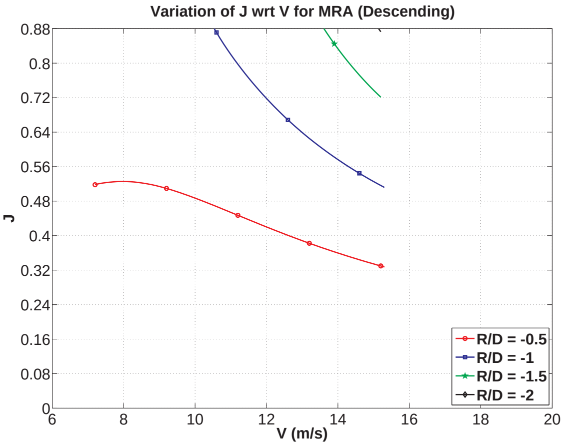

Figure 4.71. Advance ratio variation with speed for MRA aircraft.

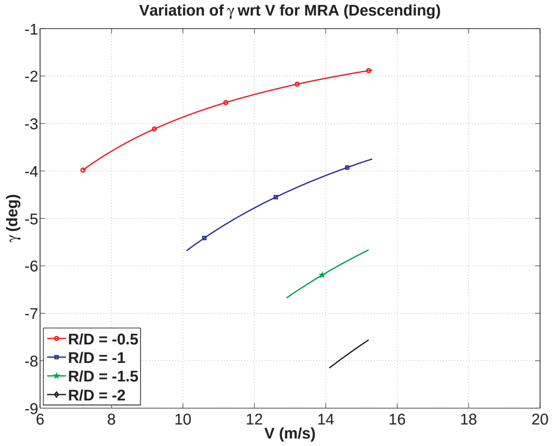

Figure 4.72. Descent angle variation with speed for MRA aircraft.

Figure 4.71 shows the variation of the advance ratio with different rates of descent for the MRA aircraft. Similar to A-A aircraft, advance ratio increases with increasing rate of descent. Hence, the feasible maximum rate of descent for the MRA aircraft is obtained about 2 m/s. Since the maximum feasible speed for the MRA aircraft is about 15.3 m/s due to the saturation of longitudinal-mass actuator as discussed in previous sections, the feasible rate of descent is less than the A-A aircraft. Similar to A-A aircraft, increasing the rate of descent increases the descent

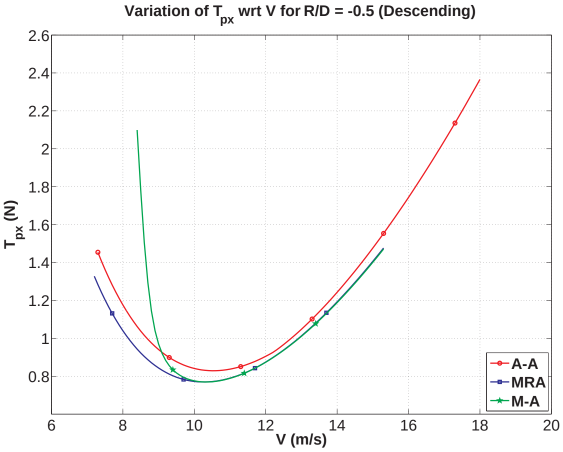

Figure 4.73. Required thrust variation with speed in descending.

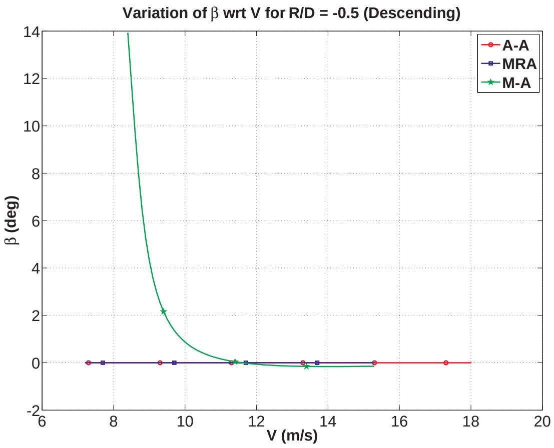

Figure 4.74. Sideslip angle variation with speed in descending.

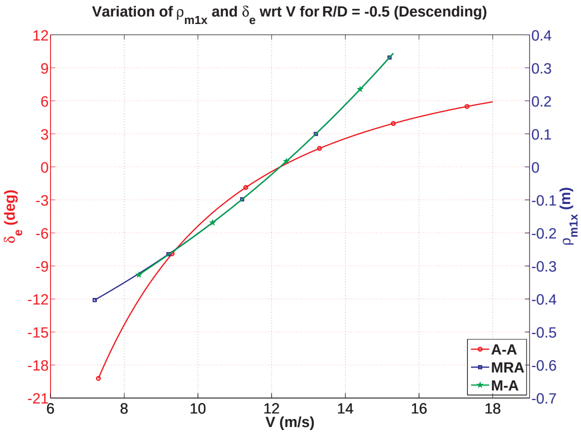

Figure 4.75. $\rho_{m_{1_x}}$ and δ_e variation with speed in descending.

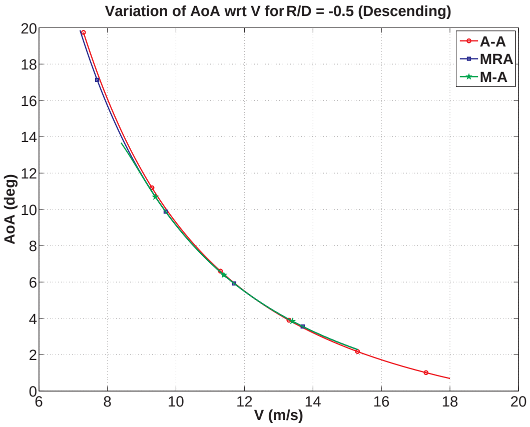

Figure 4.76. Angle of attack variation with speed in descending.

angle as can be seen in Fig. 4.72. Only the results for the MRA aircraft are presented due to the similar results with M-A aircraft and the same discussion is valid for the M-A aircraft.

The performances of three aircraft configurations are compared for descending flight when the rate of descent, R/C, (or can be called as R/D) is set to -0.5 m/s. Fig. 4.73 shows the variation of required thrust for descending. Similar to ascending flight, the M-A aircraft requires the highest thrust in lower speeds due to the requirement of

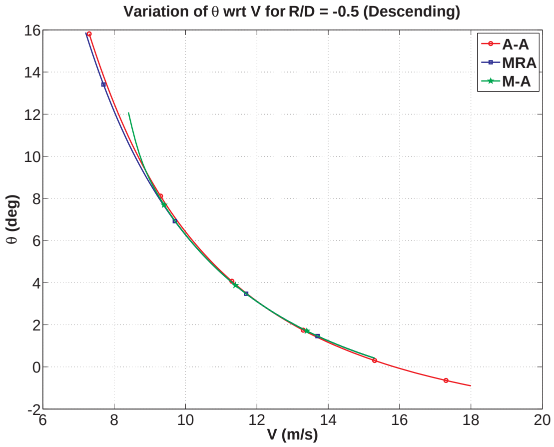

Figure 4.77. Pitch angle variation with speed in descending.

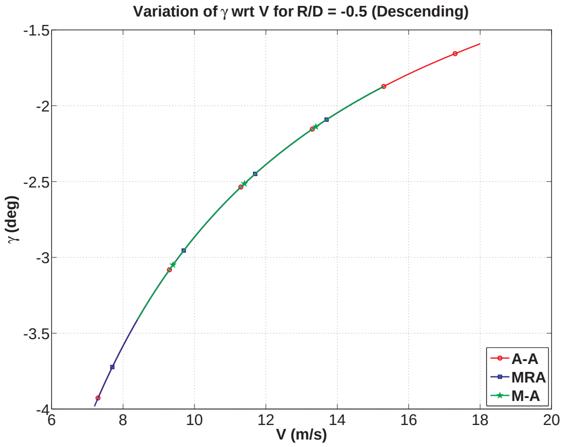

Figure 4.78. Climb angle variation with speed in descending.

higher sideslip angle in Fig. 4.74. Hence, the same discussion about required thrust is valid in here for descending flight.

Similar to previous flight cases, the maximum descending speed for the MRA and M-A aircraft is due to the saturation of longitudinal-mass actuator as shown in Fig. 4.75 while the trim is stopped at 18 m/s, which is the maximum speed for the A-A aircraft. The lowest feasible speed for the M-A aircraft is due to sideslip angle as shown in Fig. 4.74 while that is restricted for the A-A and the MRA aircraft by the maximum angle of attack allowed due to modeling constraint as can be seen in Fig. 4.76.

Figures 4.77-4.78 show the variations of pitch angle and descent angle with speed. Similar to ascending, all three aircraft have the similar pitch values. Hence, the same mission can be achieved if the same descent angle is desired.

4.5 Effect of Different Altitudes on Aircraft Trim

In this section, altitude effect on aircraft trim is presented. In the trim analyses presented in previous sections, altitude is constant and set as 200 m. Operating in different altitude causes variations in trim results since air density varies with altitude. Fig. 4.79 shows density variation with altitude for the first 1000 m [122]. Since the aircraft used is a small airplane, reasonable altitudes are investigated and selected as 0, 200, 400 and 600 m.

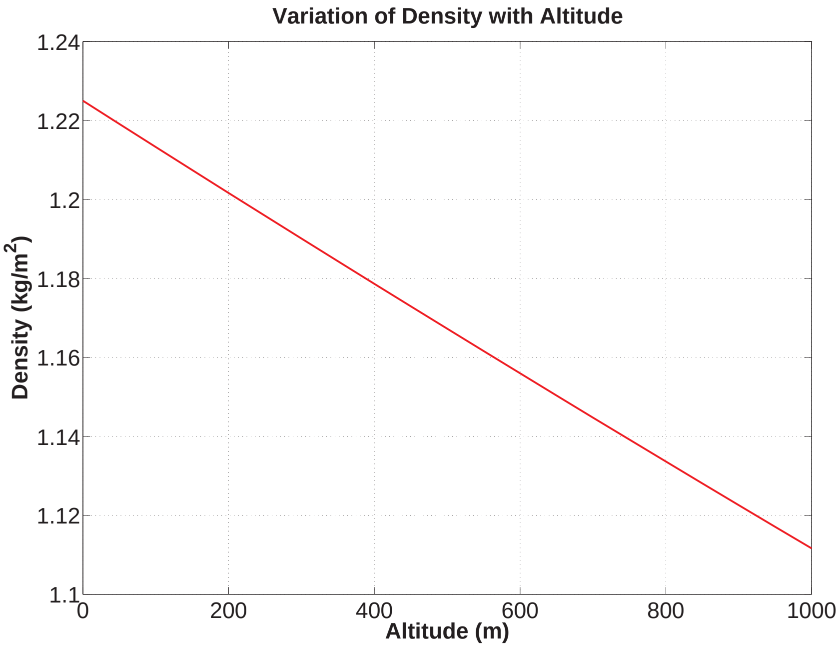

Figure 4.79. Variation of density with altitude.

Figure 4.80 shows the endurance variation with altitude for M-A aircraft. At the same trim speed, lower altitudes give higher endurance for lower speeds while higher altitudes give higher endurance for higher speed. This is due to the fact that lower thrust is required for lower speeds and higher thrust is required for higher speeds for the lower altitudes as shown in Fig. 4.81. Fig. 4.82 shows the variation of RPM with altitude for M-A aircraft. Lower altitudes require lower RPM throughout the whole feasible trim speeds. On the other hand, RPM changes among different altitudes are higher for lower speeds. When the speed increases, the motor speed for different

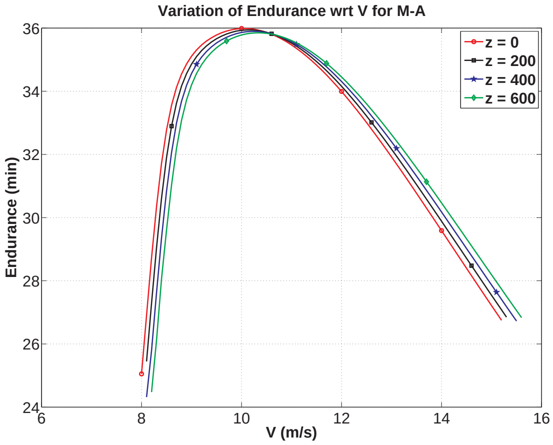

Figure 4.80. Variation of endurance with altitude for M-A aircraft.

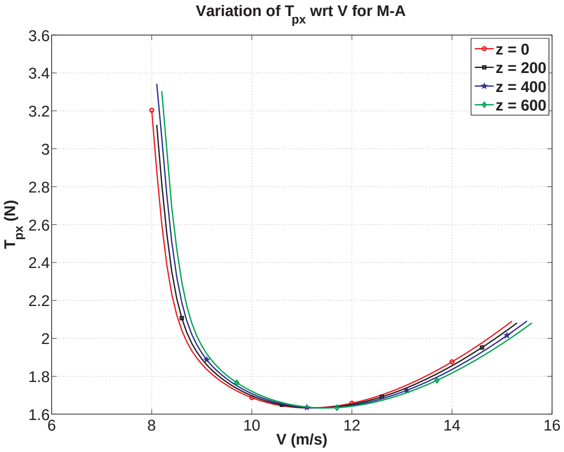

Figure 4.81. Variation of required thrust with altitude for M-A aircraft.

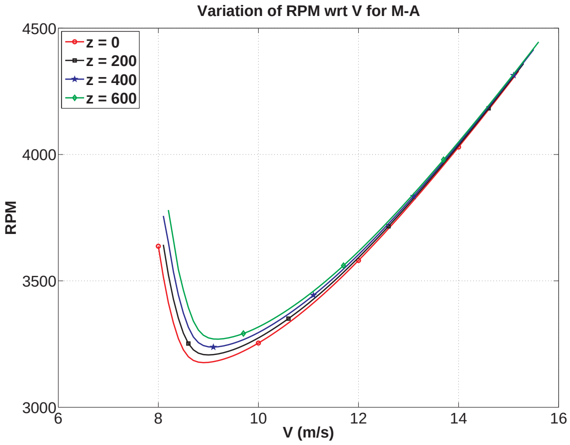

Figure 4.82. Variation of RPM with altitude for M-A aircraft.

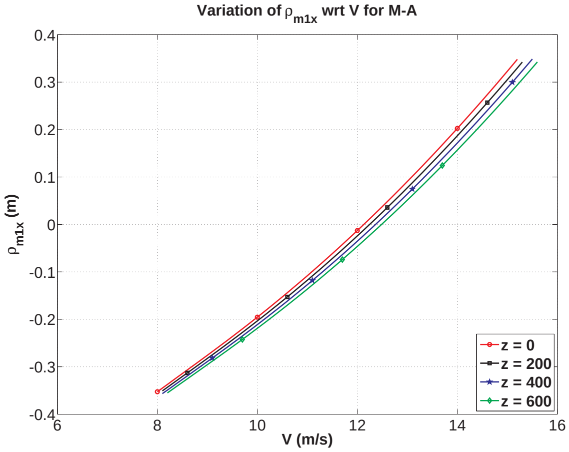

Figure 4.83. Variation of $\rho_{m_{1_x}}$ with altitude for M-A aircraft.

altitudes approaches to each other. Thrust coefficient in Eq. (2.48) is a function of aircraft speed and the motor rotational speed and thrust generated by propeller in Eq. (2.50) is affected by density. Since the change in RPM with different altitude is higher in lower speeds, higher endurance is observed for lower altitudes. For higher speeds, RPM with different altitudes are almost the same at the same trim speed. Hence, decrease in air density results in decrease in required thrust and increase in endurance.

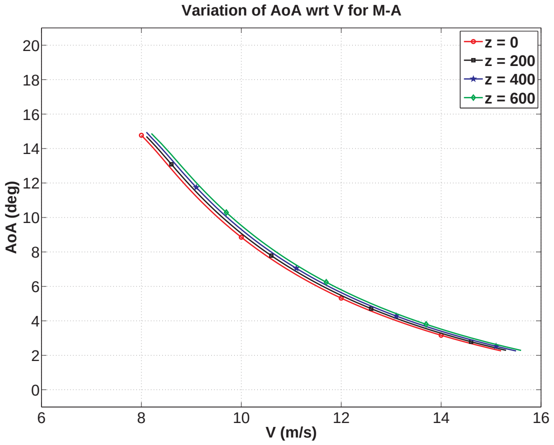

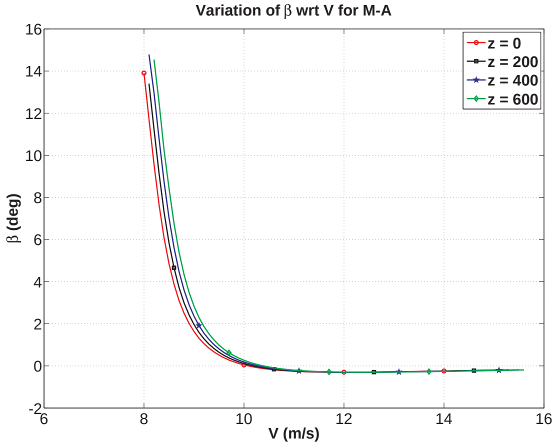

Figure 4.84. Variation of angle of attack with altitude for M-A aircraft.

Figure 4.85. Variation of sideslip with altitude for M-A aircraft.

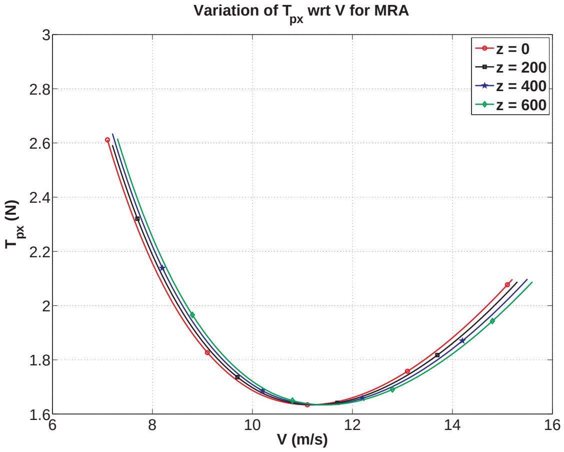

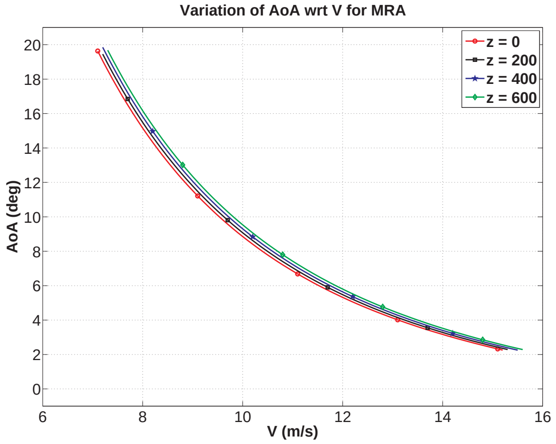

Figure 4.86. Variation of required thrust with altitude for MRA aircraft.

Figure 4.87. Variation of angle of attack with altitude for MRA aircraft.

Figure 4.83 shows the variation of longitudinally-mass position with different altitudes for M-A aircraft. For higher altitudes, position further to the back is required due to requirement of higher angle of attack with increasing altitude at the same speed as shown in Fig. 4.84. Hence, the upper limit of the feasible trim speeds are increased with higher altitude. For the lower limits of the feasible speed with different altitudes are imposed by sideslip angle as shown in Fig. 4.85. When the altitude increases, the requirement of sideslip angle also increases at the same speed.

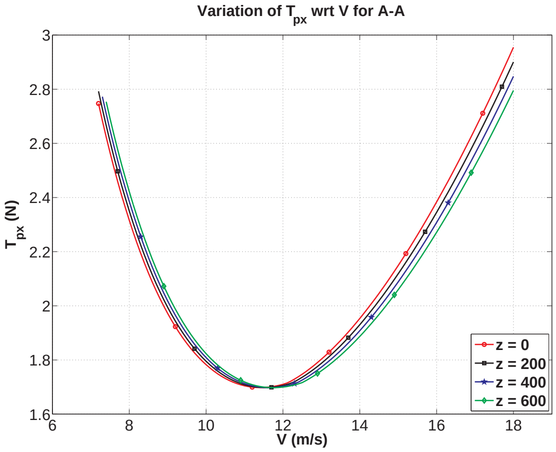

Figure 4.88. Variation of required thrust with altitude for A-A aircraft.

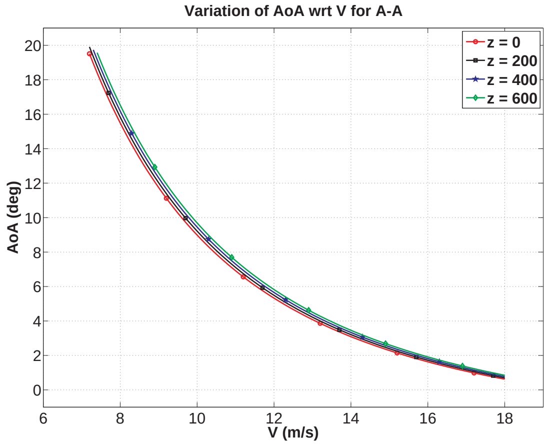

Figure 4.89. Variation of angle of attack with altitude for A-A aircraft.

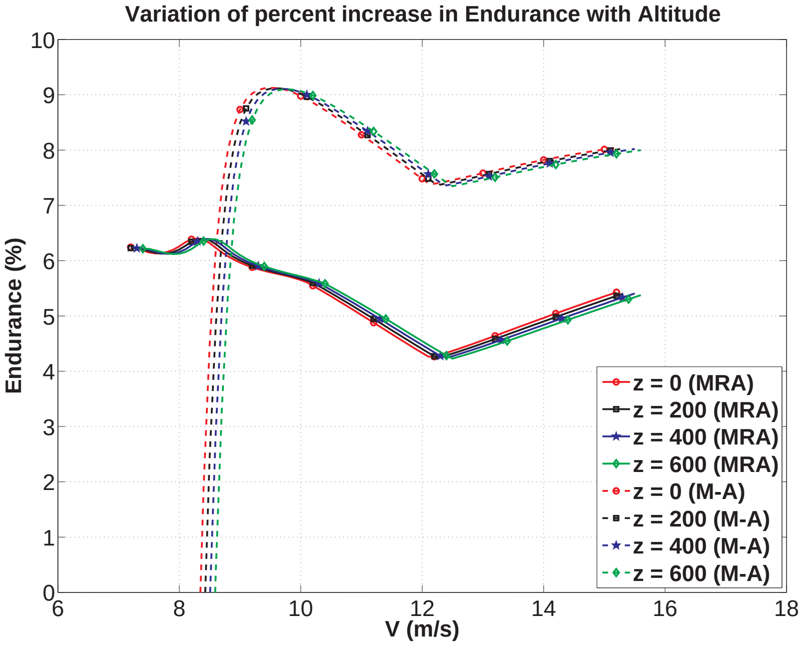

Figure 4.90. Percent increase in endurance as compared to that of A-A aircraft with altitude change.

Figure 4.86 shows the required thrust variation with altitude for MRA aircraft. Similar to M-A aircraft, lower altitudes require lower thrust in lower speeds and higher thrust in higher speeds. The upper limit of the feasible speed increases with increasing altitude for MRA aircraft similar to M-A aircraft. On the other hand, limitation for lower speed is due to requirement of angle of attack as shown in Fig. 4.87. Altitude increase requires higher angle of attack at the same speed. Same discussions are valid for the A-A aircraft (Figs. 4.88-4.89) since the A-A aircraft shows similar characteristics to the MRA aircraft with different altitudes.

Figure 4.90 shows the percent increase in endurance as compared to that of A-A aircraft with different altitudes. It can be observed that there are only slight differences with different altitudes for both MRA and M-A aircraft since the altitudes that the aircraft are operating are not too high.

4.6 Effect of Different Weights of Mass-actuators on Aircraft Trim

In this section, effects of different weights of longitudinal and lateral mass-actuators on aircraft trim are investigated. As explained in Section 2.6, the masses of the longitudinal and lateral mass-actuators are 0.3 kg and 0.1 kg, respectively. In order to investigate the effect of different weights of mass-actuators, the mass of longitudinal mass-actuator is set 0.2 kg and 0.4 kg while the mass of lateral mass-actuator is still 0.1 kg in cruise. Similarly, the mass of lateral mass-actuator is set 0.05 kg and 0.15 kg while the mass of longitudinal mass-actuator is still 0.3 kg in steady-state turn. During this analysis, the total weight of the aircraft is still the same and 1.9 kg. Results are compared to the configuration of the current mass-actuators. Changing the weights of mass-actuators does not effect the trim results for A-A aircraft. Due to the MRA aircraft has the similar characteristics to the M-A aircraft, only the results with M-A aircraft is presented.

Figure 4.91 shows the variation of positions of longitudinal mass-actuator with different weights for M-A aircraft in cruise. In spite of the required thrust are all the same for different mass configurations as shown in 4.92, the positions of the longitu-

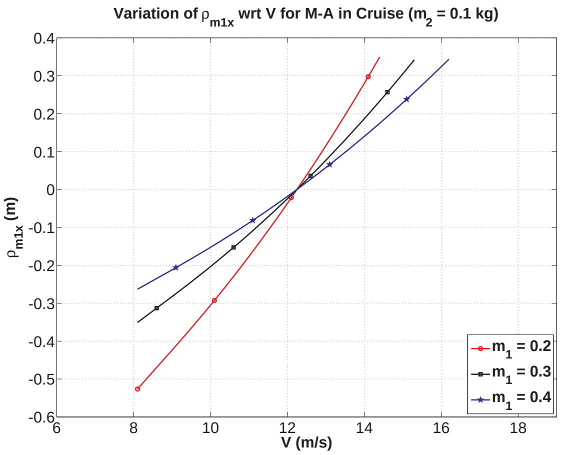

Figure 4.91. Variation of $\rho_{m_{1_x}}$ with m_1 for M-A aircraft in cruise.

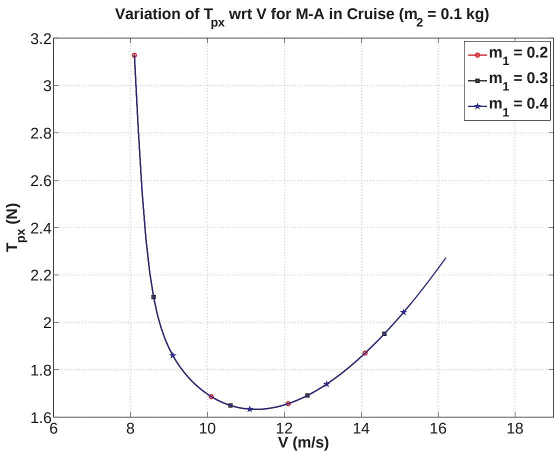

Figure 4.92. Variation of required thrust with m_1 for M-A aircraft in cruise.

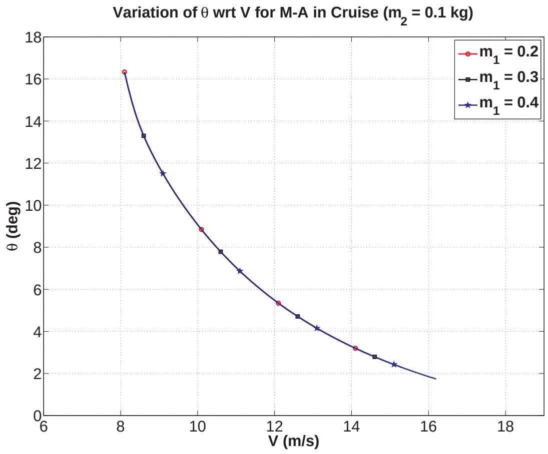

Figure 4.93. Variation of pitch angle with m_1 for M-A aircraft in cruise.

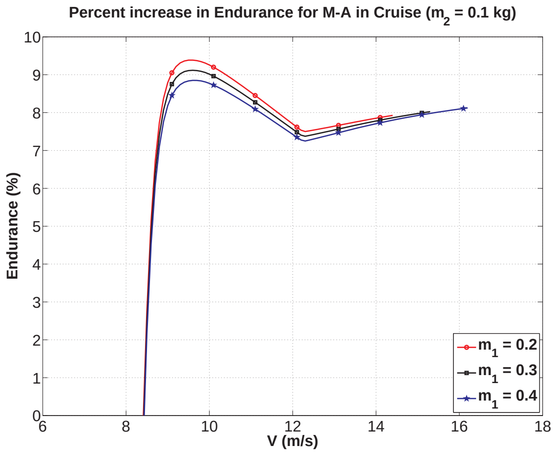

Figure 4.94. Percent increase in endurance with different m_1 in cruise.

dinal mass-actuator are different. The first observation is that heavier mass-actuator requires smaller deviation in magnitude from the zero-position in both positive and negative positions. The second observation is that the heavier mass-actuator increases the maximum feasible speed since it can produce higher moment due to its weight at the same speed. As one may remember from Section 4.2.3, the lowest feasible speed limit for M-A aircraft is due to the highest limit of sideslip angle.

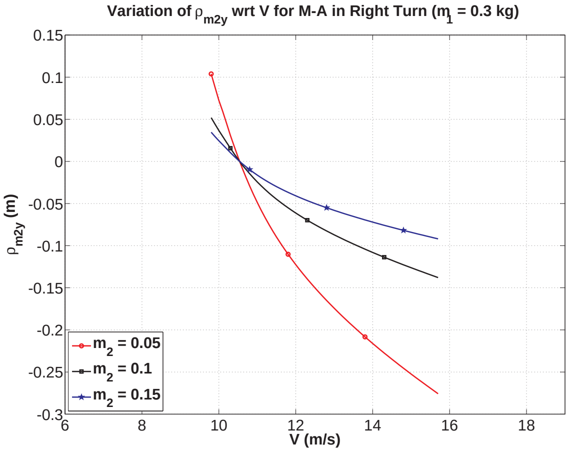

Figure 4.95. Variation of ρ_{m2_y} with m_2 for M-A aircraft in right turn.

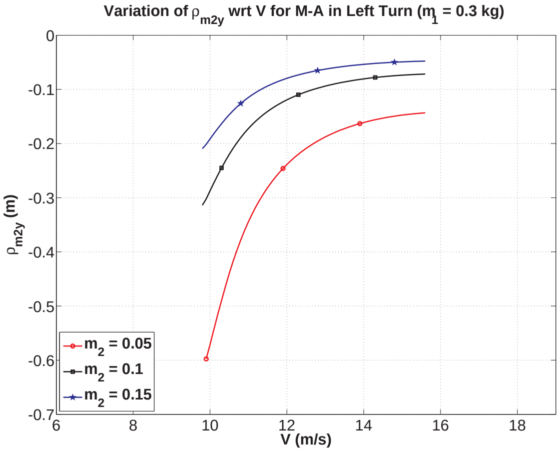

Figure 4.96. Variation of ρ_{m2_y} with m_2 for M-A aircraft in left turn.

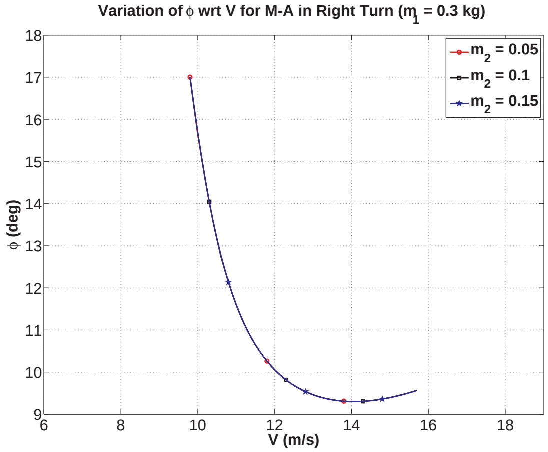

Figure 4.97. Variation of bank angle with m_2 for M-A aircraft in right turn.

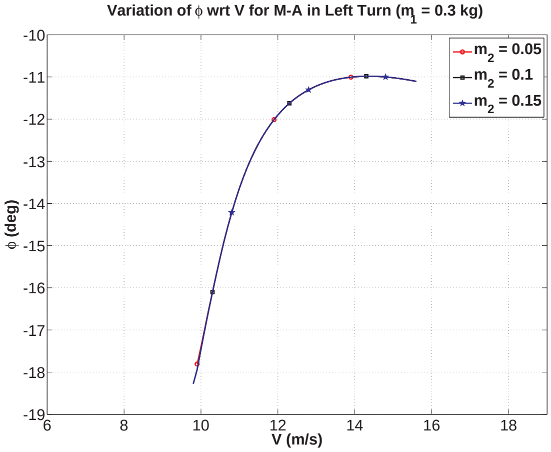

Figure 4.98. Variation of bank angle with m_2 for M-A aircraft in left turn.

Figure 4.93 shows the variation of pitch angle for M-A aircraft in cruise flight. It can be seen that pitch angles for all the configurations are the same. On the other hand, lighter mass-actuator configuration provides slight percent increase in endurance as compared to the A-A aircraft as shown in Fig. 4.94, especially in mid speed range. This is due to the fact that the servo for the longitudinal mass-actuator requires less current to hold it at the desired position in Eqs. (2.23)-(2.25) since the weight of the mass-actuator is lighter while the pitch angle is the same with others at the same speed.

Figures 4.95-4.96 show the variation of positions of lateral mass-actuator with different weights for M-A aircraft in steady-state turn. Similar to longitudinal mass-actuator, higher mass decreases the required displacement. Furthermore, the bank angles that the lateral mass-actuator produced are the same with different masses as shown in Figs. 4.97-4.98 since the same rolling moments are produced even though the weights are different. Since the effect of the different weights of lateral mass-actuator on servo current is the same with longitudinal mass-actuator, results are not presented in here and the same discussion is valid. As expected, using different weights of mass-actuators results in similar trim conditions with different positions if the total weight of the aircraft is not increased.

4.7 Summary of the Chapter

In this chapter, trim analyses of cruise, steady-state turn, ascending and descending were presented. The analysis for cruise showed that MRA airplane gives higher endurance than A-A airplane for whole feasible speed range while M-A airplane gives higher endurance than A-A airplane only for mid and higher speed ranges due to high trim values of sideslip angle in low speeds. The analysis for steady-state turn showed that results between right and left turns are not the same due to propeller effect. Results also showed that required thrust for right turn is less than left turn at the same speed since propeller turns clockwise. The trim analyses of ascending and descending showed that maximum rate of ascent/descent is higher for A-A airplane than the others since maximum position of longitudinal mass-actuator is saturated due to limitation of aircraft size. On the other hand, it was observed that comparison between three aircraft configurations for required thrust are similar to cruise at the same speed and endurance increases by using mass-actuators. The effect of altitude variation on aircraft trim was also investigated. Results showed that endurance for different altitudes are similar since the airplanes fly in low altitudes. Finally, the effect of different weights of mass-actuators on aircraft trim was investigated. Results showed that using heavier mass without increasing total weight of the aircraft increases the maximum feasible speed for MRA and M-A airplanes. However, that would decrease the endurance slightly with heavier mass at the nominal conditions since actuator performances are included in the trim analyses.

CHAPTER 5

CONTROLLABILITY ANALYSES AND CONTROL DESIGN

In this chapter, linearization of equations of motion to study the controllability and control design is presented at first. Then, controllability analyses based on linearized state-space matrices are presented. Controllability of all three aircraft are investigated for trim results with propeller effect included for cruise, steady-state turn and ascending/descending presented in Chapter 4. Further, level or quality of controllability is investigated for all three aircraft. The level or quality of controllability is to determine how controllable an aircraft configuration is at a trim condition relative to the other trim conditions or relative to the other aircraft configurations at the same trim condition. Finally, control design procedure is presented.

5.1 Linearization of Equations of Motion

In this section, linearization of equations of motion is carried out. The linearized equations are used to analyze the controllability of airplane with mass-actuation and to design a controller to track altitude or rate of ascent/descent, airspeed and turn rate commands.

Translational and rotational kinematics, Eqs. (2.2)-(2.5), and dynamics, Eqs. (2.6) (after multiplied by matrix ϵ) and (2.9) (after multiplied by matrix $\mathbf{I_t}$) without the wind components along with electric motor dynamics from Eqs. (2.11) and (2.12) are represented in compact form as

$$\underline{h}(\dot{\underline{x}}) = \underline{f}(\underline{x}, \dot{\underline{x}}, \underline{u}, \dot{\underline{u}}, \ddot{\underline{u}}, \underline{v}) \tag{5.1}$$

where

$$\underline{x} = \begin{bmatrix} V & \beta & \alpha & p & q & r & \psi & \theta & \phi & x & y & z & \boldsymbol{\iota}_m & \omega_p \end{bmatrix}^T \tag{5.2}$$

$$\underline{v} = \begin{bmatrix} X & Y & Z & \mathcal{L} & \mathcal{M} & \mathcal{N} & T_x & T_y & T_z & \boldsymbol{\tau}_{p_x} & \boldsymbol{\tau}_{p_y} & \boldsymbol{\tau}_{p_z} \end{bmatrix}^T \tag{5.3}$$

$$\underline{u} = \begin{bmatrix} \delta_a & \delta_e & \delta_r & \delta_T & \rho_{m_{jx}} & \rho_{m_{jy}} & \rho_{m_{jz}} \end{bmatrix}^T \tag{5.4}$$

Additionally, aerodynamics from Eqs. (2.30)-(2.35) and components of propeller thrust and torque from Eqs. (2.50)-(2.51) are written in compact form as

$$\underline{v} = \underline{g}(\underline{x}, \dot{\underline{x}}, \underline{u}) \tag{5.5}$$

Note that the definition of input vector $\underline{u}$ in Eq. (5.4) includes both aerodynamic control surface deflections and mass-actuator positions. This is done despite the fact that A-A aircraft does not have mass-actuation related control variables and aircraft with mass-actuation does not have control surfaces with the exception of rudder in some cases. Furthermore, only the direct torque effect in Eq. (2.61) is considered as the propeller torque and propeller frame is coincided with the airplane body frame during the linearization. Hence, y- and z- components of the propeller thrust ($T_y = T_z = 0$) and torque ($\boldsymbol{\tau}_{p_y} = \boldsymbol{\tau}_{p_z} = 0$) are assumed to be zero. With this combined input/control vector, the linearization is carried out only once and then the respective columns of the input/control matrix are extracted for each aircraft configuration.

Linearization is carried out in two steps: (i) Eqs. (5.1) and (5.5) are linearized separately for each trim condition, and (ii) the linearized Eq. (5.5) is substituted in the linearized Eq. (5.1) to obtain the final form of the linearized equations.

Linearization of Eqs. (5.1) and (5.5) yields respectively in a matrix form

$$\mathbf{L}\Delta\dot{\underline{x}} = \mathbf{A_0}\Delta\underline{x} + \mathbf{A_1}\Delta\dot{\underline{x}} + \mathbf{B_0}\Delta\underline{u} + \mathbf{B_1}\Delta\dot{\underline{u}} + \mathbf{B_2}\Delta\ddot{\underline{u}} + \mathbf{C}\Delta\underline{v} \tag{5.6}$$

$$\Delta\underline{v} = \mathbf{E_0}\Delta\underline{x} + \mathbf{E_1}\Delta\dot{\underline{x}} + \mathbf{F}\Delta\underline{u} \tag{5.7}$$

Substituting Eq. (5.7) into Eq. (5.6) results in the linearized equations of motion as

$$\Delta\dot{\underline{x}} = \mathbf{A_i}\Delta\underline{x} + \mathbf{B_{0i}}\Delta\underline{u} + \mathbf{B_{1i}}\Delta\dot{\underline{u}} + \mathbf{B_{2i}}\Delta\ddot{\underline{u}} \tag{5.8}$$

where

$$\mathbf{A_i} = [\mathbf{L} - (\mathbf{A_1} + \mathbf{CE_1})]^{-1}[\mathbf{A_0} + \mathbf{CE_0}] \tag{5.9}$$

$$\mathbf{B_{0i}} = [\mathbf{L} - (\mathbf{A_1} + \mathbf{CE_1})]^{-1}[\mathbf{B_0} + \mathbf{CF}] \tag{5.10}$$

$$\mathbf{B_{1i}} = [\mathbf{L} - (\mathbf{A_1} + \mathbf{CE_1})]^{-1}\mathbf{B_1} \tag{5.11}$$

$$\mathbf{B_{2i}} = [\mathbf{L} - (\mathbf{A_1} + \mathbf{CE_1})]^{-1}\mathbf{B_2} \tag{5.12}$$

where index i indicates each trim condition the equations are linearized around, which means a different set of $\mathbf{A}$, $\mathbf{B_0}$, $\mathbf{B_1}$ and $\mathbf{B_2}$ matrices for each trim condition. The elements of matrices in Eqs. (5.6)-(5.7) are presented in Appendix B.

5.2 Controllability Analysis

In this section, controllability of all three aircraft are investigated. After the linearization of equations of motions, all matrices for all three aircraft in Eq. (5.8) are calculated for every trim conditions obtained for cruise flight in Section 4.2, steady-state turn flight in Section 4.3 and ascending/descending flight in Section 4.4. In this study, the controllability analysis is performed based on $\mathbf{A_i}$ and $\mathbf{B_{0_i}}$ matrices, ignoring $\mathbf{B_{1_i}}$ and $\mathbf{B_{2_i}}$ matrices associated with the derivatives of the control variables. The controllability matrix is constructed from $\mathbf{A_i}$ and $\mathbf{B_{0_i}}$ matrices as

$$\mathbf{Co} = [\mathbf{B_{0i}} \quad \mathbf{A_i}\mathbf{B_{0i}} \quad \mathbf{A_i}^2\mathbf{B_{0i}} \quad \dots \quad \mathbf{A_i}^{n-1}\mathbf{B_{0i}}] \tag{5.13}$$

where n is the order of the system and rank of $\mathbf{Co}$ implies complete controllability if it is equal to n. However, since the numerical computation of rank is not reliable, a different approach is taken to determine controllability. A similarity transformation matrix $\mathbf{T}$ is determined that results in new state, control and output matrices as

$$\mathbf{\bar{A}_i} = \mathbf{T A_i T^T} \tag{5.14}$$

$$\mathbf{\bar{B}_{0_i}} = \mathbf{T B_{0i}} \tag{5.15}$$

$$\mathbf{\bar{C}_i} = \mathbf{C T^T} \tag{5.16}$$

where

$$\mathbf{\bar{A}_i} = \begin{bmatrix} \mathbf{A_{uc}} & \mathbf{0} \\ \mathbf{A_{21}} & \mathbf{A_c} \end{bmatrix} \tag{5.17}$$

$$\mathbf{\bar{B}_{0_i}} = \begin{bmatrix} \mathbf{0} & \mathbf{B_c} \end{bmatrix}^T \tag{5.18}$$

$$\mathbf{\bar{C}_i} = \begin{bmatrix} \mathbf{C_{uc}} & \mathbf{C_c} \end{bmatrix} \tag{5.19}$$

such that the new state-space representation has the controllable and uncontrollable states separated. $(\mathbf{A_c}, \mathbf{B_c})$ is controllable part of the matrix, and $\mathbf{A_{uc}}$ represents the uncontrollable parts. This analysis is carried out in $MATLAB$ using $ctrbf$ command. Through this analysis, it is determined that the number of controllable states is equal to 14, i.e., there is no uncontrollable states, in all cruise, steady-state turn and ascending/descending trim conditions studied for A-A, MRA and M-A aircraft within the feasible speed range.

5.3 Quality of Controllability

In Section 3.1, propeller effect on aircraft performance was discussed. In this section, only the direct torque effect due to the propeller is considered to understand the propeller effect on quality of controllability. Results with and without propeller effect are obtained and compared. During the quality of controllability analyses, components of propeller torque are removed in Eq. (5.3) for the results without the propeller effect. Quality of controllability analysis is done in two cases. In the first case, some metrics for level of controllability are defined and the aircraft configurations are compared based on these metrics. In the second case, control effectiveness based on control/input matrix is investigated. Finally, both quality of controllability methods are compared.

5.3.1 Metrics to Quantify Level of Controllability

Consider a state-space representation of a linear system

$$\Delta\dot{x} = \mathbf{A}\Delta x + \mathbf{B}\Delta u \tag{5.20}$$

where $\Delta x \in \mathbb{R}^{n\times 1}$ and $\Delta u \in \mathbb{R}^{m\times 1}$. Let λ_i be the i^{th} eigenvalue of state matrix $\mathbf{A}$ and $w_i \in \mathbb{R}^{n\times 1}$ be the associated left eigenvector such that

$$w_i^T\mathbf{A} = \lambda_{\mathbf{i}} w_i^T \tag{5.21}$$

Popov-Belevitch-Hautus (PBH) controllability test states that ($\mathbf{A}$, $\mathbf{B}$) pair is uncontrollable if and only if there exists a left eigenvector of $\mathbf{A}$ that is orthogonal to the columns of control matrix $\mathbf{B}$, i.e.,

$$w_i^T\mathbf{B} = 0 \tag{5.22}$$

Inspired by this controllability test, a new metric for quantifying the level of controllability is introduced in this thesis, as follows.

The scalar product of an eigenvector and a column of matrix is defined as

$$\mu_{ij} = w_i^T b_j, \quad i = \{1, .., n\}, j = \{1, .., m\} \tag{5.23}$$

where w_i is the i^{th} left eigenvector of matrix $\mathbf{A}$ and b_j is the j^{th} column of matrix $\mathbf{B}$. Since μ_{ij} is the result of a scalar product operation, it can also be written as

$$\mu_{ij} = |w_i||b_j| \cos \alpha_{c_{ij}} \tag{5.24}$$

where $|w_i|$ and $|b_j|$ are the magnitudes of the corresponding quantities and $\alpha_{c_{ij}}$ is the angle between the directions represented by w_i and b_j. When eigenvector of w_i is orthogonal to column b_j, angle $\alpha_{c_{ij}}$ becomes 90 *deg* and thus $\mu_{ij} = 0$ regardless of the values of $|w_i|$ and $|b_j|$. An increase in μ_{ij} can occur when (1) eigenvector w_i and column b_j moves away from orthogonality, i.e., angle $\alpha_{c_{ij}}$ moves away from 90 *deg*, and/or (2) the magnitudes of w_i and/or b_j increase. In either case, a larger μ_{ij} is considered to indicated increased level of controllability of the state associated with eigenvector w_i from the j^{th} control variable.

Metric μ_{ij} quantifies the level of controllability for a given state and control variable pair. That is, for the multi-input multi-output system given in Eq. (5.20), there are $n \times m$ number of μ_{ij}. To quantify the level of controllability of the whole system, i.e., considering all the states and control variables, a single metric should be computed. This is done by applying the “max-min” operator of all μ_{ij} as

$$\mu = \min_{i} \left\{ \max_{j} \{\mu_{ij}\} \right\} \tag{5.25}$$

For a given index i, i.e., a given eigenvector, μ_{ij}, $j = \{1, .., m\}$ define levels of controllability from each of m number of control variables. Among these, the largest is selected to represent the highest level of controllability of the state associated with the i^{th} eigenvector from all the control variables. For example, pitch rate of an airplane is affected the most from the elevator while the other control variables may have effect on pitch rate. In such a case, μ_{ij} associated with elevator should be the highest for the pitch rate. For the complete controllability of a system, all states should be controllable. An uncontrollable state makes the whole system considered uncontrollable. Accordingly, the level of controllability of the whole system should be quantified by the least controllable state. That is why the minimum of μ_{ij} is taken over all eigenvectors, i.e., over index j.

In the literature, there are several other scalar metrics defined to measure the quality of controllability. To make a comparison with the newly defined metric μ above, one of the metrics proposed in the literature is also computed along with μ. According to Ref. [123], scalar metrics of controllability can be formulated as the minimum eigenvalue, trace, or determinant of the controllability Gramian.

$$\bar{\mu}_1 = \lambda_{min}(\mathbf{W_c}) \tag{5.26}$$

$$\bar{\mu}_2 = \frac{n}{tr\mathbf{W_c}^{-1}} \tag{5.27}$$

$$\bar{\mu}_3 = det(\mathbf{W_c}) \tag{5.28}$$

Similar to μ, the higher the scalar value, the more controllability for all three metrics as stated in Ref. [123]. For this method, the first attempt was to compute these metrics of controllability of the whole system (i.e., translational and rotational dynamics and kinematics all together). However, it became apparent that none of the three metrics led to any clear pattern for comparison between mass actuation and aerodynamic control surface actuation. This was due to the difficulty in handling very large matrices such as controllability Gramian matrix. Only when the lateral and longitudinal motions are assumed to be decoupled, the metrics as defined in Eq. (5.26) could be computed. This was because the size of the state and control matrices are reduced, which led to controllability Gramian matrices of smaller size. However, it should be noted that the longitudinal and lateral motions are not decoupled even in the cruise condition when the propeller effect is considered. Due to the tightly coupled longitudinal and lateral motions, the metrics computed for longitudinal and lateral motions separately are not reliable. The newly introduced metric μ calculation, however, can easily be computed for the whole coupled system as it does not require the handling of the Gramian matrix.

5.3.2 Analyses of Level of Controllability by Controllability Metrics

The matrix $\mathbf{A}$ for each aircraft consists of the state variables $V, \beta, \alpha, p, q, r, \theta, \phi$, which are longitudinal and lateral states. Among these states, the scalar metric in Eq. (5.25) is calculated for each aircraft separately, where j^{th} control variables are (1) elevator, aileron and rudder for A-A aircraft, (2) longitudinal mass-actuator, lateral mass-actuator and rudder for MRA aircraft, and (3) longitudinal mass-actuator and lateral mass-actuator for M-A aircraft.

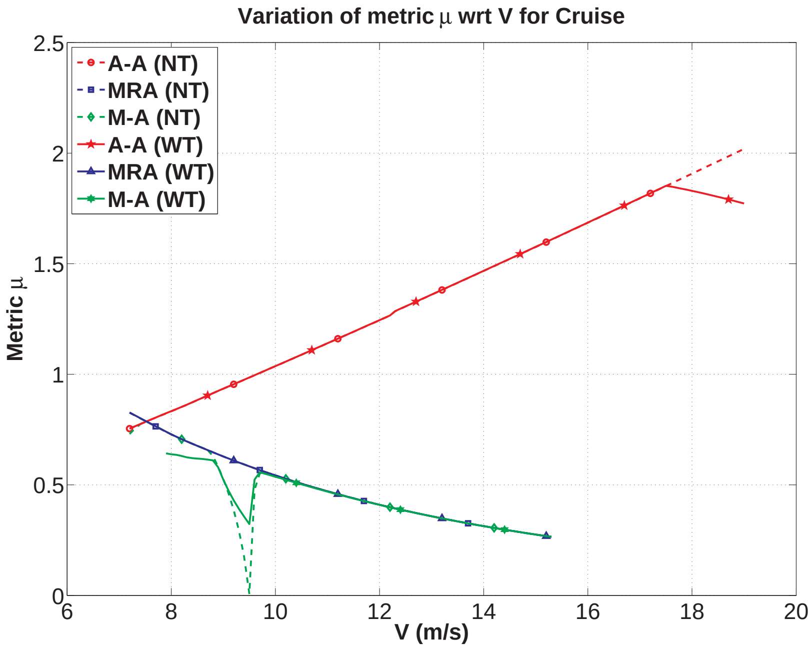

Figure 5.1. Metric μ variation with speed in cruise.

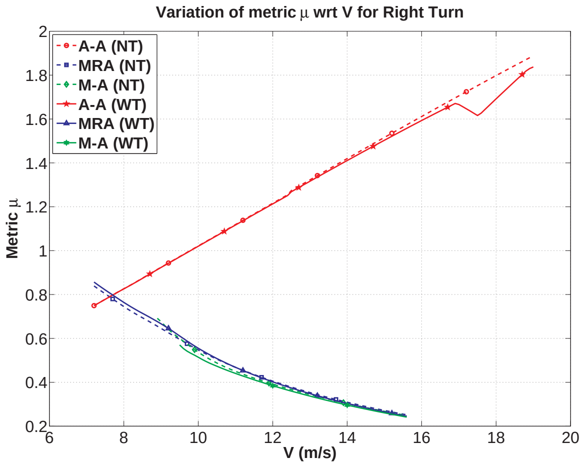

Figure 5.2. Metric μ variation with speed in right turn.

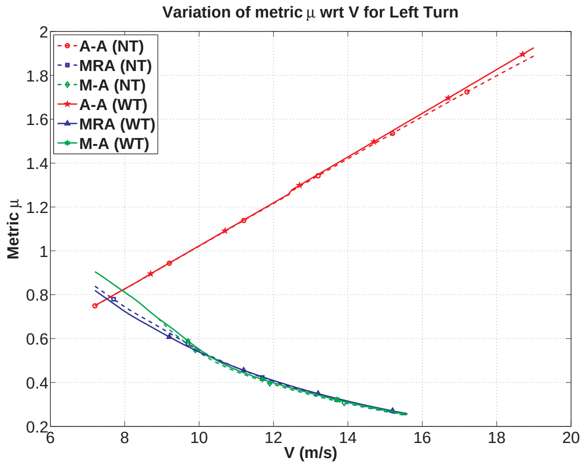

Figure 5.3. Metric μ variation with speed in left turn.

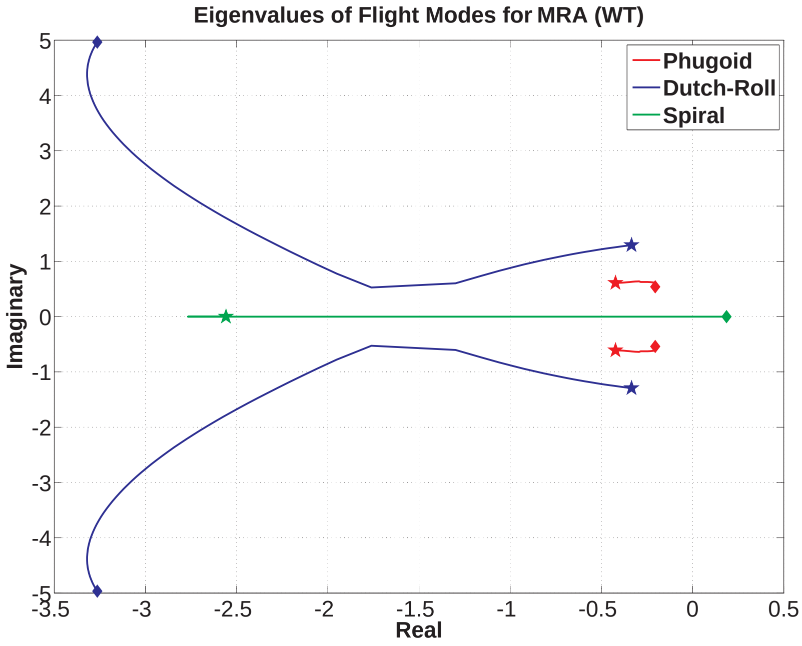

Figure 5.4. Eigenvalues of flight modes for MRA aircraft.

Figures 5.1-5.3 show the variation of controllability metric μ with respect to speed for each aircraft with propeller effect (represented as WT in the figures) and without propeller effect (represented as NT in the figures). The first observation is that including propeller effect does not significantly change the controllability metric

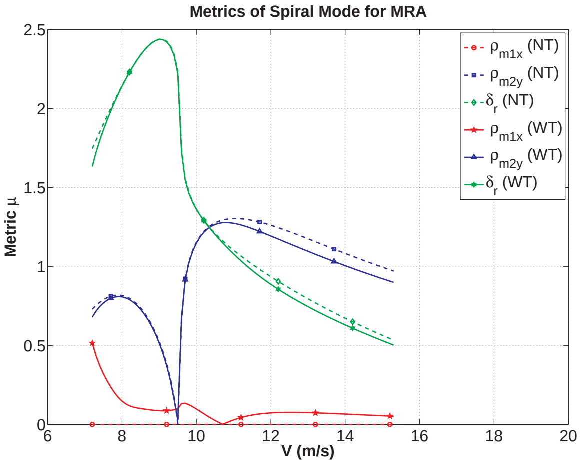

Figure 5.5. Metrics μ of spiral mode for MRA aircraft.

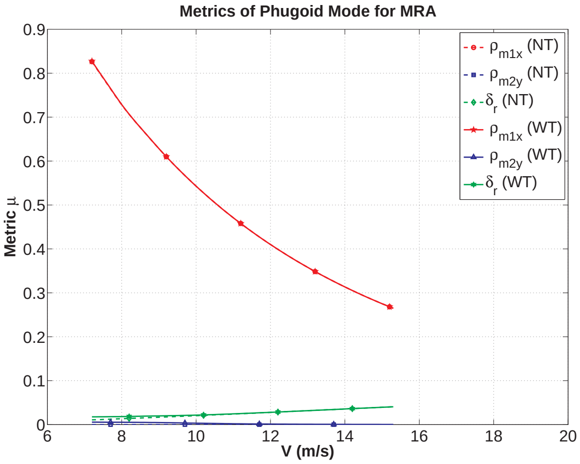

Figure 5.6. Metrics μ of phugoid mode for MRA aircraft.

μ for each flight. Second observation is that the controllability metric μ for each flight increases with increasing speed for A-A aircraft while decreases with increasing speed for both MRA and M-A aircraft. For lower speeds, all three aircraft give similar level of controllability while A-A aircraft has the highest controllability at higher speeds. Further, MRA aircraft has slightly higher controllability than M-A aircraft at lower speed while trend for both aircraft are similar when the speed increases. On the other hand, there is a dip observed for M-A aircraft (especially for NT case) in cruise flight about 9.5 m/s. To explain this, eigenvalue variation and control input specific metrics obtained for the lateral flight mode of MRA aircraft are shown in Figs. 5.4-5.5 since M-A aircraft and MRA aircraft give almost similar results.

In Fig. 5.4, the variations of eigenvalues of spiral, dutch-roll and phugoid modes with speed are shown since they are the closest modes to the right hand side of the root-locus. In that figure, star represents the lowest speed while diamond represents the highest speed. It is observed that the eigenvalues of spiral mode and dutch-roll mode have the same real value (-1.5 approximately) when the speed is about 9.5 m/s. Furthermore, it is seen that the metric obtained from the lateral mass-actuator also show a dip about 9.5 m/s as shown in Fig. 5.5. Since MRA aircraft has a rudder and M-A aircraft does not have that rudder, that dip is not seen for MRA aircraft due to the rudder is more effective at that speed for this mode. Mathematically, those observation explains the dip for mass-actuation. Physically, the reason of this can be explained by considering the inertia variation due to moving-masses. Since M-A aircraft has higher lateral angles such as sideslip and bank even in cruise flight as discussed in Section 4.2.3, the moment generated by both mass-actuators may become almost zero due to the fact that longitudinal mass-actuator can also produce yaw/roll moments and lateral mass-actuator can also produce pitch/yaw moments with angles. On the other hand, that instantaneous decrease in level of controllability does not affect the flight benefit if the M-A aircraft flies with different speeds that also have the endurance benefit as discussed in Section 4.2.3.

Figures 5.5-5.6 show the control input specific metric for spiral and phugoid modes obtained from each control input for MRA aircraft as an example with and without propeller effect. It is observed that the controllability metric μ is determined for each aircraft from either spiral mode or phugoid mode. Since those metrics have slight differences between each other, the trend of the controllability metric μ may vary. For example, the trend of the controllability metric variation for A-A aircraft (WT case) at higher speeds in cruise and right turn can be observed in Figs. 5.1 and 5.2. This is due to the fact that the controllability metric changes with speed depending on either spiral or phugoid mode variation.

Figures 5.7-5.8 show the controllability metric μ_1, formulated in Eq. (5.26) for cruise flight only since right and left turn give similar patterns. As explained before, the state-space models are written separately for the decoupled longitudinal and lateral motions. The state variables in the longitudinal model are V, α, q, θ and control variables are either elevator deflection δ_e or x-position of the longitudinally moving mass $\rho_{m_{1_x}}$. The lateral state-space model has state variables β, p, r, ϕ and control variables are either aileron deflection δ_a or y-position of the laterally moving mass $\rho_{m_{2_y}}$. It is observed that the characteristics of this metric obtained from Eq. (5.26) show similar trend with the metric obtained from Eq. (5.25). Furthermore, the dip about 9.5 m/s is also observed for mass-actuation as shown in Fig. 5.8.

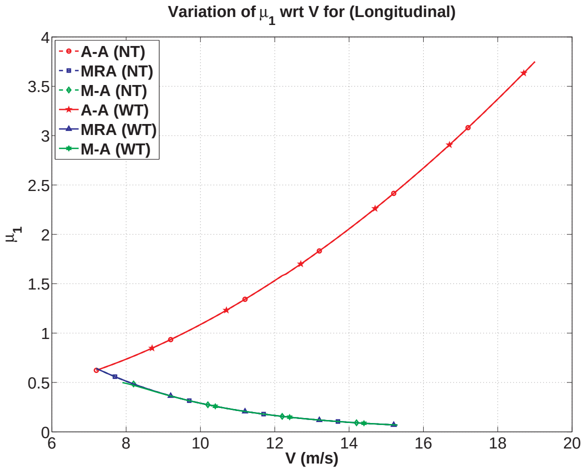

Figure 5.7. Variation of μ_1 with speed for longitudinal model in cruise .

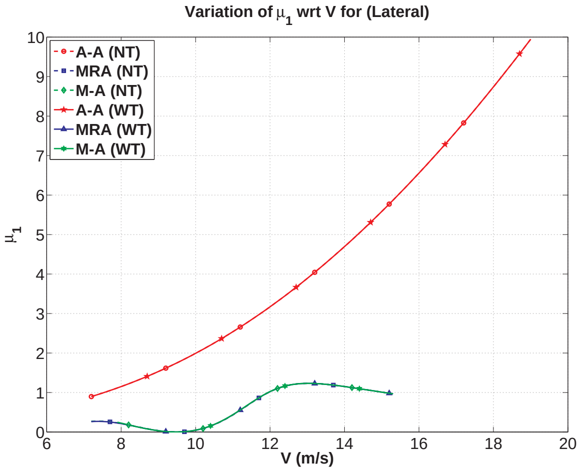

Figure 5.8. Variation of μ_1 with speed for lateral model in cruise.

5.3.3 Control/Input Matrix

The second method for quantifying controllability is based on studying the values of relevant entries of the control/input matrix. Let b_{ij} denotes the entry of **B** matrix at row i and column j in Eq. (5.20). The value of b_{ij} quantifies how much a unit change in Δu_j (j^{th} control variable) affects $\Delta \dot{x}_i$ (derivative of i^{th} state variable). In other words, the product of $b_{ij}\Delta u_j$ quantifies the effectiveness of Δu_j on $\Delta \dot{x}_i$. This can be used to compare the effectiveness of different control variables on the derivative of a given state variable. Each control variable has its saturation limits.

At a given trim condition, b_{ij} is a constant and Δu_j can vary within its saturation limits. The range of effectiveness of Δu_j can then be computed by $b_{ij}\,\Delta u_{j,min}$ at the lower limit and $b_{ij}\,\Delta u_{j,max}$ at the upper limit. Thus, $(b_{ij}\,\Delta u_{j,min},\ b_{ij}\,\Delta u_{j,max})$ defines how much $\Delta\dot{x}_i$ can be varied by Δu_j. Note that $\Delta u_{j,min}$ and $\Delta u_{j,max}$ may change with trim condition if the trim value of u_j varies with trim condition. If the physical limitations of u_j implies $u_j \in (u_{j,min}, u_{j,max})$, then $\Delta u_{j,min} = u_{j,min} - u_{j,0}$ and $\Delta u_{j,max} = u_{j,max} - u_{j,0}$ where $u_{j,0}$ is the trim value of control variable u_j. As $u_{j,0}$ will vary with different trim conditions, $\Delta u_{j,min}$ and $\Delta u_{j,max}$ will also vary even if $u_{j,min}$ and $u_{j,max}$ are fixed.

Recall that the main idea with mass-actuation is to use a longitudinally moving mass within the fuselage to generate pitching moment instead of elevator, and a laterally moving mass along the wings to generate rolling moment instead of ailerons. Thus, the effectiveness of longitudinally moving mass will be compared with that of elevator. The state variables directly affected by the longitudinal moving mass or elevator are angle-of-attack α and pitch rate q. Similarly, the state variables directly associated with laterally moving mass or aileron are sideslip angle β, roll rate p and yaw rate r. In this analysis of these lateral variables, the rudder deflection is also considered.

5.3.4 Results of Controllability Analysis by Control/Input Matrix

As explained earlier, this analysis is based on the corresponding entry of **B**-matrix (control/input matrix) to quantify how much a given control variable can induce change in the derivative of a given state. This is defined as "control effectiveness" in this study. This analysis is done and presented for all three aircraft configurations (A-A, MRA, M-A) with propeller effect (WT) and without propeller effect (NT) in the figures. Results show that the characteristics of right and left turns are similar to cruise. Hence, only the results with cruise are presented here and discussions about cruise are valid for turn.

Figure 5.9 shows the control effectiveness of elevator and longitudinally moving-mass on angle of attack derivative. The effectiveness of the elevator increases with speed as expected through the aerodynamics. This increase is only on the positive deflection range and the lower (negative) limit stays about constant throughout the whole speed range. That is, positive elevator deflection can induce larger angle of attack increase with increasing speed while negative elevator deflection induces about the same angle of attack change. Note that at the lowest cruise speed, the upper limit of elevator effectiveness range is close to zero. This implies that elevator cannot induce alpha increase at this low speed. The effectiveness of mass-actuation on the angle of attack shows an interesting variation with increasing cruise speed. At low speed, mass-actuation provides wider control effectiveness than the elevator does. This is the case even for alpha increase. That is, mass actuation can induce (more) alpha increase at low speed while the elevator cannot. The effectiveness of the mass-actuation on alpha decreases with increasing speed at the low speed range. At around 12.5 m/s, the mass-actuation effectiveness becomes zero. Beyond this speed, the mass-actuation becomes more effective with increasing speed in the positive alpha derivative direction. It is interesting to note that mass-actuation effectiveness at the upper limit comes back to zero at the upper limit of the feasible speed range. In the high speed range of the mass-actuation effectiveness, aerodynamic actuation is much more effective in the positive range. Another observation is that including propeller torque does not affect the effectiveness of elevator or longitudinally moving-mass on angle of attack change for all three aircraft configurations.

Figure 5.10 shows the aerodynamic and mass-actuation effectiveness on pitch rate. Elevator effectiveness widens with increasing speed. As in the case of alpha

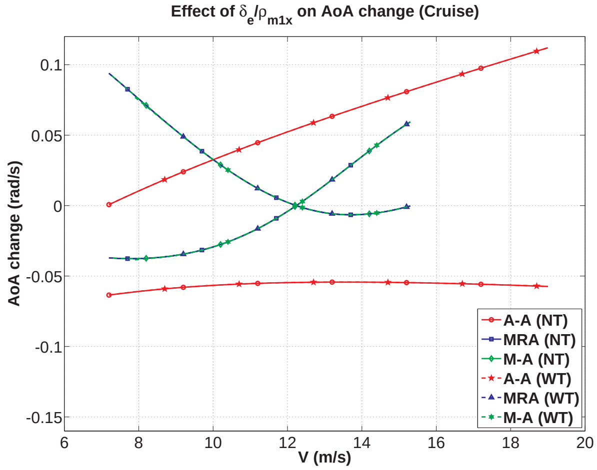

Figure 5.9. Effect of $\rho_{m_{1_x}}$ or δ_e on angle of attack change, $\Delta\dot{\alpha}$, in cruise.

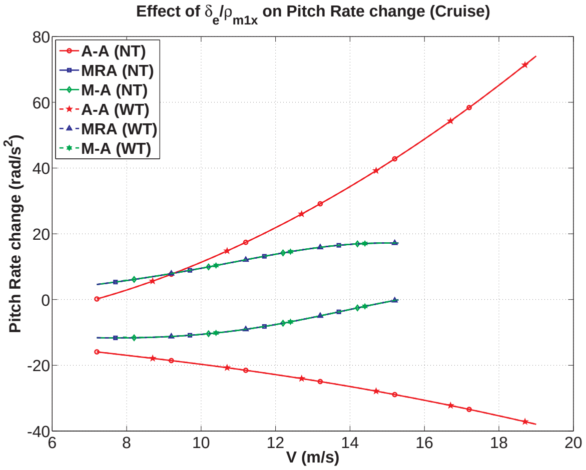

Figure 5.10. Effect of $\rho_{m_{1_x}}$ or δ_e on pitch rate change, $\Delta\dot{q}$, in cruise.

shown in Fig. 5.9, elevator effectiveness at the upper limit starts from zero at the lowest cruise speed. In general, aerodynamic actuation provides more control effectiveness except at low speed in the positive $\dot{q}$ direction. The variation of the mass-actuation effectiveness with speed shows an opposite trend in pitch rate as compared to angle-of-attack. The effectiveness on alpha is minimum (zero) in the middle of the feasible speed range (Fig. 5.9) while it is maximum for pitch rate (Fig. 5.10). The mass-actuation effectiveness goes to zero at the lower limit at the highest speeds of the feasible speed ranges. A similar observation is made in Fig. 5.9 where the effectiveness goes to zero at the upper limits at the highest feasible speeds. Similar to the effectiveness on angle of attack, propeller torque does not affect the effectiveness on pitch rate importantly.

Figures 5.11-5.12 show the effectiveness of aileron or laterally moving-mass and rudder on roll rate change. As aerodynamic control surfaces, both aileron and rudder show increasing effectiveness with increasing speed. As expected, aileron is much more effective than rudder on roll rate. The effectiveness of mass-actuation does not change

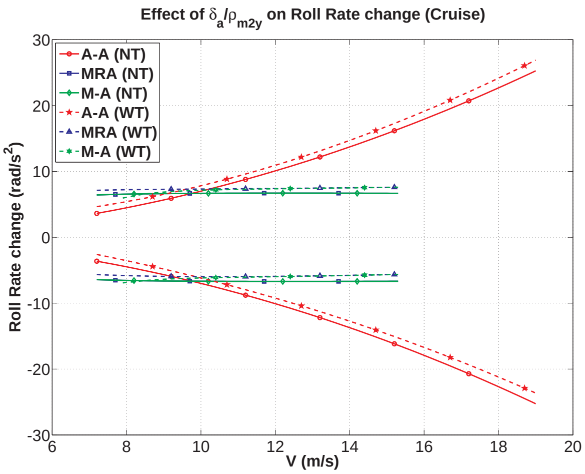

Figure 5.11. Effect of $\rho_{m_{2y}}$ or δ_a on roll rate change, $\Delta\dot{p}$, in cruise.

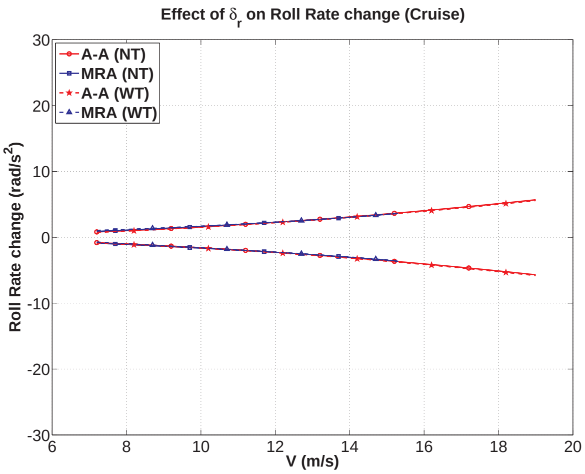

Figure 5.12. Effect of δ_r on roll rate change, $\Delta\dot{p}$, in cruise.

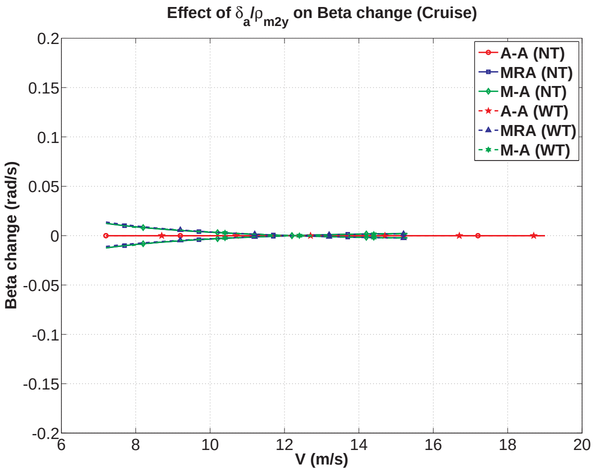

Figure 5.13. Effect of $\rho_{m_{2y}}$ or δ_a on beta change, $\Delta\dot{\beta}$, in cruise.

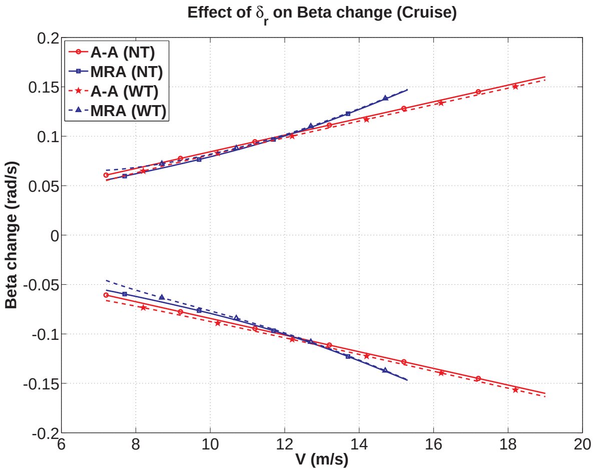

Figure 5.14. Effect of δ_r on beta change, $\Delta\dot{\beta}$, in cruise.

with speed. At low speeds, the mass-actuation is more effective than aileron while aileron effectiveness is increasingly higher with speeds faster than about 10 m/s. It is also observed that propeller affects the minimum and maximum effectiveness slightly for all three aircraft as shown in Figs. 5.11-5.12 since cruise conditions of lateral states are affected with propeller turn.

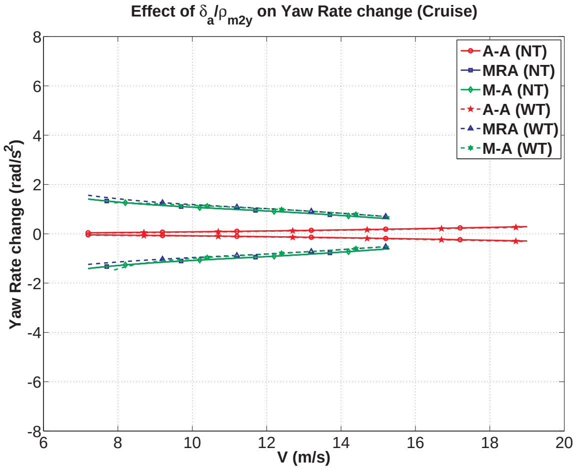

Figure 5.15. Effect of $\rho_{m_{2_y}}$ or δ_a on yaw rate change, $\Delta\dot{r}$, in cruise.

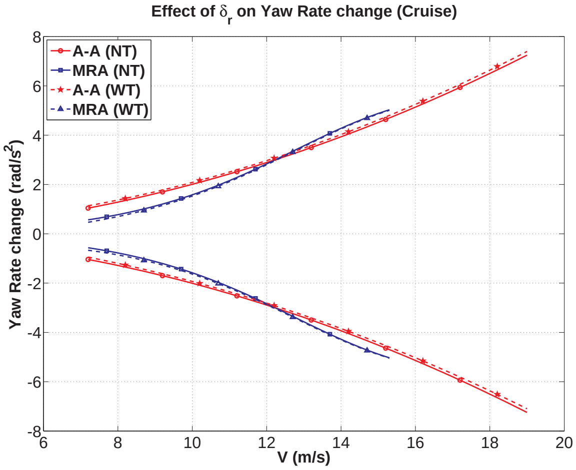

Figure 5.16. Effect of δ_r on yaw rate change, $\Delta\dot{r}$, in cruise.

Figures 5.13-5.14 show that the most effective controller is rudder on sideslip angle change. Since the A-A and MRA aircraft require rudder deflection to generate yawing moment, the result is not surprised. Additionally, it can be observed that mass-actuation has very small effect (only in low speeds) on sideslip angle in comparison to aileron deflection. Similar to effectiveness on roll rate, propeller affects the minimum and maximum boundaries of effectiveness on sideslip angle slightly.

Figures 5.15-5.16 show that rudder is more effective controller on change of yaw rate, $\Delta\dot{r}$, for higher speeds while laterally moving-mass is slightly more effective in lower speeds. Furthermore, $\rho_{m_{2_y}}$ is more effective in comparison to aileron. While speed increases, the effectiveness of aileron becomes larger. However, $\rho_{m_{2_y}}$ is still slightly more effective than the aileron. On the other hand, rudder effectiveness on yaw rate change increases with increasing speed as shown in Fig. 5.16. Similar to previous lateral states, boundaries of the effectiveness are affected by propeller slightly.

5.3.5 Comparison of Two Methods

The results of the analyses of the level of controllability by controllability metrics presented in Section 5.3.2 and by control/input matrix presented in Section 5.3.4 are comparatively discussed herein. Both methods agree that aero-actuation has increasing effectiveness with speed. They also agree that, at low speeds, mass-actuation provides slightly higher effectiveness than aero-actuation while aero-actuation gives more controllability at mid and high speed ranges. However, the two methods are not in agreement when it comes the variation of mass-actuation effectiveness with increasing cruise speed. According to the controllability metrics, the mass-actuation provides smaller control effectiveness with increasing speed while the control/input matrix analysis shows diminishing effectiveness for angle-of-attack and maximum effectiveness for pitch rate at mid speeds. Control/input matrix method also shows more effectiveness on roll rate by mass-actuation at low speeds. Control effectiveness by the lateral mass-actuator by the input/control matrix method stays relatively constant with varying speed for roll rate change.

5.4 Control Design

This section explains the control design procedure for each aircraft configuration to follow commands for altitude or rate of ascent/descent, airspeed, and yaw rate. The controller designed is a MIMO (Multi Input Multi Output) gain scheduling controller with state feedback and integral terms. The state-feedback and integral gains are determined with LQR (Linear Quadratic Regulator) method. For the LQR control, the state and input/control matrices are obtained from linearized equations discussed in Section 5.1.

5.4.1 Feedback Control

The controller is designed as a linear MIMO (Multi-Input-Multi-Output) full state feedback. Integral control terms are also included in the control design to improve the tracking performance of the commanded outputs for airplane motion. A block diagram representation of the control structure is shown in Fig. 5.17.

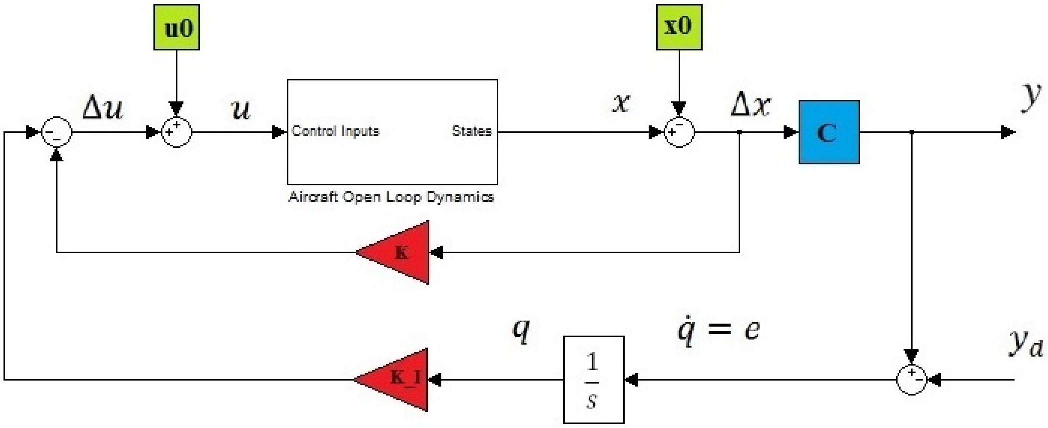

Figure 5.17. State feedback + integral control with nonlinear airplane model.

Linearized equations of motions in state-space form with error dynamics and outputs are

$$\begin{aligned} \dot{x} &= \mathbf{A}x + \mathbf{B}u \\ y &= \mathbf{C}x \\ \dot{q} &= e = \mathbf{C}x - y_d \end{aligned} \tag{5.29}$$

where x is the state vector, u is the control vector, y is the output vector, y_d is the desired output vector, e is the error between the desired and actual output vector, and q is the integral of the error vector. For improving the tracking, desired outputs are selected as velocity, altitude or rate of ascent/descent and turn rate. Thus, integral errors, q, in Eq. (5.29) are defined for cruise and steady-state turn as

$$q = \begin{bmatrix} V - V_d \\ z - z_d \\ \dot{\psi} - \dot{\psi}_d \end{bmatrix} \tag{5.30}$$

and for ascending and descending as

$$q = \begin{bmatrix} V - V_d \\ \dot{z} - \dot{z}_d \\ \dot{\psi} - \dot{\psi}_d \end{bmatrix} \tag{5.31}$$

In the state space, x- and y- positions and the yaw angle, ψ, for cruise and steady-state turn and x-, y- and z- positions and the yaw angle, ψ, for ascending and descending are removed when controller is designed. States for cruise and steady-state turn are defined as

$$x = \begin{bmatrix} V & \beta & \alpha & p & q & r & \theta & \phi & z & 1_m & \omega_p \end{bmatrix}^T \tag{5.32}$$

and states for ascending and descending are defined as

$$x = \begin{bmatrix} V & \beta & \alpha & p & q & r & \theta & \phi & 1_m & \omega_p \end{bmatrix}^T \tag{5.33}$$

The state-space equations with integral states augmented can be written as

$$\begin{bmatrix} \dot{x} \\ \dot{q} \end{bmatrix} = \begin{bmatrix} \mathbf{A} & \mathbf{0} \\ \mathbf{C} & \mathbf{0} \end{bmatrix} \hat{x} + \begin{bmatrix} \mathbf{B} \\ \mathbf{0} \end{bmatrix} u + \begin{bmatrix} \mathbf{0} \\ -\mathbf{I_{3X3}} \end{bmatrix} y_d \tag{5.34}$$

where the augmented state vector is

$$\hat{x} = \begin{bmatrix} x \\ q \end{bmatrix} \tag{5.35}$$

Rewriting Eq. (5.34) in compact form yields

$$\begin{aligned}\dot{\hat{x}} &= \hat{\mathbf{A}}\hat{x} + \hat{\mathbf{B}}u + \hat{\mathbf{D}}y_d \\ y &= \hat{\mathbf{C}}\hat{x}\end{aligned} \tag{5.36}$$

where

$$\hat{\mathbf{A}} = \begin{bmatrix} \mathbf{A} & \mathbf{0} \\ \mathbf{C} & \mathbf{0} \end{bmatrix} , \hat{\mathbf{B}} = \begin{bmatrix} \mathbf{B} \\ \mathbf{0} \end{bmatrix} , \hat{\mathbf{C}} = \begin{bmatrix} \mathbf{C} & \mathbf{0} \end{bmatrix} , \hat{\mathbf{D}} = \begin{bmatrix} \mathbf{0} \\ -\mathbf{I_{3X3}} \end{bmatrix} \tag{5.37}$$

The state feedback law for the augmented system is

$$\begin{aligned}u &= [-\mathbf{K} \quad -\mathbf{K_I}]\hat{x} \\ &= -\mathbf{K}x - \mathbf{K_I}q\end{aligned} \tag{5.38}$$

Finally, closed loop system can be written as

$$\begin{aligned}\dot{\hat{x}} &= \hat{\mathbf{A}}\hat{x} + \hat{\mathbf{B}}[-\mathbf{K} \quad -\mathbf{K_I}]\hat{x} + \hat{\mathbf{D}}y_d \\ &= \left(\hat{\mathbf{A}} - \hat{\mathbf{B}}[\mathbf{K} \quad \mathbf{K_I}]\right)\hat{x} + \hat{\mathbf{D}}y_d\end{aligned} \tag{5.39}$$

This linear controller is implemented for nonlinear system of the airplane. As stated earlier, integral of the error is also considered for control design to track the desired output.

5.4.2 Linear Quadratic Regulator

This section gives a brief summary of the Linear Quadratic Regulator (LQR) method used for computing the gains for the state feedback and integral control. Consider a linear time invariant (LTI) system with the state-space representation

$$\dot{x} = \mathbf{A}x + \mathbf{B}u \ , \quad x(t_0) = x_0 \tag{5.40}$$

The objective is to find a control input, $u(t)$, that stabilizes the closed loop system with fast but not very large transient state and control responses. In optimal control theory, a quadratic cost function is defined as [124]

$$J(t_0, x_0, u) = \frac{1}{2}\int_0^{\infty}(x^T\mathbf{Q}x + u^T\mathbf{R}u)dt \tag{5.41}$$

where $\mathbf{Q}$ is a positive semidefinite weighting matrix that penalizes the deviation of state variables from their nominal values and $\mathbf{R}$ is a positive semidefinite weighting matrix that penalizes the deviation of control variables from their nominal values. To find a optimal solution, it is desired to minimize the cost function with the constraints of the system dynamics in Eq. (5.41). The optimal control law to minimize the cost is found to be

$$u = -\mathbf{K}x \tag{5.42}$$

where

$$\mathbf{K} = \mathbf{R}^{-1}\mathbf{B}^T\mathbf{P} \tag{5.43}$$

Covariance matrix $\mathbf{P}$ can be found from continuous time Algebraic Riccati Equation

$$0 = \mathbf{PA} + \mathbf{A}^T\mathbf{P} + \mathbf{Q} - \mathbf{PBR}^{-1}\mathbf{B}^T\mathbf{P} \tag{5.44}$$

Substituting the control input found from Eq. (5.42) into Eq. (5.40), closed loop system dynamics becomes

$$\dot{x} = (\mathbf{A} - \mathbf{BK})x \tag{5.45}$$

which is guaranteed to be stable.

In this study, optimal control gain $\mathbf{K}$ is found using *lqr* command in MATLAB. Weighting matrices $\mathbf{Q}$ and $\mathbf{R}$ are tuned for each operating flight conditions to result in satisfactory closed loop response in the nonlinear system.

5.4.3 Gain Scheduling

In the previous sections, LQR-based linear controller is designed based on a linear model obtained for a specific trim flight condition. This section describes the gain scheduling approach used to develop a nonlinear controller for the whole flight envelop from the individual linear controllers developed for a set of trim conditions. Nonlinear equations of motion as described in Section 2.1 can be written in a compact form as

$$\dot{x} = f(x, u, s) \tag{5.46}$$

where s is the scheduling variables. In an equilibrium condition, Eq. (5.46) leads to

$$0 = f(x^s, u^s, s) \tag{5.47}$$

which is solved for nominal state variables, x_0^s, and control variables, u_0^s, where superscript s represents that the nominal values are related to scheduling variables. Defining the nominal values and their perturbation

$$x = x_0^s + \Delta x \tag{5.48}$$

$$u = u_0^s + \Delta u \tag{5.49}$$

Linearization of the nonlinear equation in Eq. (5.46) results in a family of linear models with state and control matrices parameterized with scheduling variables s.

$$\Delta\dot{x} = \mathbf{A^s}\Delta x + \mathbf{B^s}\Delta u \tag{5.50}$$

where

$$\begin{aligned} A^s &= \left.\frac{\partial f}{\partial x}\right|_{(x_0^s, u_0^s, s)} \\ B^s &= \left.\frac{\partial f}{\partial u}\right|_{(x_0^s, u_0^s, s)} \end{aligned} \tag{5.51}$$

Family of linear controllers with state feedback and integral errors for scheduling variables is defined as

$$\Delta u = -\mathbf{K^s}\Delta x - \mathbf{K^s_I} q \tag{5.52}$$

Substituting Eqs. (5.48)-(5.49) into Eq. (5.52) yields as

$$u = u_0^s - \mathbf{K^s}(x - x_0^s) - \mathbf{K^s_I} q \tag{5.53}$$

In this research, 18 different operating points are considered for control design in total. For cruise and steady-state turn, airspeed and yaw rate are selected as the scheduling variables. For ascending and descending, airspeed and rate of ascent/descent are selected as the scheduling variables. Table 5.1 lists the nine operating (trim) points and the values of the corresponding scheduling variables for cruise and steady-state turn and Table 5.2 lists the nine operating (trim) points and the values of the corresponding scheduling variables for ascending and descending. For the full mission simulated, switching between the altitude-controller and the climb-rate-controller is scheduled based on time. It means that the aircraft uses the ascending/descending controller when the aircraft ascends or descends. For cruise and steady-state turn, controller switches to cruise/turn controller when the desired altitude is reached based on a predefined switching time.

Table 5.1. Nine operating points of the scheduling variables (cruise & turn)

Airspeed \ Yaw rate	**-5 deg/s**	**0 deg/s**	**5 deg/s**
10 m/s	u_1	u_2	u_3
12 m/s	u_4	u_5	u_6
15 m/s	u_7	u_8	u_9

Table 5.2. Nine operating points of the scheduling variables (ascent & descent)

Airspeed \ Rate of C/D	**4 m/s**	**0 m/s**	**-0.5 m/s**
9 m/s	u_1	u_2	u_3
12 m/s	u_4	u_5	u_6
15 m/s	u_7	u_8	u_9

Tables 5.1 and 5.2 also label the controllers designed for each of the 9 operating condition. These nine controllers are put together through a interpolation scheme to form the overall gain scheduling controller.

$$u_{gs} = \sum_{i=1}^{9} a_i(s)u_i \tag{5.54}$$

where coefficients $a_i(s)$ are calculated by the Lagrange Interpolation function based on the four neighboring nominal points. This means if a scheduling variable is in a region with four operating points, as shown in Tables 5.1 and 5.2, coefficients would be calculated based on these four operating points and the rest of coefficients would be zero. This implementation helps to avoid excessive control commands and keep the coefficients between 0 to 1. Four neighboring coefficients for cruise and steady-state turn are represented in Table 5.3.

Table 5.3. Four neighboring coefficients for scheduling variable (cruise & turn)

Airspeed \ Yaw rate	$\dot{\psi}_\mathbf{1}$	$\dot{\psi}_\mathbf{2}$
$\mathbf{V_1}$	a_{11}	a_{12}
$\mathbf{V_2}$	a_{21}	a_{22}

Respective coefficients can be found as

$$\begin{aligned} a_{11} &= \frac{(\dot{\psi}_c - \dot{\psi}_2)(V_c - V_2)}{(\dot{\psi}_1 - \dot{\psi}_2)(V_1 - V_2)} \\ a_{12} &= \frac{(\dot{\psi}_c - \dot{\psi}_1)(V_c - V_2)}{(\dot{\psi}_2 - \dot{\psi}_1)(V_1 - V_2)} \\ a_{21} &= \frac{(\dot{\psi}_c - \dot{\psi}_2)(V_c - V_1)}{(\dot{\psi}_1 - \dot{\psi}_2)(V_2 - V_1)} \\ a_{21} &= \frac{(\dot{\psi}_c - \dot{\psi}_1)(V_c - V_1)}{(\dot{\psi}_2 - \dot{\psi}_1)(V_2 - V_1)} \end{aligned} \tag{5.55}$$

where $\dot{\psi}_1$ and $\dot{\psi}_2$ are the boundaries that commanded turn rate, $\dot{\psi}_c$, operates between the interval and where V_1 and V_2 are the boundaries that commanded speed, V_c, operates between the interval. Similarly, four neighboring coefficients for ascending and descending are represented in Table 5.4.

Table 5.4. Four neighboring coefficients for scheduling variable (ascent & descent)

Airspeed $\setminus$ Rate of C/D	$\dot{\mathbf{z}}_\mathbf{1}$	$\dot{\mathbf{z}}_\mathbf{2}$
$\mathbf{V_1}$	a_{11}	a_{12}
$\mathbf{V_2}$	a_{21}	a_{22}

Respective coefficients can be found as

$$\begin{aligned} a_{11} &= \frac{(\dot{z}_c - \dot{z}_2)(V_c - V_2)}{(\dot{z}_1 - \dot{z}_2)(V_1 - V_2)} \\ a_{12} &= \frac{(\dot{z}_c - \dot{z}_1)(V_c - V_2)}{(\dot{z}_2 - \dot{z}_1)(V_1 - V_2)} \\ a_{21} &= \frac{(\dot{z}_c - \dot{z}_2)(V_c - V_1)}{(\dot{z}_1 - \dot{z}_2)(V_2 - V_1)} \\ a_{21} &= \frac{(\dot{z}_c - \dot{z}_1)(V_c - V_1)}{(\dot{z}_2 - \dot{z}_1)(V_2 - V_1)} \end{aligned} \tag{5.56}$$

where $\dot{z}_1$ and $\dot{z}_2$ are the boundaries that commanded rate of ascent/descent, $\dot{z}_c$, operates between the interval and where V_1 and V_2 are the boundaries that commanded speed, V_c, operates between the interval. If any coefficient is outside the region

$$a_i(s) = 0 \tag{5.57}$$

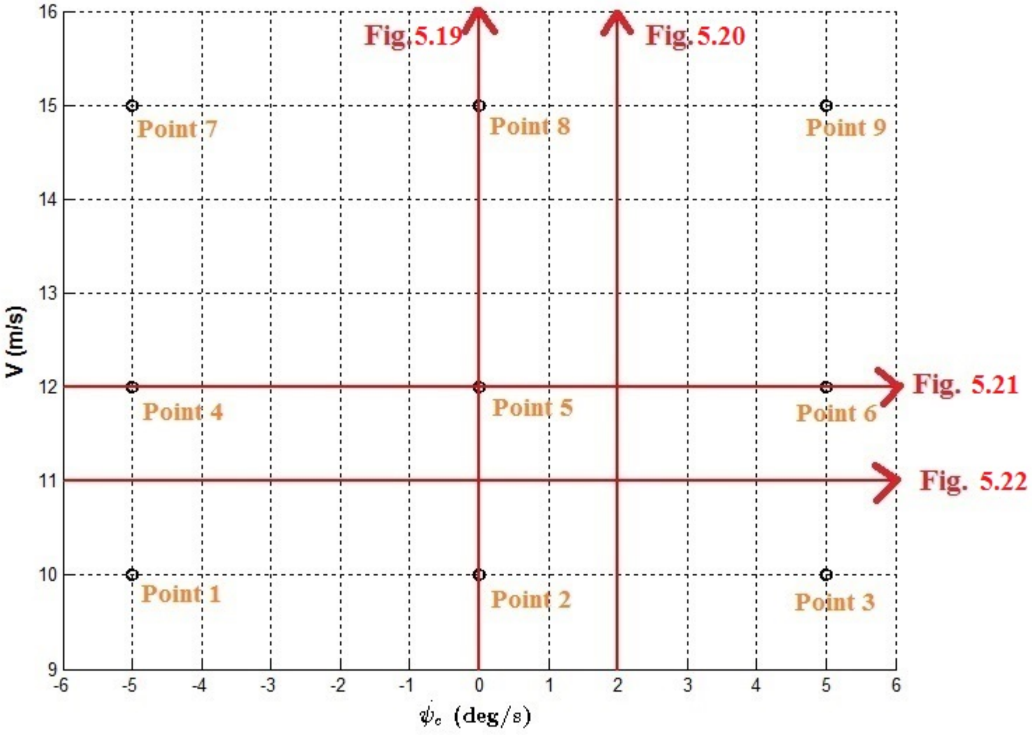

Figure 5.18. Sketch of the examples on the operating area.

Figure 5.18 shows the sketch of the examples where they are represented on the operating area and Figs. 5.19-5.22 show the variation of coefficients with respect to speed or turn rate for different cases as illustration. Only the gain scheduling for cruise and steady-state turn are represented here since the similar idea is valid for gain scheduling of ascending/descending controller. Fig. 5.19 shows the variations of the nine coefficients as the commanded speed V_c varies from 8 to 18 m/s when commanded yaw rate is 0. When $V_c < 10$ m/s, a_2 is 1 and all other coefficients are zero since operation point-2 has the lowest speed of 10 m/s. When $10 < V_c < 12$, a_2 decreases from 1 to 0 while a_5 increases from zero to 1 with increasing V_c while all the other coefficients are zero. When $V_c = 12$, $a_5 = 1$ and all the other coefficients are zero. As V_c further increases beyond 12 m/s until 15 m/s, a_5 decreases from 1 to zero while a_8 increases from 0 to 1, and all the other coefficients remain zero. Beyond 15 m/s, $a_8 = 1$ and all the others are zero. In this case, only two coefficients are nonzero, between 0 and 1, because yaw rate command happens to be one of the three nominal yaw rate values as can be seen in Fig. 5.18.

Figure 5.20 shows another case, when the commanded yaw rate $\dot{\psi}_c = 2$ deg/s, which, note that, is not one of the three nominal yaw rates as can be seen in Fig. 5.18. As a result, at any value of commanded speed V_c, four coefficients are nonzero, between 0 and 1, always adding up to 1. When $V_c < 10$ m/s, a_2 is 0.6 and a_3 is 0.4 and all other coefficients are zero since operation point-2 has the lowest speed of 10 m/s. When $10 < V_c < 12$, a_2 decreases from 0.6 to 0 and a_3 decreases from 0.4 to 0 while a_5 increases from zero to 0.6 and a_6 increases from zero to 0.4 with increasing V_c while all the other coefficients are zero. When $V_c = 12$, $a_5 = 0.6$ and $a_6 = 0.4$ while all the other coefficients are zero. As V_c further increases beyond 12 m/s until 15 m/s, a_5 decreases from 0.6 to zero and a_6 decreases from 0.4 to zero while a_8 increases from 0 to 0.6 and a_9 increases from 0 to 0.4, and all the other coefficients remain zero. Beyond 15 m/s, $a_8 = 0.6$ and $a_9 = 0.4$ while all the others are zero.

Figure 5.21 shows the variations of the nine coefficients as the commanded turn rate $\dot{\psi}_c$ varies from -7 to 7 deg/s when commanded speed is 12. When $\dot{\psi}_c < -5$ deg/s, a_4 is 1 and all other coefficients are zero since operation point-4 has the lowest turn rate of -5 deg/s. When $-5 < \dot{\psi}_c < 0$, a_4 decreases from 1 to 0 while a_5 increases from

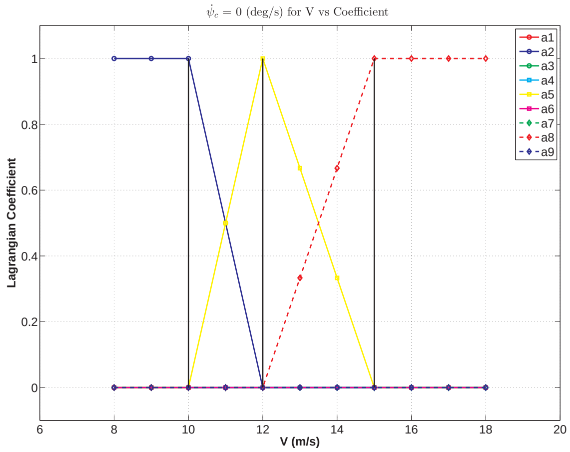

Figure 5.19. Variation of lagrangian coefficients for $\dot{\psi} = 0$ deg/s.

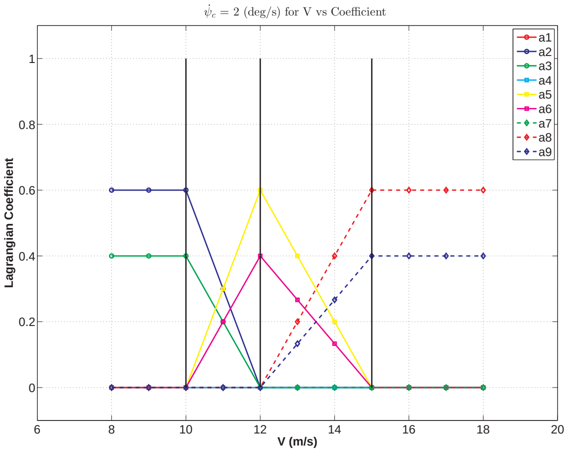

Figure 5.20. Variation of lagrangian coefficients for $\dot{\psi} = 2$ deg/s.

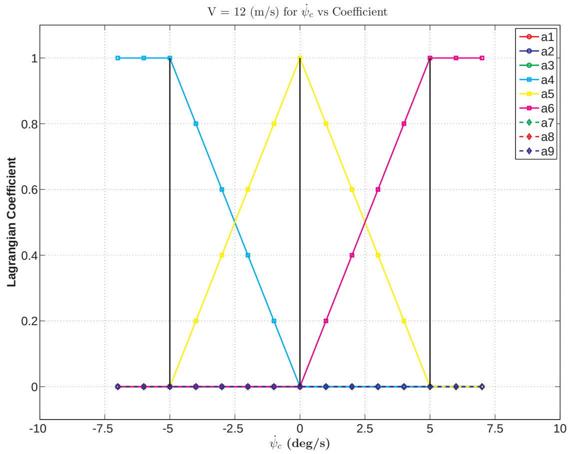

Figure 5.21. Variation of lagrangian coefficients for $V = 12$ m/s.

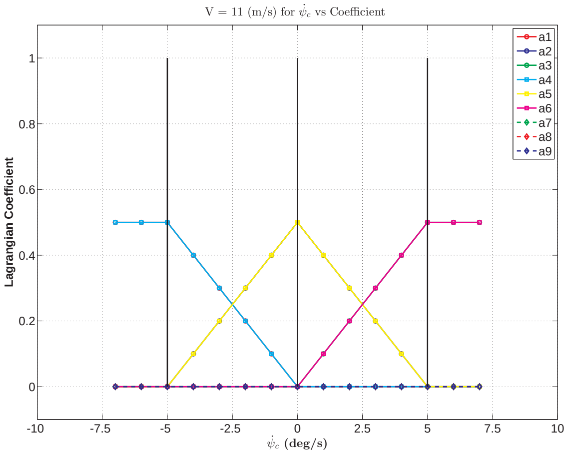

Figure 5.22. Variation of lagrangian coefficients for $V = 11$ m/s.

zero to 1 with increasing $\dot{\psi}_c$ while all the other coefficients are zero. When $\dot{\psi}_c = 0$, $a_5 = 1$ and all the other coefficients are zero. As $\dot{\psi}_c$ further increases beyond 0 deg/s until 5 deg/s, a_5 decreases from 1 to zero while a_6 increases from 0 to 1, and all the other coefficients remain zero. Beyond 5 deg/s, $a_6 = 1$ and all the others are zero. In this case, only two coefficients are nonzero, between 0 and 1, because speed command happens to be one of the three nominal speed values as can be seen in Fig. 5.18.

Figure 5.22 shows another case, when the commanded speed $V_c = 11$ m/s, which, note that again, is not one of the three nominal speeds as can be seen in Fig. 5.18. As a result, at any value of commanded yaw rate $\dot{\psi}_c$, four coefficients are nonzero, between 0 and 1, always adding up to 1. When $\dot{\psi}_c < -5$ deg/s, a_1 and a_4 are 0.5 and all other coefficients are zero since operation point-4 has the lowest turn rate of -5 deg/s. When $-5 < \dot{\psi}_c < 0$, a_1 and a_4 decrease from 0.5 to 0 while a_1 and a_5 increase from zero to 0.5 with increasing $\dot{\psi}_c$ while all the other coefficients are zero. When $\dot{\psi}_c = 0$, a_2 and a_5 are 0.5 while all the other coefficients are zero. As $\dot{\psi}_c$ further increases beyond 0 deg/s until 5 deg/s, a_2 and a_5 decrease from 0.5 to zero while a_3 and a_6 increase from 0 to 0.5, and all the other coefficients remain zero. Beyond 5 deg/s, a_3 and a_6 are 0.5 while all the others are zero.

5.5 Summary of the Chapter

In this chapter, controllability and level of controllability for three aircraft configurations were presented. Controllability results showed that MRA and M-A airplanes have full controllability within the feasible speed ranges. Level of controllability results showed that mass-actuation has similar or slightly higher controllability than aero-actuation for low speeds while aero-actuation has higher controllability in higher speeds. Furthermore, control design and gain scheduling procedure were presented. Two different controllers were designed for all three aircraft. One of them was designed for cruise and steady-state turn to track altitude, speed and turn rate. The other one was designed for ascending and descending to track rate of ascent/descent, speed and turn rate.

CHAPTER 6

RESULTS OF DYNAMIC SIMULATION

In this chapter, results of the dynamic simulations are presented. Two dynamic simulations are carried out. In the first simulation, cruise and steady-state turn cases are included only to show the performances of controller in the design operating conditions and in transition between them. In the second simulation, a full mission is defined including ascending/descending phases in addition to cruise and turn. Furthermore, wind is also included in the full mission to see the responses of the closed-loop system to various wind encounters. As stated earlier, three aircraft are considered during the simulation. Operating points explained in Chapter 5.4 are used to design a controller of each airplane for comparison. Furthermore, all the propeller effects including direct torque, propeller aerodynamic and gyroscopic effects are considered in the missions even though the gyroscopic effect is not considered in the trim analyses.

6.1 Dynamic Simulation for Cruise and Steady-State Turn

In the first mission, a scenario is defined including cruise flight, right turn and left turn with different speeds. Fig. 6.1 shows the trajectory of each airplane in X-Y plane. Commanded speeds and turn rates are shown in Fig. 6.2. At the beginning, cruise flight starts with the speed of 10 m/s, which is represented as operating point 2 in Table 5.1. Then, the speed is commanded from 10 m/s to 11 m/s at 100 s. The purpose of selecting the second speed is to see the gain scheduling performances of each airplane when the commanded speed is between the nominal speeds of the operating conditions used in the gain scheduling controller design. At 300 s, turn rate is commanded for 5 deg/s, which is a right turn. This turn command continues until the aircraft makes 2.5 loops (i.e., the yaw angle changes by $2.5 \times 360 = 900$ deg). At 650 s, the speed of the airplane is commanded from 11 m/s to 12 m/s, which corresponds to operating point 5 in Table 5.1 since $\dot{\psi}_c = 0$. Between 650-1000 s, the airplane flies in cruise condition with 12 m/s. At 1000 s, the airplane starts to have a turn left with -5 deg/s, which corresponds to operating point 4 in Table 5.1 since the speed is 12 m/s. Similar to right turn, the turn command ends when the aircraft yaw angle decreases by $2.5 \times 360 = 900$ deg. At 1400 s, the speed is commanded from 12 m/s to 15 m/s, which corresponds to operating point 8 in Table 5.1. The simulation ends when time reaches to 1800 s.

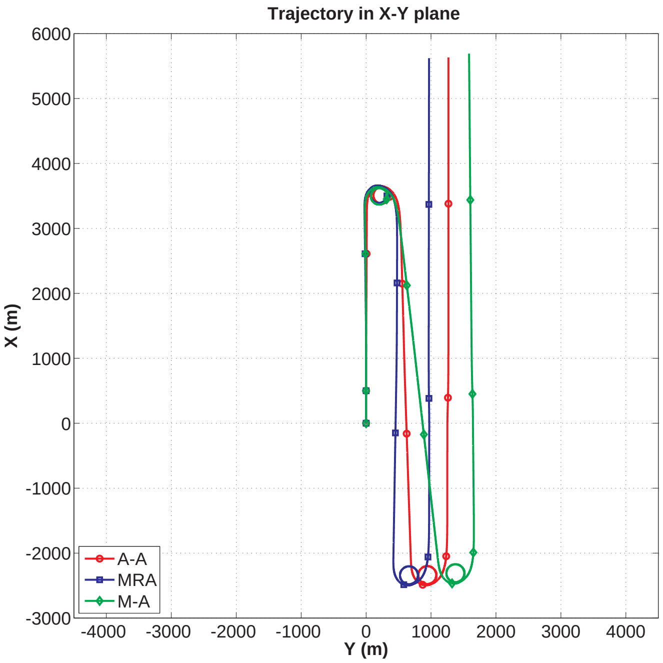

Figure 6.1. Trajectory of airplanes in X-Y plane.

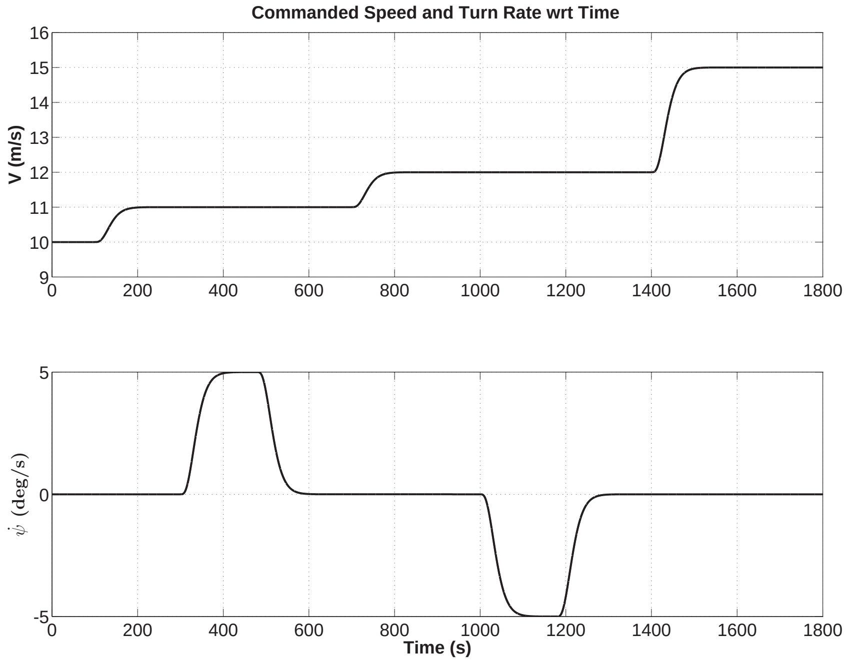

Figure 6.2. Commanded speed and turn rate with time.

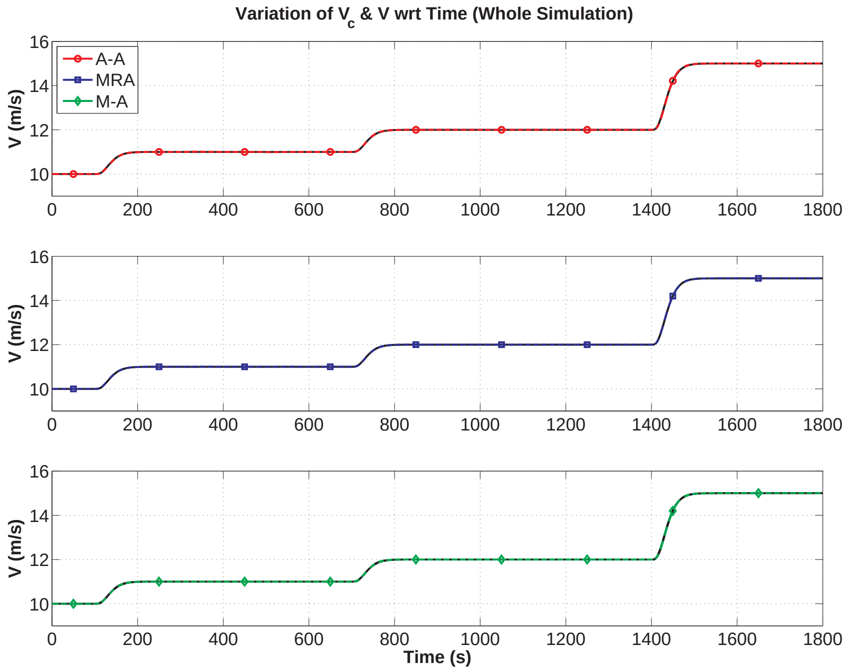

Figure 6.3. Variation of velocity and commanded speed with time.

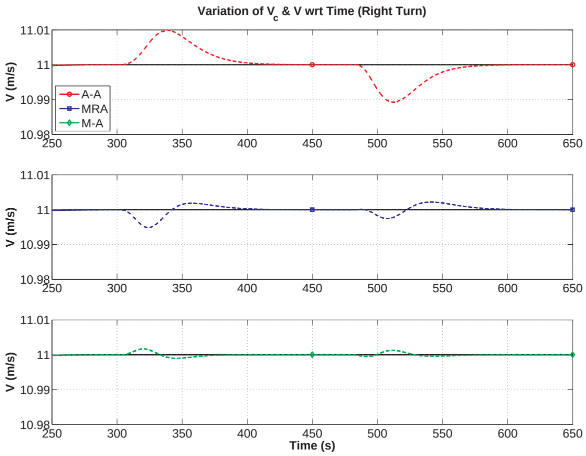

Figure 6.4. Variation of velocity and commanded speed with time (right turn).

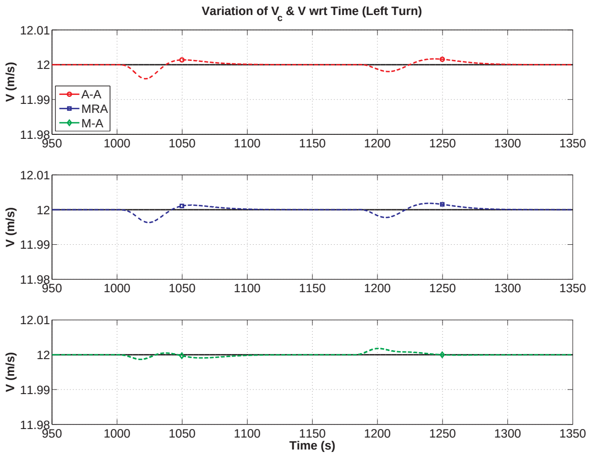

Figure 6.5. Variation of velocity and commanded speed with time (left turn).

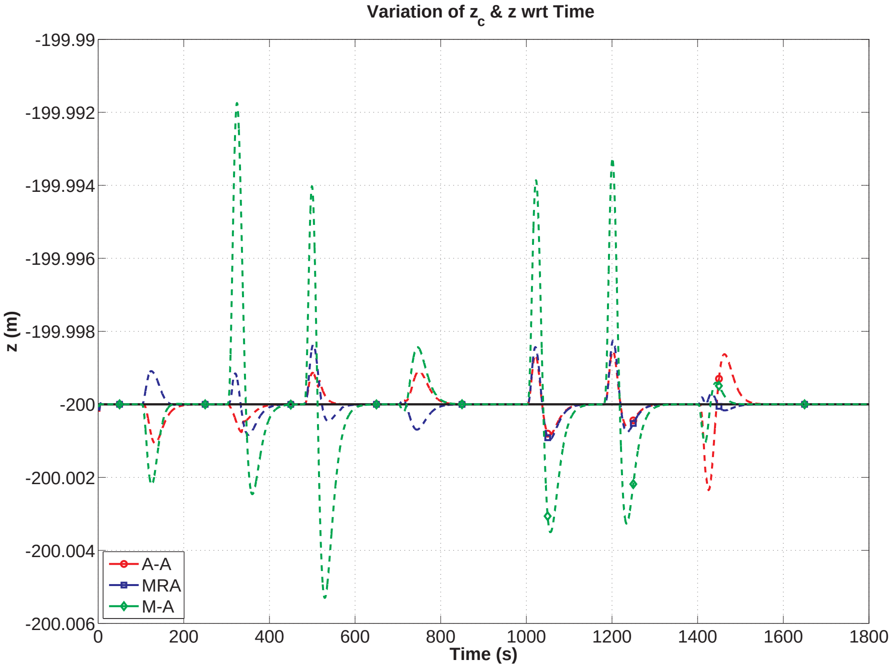

Figure 6.6. Variation of altitude and commanded altitude with time.

Figures 6.3-6.10 show the tracking performances of the commanded speed, altitude or turn rates with respect to time. In these figures, black line represents the commanded speed, altitude or turn rate. Fig. 6.3 shows the variation of commanded

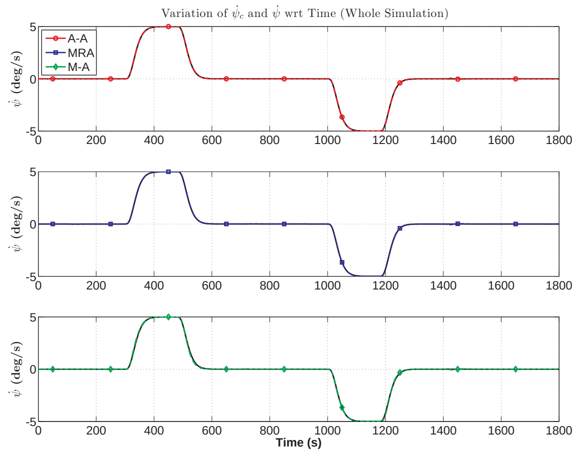
Variation of $\dot{\psi}_c$ and $\dot{\psi}$ wrt Time (Whole Simulation)

Figure 6.7. Variation of turn rate and commanded turn rate with time.

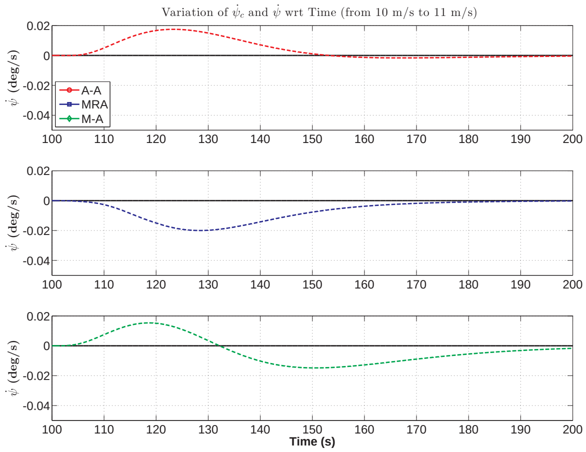
Variation of $\dot{\psi}_c$ and $\dot{\psi}$ wrt Time (from 10 m/s to 11 m/s)

Figure 6.8. Turn rate and commanded turn rate with time (from 10 to 11 m/s).

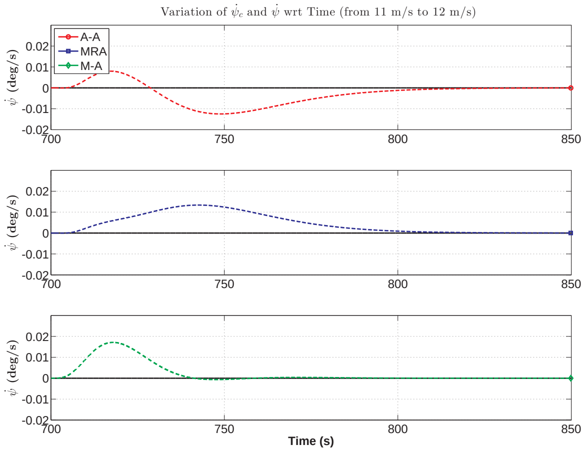
Variation of $\dot{\psi}_c$ and $\dot{\psi}$ wrt Time (from 11 m/s to 12 m/s)

Figure 6.9. Turn rate and commanded turn rate with time (from 11 to 12 m/s).

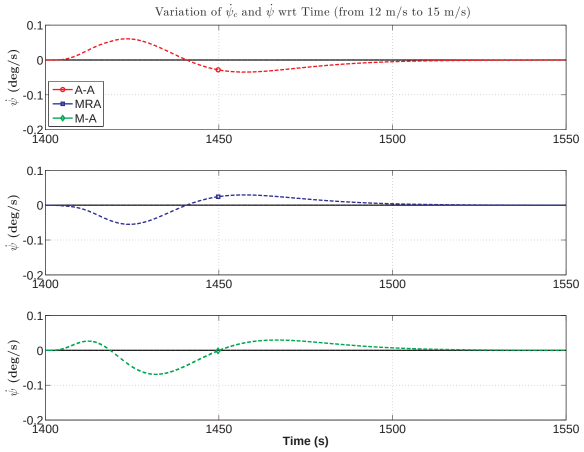
Variation of $\dot{\psi}_c$ and $\dot{\psi}$ wrt Time (from 12 m/s to 15 m/s)

Figure 6.10. Turn rate and commanded turn rate with time (from 12 to 15 m/s).

speed and the airplane speed with respect to time. It is seen that commanded speed can be tracked successfully during the simulation. A closer look at right turn in Fig. 6.4 and left turn in Fig. 6.5 can show that the controller designed for each airplane can successfully track the commanded speed even during the transition from cruise to turn. Fig. 6.6 shows the variation of altitude with respect to time for each airplane. During the transition of tracking a varying speed or turn rate commands, there seems to be very small deviations from the commanded altitude. Figs. 6.7-6.10 show the tracking performance of turn rate commands during the simulation. While tracking a varying speed command, Figs. 6.8-6.10 shows the performance of keeping the turn rate at 0, as commanded. After the transition, the controller reduces the tracking error to zero at the steady-state.

Figures 6.11-6.14 show the time histories of states of each airplane and Figs. 6.16-6.19 show the time histories of control inputs. Moreover, thrust and torque produced by propulsion system are shown in Fig. 6.15.

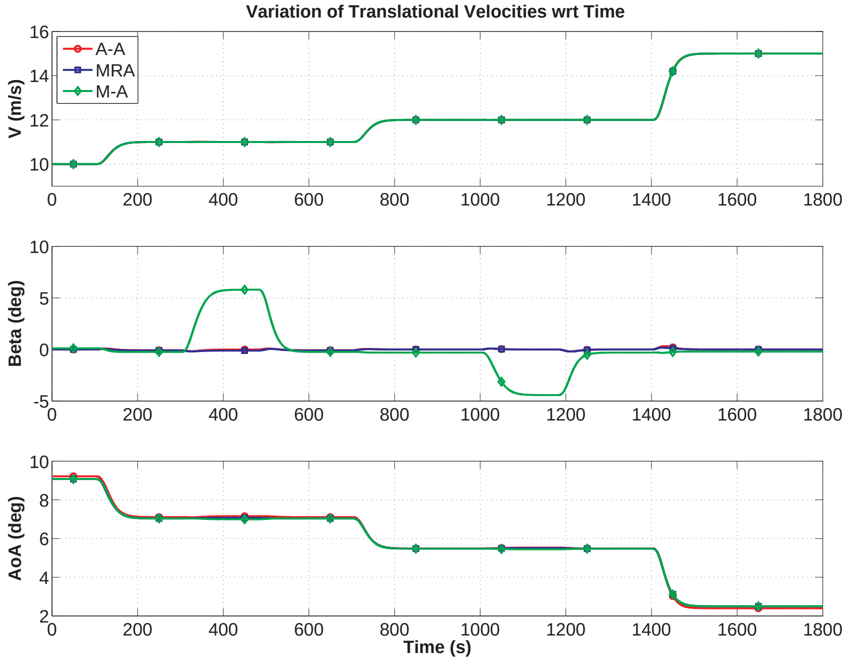

Figure 6.11. Variation of translational velocities with time.

Figure 6.11 shows the airspeed, sideslip angle and angle of attack responses during the simulation. Airspeed and angle of attack responses are very similar among the three airplane configurations. Regarding the sideslip angle, A-A and MRA aircraft have almost the same response. However, M-A aircraft has small nonzero sideslip

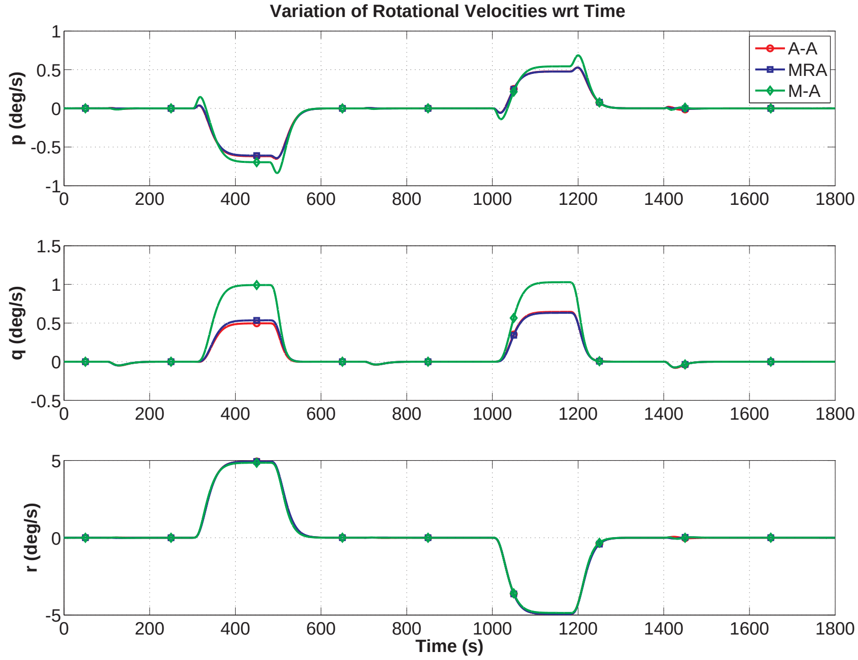

Figure 6.12. Variation of rotational velocities with time.

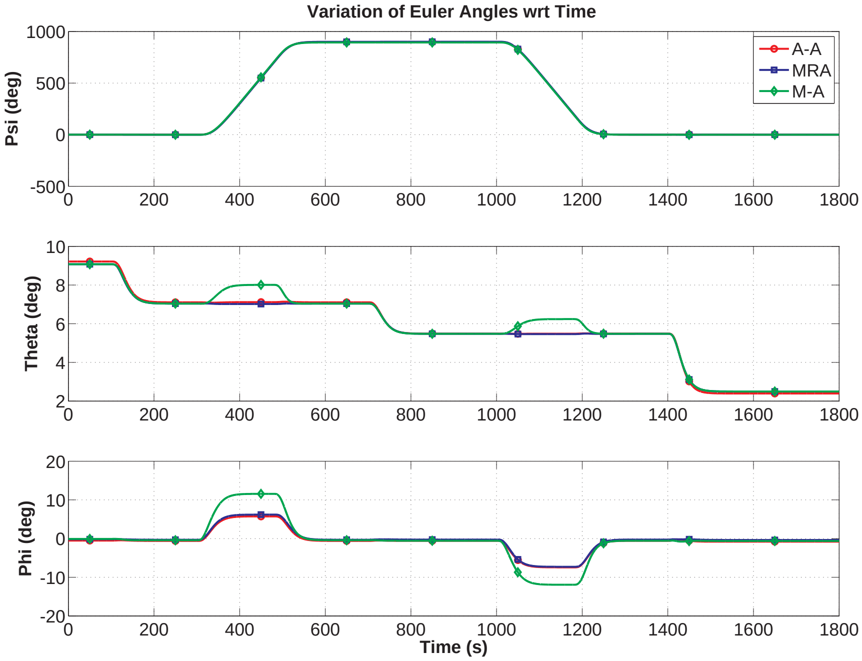

Figure 6.13. Variation of euler angles with time.

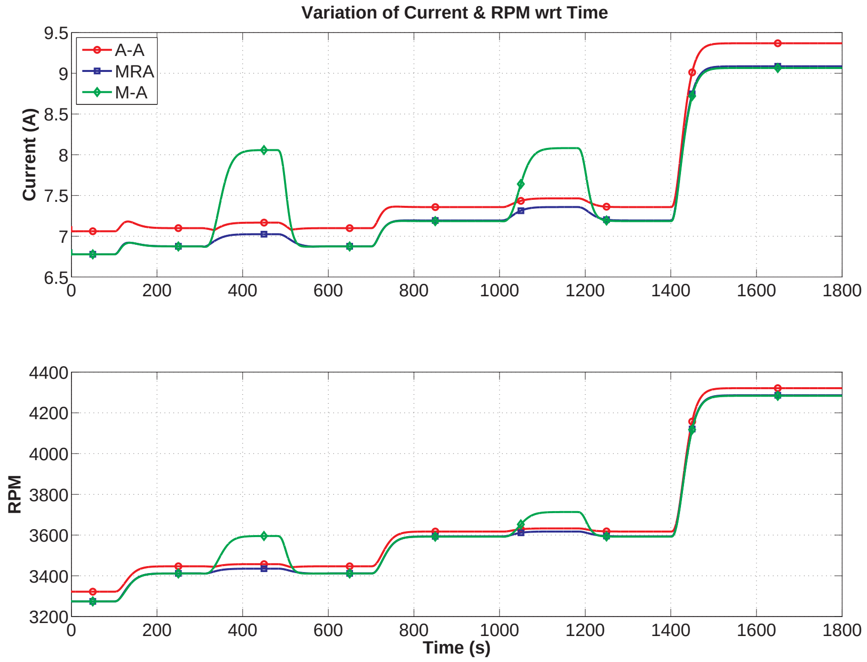

Figure 6.14. Variation of current & RPM with time.

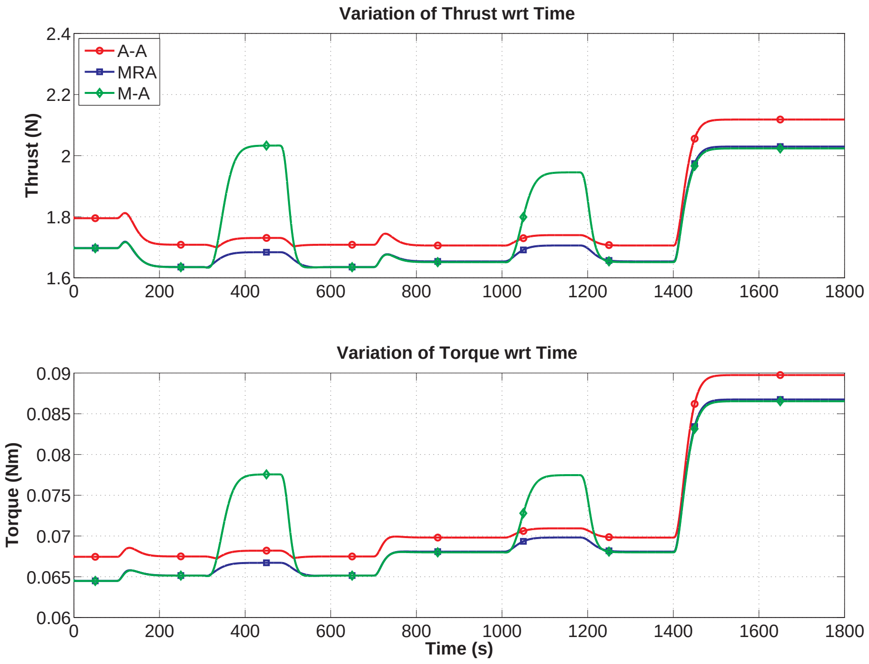

Figure 6.15. Variation of thrust and torque with time.

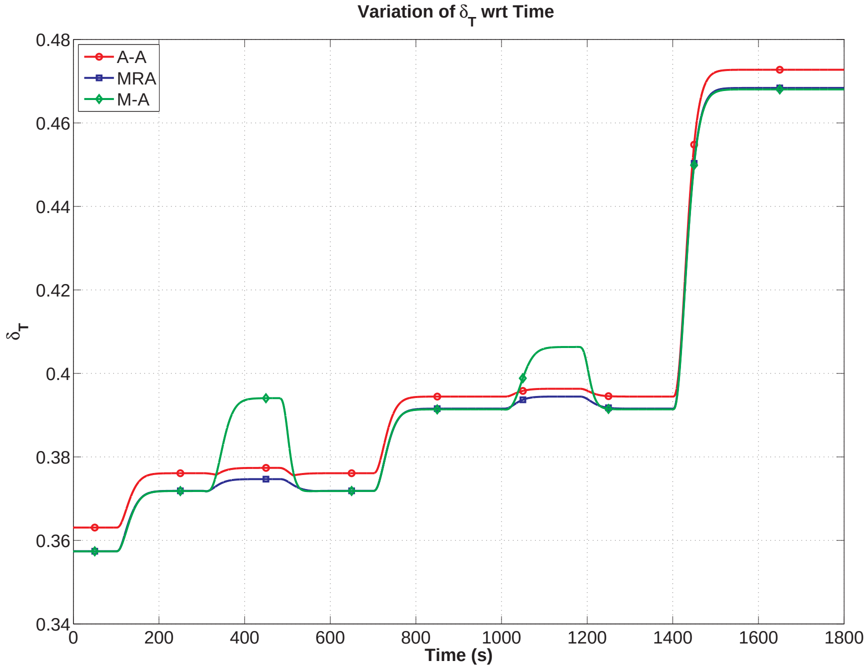

Figure 6.16. Variation of δ_T with time.

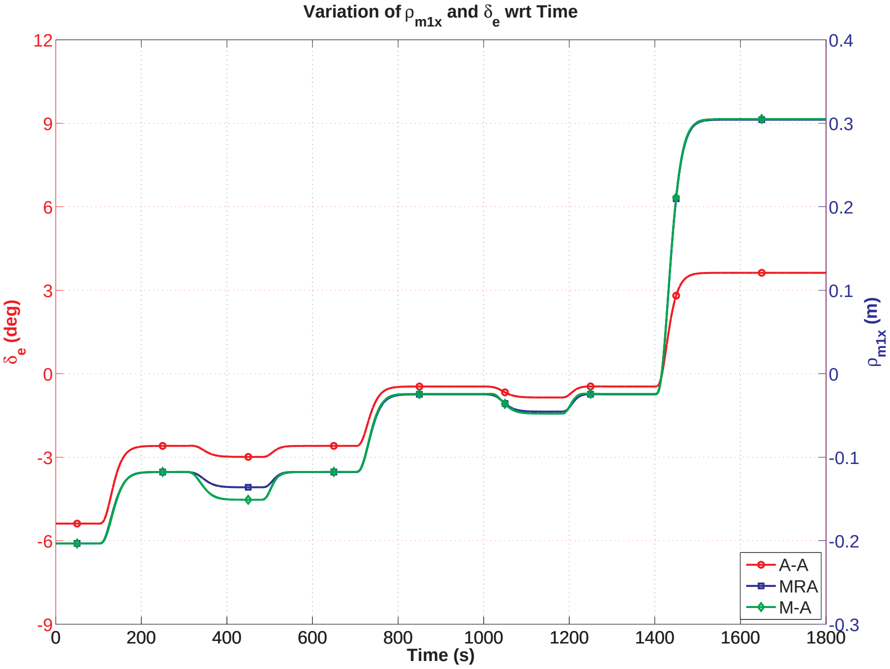

Figure 6.17. Variation of $\rho_{m_{1_x}}$ and δ_e with time.

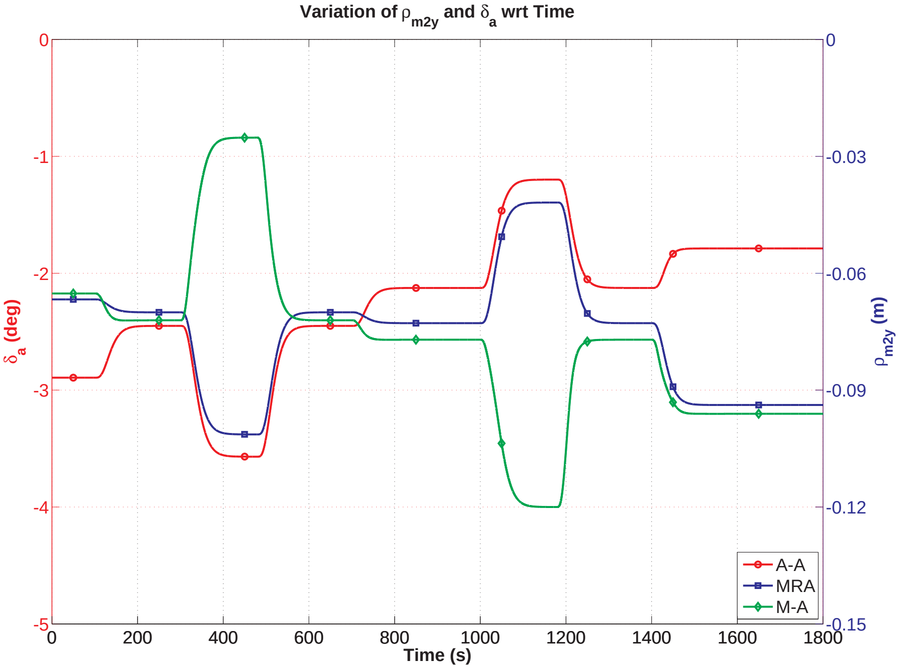

Figure 6.18. Variation of $\rho_{m_{2_y}}$ and δ_a with time.

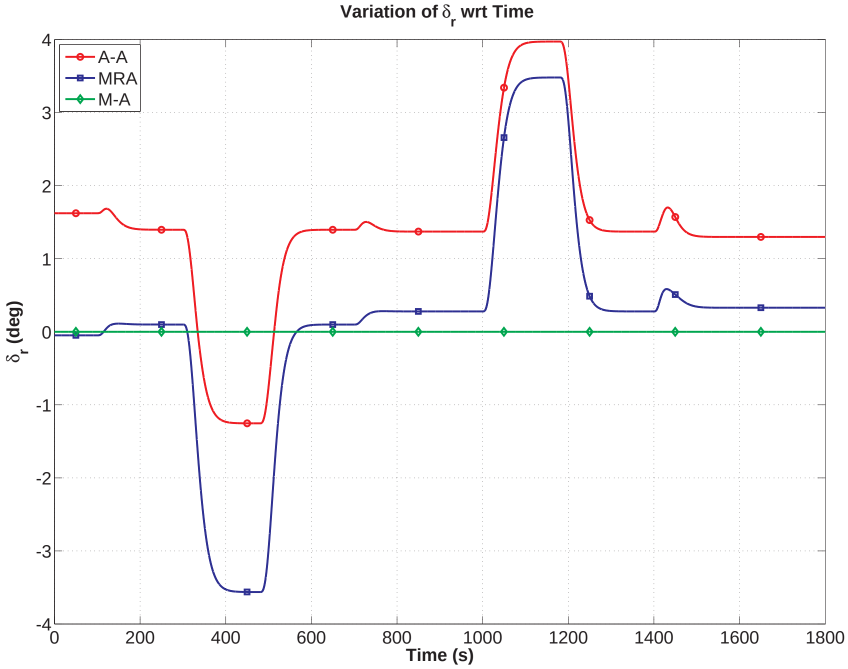

Figure 6.19. Variation of δ_r with time.

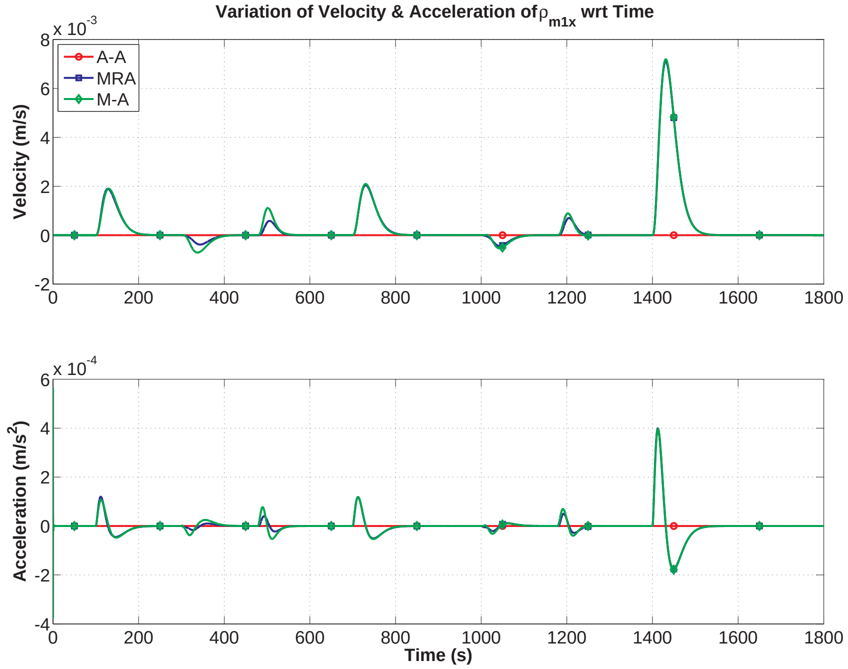

Figure 6.20. Variation of velocity & acceleration of longitudinal-actuator with time.

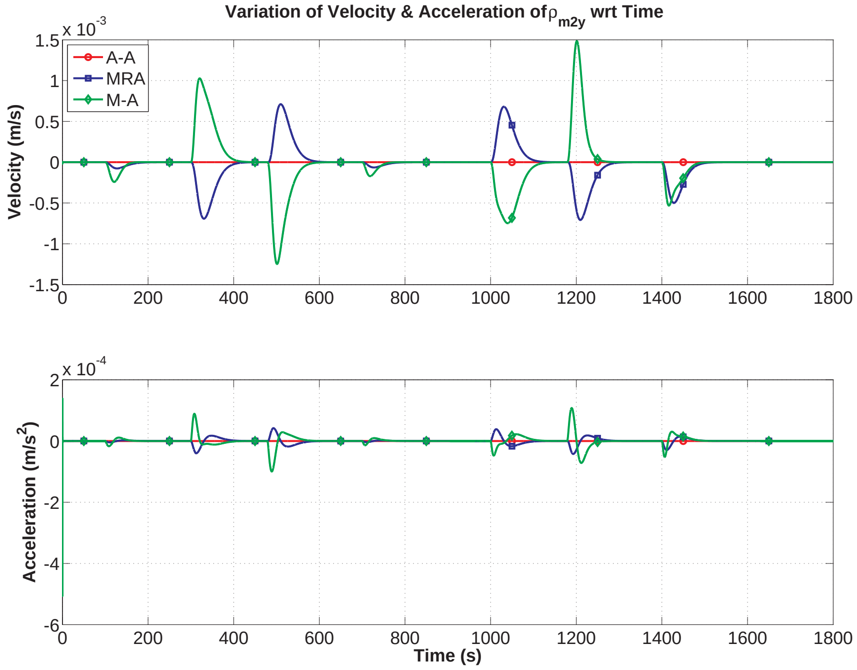

Figure 6.21. Variation of velocity & acceleration of lateral-actuator with time.

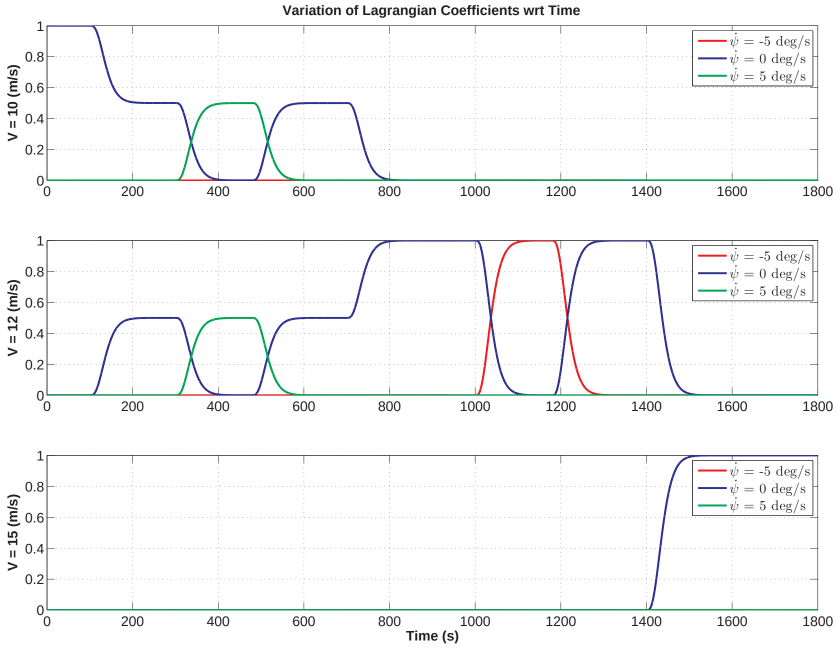

Figure 6.22. Variation of lagrangian coefficients with time.

angle in cruise flight and large sideslip angles during the turns. This is consistent with the observation in the trim analysis. Since M-A aircraft does not have any mechanism to generate yawing moment, the aircraft cannot make a turn without having sideslip angle. The sideslip angle even in the cruise condition is due to the effect of the propeller, especially when the commanded speed is not at one of the design trim values.

The benefit of using mass-actuators can be seen in Figs. 6.14-6.16. In these figures, MRA aircraft requires less thrust and torque than the A-A aircraft during all phases of the flight. Thus, less current is required for MRA airplane to run the electric motor as can be seen in Fig. 6.14. That confirms the results of longer endurance for mass-actuation obtained in Chapter 4. On the other hand, it can be seen that M-A aircraft requires more thrust and torque than A-A aircraft during the turn. Since the effect of sideslip is included in drag calculation and M-A aircraft requires some sideslip angle, especially higher in lower speeds, these results are expected. However, M-A aircraft shows benefits in terms of current, thrust and torque during all phases of cruise flight in the simulation even if it requires some sideslip angle. That confirms the benefit of using mass-actuation, especially if longer cruise flight is desired. Furthermore, another observation is made, when M-A and MRA aircraft results are compared. For the speed 10 m/s, MRA aircraft requires slightly higher current, as seen in Fig. 6.14. When the speed increases, particularly between 12 and 15 m/s, M-A airplane requires less thrust, torque and current than MRA airplane for higher speeds. Even though the M-A airplane has the handicap of flying with some sideslip angle, MRA aircraft uses rudder, which is an aerodynamic control surface and causes drag increase when deflected. Hence, M-A airplane has longer endurance for middle and higher speeds and the simulation confirms the results obtained in Fig. 4.34.

Figures 6.16-6.19 show the time histories of control inputs. As time increases, longitudinal mass-actuators for both MRA and M-A aircraft move forward as can be seen in Fig. 6.17. This is because the commanded speed increases with time and the requirement of angle of attack decreases with increasing speed as shown in trim analyses. Moving the longitudinal mass-actuator forward causes the decrease in angle of attack. Similar discussion is valid for A-A airplane. Deflecting the elevator from negative to positive causes a decrease in the angle of attack which is required for higher speeds. Fig. 6.18 shows the time histories of aileron deflection or position of the lateral mass-actuator. For M-A aircraft, lateral mass-actuator moves to right when the airplane turns right and to left when the airplane turns left. However, the position of the lateral moving-mass for MRA airplane and aileron deflection for A-A airplane show different trend. Since both aircraft use rudder, right or left turn is performed by more rudder deflection while M-A airplane does not have rudder as can be seen in Fig. 6.19.

Figures 6.20-6.21 show the velocity and acceleration of longitudinal and lateral mass-actuators when they are commanded to move. As can be seen in these figures, velocity and acceleration of mass-actuators are within feasible limits as discussed in Section 2.6. It can be said that change in positions for mass-actuators can be performed accurately when the speed or turn rate is commanded. Hence, it shows that mass-actuators can be used as a control mechanism for small unmanned airplanes in different flight phases.

Figure 6.22 shows the changes in the interpolation coefficients of the gain scheduling controller with respect to time. At the beginning, it can be seen that one Lagrangian coefficient is equal to 1 and all the others are zero since simulation starts with 10 m/s in cruise flight. When the speed is commanded from 10 m/s to 11 m/s, interpolation between operating points 2 and 5 as shown in Table 5.1 are performed. Then, coefficients for right turn with 11 m/s is interpolated between operating points 3 and 6. After the speed is commanded from 11 m/s to 12 m/s, only the coefficient for operating point 5 is 1 and the others are zero. For left turn with 12 m/s, only the coefficient for operating point 4 is 1. Finally, only the coefficient for operating point 8 is 1 after the speed is commanded from 12 m/s to 15 m/s.

6.2 Dynamic Simulation for Full Mission

In the second simulation, a scenario is defined as a full mission including climb, cruise, steady-state turn, descent and transition between these modes. Wind effect is also included in this full mission to see the performance of the closed-loop system during wind encounters. Fig. 6.23 shows the trajectory of each airplane in X-Y plane and Fig. 6.24 shows the altitude variation of each airplane with time. Commanded speed, turn rate, altitude and rate of ascent/descent are shown in Figs. 6.25-6.26. Since the aircraft is considered to be hand launched (thrown into the air by a person) for take-off, 11 m/s is the commanded speed at the beginning and assumed to be the average of this type of airplane right after thrown by a human. The simulation starts with the initial speed 9 m/s and the initial climb angle 5 deg. Hence, it is assumed that all aircraft are thrown with a speed below the average and with a positive angle relative to the ground. After 10 s, the speed is commanded from 11 m/s to 12 m/s and rate of climb is commanded from 0 m/s to 4 m/s for ascending. Ascending flight continues until the aircraft reaches to 200 m, which is commanded altitude for the mission, and it occurs about 150 s. Before reaching the commanded altitude, rate of climb is commanded from 4 m/s to 0 m/s. At 200 s, ascent/descent controller is switched to cruise/turn controller after the climb to the desired altitude is achieved. Each aircraft is exposed to an updraft (a vertical wind) with the speed -1 m/s at 300 s and headwind with the speed -2 m/s at 500 s for a period of 40 s when they fly in cruise condition as shown in Fig. 6.27. At 685 s, the aircraft starts to have a right turn with 5 deg/s. Turn command ends when the aircraft yaw angle increases by $2.5 \times 360 = 900$ deg. At 1020 s, the speed is commanded from 12 m/s to 9 m/s since the aircraft are assumed to have no landing gear and are desired to be landed with a low speed. At 1170 s, turn rates with small magnitudes are commanded for about 25 s for each aircraft to make them to return to the coordinates where the mission begins. At 1300 s, cruise/turn controller is switched to ascent/descent controller to initiate the descent. At 1350 s, rate of descent is commanded from 0 m/s to -0.5 m/s for descending and it descends for about 350 s. Before the aircraft lands, rate of descent is commanded from -0.5 m/s to 0 m/s to reduce the descent angle. The simulation ends when the aircraft touches the ground (i.e., when $z = 0$) at 1800 s. Since the performances of controllers for cruise and steady-state turns are discussed in the previous section, only the effect of wind on aircraft motion, performances of ascending/descending flight and the effect of controller switches on aircraft motion will be presented here.

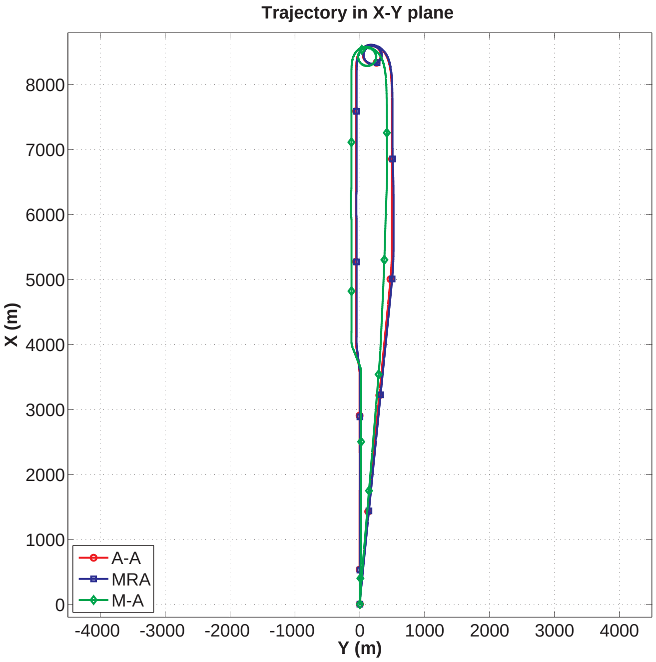

Figure 6.23. Trajectory of airplanes in X-Y plane in full mission.

As explained before, the aircraft are assumed to be exposed to updraft wind starting at 300 s and headwind at 500 s as shown in Fig. 6.27 while they are flying in cruise condition. Figs. 6.28-6.29 show the variation of speed, Figs. 6.30-6.31 show the variation of turn rate and Figs. 6.32-6.33 show the variation of altitude when the aircraft are exposed to wind. Especially when the wind speed starts to increase or decrease, deviations are observed. However, it can be seen from these figures that all three aircraft configurations can track the commanded inputs during cruise flight even if the wind exists.

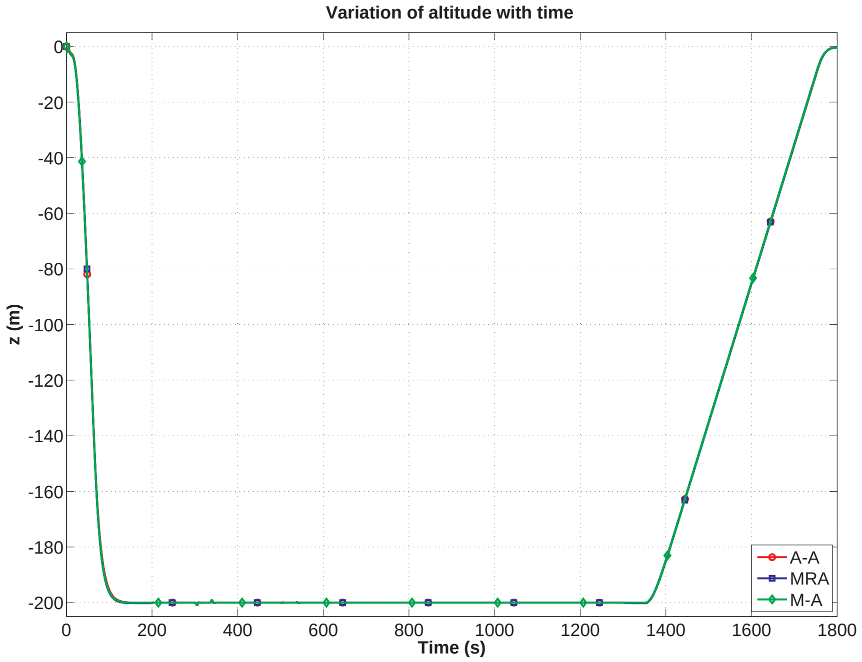

Figure 6.24. Variation of altitude with time in full mission.

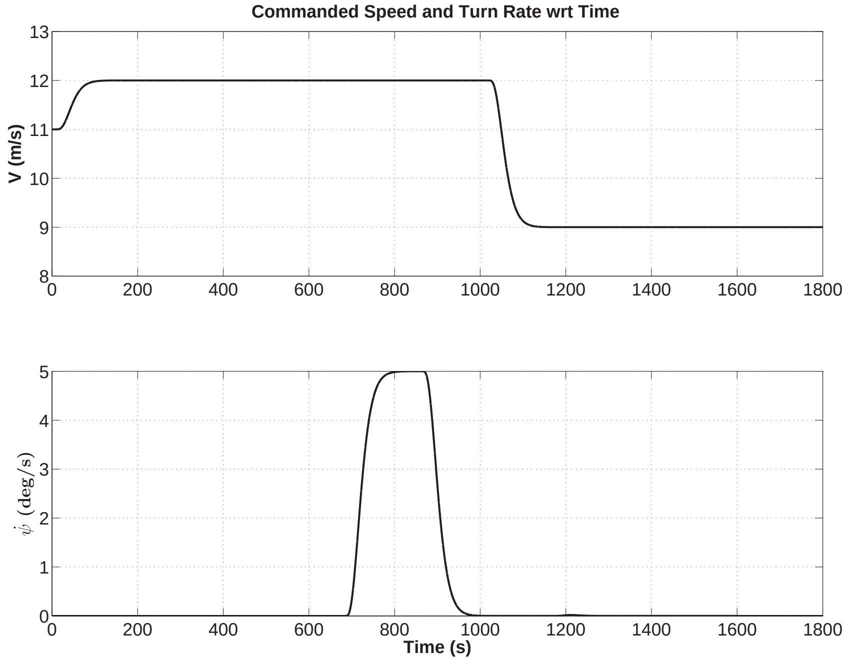

Figure 6.25. Commanded speed and turn rate with time.

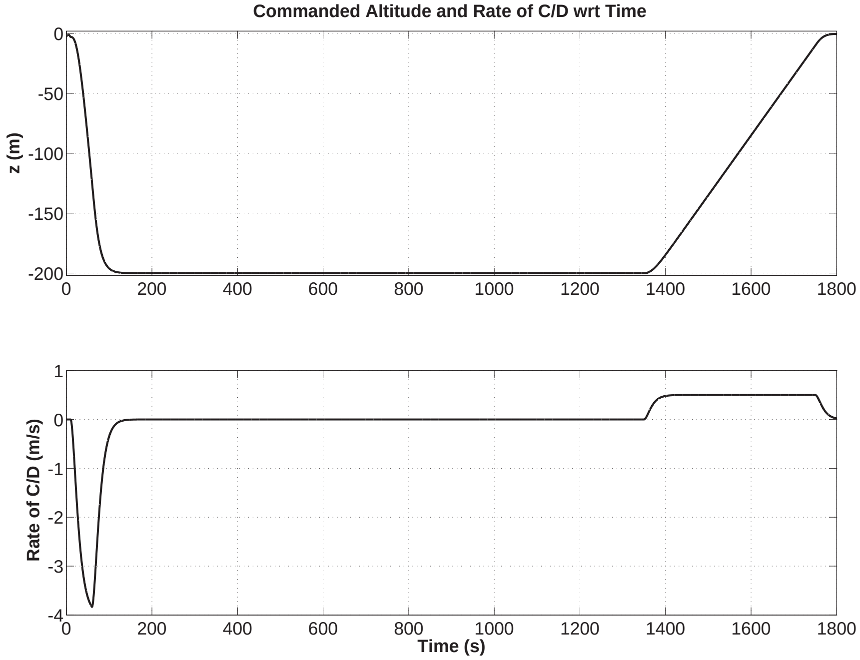

Figure 6.26. Commanded altitude and rate of ascent/descent with time.

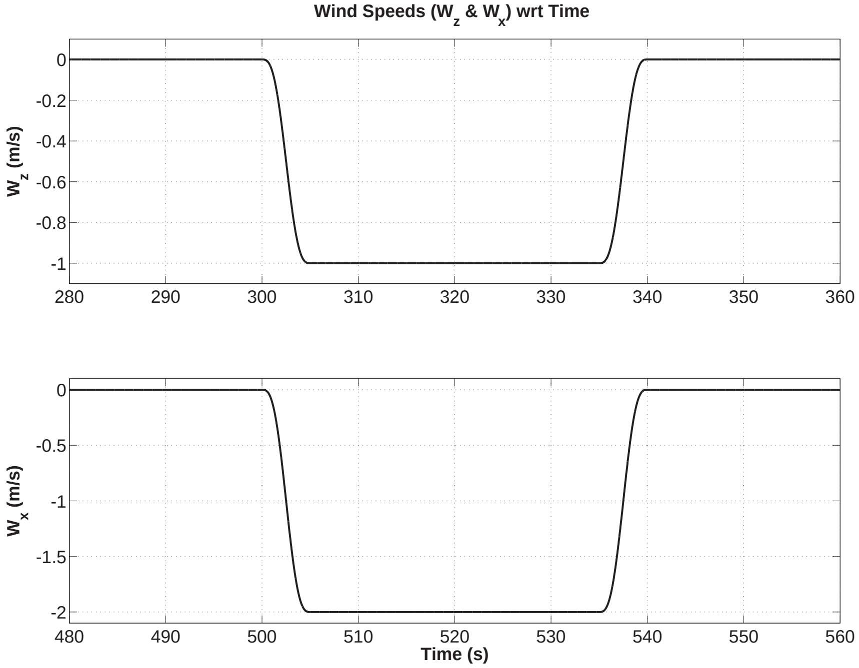

Figure 6.27. Wind speeds with time in full mission.

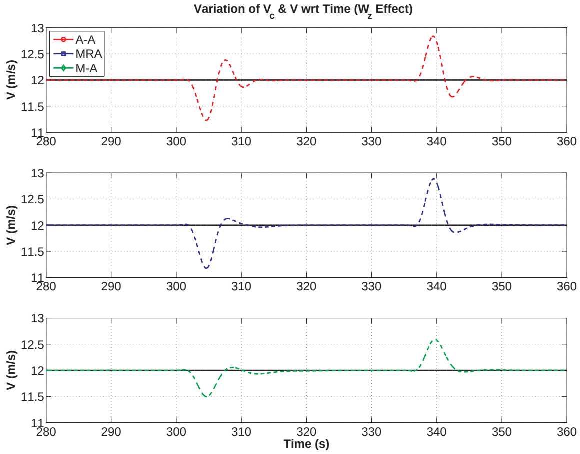

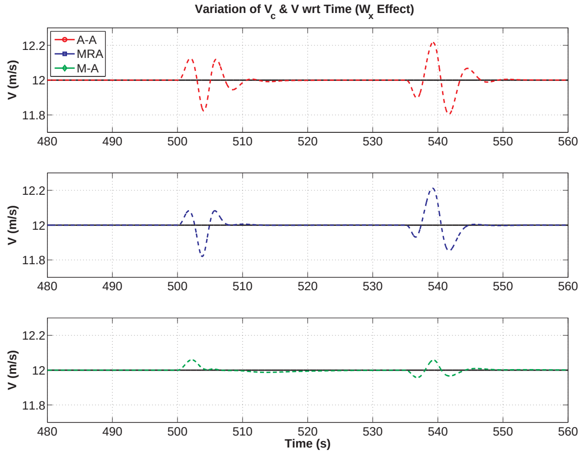

Figure 6.28. Effect of W_z on speed with time.

Figure 6.29. Effect of W_x on speed with time.

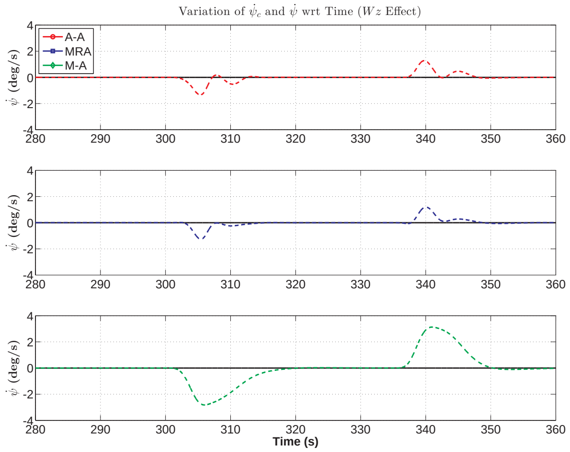

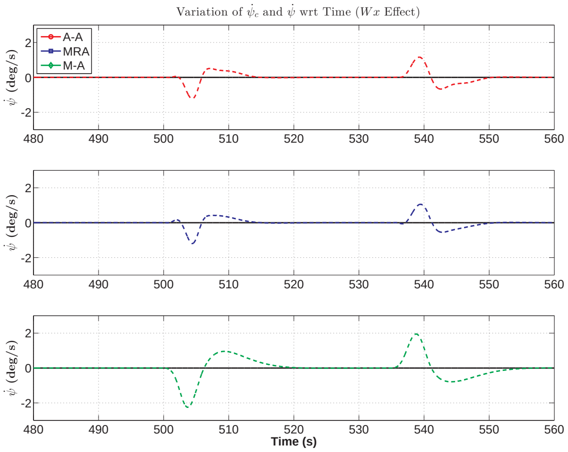

Figure 6.30. Effect of W_z on turn rate with time.

Figure 6.31. Effect of W_x on turn rate with time.

Figures 6.34-6.35 show the variation of the position of longitudinal mass-actuator or elevator deflection during the wind encounters. It can be seen that updraft wind requires more control input than headwind during the wind speed transitions. This is due to the fact that updraft wind is more effective on altitude change than the headwind as can be seen in Figs. 6.32-6.33. Figs. 6.36-6.37 show the variation of the position of lateral mass-actuator or aileron deflection and Figs. 6.38-6.39 show the variation of the rudder deflection during the wind exposure. It can be observed

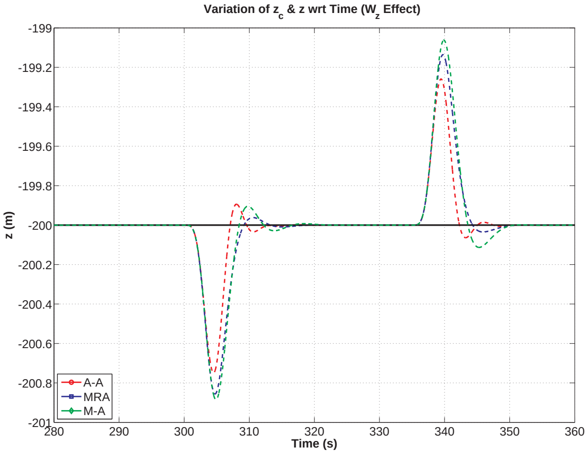

Figure 6.32. Effect of W_z on altitude with time.

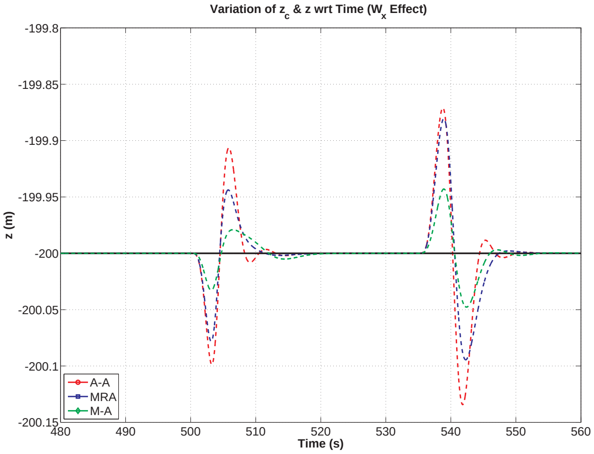

Figure 6.33. Effect of W_x on altitude with time.

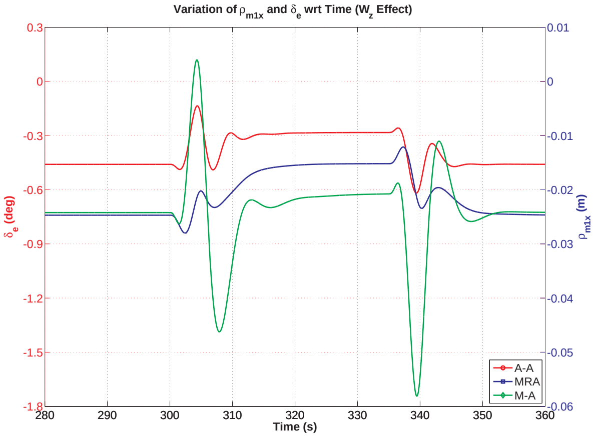

Figure 6.34. Effect of W_z on $\rho_{m_{1_x}}$ and δ_e with time.

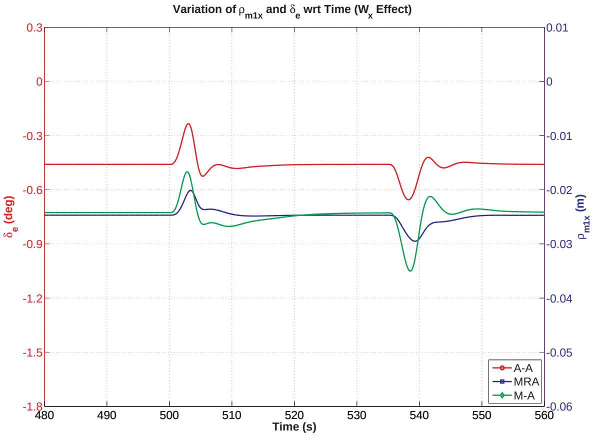

Figure 6.35. Effect of W_x on $\rho_{m_{1_x}}$ and δ_e with time.

that A-A and MRA aircraft uses more rudder than aileron or lateral mass-actuator to compensate for the wind effect. On the other hand, M-A aircraft requires more lateral-mass motion since it has no rudder. Figures 6.40-6.41 show the variation of throttle input when the aircraft are exposed to wind. Since updraft pushes the aircraft up, all aircraft require less throttle to stay at the commanded altitude while experiencing updraft. After the wind exposure, all aircraft return to its nominal cruise condition.

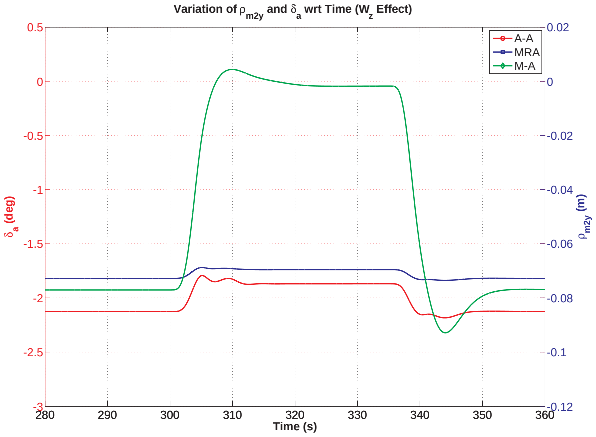

Figure 6.36. Effect of W_z on $\rho_{m_{2y}}$ and δ_a with time.

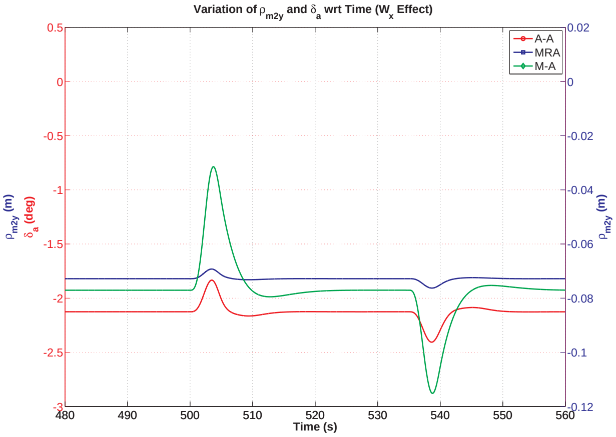

Figure 6.37. Effect of W_x on $\rho_{m_{2y}}$ and δ_a with time.

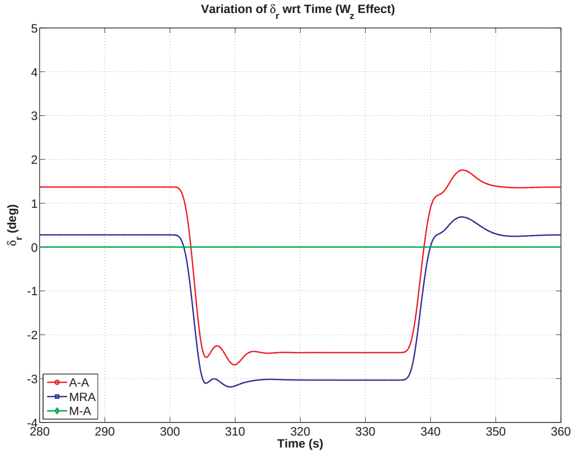

Figure 6.38. Effect of W_z on δ_r with time.

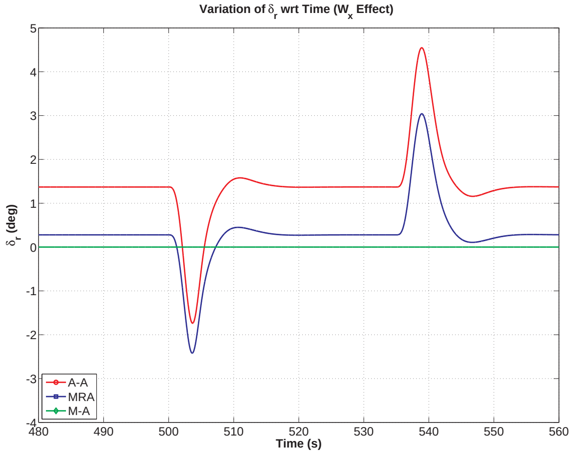

Figure 6.39. Effect of W_x on δ_r with time.

Figure 6.42-6.43 show the variation of yaw and pitch angles during the wind exposure. It can be observed that updraft wind significantly changes the pitch angle for all aircraft after the wind speed reaches to steady speed. Especially variation of elevator/longitudinal mass-actuator and throttle are affected due to change in pitch angle during the presence of wind. On the other hand, yaw angle of M-A aircraft is most affected by updraft wind. Since the change in y- position is not controlled, drift from the trajectory is observed for all aircraft. It is more visible for M-A aircraft

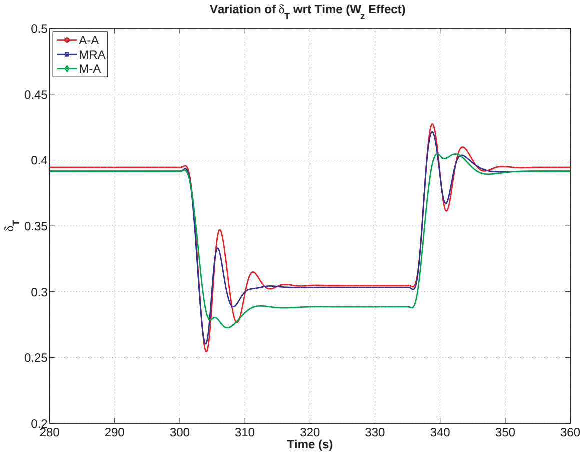

Figure 6.40. Effect of W_z on δ_T with time.

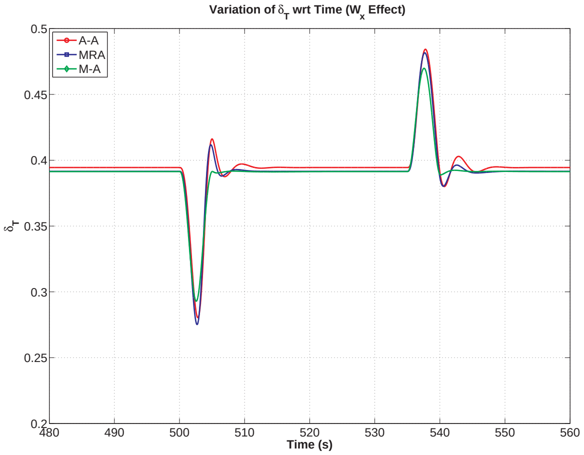

Figure 6.41. Effect of W_x on δ_T with time.

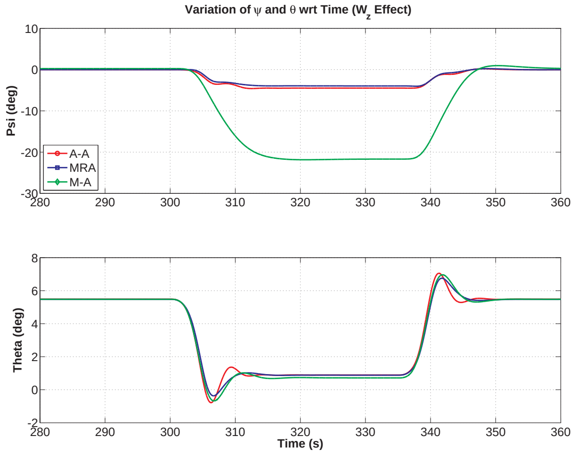

Figure 6.42. Effect of W_z on ψ and θ with time.

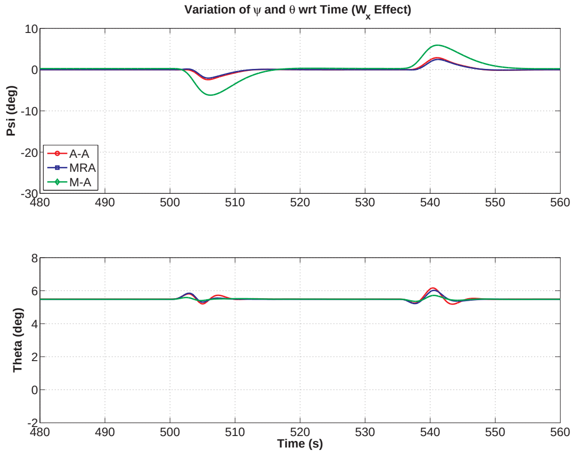

Figure 6.43. Effect of W_x on ψ and θ with time.

since it has no rudder mechanism. Furthermore, changes in yaw and pitch angles are smaller when the aircraft are exposed to headwind as compared to those during the updraft wind.

As stated earlier, ascending flight is between 0-150 s and descending flight is between 1350-1800 s. Furthermore, switching controller between ascent/descent and cruise/turn cases are done at 200 s and 1300 s. Figs. 6.44-6.45 show the variation of speed, Figs. 6.46-6.47 show the variation of turn rate and Figs. 6.48-6.49 show the

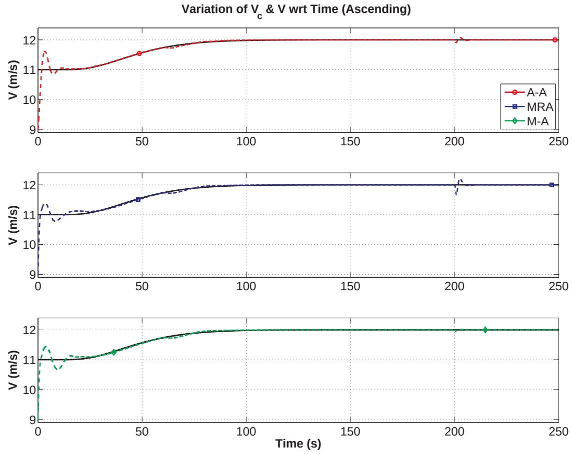

Figure 6.44. Variation of speed and commanded speed with time in ascending.

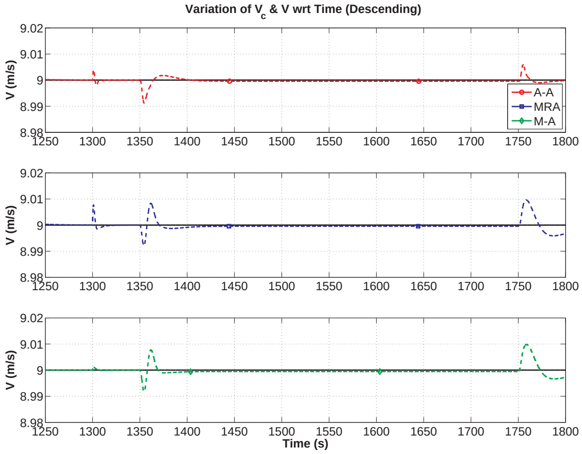

Figure 6.45. Variation of speed and commanded speed with time in descending.

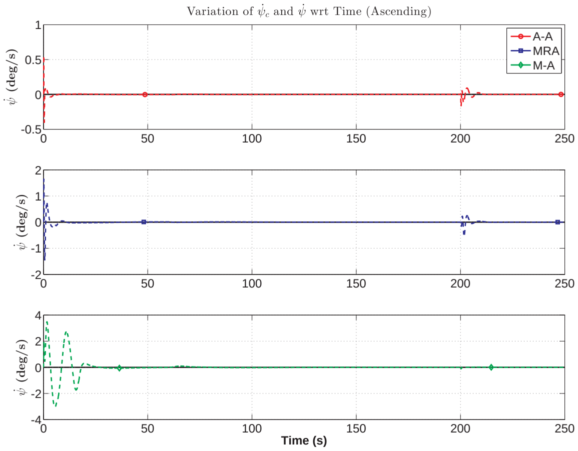

Figure 6.46. Variation of $\dot{\psi}$ and $\dot{\psi}_c$ with time in ascending.

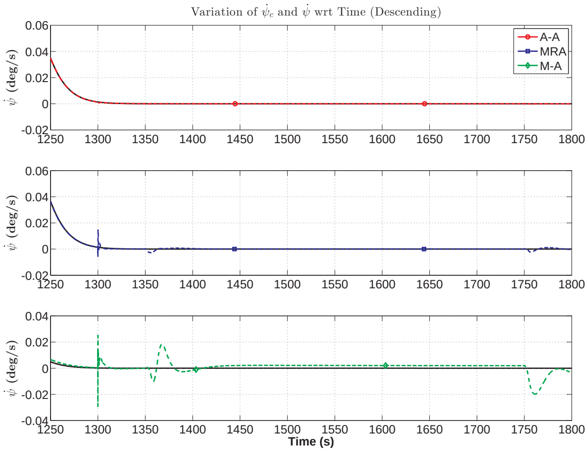

Figure 6.47. Variation of $\dot{\psi}$ and $\dot{\psi}_c$ with time in descending.

variation of rate of ascent/descent when the aircraft are in ascending/descending and during the switching between the controllers occurs. For ascending, it can be seen that commanded inputs for each aircraft are successfully tracked by the controller immediately even after the hand launch. Furthermore, it is observed that transition between cruise and descent are successfully accomplished by the aircraft controller for each commanded input. It can be also seen that controller of each aircraft can

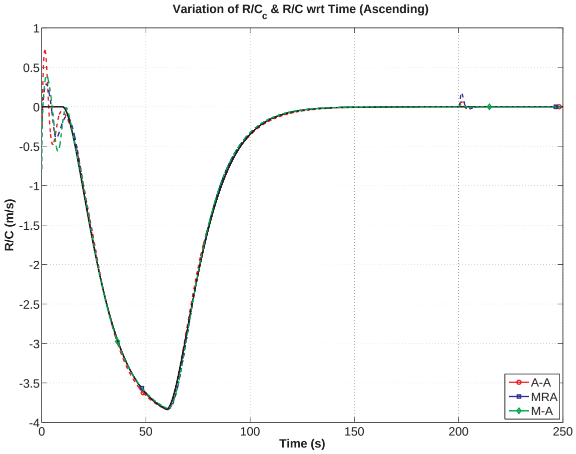

Figure 6.48. Variation of R/C and commanded R/C with time in ascending.

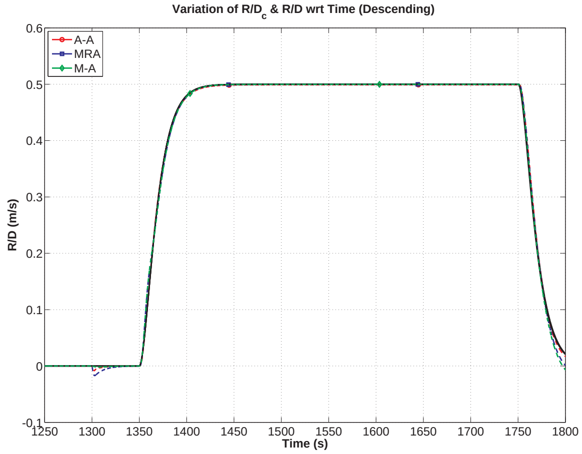

Figure 6.49. Variation of R/D and commanded R/D with time in descending.

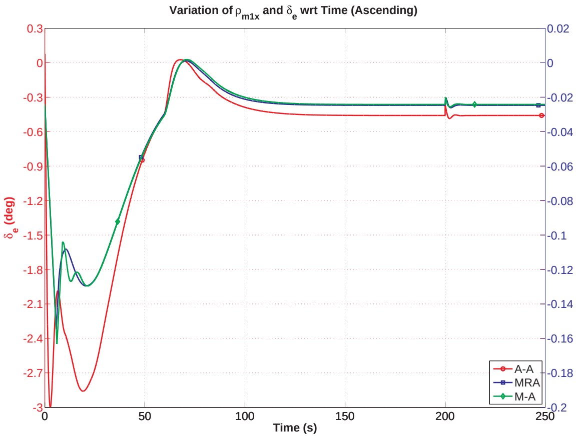

Figure 6.50. Variation of ρ_{m1_x} and δ_e with time in ascending.

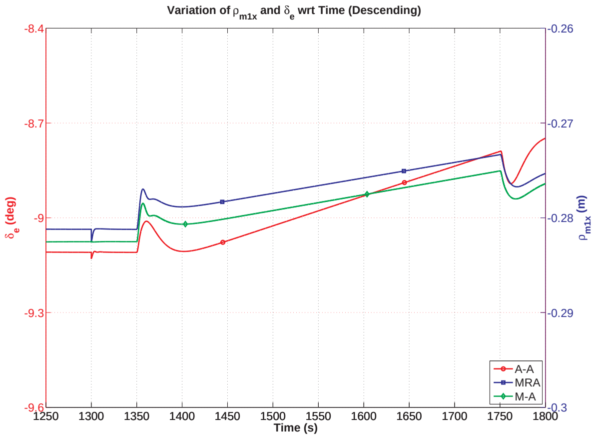

Figure 6.51. Variation of ρ_{m1_x} and δ_e with time in descending.

compensate for the transients during the controller switching from climb-rate controller to altitude-hold controller after the climb is complete, and from altitude-hold to descend-rate controller to initiate the descent.

Figures 6.50-6.51 show the variation of the position of longitudinal mass-actuator or elevator deflection, Figs. 6.52-6.53 show the variation of the position of lateral mass-actuator or aileron deflection, Figs. 6.54-6.55 show the variation of rudder deflection and Figs. 6.56-6.57 show the variation of throttle input during ascend-

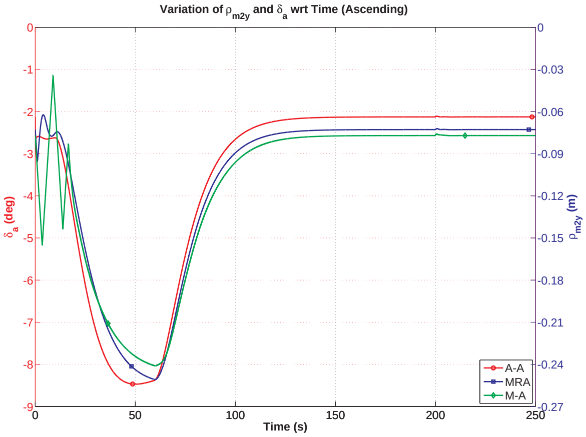

Figure 6.52. Variation of $\rho_{m_{2_y}}$ and δ_a with time in ascending.

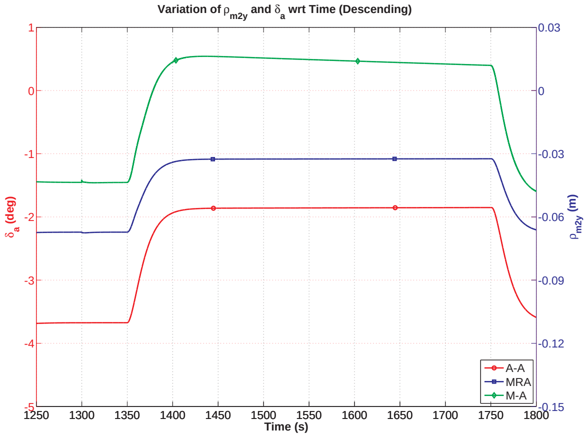

Figure 6.53. Variation of $\rho_{m_{2_y}}$ and δ_a with time in descending.

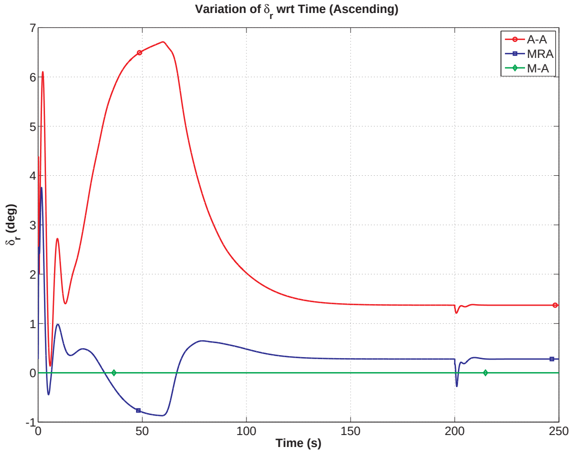

Figure 6.54. Variation of δ_r with time in ascending.

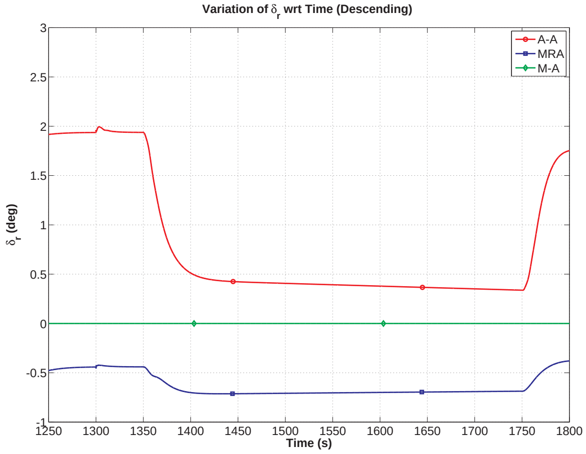

Figure 6.55. Variation of δ_r with time in descending.

ing/descending and the switching between the controllers. The first observation is that there are some instantaneous deviations during the time of switching the controllers. This is especially apparent with the throttle response when the controller is switched from ascent/descent to cruise/turn case. On the other hand, those deviations are successfully compensated for by the controllers and all the aircraft can return to their nominal conditions for cruise. The second observation is that all the

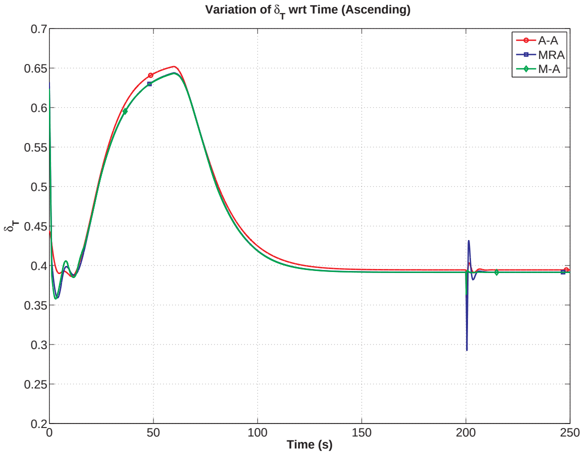

Figure 6.56. Variation of δ_T with time in ascending.

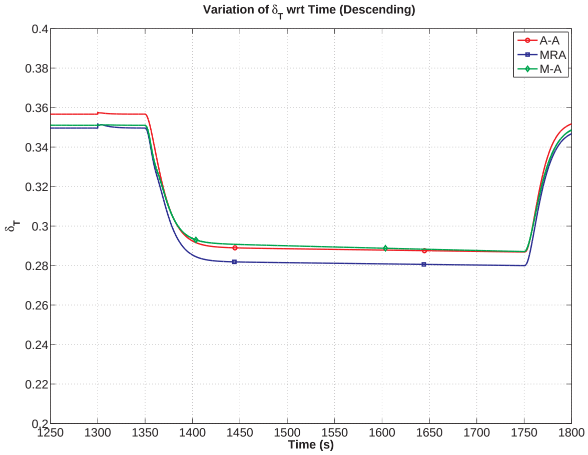

Figure 6.57. Variation of δ_T with time in descending.

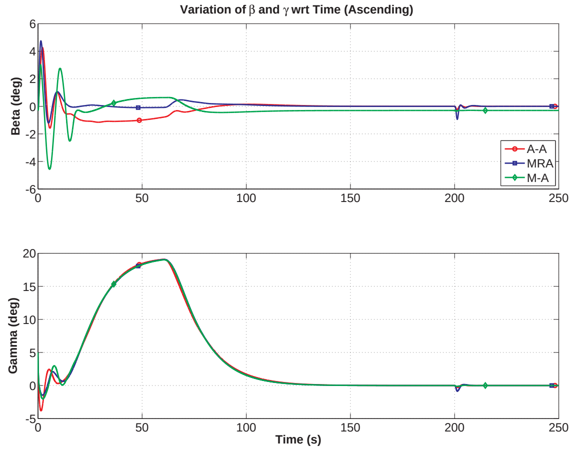

Figure 6.58. Variation of β and γ with time in ascending.

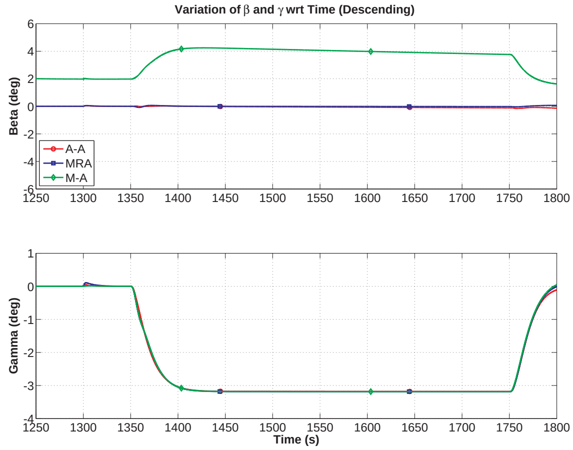

Figure 6.59. Variation of β and γ with time in descending.

control inputs vary during the ascending. This is because the commanded rate of climb varies during the ascending as shown in Fig. 6.48.

Figures 6.58-6.59 show the variation of sideslip and flight path angles during ascending/descending and the switching between the controllers. As explained before, rate of climb varies during the ascending flight. Hence, sideslip and ascent angles vary

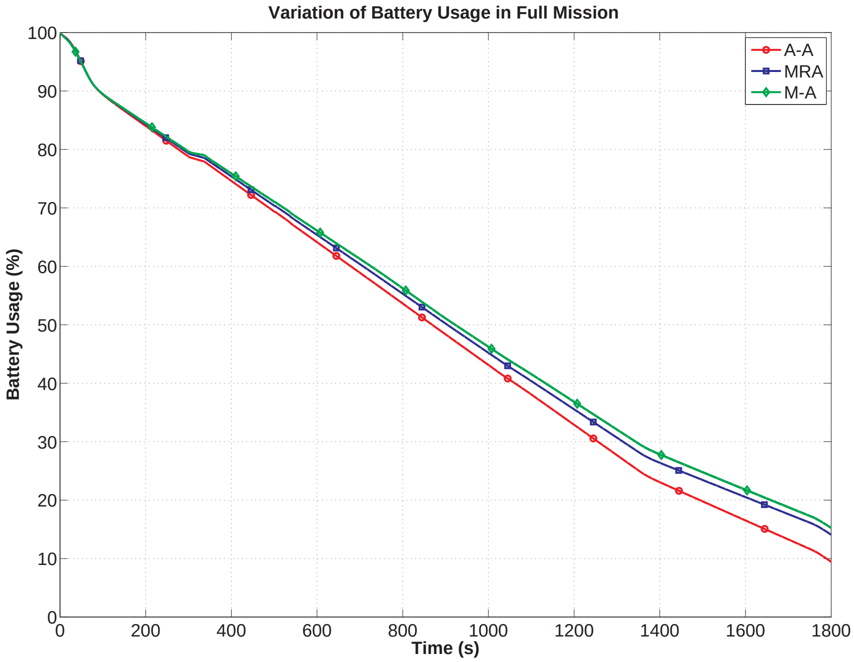

Figure 6.60. Battery usage of airplanes in full mission.

with time in ascending. On the other hand, all the aircraft states such as sideslip angle can be controlled even though the commanded rate of ascent is not constant.

Figure 6.60 shows the battery usage for each aircraft during the flight. Full mission includes all the phases of flight and transitions between them. At the end of the mission, the battery usage for A-A aircraft is % 90.5, the battery usage for MRA aircraft is % 86, and the battery usage for M-A aircraft is % 85 approximately. This full mission confirms that using mass-actuation decreases the battery usage and provides longer endurance if the total weight of the aircraft is kept at the same weight. Furthermore, M-A aircraft has still slightly less battery usage since MRA aircraft uses rudder to fly with zero sideslip angle.

6.3 Summary of the Chapter

In this chapter, two different simulations were run for all aircraft configurations. Results showed that M-A and MRA airplanes can successfully complete their missions including cruise, steady-state turn, ascending and descending with designed controllers for mass-actuation. Furthermore, wind encounters during the mission can be successfully overcome by mass-actuators. Results also showed that using mass-actuation results in saving the battery usage in a defined mission including all phases of flight and transitions between them.

CHAPTER 7

CONCLUSIONS AND FUTURE WORK

7.1 Conclusions

This work investigates feasibility of internally moving-mass actuation for controlling a small fixed-wing unmanned aircraft instead of conventional aerodynamic control surfaces. Two moving masses are considered: one moves longitudinally within the fuselage to generate pitching moment and the other laterally along the wings to generate rolling moment. Three different actuation configurations of the same aircraft are considered (1) aero-actuated aircraft - airplane with three standard control surfaces, (2) mass-rudder-actuated aircraft - airplane that has internal mass motion for pitching and rolling moment generation instead of elevator and aileron, respectively, while the rudder is still used for yawing moment generation, (3) mass-actuated aircraft - airplane with only mass-actuation for pitch and roll moment and there is no mechanism for direct yawing moment generation.

The main conclusion of this research is that mass-actuation is a feasible moment generation mechanism that offers an alternative to the conventional aerodynamic control surfaces for small unmanned aerial vehicles. Various analyses carried out in this research has shown that the mass-actuation is capable of generating the level of moment required to trim the aircraft in all main flight phases including steady climb, cruise, turn, and descent, and transitions between these steady flight modes. This conclusion is validated when the actuator dynamics with all the constraints such as position, speed, and acceleration limits is included in the analyses.

While the mass-actuated aircraft can fly in all the main flight phases, the feasible speed ranges for such trim flight modes are shorter, especially from the high speed side, compared to that of the aero-actuated aircraft. This is mainly because the moment needed for such flight conditions requires the placement of the mass-actuators exceeding the limits of the space available for the motion of the mass-actuation within the aircraft. Further, mass-actuation lacks the mechanism of generating yawing moment, which is provided by rudder in standard airplane. To better understand the effect of this deficiency, the propeller-induced torque is modeled in detail and included in the analyses. With the propeller-induced torque included, trim analyses show that the mass-actuated aircraft, especially in low speed, flies with large sideslip angle, which decreases with increasing speed. Mass-actuation augmented with rudder is shown to address this issue. A proper alignment of the propeller seems also to help with the yaw-moment deficiency and thud reduce the trim sideslip angle, useful especially for the mass-actuated aircraft. Despite such issues, mass-actuation alone or augmented with rudder is shown to reduce the thrust requirements, as compared to aero-actuated aircraft, in all four flight conditions in various speed ranges. This is because of the elimination of the induced drag due to the deflection of the aerodynamic control surfaces to trim the aircraft. Especially, in cruise flight, the reduced thrust results in longer endurance and range. The benefit of longer endurance is also available in steady turn. The analysis also shows that right turns result in higher endurance than the left turn due to the propeller-induced torque effect. Performance of the mass-actuation converges that of mass-rudder-actuation with increasing speed since the trim slide slip angle decreases to zero. For accurate range and endurance calculation, and for better comparison between mass- and aero-actuated aircraft, power consumption of the servos for the mass- and aero-actuators is modeled and included in the analyses along with the electric motor of the propeller. Range and endurance benefit of mass-actuation remains with all these effects considered.

In addition to trim flight analyses, the feasibility and performance of mass-actuation is also investigated in dynamic flight conditions using a full 6-DOF flight simulation. The simulation includes all important effects such as mass/inertia variation due to mass-actuation, detailed propeller torque and thrust models, dynamics of all electric servos for all the actuators and the electric motor for the propeller, power consumption by the servos and the motor, and the battery usage. Dynamic simulation of the aircraft with all three actuator configurations requires the design and implementation of a feedback controller, separately for each configuration, to fly the aircraft in a desired flight trajectory. The control design is preceded with controllability analyses. This research effort investigated not only the controllability but also the level of controllability. The level of controllability of mass-actuation is compared with that of aerodynamic actuation. The most important results of this analysis is that aircraft with mass-actuation is completely controllable in all flight conditions considered within the respective feasible speed ranges, which implies that the feedback control laws can be developed and implemented based on mass-actuation. The second important finding of this analysis is that the mass-actuation provides a comparable levels of controllability relative to the aerodynamic actuation. While aerodynamic actuation provides much higher level of controllability at high speeds, controllability by mass-actuation is similar or higher, at times, in low speed range. Once the controllability is ensured, LQR-based gain scheduling controllers are designed to track commanded climb rate, altitude, speed, and turn rate. With the implementation of the controller in the nonlinear simulation, a representative mission is flown that include, climb to a certain altitude, flying in cruise, loitering in steady turn, and descent to landing. The aircraft is flown in this mission with all three actuation configurations. The mass-actuation is successful in flying the whole mission. A comparison of battery usage between the three actuation configurations show the power saving benefit of mass-actuation as observed first through the trim analyses.

7.2 Future Work

The following discusses the ideas for future work based upon this dissertation work and its conclusions. In this dissertation, one lateral mass-actuator is considered to generate rolling moment. It is assumed that the lateral mass-actuator could pass from one wing to another when the airplane requires different flight conditions. In the future work, two lateral mass-actuators may be considered for all the flight modes analyses including trim, controllability and control design.

A real flight was achieved by using two lateral-mass actuators for roll motion based upon the preliminary work of this dissertation. For future work, longitudinal mass-actuator to generate pitching moment in addition to two lateral mass-actuators may be considered in real flight implementation. Two mass-actuators can be also considered as longitudinal mass-actuators if the aircraft design requires.

In this work, battery is proposed as one of the potential mass-actuator mechanisms. By using the weight of the battery, pitching and rolling moments can be generated without increasing the total weight of the aircraft. For this implementation, more than one battery may be required. In the future work, power distribution between the batteries to supply the power to the aircraft should be considered if battery is considered as the weight for the mass-actuators.

This study is done for a small unmanned airplane which has the total weight of 1.9 kg. In the future work, different types of aircraft with different weights may be investigated. Furthermore, a new aircraft may be designed including longitudinal and lateral mass-actuators without having any aerodynamic control surfaces.

In this study, LQR based control method was implemented. It was observed that tuning the weighting matrices requires extensive time and effort. In the future work, other control methods may be implemented to improve the controllers for this type of actuators. Moreover, only the commanded inputs were included in the control design without considering the trajectory. Hence, trajectory control with mass-actuation may be considered if a specific mission is defined.

It is also shown in this study that propeller affects the airplane motion and couples the longitudinal and lateral modes since the airplane is small. That affects the airplane with mass-actuation, especially for lower speeds since the trim value of sideslip angle is higher. To decrease the sideslip angle requirement, differential thrusts may be implemented. In the future work, two propellers with electric motors (one mounted on the left wing and the other mounted on the right wing) may be used to have differential thrusts. That would reduce the high trim value of the sideslip angle and remove the handicap of using mass-actuation not being able to generate yawing moment.

APPENDIX A

STEADY-STATE TURN TRIM WITHOUT PROPELLER EFFECT

In this appendix, results of steady-state turn without propeller effect are shown. For steady-state turn trim, it was desired to have zero sideslip turning at constant altitude when mass-actuation is used. First, turning with zero sideslip at constant altitude was attempted. Second, constant altitude constraint was removed to investigate turning with zero sideslip. Third, sideslip constraint was removed for to have a steady-state turn at constant altitude and results were compared to the airplane with aero-actuation. Then, the M-A airplane was augmented with rudder (MRA aircraft) to see if turning with zero sideslip at constant altitude is possible and results were also compared with A-A airplane. Table A.1 shows a summary of all the cases considered.

Case	Altitude Constant	Sidelip Angle Set to Zero	Rudder is Augmented
T1	Yes	Yes	No
T2	No	Yes	No
T3	Yes	No	No
T4	Yes	Yes	Yes

Table A.1. Conditions and constraints in steady-state turn trim for mass-actuation

During the trim analyses for cases $T3$, $T4$, angular velocity components p, q and r can be written in terms of ϕ, $\dot{\psi}$ and θ as formulated in Eqs. (4.6)-(4.8). Moreover, the pitch angle, θ, can be written in terms of ϕ, α and β as formulated in Eq. (4.10).

A.1 Turn with Zero Sideslip Angle at Constant Altitude for Mass-Actuated Airplane

In this section, results of case $T1$ as shown in Table A.1 are presented. For the M-A aircraft, the first attempt is to obtain trim turns with zero sideslip angle at constant altitude. If only $\rho_{m_{1_x}}$ and $\rho_{m_{2_y}}$ are used for control, the M-A aircraft has only two control variables for attitude control as opposed to A-A airplane with three control surfaces. Thus, the z-position of m_2 is included as a variable in the trim analysis when coordinated turn is desired. The range of vertical motion of m_2 is limited to be between -0.1 m and 0.1 m. In this case, the unknowns in Eqs. (4.1) and (4.2) are T_x, α, $\dot{\psi}$, $\rho_{m_{1_x}}$, $\rho_{m_{2_y}}$ and $\rho_{m_{2_z}}$ with sideslip angle $\beta = 0$. Under these conditions, attempts were made to solve Eqs. (4.1) and (4.2) with both $fsolve$ and $fmincon$. Neither method seemed to generate feasible solutions, which implied that the airplane with moving-mass actuation cannot be trimmed in a coordinated turn, i.e. with zero sideslip angle, even though m_2 is allowed to have vertical motion. To confirm this finding, another method is used to avoid relying solely on the numerical solver and optimization tools. An attempt was made to analytically solve the six equations instead of relying on a numerical solver. This attempt was expected to show the solutions if they exist, or to prove that no solution exists.

The initial goal was to reduce the set of six nonlinear equations with six unknowns to a single equation with one unknown. Then, a one-dimensional plot of this expression versus the unknown variable would reveal if the expression takes a value of zero anywhere. If so, the solution will be found; if not, this will prove that the solution does not exist. However, it was discovered that this goal was too ambitious. Instead, the set of six equations was reduced to an equation with two unknowns. This still is enough to visualize whether the solution exists by generating a two-dimensional surface plot, corresponding to the expression with two variables.

The equation obtained from the six equations in Eqs. (4.1)-(4.2) by substitution is

$$f(\alpha, \dot{\psi}, V, \phi) = 0 \tag{A.1}$$

where

$$f(\alpha, \dot{\psi}, V, \phi) = q_0 \left((M + m_1 + m_2) g \frac{\cos\theta}{\sin\phi} + Y + Z \cot\phi \right) \tag{A.2}$$

$$q_0 = \dot{\psi}_0 \sin\phi_0 \cos\theta_0 \tag{A.3}$$

$$\theta = \tan^{-1} \left(\frac{\tan\beta_0 \sin\phi_0}{\cos\alpha_0} + \tan\alpha_0 \cos\phi_0 \right) \tag{A.4}$$

$$Y = \left(C_{Y_\beta} \beta + C_{Y_{\delta_r}} \delta_r + \frac{b}{2V} (C_{y_p} p + C_{y_r} r) \right) QS \tag{A.5}$$

$$Z = \left(-C_L \cos\alpha - C_D \sin\alpha \right) QS \tag{A.6}$$

Further, the control variables can also be written in terms of $\alpha, \dot{\psi}, V, \phi$ as

$$T_x = (M + m_1 + m_2)[g \sin\theta + q_0 V \sin\alpha] - m_1 (r_0^2 + q_0^2) \rho_{m_{1_x}} - X \tag{A.7}$$

$$\begin{aligned} \rho_{m_{1_x}} = & \frac{m_2 q_0^2}{m_1 g \cos\theta} \left((1 - \cot^2\phi) + \frac{\cos\phi}{\sin^2\phi} - \frac{m_2 q_0^2}{\sin^2\phi} \right) \rho_{m_{2_z}}^2 \\ & + \left(\frac{[g \sin\theta - q_0 V \cos\alpha] m_2}{m_1 g \cos\theta \cos\phi} + \frac{m_2 q_0 V \cos\alpha \cos\phi}{m_1 g \cos\theta \sin^2\phi} + \frac{2 m_2 q_0^2}{m_1 g \cos\theta \sin\phi} \Big((M + m_1 + m_2)[g \cos\theta \sin\phi - r_0 V \cos\alpha] + Y \Big) \right) \rho_{m_{2_z}} \\ & + \frac{1}{m_1 g \cos\theta \sin\phi} \left((I_{yy} - I_{zz}) q_0^2 \cot\phi + \mathcal{L} + \frac{[g \sin\theta - q_0 V \cos\alpha] \tan^2\phi}{q_0^2} \Big((M + m_1 + m_2)[g \cos\theta \sin\phi - r_0 V \cos\alpha] + Y \Big) \right) \\ & + \frac{1}{m_1 g \cos\theta \sin\phi} \left(\tan\phi \Big((M + m_1 + m_2)[g \cos\theta \sin\phi - r_0 V \cos\alpha] + Y \Big)^2 \right) \\ & + \frac{1}{m_1 g \cos\theta \sin\phi} \left((\tan^2\phi - 1) \Big((M + m_1 + m_2)[g \cos\theta \sin\phi - r_0 V \cos\alpha] + Y \Big) \right) \end{aligned} \tag{A.8}$$

$$\rho_{m_{2_y}} = \frac{-(M + m_1 + m_2)[g \cos\theta \cos\phi + q_0 V \cos\alpha] + (m_2 q_0^2 \rho_{m_{2_z}}) - Z}{m_2 q_0 r_0} \tag{A.9}$$

$$\begin{aligned} \rho_{m_{2_z}} = & \Bigg([q_0 V \cos\alpha - g \cos\theta \cos\phi] \Big(\mathcal{N} + I_{zz} (q_0^2 \cot\phi) \Big) + [q_0 V \cos\alpha \cot\phi] \Big(-\mathcal{M} + I_{yy} (q_0^2 \cot\phi) \Big) \\ & + \frac{(q_0 V \cos\alpha - g \cos\theta \cos\phi)(q_0 V \sin\alpha - g \cos\theta \cos\phi)}{(q_0^2 \cot\phi)} \Big((M + m_1 + m_2)[g \cos\theta \sin\phi - q_0 V \cos\alpha \cot\phi] + Y \Big) \Bigg) \\ & * \frac{1}{m_2 \left(g q_0 V \left(\frac{\cos\phi \sin^2\phi \cos\theta \sin\alpha + \cos^2\theta \sin\theta \cos\alpha}{\sin\phi} \right) - q_0^2 V^2 \left(\frac{\sin\alpha \cos\alpha}{\sin^2\phi} \right) \right)} \end{aligned} \tag{A.10}$$

Note that the above equations depend on airspeed V and bank angle ϕ in addition to angle-of-attack α and yaw rate $\dot{\psi}$. To be able to visualize the expression

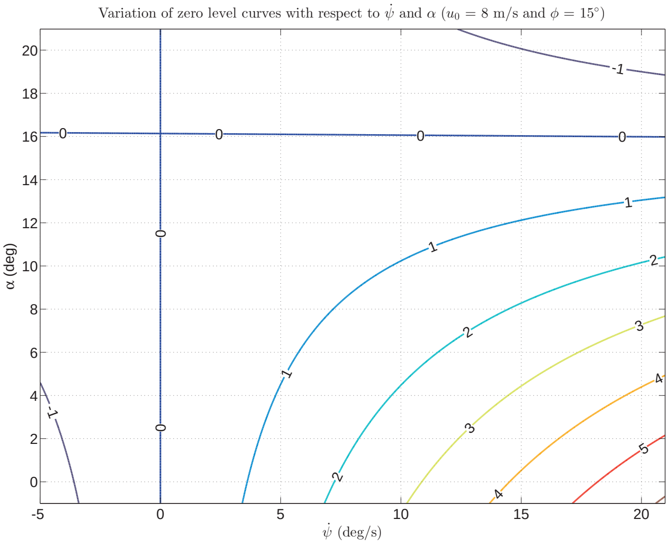

Figure A.1. The zero level curves in terms of $u_0 = 8\ m/s$ and $\phi = 15°$.

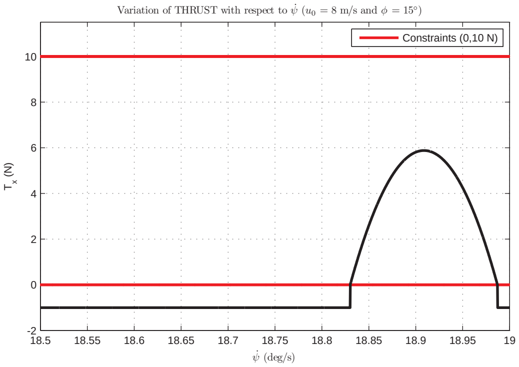

Figure A.2. Required thrust when $u_0 = 8\ m/s$ and $\phi = 15°$.

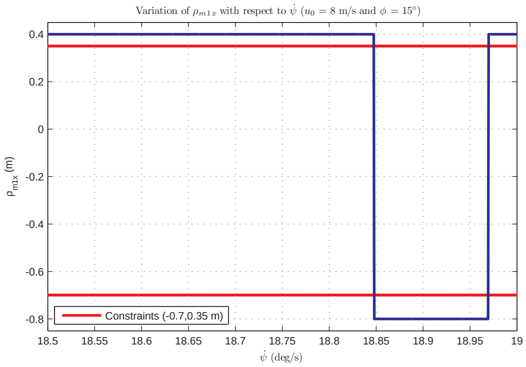

Figure A.3. $\rho_{m_{1_x}}$ when $u_0 = 8\ m/s$ and $\phi = 15°$.

in Eq. (A.2) as a two-dimensional surface or contour plot, two of the four should be specified. In this study, contour plots for specified V and ϕ are plotted in $(\alpha,\ \dot{\psi})$ space. For the specified V and ϕ, the values of α and $\dot{\psi}$ that make $f(\alpha, \dot{\psi}, V, \phi)$ in Eq. (A.2) zero (shown by zero level curves) satisfy Eqs. (4.1)-(4.2). That is, the zero level curves show where in $(\alpha,\ \dot{\psi})$ space a coordinated turn might be possible for the M-A airplane. To obtain a definite answer, the values of the control variables over the zero-level curves should be analyzed to see whether the control variables are within

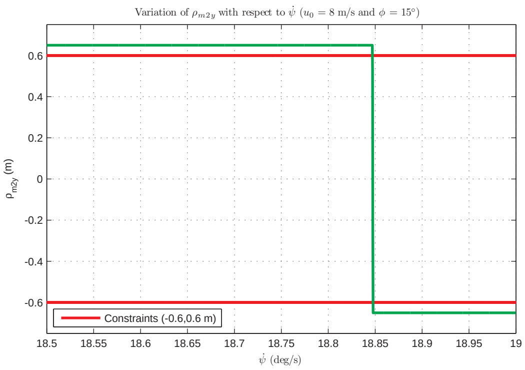

Figure A.4. ρ_{m2_y} when $u_0 = 8\ m/s$ and $\phi = 15°$.

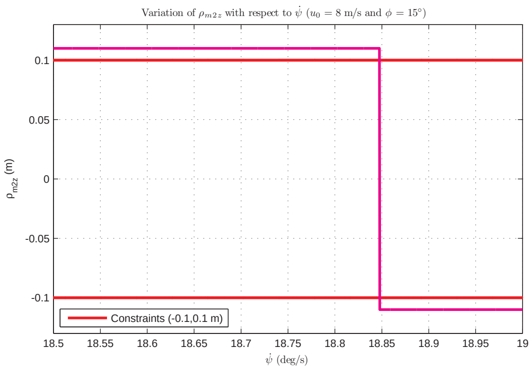

Figure A.5. ρ_{m2_z} when $u_0 = 8\ m/s$ and $\phi = 15°$.

their limits. If there is a point on the zero-level curves at which all control variables are within their limits, then that point will represent a feasible trim condition. Fig. A.1 shows a contour plot, specifically zero-level curve, of the surface corresponding to $f(\alpha, \dot{\psi}, V, \phi)$ in Eq. (A.2) when $u_0 = 8\ m/s$ and $\phi = 15$ degrees. It can be seen from Fig. A.1 that there are two branches of the zero-level curve: (1) when $\dot{\psi} = 0$, which is not a solution of physical significance since steady turns are sought, (2) when α changes slowly about 16 degrees for varying $\dot{\psi}$. Possible solutions of interest are in the positive range of $\dot{\psi}$ since the bank angle is positive. Figs. A.2-A.5 shows the values of the control variables along this branch of $f(\alpha, \dot{\psi}, V, \phi)$ zero-level curve.

Table A.2. Angle of attack for specified u_0 and ϕ

$u_0 \setminus \phi$	5°	15°	25°
$8\ m/s$	15.5392°	15.9954°	17.1731°
$12\ m/s$	5.4996°	5.7005°	6.1815°
$16\ m/s$	1.8564°	1.9692°	2.2167°

In Figs. A.2-A.5, the data points outside the respective constraints are not represented by the actual values. Instead, the actual values of such data points are

Table A.3. Indicator if control variables are within limits (Y = Yes, N = No)

u_0 - ϕ_0	T_x	$\rho_{m_{1_x}}$	$\rho_{m_{2_y}}$	$\rho_{m_{2_z}}$
8 m/s - 5°	Y	Y	Y	N
8 m/s - 15°	Y	Y	Y	N
8 m/s - 25°	N	N	N	N
12 m/s - 5°	Y	Y	Y	N
12 m/s - 15°	Y	Y	Y	N
12 m/s - 25°	N	N	N	N
16 m/s - 5°	Y	Y	Y	N
16 m/s - 15°	Y	Y	Y	N
16 m/s - 25°	Y	Y	Y	N

replaced by constant values that are chosen to be slightly larger than the actual constraint limits. For example, T_x is between 0 and 10; T_x values larger than and equal to 11 are set to 11 and T_x values smaller than and equal to -1 are set to -1. This is done to be able to focus on regions where the feasible solution may exist.

Figure A.2 shows that required thrust is within its limits in a small interval on the positive-$\dot{\psi}$ branch. However, other control variables as shown is Figs. A.3-A.5 either do not fall within their respective limits, or there is only a singular value within the limits. This analysis confirms that there is no feasible solution for steady turn of the M-A aircraft with zero sideslip angle. This finding is consistent with the outcome of the $fsolve$ and $fmincon$ commands failing to find feasible solutions.

This analysis was repeated for different values of u_0 and ϕ_0 and is summarized in Tables A.2 and A.3. Since the bank angle, ϕ, is assigned as positive values for different cases, only the positive-$\dot{\psi}$ branch is investigated for consistency. The angle of attack values that the positive-$\dot{\psi}$ branch is close to are listed in Table A.2. Table A.3 indicates whether values for the control variables could be found within their limits along the positive-$\dot{\psi}$ branch. The tables reveal that vertical positioning of the laterally-moving mass cannot be achieved within its feasible limits. This again confirms that the M-A aircraft cannot have coordinated turn at constant altitude.

A.2 Turn with Zero Sideslip Angle When Altitude Changes for Mass-Actuated Airplane

In this section, results of case $T2$ as shown in Table A.1 are presented. Turn without sideslip angle is desired to avoid drag penalty that sideslip angle induces. Previous section showed that constant altitude steady turn with zero sideslip angle is not possible for the M-A aircraft. This section investigates whether steady turn with zero sideslip angle can be achieved if altitude is allowed to change, which is steady spiral flight. If a trim condition exists under these conditions, Eqs. (4.1)-(4.2) should be satisfied. This is investigated first by using $fsolve$ and $fmincon$ commands with the choice of six unknowns as T_x, α, $\dot{\psi}$, $\rho_{m_{1_x}}$, $\rho_{m_{2_y}}$ and θ with $\beta = 0$ and values of u_0 and ϕ specified. However, no solution was found, as was encountered in Section A.1. To rule out any numerical problem in $fsolve$ and $fmincon$ failing to find solution for the six unknowns in the six equations, Eqs. (4.1)-(4.2), this section attempts to solve the six equations analytically. The outcome of this attempt is to find solutions if exist, or to prove that there is no solution.

From the first equation of the translational dynamics in Eq. (4.1), T_x is solved in terms of the other five unknowns and two specified parameters

$$T_x = f_{TD1}(\rho_{m_{1_x}}, \rho_{m_{2_y}}, \theta, \alpha, \dot{\psi}, u_0, \phi) \tag{A.11}$$

The second equation of Eq. (4.1) gives $\rho_{m_{1_x}}$ as a function of θ, α, $\dot{\psi}$, u_0, ϕ as

$$\rho_{m_{1_x}} = f_{TD2}(\theta, \alpha, \dot{\psi}, u_0, \phi) \tag{A.12}$$

Similarly, the third equation gives $\rho_{m_{2_y}}$ as a function of θ, α, $\dot{\psi}$, u_0, ϕ as

$$\rho_{m_{2_y}} = f_{TD3}(\theta, \alpha, \dot{\psi}, u_0, \phi) \tag{A.13}$$

The first equation of the rotational dynamics in Eq. (4.2) yields a 4^{th} order polynomial of $\dot{\psi}$ with coefficients depending on θ, α, u_0, ϕ as

$$\dot{\psi}^4 + C_3(\theta, \alpha, u_0, \phi)\dot{\psi}^3 + C_2(\theta, \alpha, u_0, \phi)\dot{\psi}^2 + C_1(\theta, \alpha, u_0, \phi)\dot{\psi} + C_0(\theta, \alpha, u_0, \phi) = 0 \tag{A.14}$$

From the second and third equations of the rotational dynamics in Eq. (4.2), two nonlinear functions of θ, α, $\dot{\psi}$, u_0, ϕ are obtained as

$$0 = f_{RD2}(\theta, \alpha, \dot{\psi}, u_0, \phi) \tag{A.15}$$

$$0 = f_{RD3}(\theta, \alpha, \dot{\psi}, u_0, \phi) \tag{A.16}$$

Using the specified u_0 and ϕ, Eq. (A.14) is solved for turn rate, $\dot{\psi}$, with different θ and α. Each solution has 4 roots of Eq. (A.14). Among the four roots of the polynomial, solution yields one couple of complex numbers and two real numbers. One of the real numbers is too high for realistic case considered for the solution that is looked for. Thus, only the rest of real number can be the realistic. Using the turn rate found from Eq. (A.14) in Eqs. (A.15) and (A.16) results in two equations with two unknowns, θ and α. Even if this could be done, Eqs. (A.15)-(A.16) are too complicated to reduce them into a single equation with a single unknown. Therefore, these two equations in Eqs. (A.15) and (A.16) with the turn rate found in Eq. (A.14) are used to investigate feasible solution for spiral flight trim condition.

The numerical solutions of Eqs. (A.15) and (A.16) are sought in a domain of θ and α where θ is varied from -5 to 35 degrees and α is varied between -5 and 20 degrees. Intersection of zero isolines of f_{RD2} and f_{RD3} would give values of θ and α in a potential trim condition. These values of θ and α are used in Eqs. (A.11)-(A.13) to compute the corresponding values of T_x, $\rho_{m_{1_x}}$ and $\rho_{m_{2_y}}$. If the trim values of these control variables are within their feasible limits, the trim condition is proven to be a feasible one.

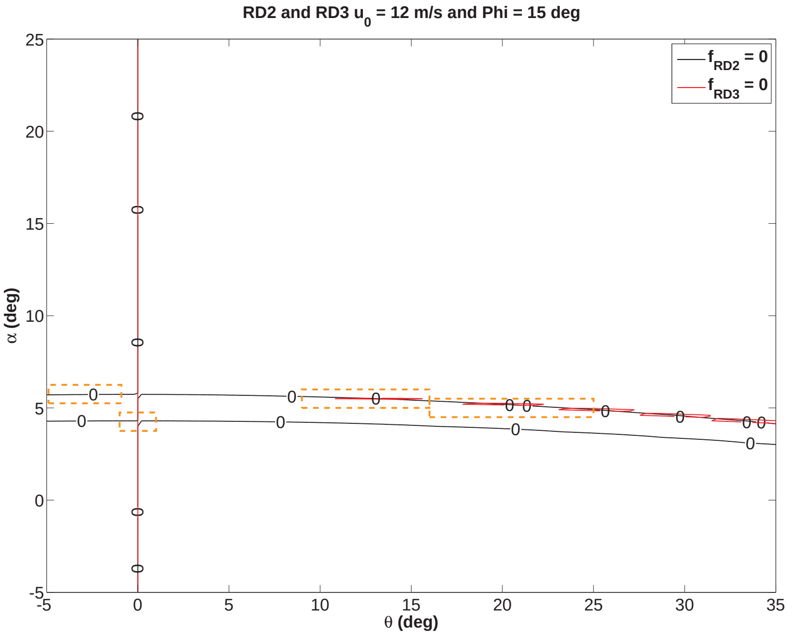

Figure A.6. The zero level curves in terms of $u_0 = 12\ m/s$ and $\phi = 15°$.

Figure A.6 shows an example of zero isolines of $f_{RD2}(\theta, \alpha, \dot{\psi})$ and $f_{RD3}(\theta, \alpha, \dot{\psi})$ when $u_0 = 12\ m/s$ and $\phi_0 = 15\ deg$. This figure shows that there might be some intersection points between $f_{RD2} = 0$ and $f_{RD3} = 0$ isolines. To better see whether there are intersection points and, if so, where they are, the regions indicated with dashed-lines are zoomed in and the isolines are redrawn with finer resolutions. Figs. A.7-A.10 show these regions. Fig. A.7 show that there are three intersection points in this region, which are potential trim conditions. To confirm whether these points indicate feasible trim conditions, the control variables should be evaluated by Eqs. (A.11), (A.12) and (A.13). This analysis reveals that $\rho_{m_{1_x}}$ is within its limits while

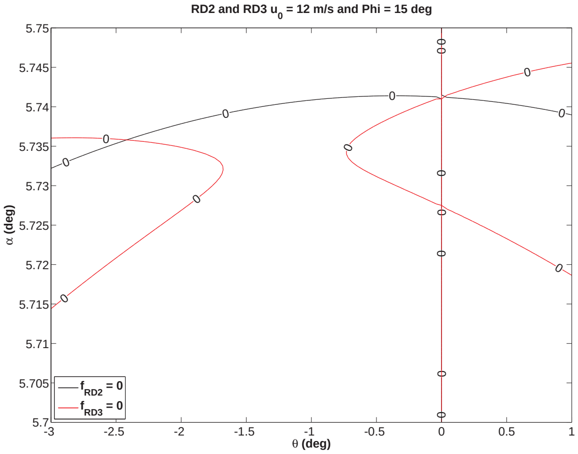

Figure A.7. Region 1 for candidate trim point.

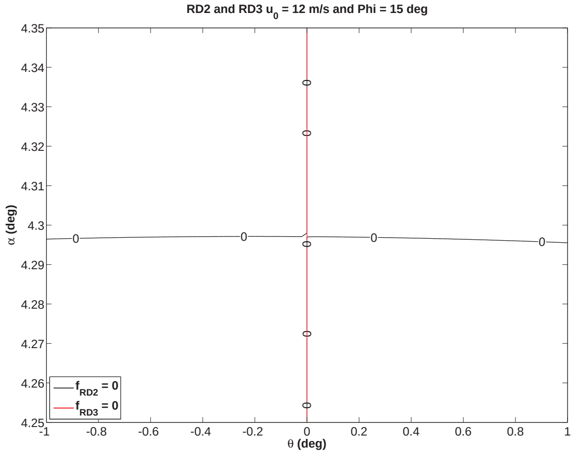

Figure A.8. Region 2 for candidate trim point.

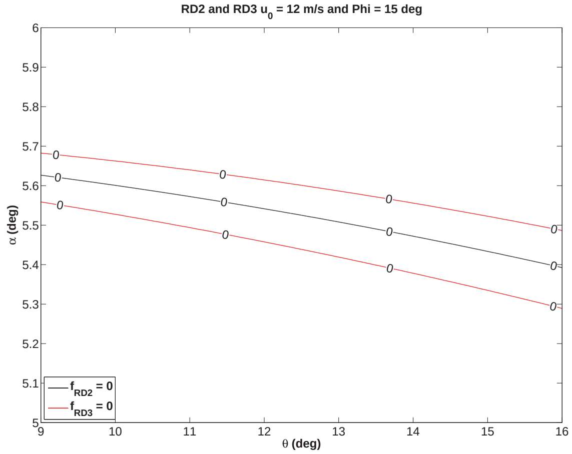

Figure A.9. Region 3 for candidate trim point.

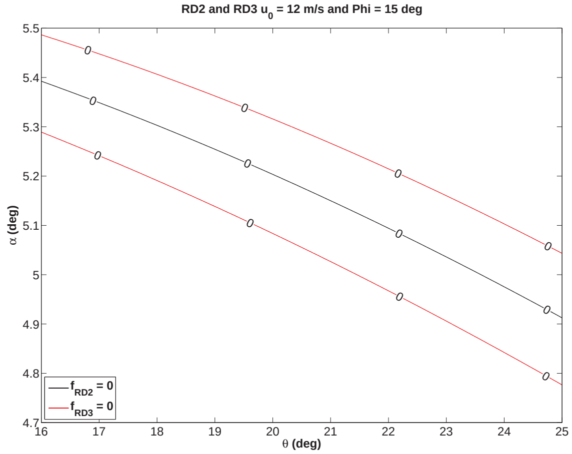

Figure A.10. Region 4 for candidate trim point.

$\rho_{m_{2_y}}$ and T_x are not. Thus, these three points cannot be feasible trim conditions. Fig. A.8 shows another intersection point of the isolines in the second region. The evaluation of the control variables at this points reveals that this point cannot be a trim point because $\rho_{m_{1_x}}$ and $\rho_{m_{2_y}}$ are not within their respective limits although T_x is. Figs. A.9 and A.10 show no intersection points and thus no potential trim condition.

In summary, it is proven that there is no feasible trim possible for $u_0 = 12\ m/s$ and $\phi_0 = 15\ deg$.

Table A.4. Yaw rate, $\dot{\psi}$, in deg/s for specified u_0 and ϕ_0

$u_0 \setminus \phi_0$	5°	15°	25°
$9\ m/s$	5.3540	16.3823	28.4436
$12\ m/s$	4.0640	12.4439	17.6624
$15\ m/s$	3.2632	9.9926	17.3815

Table A.5. Indicator if control variables are within limits (Y = Yes, N = No)

	Region 1			Region 2		
u_0 - ϕ_0	T_x	$\rho_{m_{1_x}}$	$\rho_{m_{2_y}}$	T_x	$\rho_{m_{1_x}}$	$\rho_{m_{2_y}}$
$9\ m/s$ - 5°	N	Y	N	N	N	N
$9\ m/s$ - 15°	N	Y	N	N	N	N
$9\ m/s$ - 25°	N	Y	N	Y	N	N
$12\ m/s$ - 5°	N	Y	N	Y	N	N
$12\ m/s$ - 15°	N	Y	N	Y	N	N
$12\ m/s$ - 25°	Y	N	N	Y	N	N
$15\ m/s$ - 5°	Y	Y	N	Y	N	N
$15\ m/s$ - 15°	Y	Y	N	Y	N	N
$15\ m/s$ - 25°	Y	Y	N	Y	N	N

This analysis is repeated for different u_0 and ϕ_0 values to check whether there are feasible trim points in different flight conditions. The results of nine such analyses are summarized in Tables A.4 and A.5. The real yaw rate computed by Eq. (A.14) for an intersection point in nine conditions are given in Table A.4. Table A.5 indicates whether the control variables are within their respective limits at the intersection points. For any intersection point to be a feasible trim condition, all three control variables should be within their respective limits. Since there is no such point found among the conditions investigated herein, it is safe to conclude that the M-A aircraft cannot have zero sideslip steady turn even if the altitude is allowed to vary.

A.3 Turn with Sideslip Angle at Constant Altitude for Mass-Actuated Airplane

In this section, results of case $T3$ as shown in Table A.1 are presented. Trimming the mass-actuated airplane for steady-state turn is investigated by letting β vary while setting $\rho_{m_{2_z}} = 0$ as opposed to Section A.1. The results of the trim analyses and the comparisons between the M-A and A-A aircraft are also presented in this subsection.

In Eqs. (4.1)-(4.2), there are 6 equations with 21 unknowns: V, β, α, p, q, r, θ, ϕ, $\dot{\psi}$, T_x, m_1, m_2, $\rho_{m_{1_x}}$, $\rho_{m_{1_y}}$, $\rho_{m_{1_z}}$, $\rho_{m_{2_x}}$, $\rho_{m_{2_y}}$, $\rho_{m_{2_z}}$, δ_e, δ_a and δ_r. To solve these equations, the number of unknowns should be reduced to six, which means the remaining ones should be specified. The trim analysis will be performed in two main cases: (1) For an A-A airplane, with control surfaces and no moving-masses, the unknowns will be T_x, α, ϕ, δ_e, δ_a and δ_r for specified V, $\dot{\psi}$ when there is no sideslip, β. (2) For an airplane with moving-mass actuation, the unknowns are selected to be T_x, α, ϕ, $\rho_{m_{1_x}}$, $\rho_{m_{2_y}}$ and β for specified V, $\dot{\psi}$, m_1, m_2. Furthermore, to simplify the analysis, y and z positions of longitudinal moving-mass are set to zero, $\rho_{m_{1_y}} = 0$, $\rho_{m_{1_z}} = 0$. Also, there assumed to be no motion in x and z directions for the lateral moving-mass, $\rho_{m_{2_x}} = 0$, $\rho_{m_{2_z}} = 0$.

Figures A.11-A.16 present a comparative analysis of the trim results of the A-A aircraft turning with zero sideslip angle and the M-A aircraft turning with some sideslip angle. The trim results are presented for airspeed ranging from 7 m/s to 20 m/s with three different yaw rates, $\dot{\psi} = 5, 10, 15$ deg/s. Only the results within their respective constraints are plotted.

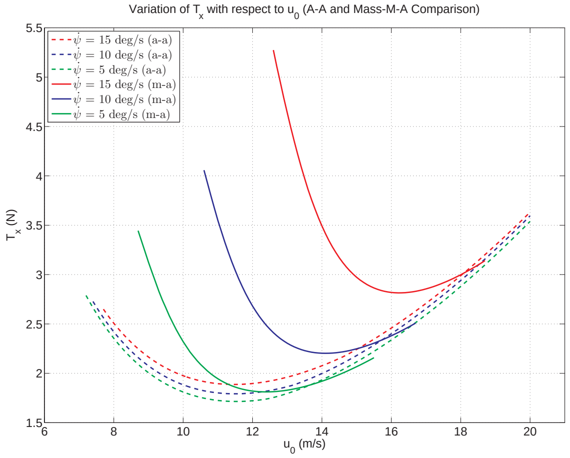

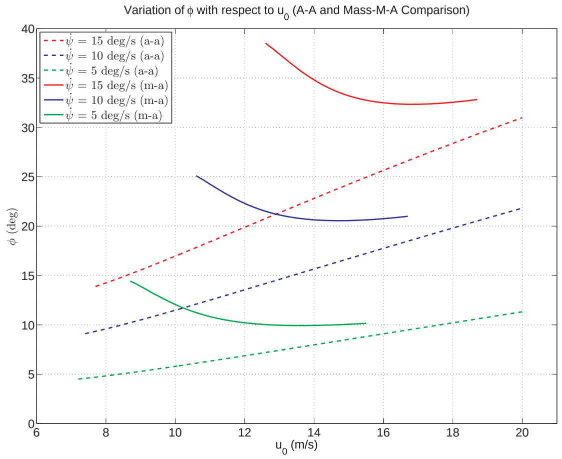

Figure A.11. Comparison of required thrust with respect to u_0.

Figure A.12. Comparison of ϕ with respect to u_0.

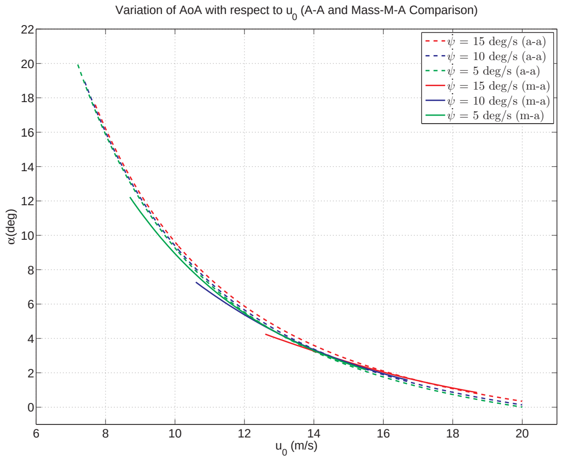

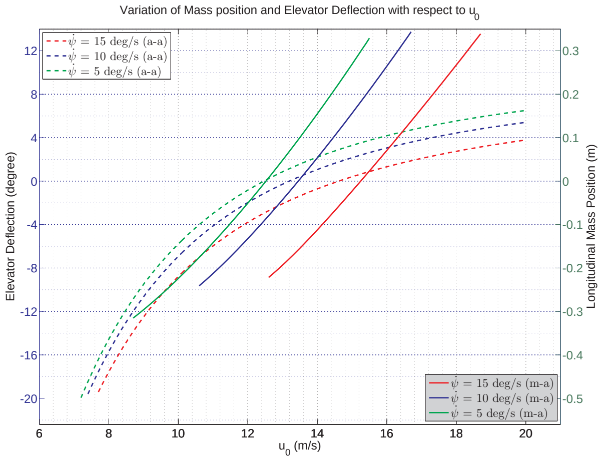

Figure A.13. Comparison of AoA with respect to u_0.

Figure A.14. Comparison between $\rho_{m_{1_x}}$ and δ_e with respect to u_0.

The first observation from the figures is the difference in the airspeed ranges in which steady-turn is feasible within the constraints on the control variables. The A-A aircraft can have steady-turns within a larger airspeed range for all three turn rates considered. There are speeds too fast and too slow for the M-A aircraft to make steady turn while the A-A aircraft can. The M-A aircraft can make turns at higher airspeed with higher turn rates and at lower airspeed with smaller turn rates. The

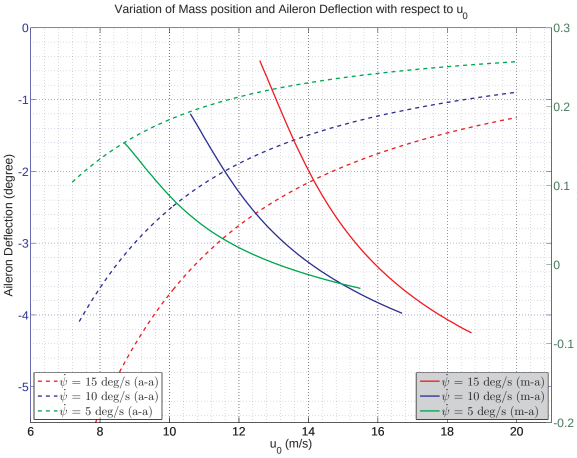

Figure A.15. Comparison between $\rho_{m_{2_y}}$ and δ_a with respect to u_0.

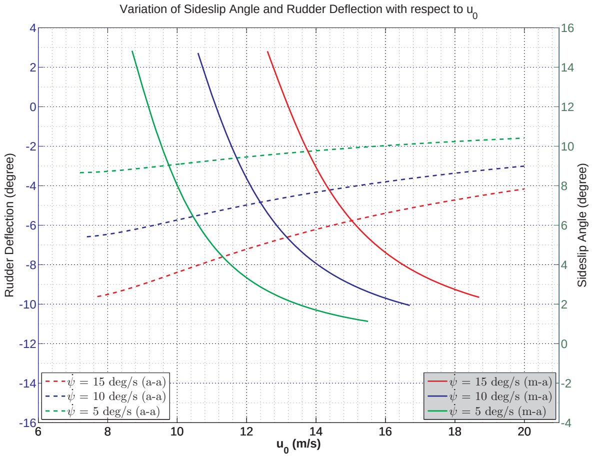

Figure A.16. Comparison between β and δ_r with respect to u_0.

A-A aircraft, on the other hand, does not need to lower its speed for shallow turns or to increase its speed for sharp turns. The upper limit of the speed range for the M-A aircraft is due to the longitudinally-moving mass reaching its forward position limit at $x = 0.35\ m$ for all turn rates, as seen in Fig. A.14. The upper speed limit of the A-A aircraft is due to upper bound on the angle-of-attack set at 20 deg, as can be seen in Fig. A.13. The lower speed limit for the M-A aircraft is caused by the upper limit for the sideslip angle set at 15 deg as shown in Fig. A.16. The A-A aircraft has lower speed limit because the elevator saturates at its lower bound at -20 deg, as seen in Fig.

As seen in Fig. A.11, with both A-A and M-A airplane, sharper turns (i.e., higher yaw rate, $\dot{\psi}$) require more thrust. However, the M-A aircraft require much greater thrust increase for the same amount of yaw rate increase, especially with low airspeeds. For the same turn rate and airspeed, the required thrust is higher with the M-A aircraft than with the A-A aircraft in the low speed range. It is the opposite for high speeds. For example, M-A aircraft turning with $\dot{\psi} = 5\ deg/s$ requires more thrust when speed is less than 12.6 m/s than the A-A aircraft does. But, when the speed is greater than 12.6 m/s, the M-A aircraft requires less thrust.

Figure A.12 shows that the M-A airplane needs to bank more than the A-A airplane does to achieve the same yaw rate throughout the whole speed range. This is because the M-A aircraft turns with sideslip angle while the A-A aircraft turns with no sideslip. The M-A aircraft needs smaller bank angle for higher airspeed with the same turn rate while the trend with the A-A aircraft is just the opposite.

Figure A.14 shows the trim values of the elevator deflection for the A-A aircraft and of the longitudinal mass position for the M-A aircraft. For low speeds with any turn rate, the longitudinal mass is placed behind the origin of the body frame of the aircraft. As more speed is desired for the same turn rate, the mass should be placed closer to the nose. As the speed increases, the position of the mass moves in front of the cm. Lower yaw rate turn at a given trim speed requires more forward position for the longitudinal mass.

Figure A.15 shows aileron deflections for the A-A aircraft and position of the lateral mass for the M-A aircraft. At low speeds for any constant positive turn rate, the lateral mass should be placed on the right side. For any constant yaw rate, as higher speed is desired, the lateral mass should move to the left. Faster than a certain speed, the lateral mass should be placed on the left although the airplane turns right. In the low speed range, for a given speed, higher turn rate requires the mass to be placed further to the right. As the speed increases, the displacement to the right decreases and the trend is reversed between $\dot{\psi} = 5$ and 10 deg/s for high speed.

Figure A.16 shows the rudder deflection for A-A aircraft and sideslip angle for the M-A aircraft. With any turn rate, low speed turns require greater sideslip angle. As the speed increases, smaller sideslip angle is needed. At a given speed, the higher the turn rate, the greater the sideslip angle.

A.4 Turn with Zero Sideslip Angle at Constant Altitude for Mass-Actuated Airplane Augmented with Rudder

In this section, results of case $T4$ as shown in Table A.1 are presented. The trim analysis of mass-actuated aircraft augmented with rudder (MRA aircraft) is presented and compared with that of the A-A aircraft, with three sets of control surfaces. Rudder deflection is considered for aircraft with mass-actuation to generate yawing moment in addition to mass-actuators in steady-state turn with zero sideslip angle at constant altitude.

In Eqs. (4.1)-(4.2), there are 6 equations with 21 unknowns: V, β, α, p, q, r, θ, ϕ, $\dot{\psi}$, T_x, m_1, m_2, $\rho_{m_{1_x}}$, $\rho_{m_{1_y}}$, $\rho_{m_{1_z}}$, $\rho_{m_{2_x}}$, $\rho_{m_{2_y}}$, $\rho_{m_{2_z}}$, δ_e, δ_a and δ_r. To solve these equations, the number of unknowns should be reduced to six, which means the remaining ones should be specified. Furthermore, to simplify the analysis, y and z positions of longitudinal moving-mass are set to zero, $\rho_{m_{1_y}} = 0$, $\rho_{m_{1_z}} = 0$. Also, there assumed to be no motion in x and z directions for the lateral moving-mass, $\rho_{m_{2_x}} = 0$, $\rho_{m_{2_z}} = 0$. Trim analysis for turning is done with both the A-A and MRA aircraft: (1) For the A-A airplane, with control surfaces and no moving-masses, the unknowns will be T_x, α, ϕ, δ_e, δ_a and δ_r for specified V, $\dot{\psi}$. (2) For a moving-mass actuated airplane augmented with rudder, δ_r, as a control surface in steady level turn, the unknowns will be T_x, α, ϕ, $\rho_{m_{1_x}}$, $\rho_{m_{2_y}}$ and δ_r for specified V, $\dot{\psi}$, m_1, and m_2 when there is no sideslip, $\beta = 0$.

Figures A.17-A.22 present a comparative analysis of the trim results of the A-A aircraft and the MRA aircraft turning with zero sideslip angle. Moreover, endurance differences are calculated for comparison in Fig. A.23. The trim results are presented for airspeed ranging from 7 m/s to 20 m/s with three different yaw rates, $\dot{\psi} = 5, 10, 15$ deg/s. Only the results within their respective constraints are plotted.

Figure A.17 shows that both A-A and MRA aircraft require more thrust for sharper turn in the whole speed range. Feasible speed range for the MRA aircraft is shorter, especially in the high speed range. This means the MRA aircraft cannot make as high-speed turns as the A-A aircraft does at the same turn rate. For both aircraft, the required thrust has a minimum at the same speed. The most important observation from Fig. A.17 is that the MRA aircraft requires less thrust than the A-A aircraft does in the whole speed range and with all turn rates. This indicates that the mass-actuation still provides drag benefit even if rudder is used over the A-A aircraft.

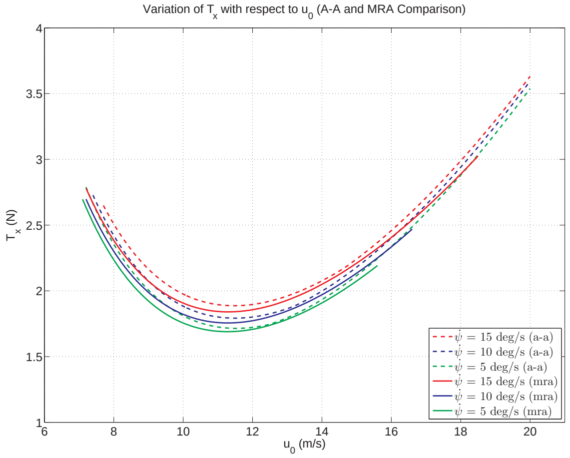

Figure A.17. Comparison of required thrust with respect to u_0.

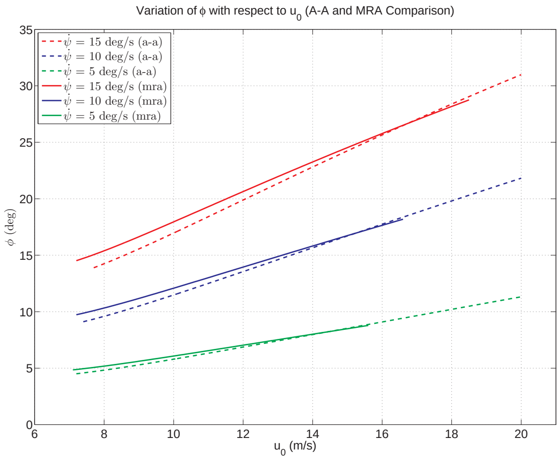

Figure A.18. Comparison of ϕ with respect to u_0.

Figure A.18 shows the trim bank angle variation with speed for three yaw rates. With a given turn rate, more bank angle is required for higher speed for both aircraft. However, the A-A aircraft requires less bank than the MRA aircraft does throughout almost all feasible speed range. The bank angle variation has higher slope for the A-A aircraft and as a result the MRA aircraft bank angle is the same and slightly lower than that of the A-A aircraft in the high end of the feasible speed range.

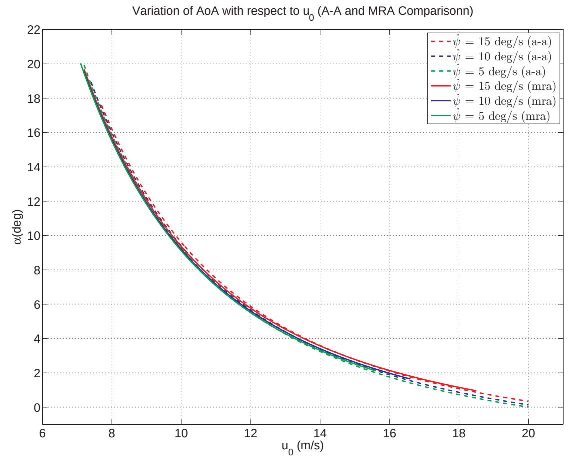

Figure A.19. Comparison of AoA with respect to u_0.

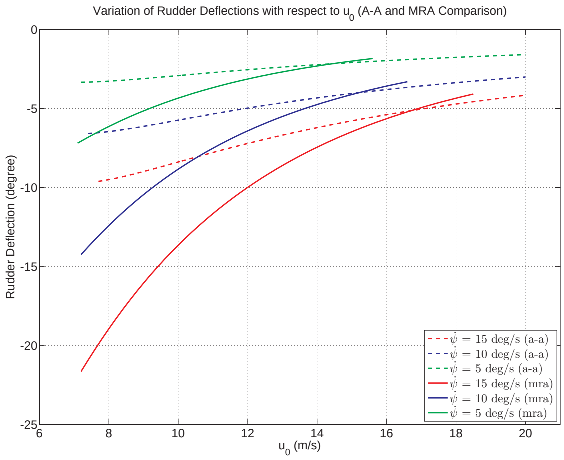

Figure A.20. Comparison of δ_r with respect to u_0.

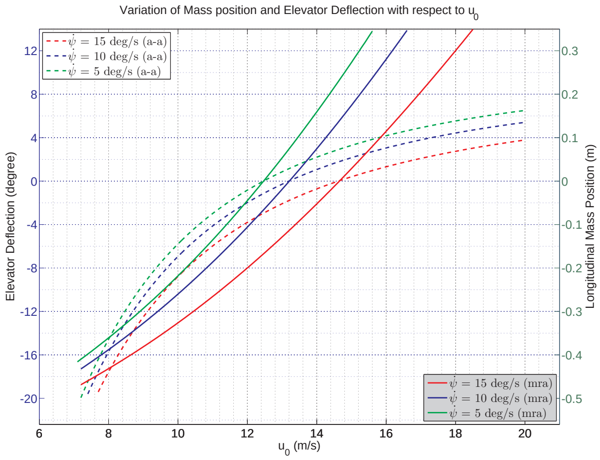

Figure A.21. Comparison between $\rho_{m_{1_x}}$ and δ_e with respect to u_0.

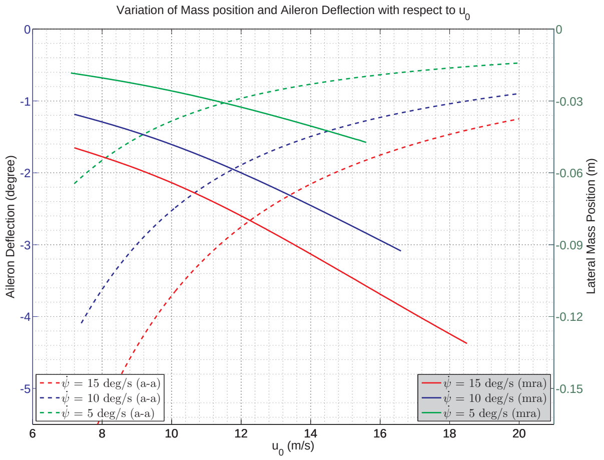

Figure A.22. Comparison between $\rho_{m_{2_y}}$ and δ_a with respect to u_0.

The variation of angle of attack are shown in Fig. A.19. For both aircraft, the trim angle of attack decreases with increasing speed. For low speed, the A-A aircraft has slightly higher angle of attack while the MRA aircraft flies with slightly higher angle in high speeds.

Figure A.20 shows that for low airspeed, MRA aircraft requires larger rudder deflection. Rudder deflection difference between the two aircraft becomes smaller

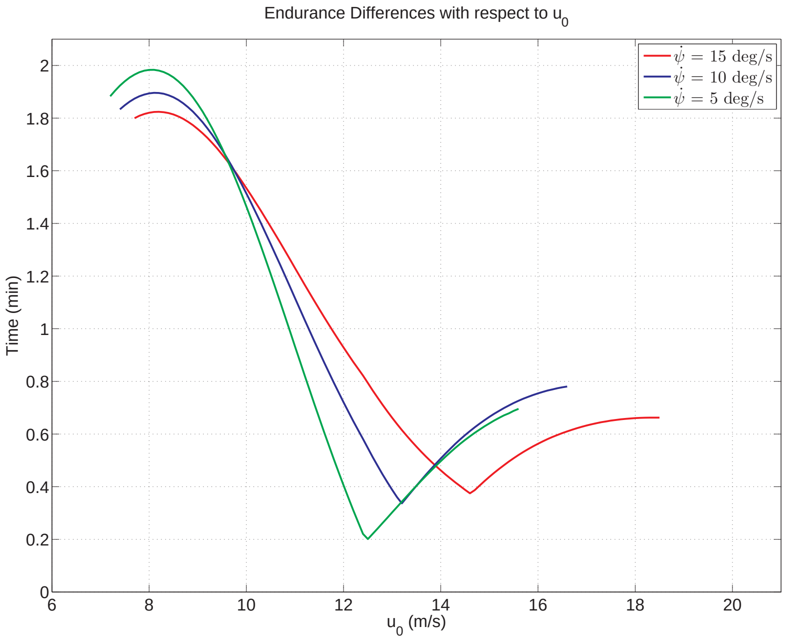

Figure A.23. Endurance differences with respect to u_0.

with increasing airspeed. Only for small speed range closer to maximum feasible speed, the A-A aircraft needs more rudder deflection.

Figure A.21 shows the trim values of the elevator deflection for the A-A aircraft and of the longitudinal mass position for the MRA aircraft. With each turn rate considered, for lower speeds, the longitudinal mass is placed behind the center of mass of the aircraft. As more speed is desired for the same turn rate, the mass should more further towards the nose. Beyond certain speed, the position of the mass moves in front of the center of mass of the aircraft. The lower the yaw rate at a given trim speed, the more forward position for the longitudinal mass is required. Moreover, at a certain trim airspeed for each yaw rate, no elevator deflection or longitudinal mass position is needed since there is no pitching moment induced at that condition, for example, at airspeed of 14.7 m/s when the turn rate is 15 deg/s.

Figure A.22 shows aileron deflections for the A-A aircraft and position of the lateral mass for the MRA aircraft. For sharper turn with the MRA aircraft, larger mass displacement is required.

Figure A.17 showed that the MRA aircraft with employment of rudder for zero sideslip turn requires lower thrust in turns throughout the whole feasible speed range. Fig. A.23 show the endurance difference between the A-A and MRA aircraft. The MRA aircraft can stay longer in air while turning than the A-A aircraft does in the whole feasible speed ranges with all three turn rates considered. The maximum endurance benefit is seen at low speed with all three turn rates. The endurance benefit drops to its lowest in the middle of the speed range.

APPENDIX B

LINEARIZED MATRICES IN THE STATE-SPACE EQUATIONS

In this appendix, the elements of linearized matrices in the state-space equations in Eqs. (5.6) and (5.7) are presented. In the equations, j represents the number of mass-actuators to give a general statement of the equations. In this dissertation, two mass-actuators are considered. Hence, $j = \{1, 2\}$ in all linearized equations.

B.1 Linearized Matrix A_0

The matrix $\mathbf{A_0}$ is defined as

$$\mathbf{A_0} = A_0(i,k), \quad \mathbf{A_0} \in \mathbb{R}^{14\times 14} \quad i = \{1,..,14\}, k = \{1,..,14\}$$

The elements of $\mathbf{A_0}$ are presented below.

$$A_0(1,1) = r_0 \sin\beta_0 - q_0 \cos\beta_0 \sin\alpha_0$$

$$A_0(1,2) = V_0(r_0 \cos\beta_0 + q_0 \sin\beta_0 \sin\alpha_0)$$

$$A_0(1,3) = -V_0 q_0 \cos\beta_0 \cos\alpha_0$$

$$A_0(1,4) = -\frac{1}{m_T}\sum_{j=1}^{k} m_j(q_0\rho_{m_{jy}} + r_0\rho_{m_{jz}})$$

$$A_0(1,5) = -V_0 \cos\beta_0 \sin\alpha_0 - \frac{1}{m_T}\sum_{j=1}^{k} m_j(2\dot{\rho}_{m_{jz}} + p_0\rho_{m_{jy}} - 2q_0\rho_{m_{jx}})$$

$$A_0(1,6) = V_0 \sin\beta_0 - \frac{1}{m_T}\sum_{j=1}^{k} m_j(-2\dot{\rho}_{m_{jy}} + p_0\rho_{m_{jz}} - 2r_0\rho_{m_{jx}})$$

$$A_0(1,7) = 0$$

$$A_0(1,8) = -g\cos\theta_0$$

$$A_0(1,9) = 0$$

$$A_0(1,10:14) = 0$$

$$A_0(2,1) = p_0 \cos\beta_0 \sin\alpha_0 - r_0 \cos\beta_0 \cos\alpha_0$$

$$A_0(2,2) = V_0(-p_0 \sin\beta_0 \sin\alpha_0 + r_0 \sin\beta_0 \cos\alpha_0)$$

$$A_0(2,3) = V_0(p_0 \cos\beta_0 \cos\alpha_0 + r_0 \cos\beta_0 \sin\alpha_0)$$

$$A_0(2,4) = V_0 \cos\beta_0 \sin\alpha_0 - \frac{1}{m_T}\sum_{j=1}^{k} m_j(-2\dot{\rho}_{m_{jz}} - 2p_0\rho_{m_{jy}} + q_0\rho_{m_{jx}})$$

$$A_0(2,5) = -\frac{1}{m_T}\sum_{j=1}^{k} m_j(p_0\rho_{m_{jx}} + r_0\rho_{m_{jz}})$$

$$A_0(2,6) = -V_0 \cos\beta_0 \cos\alpha_0 - \frac{1}{m_T}\sum_{j=1}^{k} m_j(2\dot{\rho}_{m_{jx}} + q_0\rho_{m_{jz}} - 2r_0\rho_{m_{jy}})$$

$$A_0(2,7) = 0$$

$$A_0(2,8) = -g\sin\theta_0\sin\phi_0$$

$$A_0(2,9) = g\cos\theta_0\cos\phi_0$$

$$A_0(2,10:14) = 0$$

$$A_0(3,1) = q_0\cos\beta_0\cos\alpha_0 - p_0\sin\beta_0$$

$$A_0(3,2) = -V_0(q_0\sin\beta_0\cos\alpha_0 + p_0\cos\beta_0)$$

$$A_0(3,3) = -V_0 q_0\cos\beta_0\sin\alpha_0$$

$$A_0(3,4) = -V_0\sin\beta_0 - \frac{1}{m_T}\sum_{j=1}^{k} m_j(2\dot{\rho}_{m_{j_y}} - 2p_0\rho_{m_{j_z}} + r_0\rho_{m_{j_x}})$$

$$A_0(3,5) = V_0\cos\beta_0\cos\alpha_0 - \frac{1}{m_T}\sum_{j=1}^{k} m_j(-2\dot{\rho}_{m_{j_x}} - 2q_0\rho_{m_{j_z}} + r_0\rho_{m_{j_y}})$$

$$A_0(3,6) = -\frac{1}{m_T}\sum_{j=1}^{k} m_j(p_0\rho_{m_{j_x}} + q_0\rho_{m_{j_y}})$$

$$A_0(3,7) = 0$$

$$A_0(3,8) = -g\sin\theta_0\cos\phi_0$$

$$A_0(3,9) = -g\cos\theta_0\sin\phi_0$$

$$A_0(3,10:14) = 0$$

$$A_0(4,1) = \sum_{j=1}^{k} m_j\Big(\rho_{m_{j_z}}(r_0\cos\beta_0\cos\alpha_0 - p_0\cos\beta_0\sin\alpha_0) - \rho_{m_{j_y}}(p_0\sin\beta_0 - q_0\cos\beta_0\cos\alpha_0)\Big)$$

$$A_0(4,2) = V_0\sum_{j=1}^{k} m_j\Big(\rho_{m_{j_z}}(-r_0\sin\beta_0\cos\alpha_0 + p_0\sin\beta_0\sin\alpha_0) - \rho_{m_{j_y}}(p_0\cos\beta_0 + q_0\sin\beta_0\cos\alpha_0)\Big)$$

$$A_0(4,3) = V_0\sum_{j=1}^{k} m_j\Big(\rho_{m_{j_z}}(-r_0\cos\beta_0\sin\alpha_0 - p_0\cos\beta_0\cos\alpha_0) - \rho_{m_{j_y}}(q_0\cos\beta_0\sin\alpha_0)\Big)$$

$$\begin{aligned} A_0(4,4) = {} & (I_{xz}q_0 - I_{xy}r_0) + \sum_{j=1}^{k} m_j\Bigg\{(q_0\rho_{m_{j_x}}\rho_{m_{j_z}} - r_0\rho_{m_{j_x}}\rho_{m_{j_y}}) \\ & + V_0(-\rho_{m_{j_z}}\cos\beta_0\sin\alpha_0 - \rho_{m_{j_y}}\sin\beta_0) - 2(\dot{\rho}_{m_{j_y}}\rho_{m_{j_y}} + \dot{\rho}_{m_{j_z}}\rho_{m_{j_z}})\Bigg\} \end{aligned}$$

$$\begin{aligned} A_0(4,5) = {} & \Big(I_{xz}p_0 + 2I_{yz}q_0 + (I_{yy} - I_{zz})r_0\Big) + \sum_{j=1}^{k} m_j\Bigg\{\Big(\rho_{m_{j_z}}(p_0\rho_{m_{j_x}} + 2q_0\rho_{m_{j_y}} + r_0\rho_{m_{j_z}}) - r_0\rho_{m_{j_y}}^2\Big) \\ & + \rho_{m_{j_y}}V_0\cos\beta_0\cos\alpha_0 + 2\dot{\rho}_{m_{j_x}}\rho_{m_{j_y}}\Bigg\} \end{aligned}$$

$$\begin{aligned} A_0(4,6) = {} & \Big(-I_{xy}p_0 + (I_{yy} - I_{zz})q_0 - 2I_{yz}r_0\Big) + \sum_{j=1}^{k} m_j\Bigg\{\Big(-\rho_{m_{j_y}}(p_0\rho_{m_{j_x}} + q_0\rho_{m_{j_y}} + 2r_0\rho_{m_{j_z}}) + q_0\rho_{m_{j_z}}^2\Big) \\ & + \rho_{m_{j_z}}V_0\cos\beta_0\cos\alpha_0 + 2\dot{\rho}_{m_{j_x}}\rho_{m_{j_z}}\Bigg\} \end{aligned}$$

$$A_0(4,7) = 0$$

$$A_0(4,8) = -g\sum_{j=1}^{k} m_j(-\rho_{m_{j_y}}\sin\theta_0\cos\phi_0 + \rho_{m_{j_z}}\sin\theta_0\sin\phi_0)$$

$$A_0(4,9) = -g\sum_{j=1}^{k} m_j(-\rho_{m_{j_y}}\cos\theta_0\sin\phi_0 - \rho_{m_{j_z}}\cos\theta_0\cos\phi_0)$$

$$A_0(4,10:14) = 0$$

$$A_0(5,1) = \sum_{j=1}^{k} m_j\Big(\rho_{m_{j_x}}(p_0\sin\beta_0 - q_0\cos\beta_0\cos\alpha_0) + \rho_{m_{j_z}}(r_0\sin\beta_0 - q_0\cos\beta_0\sin\alpha_0)\Big)$$

$$A_0(5,2) = V_0\sum_{j=1}^{k} m_j\Big(\rho_{m_{j_x}}(p_0\cos\beta_0 + q_0\sin\beta_0\cos\alpha_0) + \rho_{m_{j_z}}(r_0\cos\beta_0 + q_0\sin\beta_0\sin\alpha_0)\Big)$$

$$A_0(5,3) = V_0\sum_{j=1}^{k} m_j\Big(\rho_{m_{j_x}}(q_0\cos\beta_0\sin\alpha_0) - \rho_{m_{j_z}}(q_0\cos\beta_0\cos\alpha_0)\Big)$$

$$\begin{aligned} A_0(5,4) = {} & \Big(-2I_{xz}p_0 - I_{yz}q_0 + (I_{zz}-I_{xx})r_0\Big) + \sum_{j=1}^{k} m_j\Bigg\{\Big(r_0\rho^2_{m_{j_x}} - \rho_{m_{j_z}}(2p_0\rho_{m_{j_x}} + q_0\rho_{m_{j_y}} + r_0\rho_{m_{j_z}})\Big) \\ & + \rho_{m_{j_x}}V_0\sin\beta_0 + 2\dot{\rho}_{m_{j_y}}\rho_{m_{j_x}}\Bigg\} \end{aligned}$$

$$\begin{aligned} A_0(5,5) = {} & (-I_{yz}p_0 + I_{xy}r_0) + \sum_{j=1}^{k} m_j\Bigg\{(r_0\rho_{m_{j_x}}\rho_{m_{j_y}} - p_0\rho_{m_{j_y}}\rho_{m_{j_z}}) \\ & + V_0(-\rho_{m_{j_x}}\cos\beta_0\cos\alpha_0 - \rho_{m_{j_z}}\cos\beta_0\sin\alpha_0) - 2(\dot{\rho}_{m_{j_x}}\rho_{m_{j_x}} + \dot{\rho}_{m_{j_z}}\rho_{m_{j_z}})\Bigg\} \end{aligned}$$

$$\begin{aligned} A_0(5,6) = {} & \Big((I_{zz}-I_{xx})p_0 + I_{xy}q_0 + 2I_{xz}r_0\Big) + \sum_{j=1}^{k} m_j\Bigg\{\Big(-p_0\rho^2_{m_{j_z}} + \rho_{m_{j_x}}(p_0\rho_{m_{j_x}} + q_0\rho_{m_{j_y}} + 2r_0\rho_{m_{j_z}})\Big) \\ & + \rho_{m_{j_z}}V_0\sin\beta_0 + 2\dot{\rho}_{m_{j_y}}\rho_{m_{j_z}}\Bigg\} \end{aligned}$$

$$A_0(5,7) = 0$$

$$A_0(5,8) = g\sum_{j=1}^{k} m_j(-\rho_{m_{j_z}}\cos\theta_0 + \rho_{m_{j_x}}\sin\theta_0\cos\phi_0)$$

$$A_0(5,9) = g\sum_{j=1}^{k} m_j(\rho_{m_{j_x}}\cos\theta_0\sin\phi_0)$$

$$A_0(5,10:14) = 0$$

$$A_0(6,1) = \sum_{j=1}^{k} m_j\Big(\rho_{m_{j_y}}(-r_0\sin\beta_0 + q_0\cos\beta_0\sin\alpha_0) - \rho_{m_{j_x}}(r_0\cos\beta_0\cos\alpha_0 - p_0\cos\beta_0\sin\alpha_0)\Big)$$

$$A_0(6,2) = V_0\sum_{j=1}^{k} m_j\Big(\rho_{m_{j_y}}(-r_0\cos\beta_0 - q_0\sin\beta_0\sin\alpha_0) - \rho_{m_{j_x}}(-r_0\sin\beta_0\cos\alpha_0 + p_0\sin\beta_0\sin\alpha_0)\Big)$$

$$A_0(6,3) = V_0\sum_{j=1}^{k} m_j\Big(\rho_{m_{j_y}}(q_0\cos\beta_0\cos\alpha_0) + \rho_{m_{j_x}}(r_0\cos\beta_0\sin\alpha_0 + p_0\cos\beta_0\cos\alpha_0)\Big)$$

$$\begin{aligned} A_0(6,4) = {} & \Big(2I_{xy}p_0 + (I_{xx}-I_{yy})q_0 + I_{yz}r_0\Big) + \sum_{j=1}^{k} m_j\Bigg\{\Big(-q_0\rho^2_{m_{j_x}} + \rho_{m_{j_y}}(2p_0\rho_{m_{j_x}} + q_0\rho_{m_{j_y}} + r_0\rho_{m_{j_z}})\Big) \\ & + \rho_{m_{j_x}}V_0\cos\beta_0\sin\alpha_0 + 2\dot{\rho}_{m_{j_z}}\rho_{m_{j_x}}\Bigg\} \end{aligned}$$

$$\begin{aligned}
A_0(6,5) &= \Big((I_{xx} - I_{yy})p_0 - 2I_{xy}q_0 - I_{xz}r_0\Big) + \sum_{j=1}^{k} m_j \Bigg\{ \Big(p_0\rho_{m_{j_y}}^2 - \rho_{m_{j_x}}(p_0\rho_{m_{j_x}} + 2q_0\rho_{m_{j_y}} + r_0\rho_{m_{j_z}})\Big) \\
&\quad + \rho_{m_{j_y}} V_0 \cos\beta_0 \sin\alpha_0 + 2\dot{\rho}_{m_{j_z}}\rho_{m_{j_y}} \Bigg\}
\end{aligned}$$

$$\begin{aligned}
A_0(6,6) &= (I_{yz}p_0 - I_{xz}q_0) + \sum_{j=1}^{k} m_j \Bigg\{ (p_0\rho_{m_{j_y}}\rho_{m_{j_z}} - q_0\rho_{m_{j_x}}\rho_{m_{j_z}}) \\
&\quad + V_0(-\rho_{m_{j_y}} \sin\beta_0 - \rho_{m_{j_x}} \cos\beta_0 \cos\alpha_0) - 2(\dot{\rho}_{m_{j_x}}\rho_{m_{j_x}} + \dot{\rho}_{m_{j_y}}\rho_{m_{j_y}}) \Bigg\}
\end{aligned}$$

$$A_0(6,7) = 0$$

$$A_0(6,8) = g\sum_{j=1}^{k} m_j(\rho_{m_{j_y}} \cos\theta_0 - \rho_{m_{j_x}} \sin\theta_0 \sin\phi_0)$$

$$A_0(6,9) = g\sum_{j=1}^{k} m_j(\rho_{m_{j_x}} \cos\theta_0 \cos\phi_0)$$

$$A_0(6,10:14) = 0$$

$$A_0(7,1:4) = 0$$

$$A_0(7,5) = \frac{\sin\phi_0}{\cos\theta_0}$$

$$A_0(7,6) = \frac{\cos\phi_0}{\cos\theta_0}$$

$$A_0(7,7) = 0$$

$$A_0(7,8) = \frac{\sin\theta_0(q_0\sin\phi_0 + r_0\cos\phi_0)}{\cos\theta_0^2}$$

$$A_0(7,9) = \frac{(q_0\cos\phi_0 - r_0\sin\phi_0)}{\cos\theta_0}$$

$$A_0(7,10:14) = 0$$

$$A_0(8,1:4) = 0$$

$$A_0(8,5) = \cos\phi_0$$

$$A_0(8,6) = -\sin\phi_0$$

$$A_0(8,7) = 0$$

$$A_0(8,8) = 0$$

$$A_0(8,9) = -q_0\sin\phi_0 - r_0\cos\phi_0$$

$$A_0(8,10:14) = 0$$

$$A_0(9,1:4) = 0$$

$$A_0(9,5) = \sin\phi_0\tan\theta_0$$

$$A_0(9,6) = \cos\phi_0\tan\theta_0$$

$$A_0(9,7) = 0$$

$$A_0(9,8) = (q_0\sin\phi_0 + r_0\cos\phi_0)(\tan\theta_0^2 + 1)$$

$$A_0(9,9) = (q_0\cos\phi_0 - r_0\sin\phi_0)\tan\theta_0$$

$$A_0(9,10:14) = 0$$

$$\begin{aligned} A_0(10,1) = {} & \cos\beta_0 \cos\alpha_0 \cos\theta_0 \cos\psi_0 + \sin\beta_0\big(-\cos\phi_0 \sin\psi_0 + \sin\phi_0 \sin\theta_0 \cos\psi_0\big) \\ & + \cos\beta_0 \sin\alpha_0\big(\sin\phi_0 \sin\psi_0 + \cos\phi_0 \sin\theta_0 \cos\psi_0\big) \end{aligned}$$

$$\begin{aligned} A_0(10,2) = {} & V_0\Bigg(-\sin\beta_0 \cos\alpha_0 \cos\theta_0 \cos\psi_0 + \cos\beta_0\big(-\cos\phi_0 \sin\psi_0 + \sin\phi_0 \sin\theta_0 \cos\psi_0\big) \\ & + \sin\beta_0 \sin\alpha_0\big(-\sin\phi_0 \sin\psi_0 - \cos\phi_0 \sin\theta_0 \cos\psi_0\big)\Bigg) \end{aligned}$$

$$A_0(10,3) = V_0\Bigg(-\cos\beta_0 \sin\alpha_0 \cos\theta_0 \cos\psi_0 + \cos\beta_0 \cos\alpha_0\big(\sin\phi_0 \sin\psi_0 + \cos\phi_0 \sin\theta_0 \cos\psi_0\big)\Bigg)$$

$$A_0(10,4:6) = 0$$

$$\begin{aligned} A_0(10,7) = {} & V_0\Bigg(-\cos\beta_0 \cos\alpha_0 \cos\theta_0 \sin\psi_0 + \sin\beta_0\big(-\cos\phi_0 \cos\psi_0 - \sin\phi_0 \sin\theta_0 \sin\psi_0\big) \\ & + \cos\beta_0 \sin\alpha_0\big(\sin\phi_0 \cos\psi_0 - \cos\phi_0 \sin\theta_0 \sin\psi_0\big)\Bigg) \end{aligned}$$

$$A_0(10,8) = V_0\Bigg(-\cos\beta_0 \cos\alpha_0 \sin\theta_0 \cos\psi_0 + \sin\beta_0\big(\sin\phi_0 \cos\theta_0 \cos\psi_0\big) + \cos\beta_0 \sin\alpha_0\big(\cos\phi_0 \cos\theta_0 \cos\psi_0\big)\Bigg)$$

$$A_0(10,9) = V_0\Bigg(\sin\beta_0\big(\sin\phi_0 \sin\psi_0 + \cos\phi_0 \sin\theta_0 \cos\psi_0\big) + \cos\beta_0 \sin\alpha_0\big(\cos\phi_0 \sin\psi_0 - \sin\phi_0 \sin\theta_0 \cos\psi_0\big)\Bigg)$$

$$A_0(10,10:14) = 0$$

$$\begin{aligned} A_0(11,1) = {} & \cos\beta_0 \cos\alpha_0 \cos\theta_0 \sin\psi_0 + \sin\beta_0\big(\cos\phi_0 \cos\psi_0 + \sin\phi_0 \sin\theta_0 \sin\psi_0\big) \\ & + \cos\beta_0 \sin\alpha_0\big(-\sin\phi_0 \cos\psi_0 + \cos\phi_0 \sin\theta_0 \sin\psi_0\big) \end{aligned}$$

$$\begin{aligned} A_0(11,2) = {} & V_0\Bigg(-\sin\beta_0 \cos\alpha_0 \cos\theta_0 \sin\psi_0 + \cos\beta_0\big(\cos\phi_0 \cos\psi_0 + \sin\phi_0 \sin\theta_0 \sin\psi_0\big) \\ & + \sin\beta_0 \sin\alpha_0\big(\sin\phi_0 \cos\psi_0 - \cos\phi_0 \sin\theta_0 \sin\psi_0\big)\Bigg) \end{aligned}$$

$$A_0(11,3) = V_0\Bigg(-\cos\beta_0 \sin\alpha_0 \cos\theta_0 \sin\psi_0 + \cos\beta_0 \cos\alpha_0\big(-\sin\phi_0 \cos\psi_0 + \cos\phi_0 \sin\theta_0 \sin\psi_0\big)\Bigg)$$

$$A_0(11,4:6) = 0$$

$$\begin{aligned} A_0(11,7) = {} & V_0\Bigg(\cos\beta_0 \cos\alpha_0 \cos\theta_0 \cos\psi_0 + \sin\beta_0\big(-\cos\phi_0 \sin\psi_0 + \sin\phi_0 \sin\theta_0 \cos\psi_0\big) \\ & + \cos\beta_0 \sin\alpha_0\big(\sin\phi_0 \sin\psi_0 + \cos\phi_0 \sin\theta_0 \cos\psi_0\big)\Bigg) \end{aligned}$$

$$A_0(11,8) = V_0\Bigg(-\cos\beta_0 \cos\alpha_0 \sin\theta_0 \sin\psi_0 + \sin\beta_0\big(\sin\phi_0 \cos\theta_0 \sin\psi_0\big) + \cos\beta_0 \sin\alpha_0\big(\cos\phi_0 \cos\theta_0 \sin\psi_0\big)\Bigg)$$

$$A_0(11,9) = V_0\Bigg(\sin\beta_0\big(-\sin\phi_0 \cos\psi_0 + \cos\phi_0 \sin\theta_0 \sin\psi_0\big) + \cos\beta_0 \sin\alpha_0\big(-\cos\phi_0 \cos\psi_0 - \sin\phi_0 \sin\theta_0 \sin\psi_0\big)\Bigg)$$

$$A_0(11,10:14) = 0$$

$$A_0(12,1) = -\cos\beta_0 \cos\alpha_0 \sin\theta_0 + \sin\beta_0 \sin\phi_0 \cos\theta_0 + \cos\beta_0 \sin\alpha_0 \cos\phi_0 \cos\theta_0$$

$$A_0(12,2) = V_0\Bigg(\sin\beta_0 \cos\alpha_0 \sin\theta_0 + \cos\beta_0 \sin\phi_0 \cos\theta_0 - \sin\beta_0 \sin\alpha_0 \cos\phi_0 \cos\theta_0\Bigg)$$

$$A_0(12,3) = V_0\bigg(\cos\beta_0 \sin\alpha_0 \sin\theta_0 + \cos\beta_0 \cos\alpha_0 \cos\phi_0 \cos\theta_0 \bigg)$$

$$A_0(12,4:7) = 0$$

$$A_0(12,8) = V_0\bigg(-\cos\beta_0 \cos\alpha_0 \cos\theta_0 - \sin\beta_0 \sin\phi_0 \sin\theta_0 - \cos\beta_0 \sin\alpha_0 \cos\phi_0 \sin\theta_0 \bigg)$$

$$A_0(12,9) = V_0\bigg(\sin\beta_0 \cos\phi_0 \cos\theta_0 - \cos\beta_0 \sin\alpha_0 \sin\phi_0 \cos\theta_0 \bigg)$$

$$A_0(12,10:14) = 0$$

$$A_0(13,1:12) = 0$$

$$A_0(13,13) = -\frac{R}{L}$$

$$A_0(13,14) = -\frac{k_e}{L}$$

$$A_0(14,1:12) = 0$$

$$A_0(14,13) = \frac{k_T}{J_p + J_m}$$

$$A_0(14,14) = -\frac{k_T}{J_p + J_m}$$

B.2 Linearized Matrix A_1

The matrix $\mathbf{A_1}$ is defined as

$$\mathbf{A_1} = A_1(i,k), \quad \mathbf{A_1} \in \mathbb{R}^{14\times14} \quad i = \{1,..,14\}, k = \{1,..,14\}$$

The elements of $\mathbf{A_1}$ are presented below.

$$A_1(1,1:4) = 0$$

$$A_1(1,4) = 0$$

$$A_1(1,5) = -\frac{1}{m_T}\sum_{j=1}^{k} m_j \rho_{m_{j_z}}$$

$$A_1(1,6) = \frac{1}{m_T}\sum_{j=1}^{k} m_j \rho_{m_{j_y}}$$

$$A_1(1,7:14) = 0$$

$$A_1(2,1:4) = 0$$

$$A_1(2,4) = \frac{1}{m_T}\sum_{j=1}^{k} m_j \rho_{m_{j_z}}$$

$$A_1(2,5) = 0$$

$$A_1(2,6) = -\frac{1}{m_T}\sum_{j=1}^{k} m_j \rho_{m_{j_x}}$$

$$A_1(2,7:14) = 0$$

$$A_1(3,1:4) = 0$$

$$A_1(3,4) = -\frac{1}{m_T}\sum_{j=1}^{k} m_j \rho_{m_{j_y}}$$

$$A_1(3,5) = \frac{1}{m_T}\sum_{j=1}^{k} m_j \rho_{m_{j_x}}$$

$$A_1(3,6) = 0$$

$$A_1(3,7:14) = 0$$

$$A_1(4,1) = \sum_{j=1}^{k} m_j \Big(\rho_{m_{j_z}} \sin\beta_0 - \rho_{m_{j_y}} \cos\beta_0 \sin\alpha_0\Big)$$

$$A_1(4,2) = V_0 \sum_{j=1}^{k} m_j \Big(\rho_{m_{j_z}} \cos\beta_0 + \rho_{m_{j_y}} \sin\beta_0 \sin\alpha_0\Big)$$

$$A_1(4,3) = V_0 \sum_{j=1}^{k} m_j \Big(-\rho_{m_{j_y}} \cos\beta_0 \cos\alpha_0\Big)$$

$$A_1(4,4:14) = 0$$

$$A_1(5,1) = \sum_{j=1}^{k} m_j \Big(\rho_{m_{j_x}} \cos\beta_0 \sin\alpha_0 - \rho_{m_{j_z}} \cos\beta_0 \cos\alpha_0\Big)$$

$$A_1(5,2) = V_0 \sum_{j=1}^{k} m_j \Big(-\rho_{m_{j_x}} \sin\beta_0 \sin\alpha_0 + \rho_{m_{j_z}} \sin\beta_0 \cos\alpha_0\Big)$$

$$A_1(5,3) = V_0 \sum_{j=1}^{k} m_j \Big(\rho_{m_{j_x}} \cos\beta_0 \cos\alpha_0 + \rho_{m_{j_z}} \cos\beta_0 \sin\alpha_0\Big)$$

$$A_1(5,4:14) = 0$$

$$A_1(6,1) = \sum_{j=1}^{k} m_j \Big(\rho_{m_{j_y}} \cos\beta_0 \cos\alpha_0 - \rho_{m_{j_x}} \sin\beta_0\Big)$$

$$A_1(6,2) = V_0 \sum_{j=1}^{k} m_j \Big(-\rho_{m_{j_y}} \sin\beta_0 \cos\alpha_0 - \rho_{m_{j_x}} \cos\beta_0\Big)$$

$$A_1(6,3) = V_0 \sum_{j=1}^{k} m_j \Big(-\rho_{m_{j_y}} \cos\beta_0 \sin\alpha_0\Big)$$

$$A_1(6,4:14) = 0$$

$$A_1(7,1:14) = 0$$

$$A_1(8,1:14) = 0$$

$$A_1(9,1:14) = 0$$

$$A_1(10,1:14) = 0$$

$$
\begin{aligned}
&A_1(11,1:14) = 0\\
&A_1(12,1:14) = 0\\
&A_1(13,1:14) = 0\\
&A_1(14,1:14) = 0
\end{aligned}
$$

B.3 Linearized Matrix B_0

The matrix $\mathbf{B_0}$ is defined as

$$\mathbf{B_0} = B_0(i,k), \quad \mathbf{B_0} \in \mathbb{R}^{14\times 10} \quad i = \{1,..,14\}, k = \{1,..,10\}$$

The elements of $\mathbf{B_0}$ are presented below.

$$
\begin{aligned}
B_0(1,1:4) &= 0\\
B_0(1,(3j+2)) &= \frac{1}{m_T} m_j(q_0^2 + r_0^2)\\
B_0(1,(3j+3)) &= -\frac{1}{m_T} m_j(p_0 q_0)\\
B_0(1,(3j+4)) &= -\frac{1}{m_T} m_j(p_0 r_0)\\
B_0(2,1:4) &= 0\\
B_0(2,(3j+2)) &= -\frac{1}{m_T} m_j(p_0 q_0)\\
B_0(2,(3j+3)) &= \frac{1}{m_T} m_j(p_0^2 + r_0^2)\\
B_0(2,(3j+4)) &= -\frac{1}{m_T} m_j(r_0 q_0)\\
B_0(3,1:4) &= 0\\
B_0(3,(3j+2)) &= -\frac{1}{m_T} m_j(p_0 r_0)\\
B_0(3,(3j+3)) &= -\frac{1}{m_T} m_j(q_0 r_0)\\
B_0(3,(3j+4)) &= \frac{1}{m_T} m_j(p_0^2 + q_0^2)\\
B_0(4,1:4) &= 0\\
B_0(4,(3j+2)) &= m_j\Bigg(p_0\big(q_0\rho_{m_{jz}} - r_0\rho_{m_{jy}}\big)\Bigg)\\
B_0(4,(3j+3)) &= m_j\Bigg\{g\cos\phi_0\cos\theta_0 + \Bigg(q_0^2\rho_{m_{jz}} - \Big(\ddot{\rho}_{m_{jz}} + r_0(p_0\rho_{m_{jx}} + 2q_0\rho_{m_{jy}} + r_0\rho_{m_{jz}})\Big)\Bigg)\\
&\qquad + V_0\Bigg(-p_0\sin\beta_0 + q_0\cos\beta_0\cos\alpha_0\Bigg) - 2\Bigg(p_0\dot{\rho}_{m_{jy}} - q_0\dot{\rho}_{m_{jx}}\Bigg)\Bigg\}
\end{aligned}
$$

$$B_0(4,(3j+4)) = -m_j\Big\{g\sin\phi_0\cos\theta_0 + \Big(-r_0^2\rho_{m_{j_y}} + \Big(\ddot{\rho}_{m_{j_y}} + q_0(p_0\rho_{m_{j_x}} + q_0\rho_{m_{j_y}} + 2r_0\rho_{m_{j_z}})\Big)\Big) + V_0\Big(r_0\cos\beta_0\cos\alpha_0 - p_0\cos\beta_0\sin\alpha_0\Big) - 2\Big(p_0\dot{\rho}_{m_{j_z}} - r_0\dot{\rho}_{m_{j_x}}\Big)\Big\}$$

$$B_0(5,1:4) = 0$$

$$B_0(5,(3j+2)) = -m_j\Big\{g\cos\phi_0\cos\theta_0 + \Big(-p_0^2\rho_{m_{j_z}} + \Big(\ddot{\rho}_{m_{j_z}} + r_0(2p_0\rho_{m_{j_x}} + q_0\rho_{m_{j_y}} + r_0\rho_{m_{j_z}})\Big)\Big) + V_0\Big(p_0\sin\beta_0 - q_0\cos\beta_0\cos\alpha_0\Big) - 2\Big(-p_0\dot{\rho}_{m_{j_y}} + q_0\dot{\rho}_{m_{j_x}}\Big)\Big\}$$

$$B_0(5,(3j+3)) = m_j\Big(q_0\big(r_0\rho_{m_{j_x}} - p_0\rho_{m_{j_z}}\big)\Big)$$

$$B_0(5,(3j+4)) = -m_j\Big\{g\sin\theta_0 + \Big(r_0^2\rho_{m_{j_x}} - \Big(\ddot{\rho}_{m_{j_x}} + p_0(p_0\rho_{m_{j_x}} + q_0\rho_{m_{j_y}} + 2r_0\rho_{m_{j_z}})\Big)\Big) + V_0\Big(r_0\sin\beta_0 - q_0\cos\beta_0\sin\alpha_0\Big) - 2\Big(q_0\dot{\rho}_{m_{j_z}} - r_0\dot{\rho}_{m_{j_y}}\Big)\Big\}$$

$$B_0(6,1:4) = 0$$

$$B_0(6,(3j+2)) = m_j\Big\{g\sin\phi_0\cos\theta_0 + \Big(p_0^2\rho_{m_{j_y}} - \Big(\ddot{\rho}_{m_{j_y}} + q_0(2p_0\rho_{m_{j_x}} + q_0\rho_{m_{j_y}} + r_0\rho_{m_{j_z}})\Big)\Big) + V_0\Big(-r_0\cos\beta_0\cos\alpha_0 + p_0\cos\beta_0\sin\alpha_0\Big) - 2\Big(-p_0\dot{\rho}_{m_{j_z}} + r_0\dot{\rho}_{m_{j_x}}\Big)\Big\}$$

$$B_0(6,(3j+3)) = m_j\Big\{g\sin\theta_0 + \Big(-q_0^2\rho_{m_{j_x}} + \Big(\ddot{\rho}_{m_{j_x}} + p_0(p_0\rho_{m_{j_x}} + 2q_0\rho_{m_{j_y}} + r_0\rho_{m_{j_z}})\Big)\Big) + V_0\Big(-r_0\sin\beta_0 + q_0\cos\beta_0\sin\alpha_0\Big) - 2\Big(-q_0\dot{\rho}_{m_{j_z}} + r_0\dot{\rho}_{m_{j_y}}\Big)\Big\}$$

$$B_0(6,(3j+4)) = m_j\Big(r_0\big(p_0\rho_{m_{j_y}} - q_0\rho_{m_{j_x}}\big)\Big)$$

$$B_0(7,1:(3j+4)) = 0$$

$$B_0(8,1:(3j+4)) = 0$$

$$B_0(9,1:(3j+4)) = 0$$

$$B_0(10,1:(3j+4)) = 0$$

$$B_0(11,1:(3j+4)) = 0$$

$$B_0(12,1:(3j+4)) = 0$$

$$B_0(13,1:3) = 0$$

$$B_0(13,4) = \frac{\mathcal{V}_{max}}{L}$$

$$B_0(13,(3j+2):(3j+4)) = 0$$

$$B_0(14,1:(3j+4)) = 0$$

B.4 Linearized Matrix B_1

The matrix $\mathbf{B_1}$ is defined as

$$\mathbf{B_1} = B_1(i,k), \quad \mathbf{B_1} \in \mathbb{R}^{14\times 10} \quad i = \{1,..,14\}, k = \{1,..,10\}$$

The elements of $\mathbf{B_1}$ are presented below.

$$\begin{aligned}
B_1(1,1:4) &= 0 \\
B_1(1,(3j+2)) &= 0 \\
B_1(1,(3j+3)) &= \frac{1}{m_T}m_j(2r_0) \\
B_1(1,(3j+4)) &= -\frac{1}{m_T}m_j(2q_0) \\
B_1(2,1:4) &= 0 \\
B_1(2,(3j+2)) &= -\frac{1}{m_T}m_j(2r_0) \\
B_1(2,(3j+3)) &= 0 \\
B_1(2,(3j+4)) &= \frac{1}{m_T}m_j(2p_0) \\
B_1(3,1:4) &= 0 \\
B_1(3,(3j+2)) &= \frac{1}{m_T}m_j(2q_0) \\
B_1(3,(3j+3)) &= -\frac{1}{m_T}m_j(2p_0) \\
B_1(3,(3j+4)) &= 0 \\
B_1(4,1:4) &= 0 \\
B_1(4,(3j+2)) &= 2m_j(q_0\rho_{m_{j_y}} + r_0\rho_{m_{j_z}}) \\
B_1(4,(3j+3)) &= -2m_j(p_0\rho_{m_{j_y}}) \\
B_1(4,(3j+4)) &= -2m_j(p_0\rho_{m_{j_z}}) \\
B_1(5,1:4) &= 0 \\
B_1(5,(3j+2)) &= -2m_j(q_0\rho_{m_{j_x}}) \\
B_1(5,(3j+3)) &= 2m_j(p_0\rho_{m_{j_x}} + r_0\rho_{m_{j_z}}) \\
B_1(5,(3j+4)) &= -2m_j(q_0\rho_{m_{j_z}}) \\
B_1(6,1:4) &= 0 \\
B_1(6,(3j+2)) &= -2m_j(r_0\rho_{m_{j_x}}) \\
B_1(6,(3j+3)) &= -2m_j(r_0\rho_{m_{j_y}}) \\
B_1(6,(3j+4)) &= 2m_j(p_0\rho_{m_{j_x}} + q_0\rho_{m_{j_y}}) \\
B_1(7,1:(3j+4)) &= 0 \\
B_1(8,1:(3j+4)) &= 0
\end{aligned}$$

$$B_1(9, 1:(3j+4)) = 0$$
$$B_1(10, 1:(3j+4)) = 0$$
$$B_1(11, 1:(3j+4)) = 0$$
$$B_1(12, 1:(3j+4)) = 0$$
$$B_1(13, 1:(3j+4)) = 0$$
$$B_1(14, 1:(3j+4)) = 0$$

B.5 Linearized Matrix B_2

The matrix $\mathbf{B_2}$ is defined as

$$\mathbf{B_2} = B_2(i,k), \quad \mathbf{B_2} \in \mathbb{R}^{14\times 10} \quad i = \{1, .., 14\}, k = \{1, .., 10\}$$

The elements of $\mathbf{B_2}$ are presented below.

$$B_2(1, 1:4) = 0$$
$$B_2(1, (3j+2)) = -\frac{1}{m_T} m_j$$
$$B_2(1, (3j+3)) = 0$$
$$B_2(1, (3j+4)) = 0$$
$$B_2(2, 1:4) = 0$$
$$B_2(2, (3j+2)) = 0$$
$$B_2(2, (3j+3)) = -\frac{1}{m_T} m_j$$
$$B_2(2, (3j+4)) = 0$$
$$B_2(3, 1:4) = 0$$
$$B_2(3, (3j+2)) = 0$$
$$B_2(3, (3j+3)) = 0$$
$$B_2(3, (3j+4)) = -\frac{1}{m_T} m_j$$
$$B_2(4, 1:4) = 0$$
$$B_2(4, (3j+2)) = 0$$
$$B_2(4, (3j+3)) = m_j \rho_{m_{j_z}}$$
$$B_2(4, (3j+4)) = -m_j \rho_{m_{j_y}}$$

$$B_2(5,1:4) = 0$$

$$B_2(5,(3j+2)) = -m_j \rho_{m_{j_z}}$$

$$B_2(5,(3j+3)) = 0$$

$$B_2(5,(3j+4)) = m_j \rho_{m_{j_x}}$$

$$B_2(6,1:4) = 0$$

$$B_2(6,(3j+2)) = m_j \rho_{m_{j_y}}$$

$$B_2(6,(3j+3)) = -m_j \rho_{m_{j_x}}$$

$$B_2(6,(3j+4)) = 0$$

$$B_2(7,1:(3j+4)) = 0$$

$$B_2(8,1:(3j+4)) = 0$$

$$B_2(9,1:(3j+4)) = 0$$

$$B_2(10,1:(3j+4)) = 0$$

$$B_2(11,1:(3j+4)) = 0$$

$$B_2(12,1:(3j+4)) = 0$$

$$B_2(13,1:(3j+4)) = 0$$

$$B_2(14,1:(3j+4)) = 0$$

B.6 Linearized Matrix C

The matrix **C** is defined as

$$\mathbf{C} = C(i,k), \quad \mathbf{C} \in \mathbb{R}^{14\times12} \quad i = \{1,..,14\}, k = \{1,..,12\}$$

The elements of **C** are presented below.

$$C(1,1) = \frac{1}{m_T}$$

$$C(1,2:6) = 0$$

$$C(1,7) = \frac{1}{m_T}$$

$$C(1,8:12) = 0$$

$$C(2,1) = 0$$

$$C(2,2) = \frac{1}{m_T}$$

$$
\begin{aligned}
C(2,3:7) &= 0\\
C(2,8) &= \frac{1}{m_T}\\
C(2,9:12) &= 0\\
C(3,1:2) &= 0\\
C(3,3) &= \frac{1}{m_T}\\
C(3,4:8) &= 0\\
C(3,9) &= \frac{1}{m_T}\\
C(3,10:12) &= 0\\
C(4,1:3) &= 0\\
C(4,4) &= 1\\
C(4,5:9) &= 0\\
C(4,10) &= 1\\
C(4,11:12) &= 0\\
C(5,1:4) &= 0\\
C(5,5) &= 1\\
C(5,6:10) &= 0\\
C(5,11) &= 1\\
C(5,12) &= 0\\
C(6,1:5) &= 0\\
C(6,6) &= 1\\
C(6,7:11) &= 0\\
C(6,12) &= 1\\
C(7,1:12) &= 0\\
C(8,1:12) &= 0\\
C(9,1:12) &= 0\\
C(10,1:12) &= 0\\
C(11,1:12) &= 0\\
C(12,1:12) &= 0\\
C(13,1:12) &= 0\\
C(14,1:9) &= 0\\
C(14,10) &= -\frac{1}{J_p + J_m}\\
C(14,11:12) &= 0
\end{aligned}
$$

B.7 Linearized Matrix E_0

The matrix $\mathbf{E_0}$ is defined as

$$\mathbf{E_0} = E_0(i,k), \quad \mathbf{E_0} \in \mathbb{R}^{12\times 14} \quad i = \{1,..,12\}, k = \{1,..,14\}$$

In Section 2.6 the last three terms of C_D expression in Eq. (2.67) are added to model the contribution of sideslip angle on drag. The coefficients K_2, K_1 and K_0 are second order polynomials of β and determined based on experimental data of a micro air vehicle [117]. Hence, K_2, K_1 and K_0 are defined as

$$K_2(\beta) = K_{22}|\beta^2| + K_{21}|\beta| + K_{20}$$

$$K_1(\beta) = K_{12}|\beta^2| + K_{11}|\beta| + K_{10}$$

$$K_0(\beta) = K_{02}|\beta^2| + K_{01}|\beta| + K_{00}$$

The elements of $\mathbf{E_0}$ are presented below.

$$\begin{aligned} E_0(1,1) = (\rho_{air} S V_0)\Bigg(& \sin\alpha_0\Big(C_{L_0} + C_{L_\alpha}\alpha_0 + C_{L_{\delta_e}}\delta_e + \frac{c}{4V_0}(C_{L_q}q_0 + C_{L_{\dot\alpha}}\dot\alpha)\Big) \\ & - \cos\alpha_0\Big(C_{D_{\delta_e}}|\delta_e| + C_{D_{\delta_r}}|\delta_r| + C_{D_{\delta_a}}|\delta_a| + K_2(\beta_0){\alpha_0}^2 + K_1(\beta_0)\alpha_0 + K_0(\beta_0)\Big)\Bigg) \end{aligned}$$

$$\begin{aligned} E_0(1,2) = -\frac{1}{2}(\rho_{air} S V_0^2)\cos\alpha_0\Bigg(& \Big(2K_{22}|\beta_0|\ sgn(\beta_0) + K_{21}\ sgn(\beta_0)\Big)\alpha_0^2 \\ & + \Big(2K_{12}|\beta_0|\ sgn(\beta_0) + K_{11}\ sgn(\beta_0)\Big)\alpha_0 + \Big(2K_{02}|\beta_0|\ sgn(\beta_0) + K_{01}\ sgn(\beta_0)\Big)\Bigg) \end{aligned}$$

$$\begin{aligned} E_0(1,3) = \frac{1}{2}(\rho_{air} S V_0^2)\Bigg(& \cos\alpha_0\Big(C_{L_0} + C_{L_\alpha}\alpha_0 + C_{L_{\delta_e}}\delta_e + \frac{c}{2V_0}(C_{L_q}q_0 + C_{L_{\dot\alpha}}\dot\alpha) - \big(2K_2(\beta_0)\alpha_0 + K_1(\beta_0)\big)\Big) \\ & + \sin\alpha_0\Big(C_{L_\alpha} + C_{D_{\delta_e}}|\delta_e| + C_{D_{\delta_r}}|\delta_r| + C_{D_{\delta_a}}|\delta_a| + K_2(\beta_0){\alpha_0}^2 + K_1(\beta_0)\alpha_0 + K_0(\beta_0)\Big)\Bigg) \end{aligned}$$

$$E_0(1,4) = 0$$

$$E_0(1,5) = \frac{1}{2}(\rho_{air} S V_0)\sin\alpha_0 \frac{c}{2} C_{L_q}$$

$$E_0(1,6) = 0$$

$$E_0(1,7:14) = 0$$

$$E_0(2,1) = (\rho_{air} S V_0)\left(C_{Y_\beta}\beta + C_{Y_{\delta_r}}\delta_r + \frac{b}{4V_0}(C_{y_p} p_0 + C_{y_r} r_0)\right)$$

$$E_0(2,2) = \frac{1}{2}(\rho_{air} S V_0^2) C_{Y_\beta}$$

$$E_0(2,3) = 0$$

$$E_0(2,4) = \frac{1}{2}(\rho_{air} S V_0)\frac{b}{2} C_{y_p}$$

$$E_0(2,5) = 0$$

$$E_0(2,6) = \frac{1}{2}(\rho_{air} S V_0)\frac{b}{2} C_{y_r}$$

$$E_0(2,7:14) = 0$$

$$\begin{aligned} E_0(3,1) = -(\rho_{air} S V_0)\Bigg(& \cos\alpha_0\Big(C_{L_0} + C_{L_\alpha}\alpha_0 + C_{L_{\delta_e}}\delta_e + \frac{c}{4V_0}(C_{L_q} q_0 + C_{L_{\dot\alpha}}\dot\alpha)\Big) \\ & + \sin\alpha_0\Big(C_{D_{\delta_e}}|\delta_e| + C_{D_{\delta_r}}|\delta_r| + C_{D_{\delta_a}}|\delta_a| + K_2(\beta_0){\alpha_0}^2 + K_1(\beta_0)\alpha_0 + K_0(\beta_0)\Big)\Bigg) \end{aligned}$$

$$\begin{aligned} E_0(3,2) = -\frac{1}{2}(\rho_{air} S V_0^2)\sin\alpha_0\Bigg(& \Big(2K_{22}|\beta_0|\ sgn(\beta_0) + K_{21}\ sgn(\beta_0)\Big)\alpha_0^2 \\ & + \Big(2K_{12}|\beta_0|\ sgn(\beta_0) + K_{11}\ sgn(\beta_0)\Big)\alpha_0 + \Big(2K_{02}|\beta_0|\ sgn(\beta_0) + K_{01}\ sgn(\beta_0)\Big)\Bigg) \end{aligned}$$

$$\begin{aligned} E_0(1,3) = \frac{1}{2}(\rho_{air} S V_0^2)\Bigg(& \sin\alpha_0\Big(C_{L_0} + C_{L_\alpha}\alpha_0 + C_{L_{\delta_e}}\delta_e + \frac{c}{2V_0}(C_{L_q} q_0 + C_{L_{\dot\alpha}}\dot\alpha) - \big(2K_2(\beta_0)\alpha_0 + K_1(\beta_0)\big)\Big) \\ & - \cos\alpha_0\Big(C_{L_\alpha} + C_{D_{\delta_e}}|\delta_e| + C_{D_{\delta_r}}|\delta_r| + C_{D_{\delta_a}}|\delta_a| + K_2(\beta_0){\alpha_0}^2 + K_1(\beta_0)\alpha_0 + K_0(\beta_0)\Big)\Bigg) \end{aligned}$$

$$E_0(3,4) = 0$$

$$E_0(3,5) = -\frac{1}{2}(\rho_{air} S V_0)\cos\alpha_0\frac{c}{2} C_{L_q}$$

$$E_0(3,6) = 0$$

$$E_0(3,7:14) = 0$$

$$E_0(4,1) = (\rho_{air} S b V_0)\left(C_{l_\beta}\beta_0 + C_{l_{\delta_a}}\delta_a + C_{l_{\delta_r}}\delta_r + \frac{b}{4V_0}(C_{l_p} p_0 + C_{l_r} r_0)\right)$$

$$E_0(4,2) = \frac{1}{2}(\rho_{air} S b V_0^2) C_{l_\beta}$$

$$E_0(4,3) = 0$$

$$E_0(4,4) = \frac{1}{2}(\rho_{air} S b V_0)\frac{b}{2} C_{l_p}$$

$$E_0(4,5) = 0$$

$$E_0(4,6) = \frac{1}{2}(\rho_{air} S b V_0)\frac{b}{2} C_{l_r}$$

$$E_0(4,7:14) = 0$$

$$E_0(5,1) = (\rho_{air} S c V_0)\left(C_{m_0} + C_{m_\alpha}\alpha_0 + C_{m_{\delta_e}}\delta_e + \frac{c}{4V_0}(C_{m_q} q_0 + C_{m_{\dot\alpha}}\dot\alpha)\right)$$

$$E_0(5,2) = 0$$

$$E_0(5,3) = \frac{1}{2}(\rho_{air} S c V_0^2) C_{m_\alpha}$$

$$E_0(5,4) = 0$$

$$E_0(5,5) = \frac{1}{2}(\rho_{air} S c V_0) \frac{c}{2} C_{m_q}$$

$$E_0(5,6) = 0$$

$$E_0(5,7:14) = 0$$

$$E_0(6,1) = (\rho_{air} S b V_0) \left(C_{n_\beta} \beta_0 + C_{n_{\delta_a}} \delta_a + C_{n_{\delta_r}} \delta_r + \frac{b}{4V_0} (C_{n_p} p_0 + C_{n_r} r_0) \right)$$

$$E_0(6,2) = \frac{1}{2}(\rho_{air} S b V_0^2) C_{n_\beta}$$

$$E_0(6,3) = 0$$

$$E_0(6,4) = \frac{1}{2}(\rho_{air} S b V_0) \frac{b}{2} C_{n_p}$$

$$E_0(6,5) = 0$$

$$E_0(6,6) = \frac{1}{2}(\rho_{air} S b V_0) \frac{b}{2} C_{n_r}$$

$$E_0(6,7:14) = 0$$

$$E_0(7,1) = \frac{\partial T_x}{\partial V_0}$$

$$E_0(7,2:13) = 0$$

$$E_0(7,14) = \frac{\partial T_x}{\partial \omega_{p_0}}$$

$$E_0(8,1) = \frac{\partial T_y}{\partial V_0}$$

$$E_0(8,2:13) = 0$$

$$E_0(8,14) = \frac{\partial T_y}{\partial \omega_{p_0}}$$

$$E_0(9,1) = \frac{\partial T_z}{\partial V_0}$$

$$E_0(9,2:13) = 0$$

$$E_0(9,14) = \frac{\partial T_z}{\partial \omega_{p_0}}$$

$$E_0(10,1) = \frac{\partial \tau_{p_x}}{\partial V_0}$$

$$E_0(10,2:13) = 0$$

$$E_0(10,14) = \frac{\partial \tau_{p_x}}{\partial \omega_{p_0}}$$

$$E_0(11,1) = \frac{\partial \tau_{p_y}}{\partial V_0}$$

$$E_0(11,2:13) = 0$$

$$E_0(11,14) = \frac{\partial \tau_{p_y}}{\partial \omega_{p_0}}$$

$$E_0(12,1) = \frac{\partial \tau_{p_z}}{\partial V_0}$$

$$E_0(12, 2:13) = 0$$
$$E_0(12, 14) = \frac{\partial \tau_{p_z}}{\partial \omega_{p_0}}$$

B.8 Linearized Matrix E_1

The matrix $\mathbf{E_1}$ is defined as

$$\mathbf{E_1} = E_1(i, k), \quad \mathbf{E_1} \in \mathbb{R}^{12\times 14} \quad i = \{1, .., 12\}, k = \{1, .., 14\}$$

The elements of $\mathbf{E_1}$ are presented below.

$$E_1(1, 1:2) = 0$$
$$E_1(1, 3) = \frac{1}{2}(\rho_{air} S V_0)\sin\alpha_0 \frac{c}{2} C_{L_{\dot{\alpha}}}$$
$$E_1(1, 4:14) = 0$$
$$E_1(2, 1:14) = 0$$
$$E_1(3, 1:2) = 0$$
$$E_1(3, 3) = -\frac{1}{2}(\rho_{air} S V_0)\cos\alpha_0 \frac{c}{2} C_{L_{\dot{\alpha}}}$$
$$E_1(3, 4:14) = 0$$
$$E_1(4, 1:14) = 0$$
$$E_1(5, 1:2) = 0$$
$$E_1(5, 3) = \frac{1}{2}(\rho_{air} S c V_0) \frac{c}{2} C_{m_{\dot{\alpha}}}$$
$$E_1(5, 4:14) = 0$$
$$E_1(6, 1:14) = 0$$
$$E_1(7, 1:14) = 0$$
$$E_1(8, 1:14) = 0$$
$$E_1(9, 1:14) = 0$$
$$E_1(10, 1:14) = 0$$
$$E_1(11, 1:14) = 0$$
$$E_1(12, 1:14) = 0$$

B.9 Linearized Matrix F

The matrix $\mathbf{F}$ is defined as

$$\mathbf{F} = F(i,k), \quad \mathbf{F} \in \mathbb{R}^{12\times 10} \quad i = \{1,..,12\}, k = \{1,..,10\}$$

The elements of $\mathbf{F}$ are presented below.

$$
\begin{aligned}
F(1,1) &= -\frac{1}{2}(\rho_{air}SV_0^2)\Big(\cos\alpha_0 C_{D_{\delta_a}}\ sgn(\delta_a)\Big)\\
F(1,2) &= \frac{1}{2}(\rho_{air}SV_0^2)\Big(\sin\alpha_0 C_{L_{\delta_e}} - \cos\alpha_0 C_{D_{\delta_e}} sgn(\delta_e)\Big)\\
F(1,3) &= -\frac{1}{2}(\rho_{air}SV_0^2)\Big(\cos\alpha_0 C_{D_{\delta_r}}\ sgn(\delta_r)\Big)\\
F(1,4) &= 0\\
F(1,(3j+2)) &= 0\\
F(1,(3j+3)) &= 0\\
F(1,(3j+4)) &= 0\\
F(2,1) &= 0\\
F(2,2) &= 0\\
F(2,3) &= \frac{1}{2}(\rho_{air}SV_0^2)C_{Y_{\delta_r}}\\
F(2,4) &= 0\\
F(2,(3j+2)) &= 0\\
F(2,(3j+3)) &= 0\\
F(2,(3j+4)) &= 0\\
F(3,1) &= -\frac{1}{2}(\rho_{air}SV_0^2)\Big(\sin\alpha_0 C_{D_{\delta_a}}\ sgn(\delta_a)\Big)\\
F(3,2) &= -\frac{1}{2}(\rho_{air}SV_0^2)\Big(\cos\alpha_0 C_{L_{\delta_e}} + \sin\alpha_0 C_{D_{\delta_e}} sgn(\delta_e)\Big)\\
F(3,3) &= -\frac{1}{2}(\rho_{air}SV_0^2)\Big(\sin\alpha_0 C_{D_{\delta_r}}\ sgn(\delta_r)\Big)\\
F(3,4) &= 0\\
F(3,(3j+2)) &= 0\\
F(3,(3j+3)) &= 0\\
F(3,(3j+4)) &= 0\\
F(4,1) &= \frac{1}{2}(\rho_{air}SbV_0^2)C_{l_{\delta_a}}\\
F(4,2) &= 0\\
F(4,3) &= \frac{1}{2}(\rho_{air}SbV_0^2)C_{l_{\delta_r}}\\
F(4,4) &= 0\\
F(4,(3j+2)) &= 0
\end{aligned}
$$

$$F(4,(3j+3)) = 0$$

$$F(4,(3j+4)) = 0$$

$$F(5,1) = 0$$

$$F(5,2) = \frac{1}{2}(\rho_{air} S c V_0^2) C_{m_{\delta_e}}$$

$$F(5,3) = 0$$

$$F(5,4) = 0$$

$$F(5,(3j+2)) = 0$$

$$F(5,(3j+3)) = 0$$

$$F(5,(3j+4)) = 0$$

$$F(6,1) = \frac{1}{2}(\rho_{air} S b V_0^2) C_{n_{\delta_a}}$$

$$F(6,2) = 0$$

$$F(6,3) = \frac{1}{2}(\rho_{air} S b V_0^2) C_{n_{\delta_r}}$$

$$F(6,4) = 0$$

$$F(6,(3j+2)) = 0$$

$$F(6,(3j+3)) = 0$$

$$F(6,(3j+4)) = 0$$

$$F(7,1:(3j+4)) = 0$$

$$F(8,1:(3j+4)) = 0$$

$$F(9,1:(3j+4)) = 0$$

$$F(10,1:(3j+4)) = 0$$

$$F(11,1:(3j+4)) = 0$$

$$F(12,1:(3j+4)) = 0$$

B.10 Linearized Matrix L

The matrix **L** is defined as

$$\mathbf{L} = L(i,k), \quad \mathbf{L} \in \mathbb{R}^{14\times 14} \quad i = \{1,..,14\}, k = \{1,..,14\}$$

The elements of **L** are presented below.

$$F(1,1) = \cos\alpha_0 \cos\beta_0$$

$$
\begin{aligned}
F(1,2) &= -V_0 \cos\alpha_0 \sin\beta_0 \\
F(1,3) &= -V_0 \sin\alpha_0 \cos\beta_0 \\
F(1,4:14) &= 0 \\
F(2,1) &= \sin\beta_0 \\
F(2,2) &= V_0 \cos\beta_0 \\
F(2,3) &= 0 \\
F(2,4:14) &= 0 \\
F(3,1) &= \sin\alpha_0 \cos\beta_0 \\
F(3,2) &= -V_0 \sin\alpha_0 \sin\beta_0 \\
F(3,3) &= V_0 \cos\alpha_0 \cos\beta_0 \\
F(3,4:14) &= 0 \\
F(4,1:3) &= 0 \\
F(4,4) &= I_{xx} + \sum_{j=1}^{k} m_j(\rho_{m_{j_y}}^2 + \rho_{m_{j_z}}^2) \\
F(4,5) &= -I_{xy} - \sum_{j=1}^{k} m_j \rho_{m_{j_x}} \rho_{m_{j_y}} \\
F(4,6) &= -I_{xz} - \sum_{j=1}^{k} m_j \rho_{m_{j_x}} \rho_{m_{j_z}} \\
F(4,7:14) &= 0 \\
F(5,1:3) &= 0 \\
F(5,4) &= -I_{xy} - \sum_{j=1}^{k} m_j \rho_{m_{j_x}} \rho_{m_{j_y}} \\
F(5,5) &= I_{yy} + \sum_{j=1}^{k} m_j(\rho_{m_{j_x}}^2 + \rho_{m_{j_z}}^2) \\
F(5,6) &= -I_{yz} - \sum_{j=1}^{k} m_j \rho_{m_{j_y}} \rho_{m_{j_z}} \\
F(5,7:14) &= 0 \\
F(6,1:3) &= 0 \\
F(6,4) &= -I_{xz} - \sum_{j=1}^{k} m_j \rho_{m_{j_x}} \rho_{m_{j_z}} \\
F(6,5) &= -I_{yz} - \sum_{j=1}^{k} m_j \rho_{m_{j_y}} \rho_{m_{j_z}} \\
F(6,6) &= I_{zz} + \sum_{j=1}^{k} m_j(\rho_{m_{j_x}}^2 + \rho_{m_{j_y}}^2) \\
F(6,7:14) &= 0
\end{aligned}
$$

$$F(7,1:6)=0$$

$$F(7,7)=1$$

$$F(7,8:14)=0$$

$$F(8,1:7)=0$$

$$F(8,8)=1$$

$$F(8,9:14)=0$$

$$F(9,1:8)=0$$

$$F(9,9)=1$$

$$F(9,10:14)=0$$

$$F(10,1:9)=0$$

$$F(10,10)=1$$

$$F(10,11:14)=0$$

$$F(11,1:10)=0$$

$$F(11,11)=1$$

$$F(11,12:14)=0$$

$$F(12,1:11)=0$$

$$F(12,12)=1$$

$$F(12,13:14)=0$$

$$F(13,1:12)=0$$

$$F(13,13)=1$$

$$F(13,14)=0$$

$$F(14,1:13)=0$$

$$F(14,14)=1$$

REFERENCES

[1] L. Chen, G. Zhou, X. J. Yan, and D. P. Duan, "Composite control of stratospheric airships with moving masses," *Journal of Aircraft*, vol. 49, no. 3, pp. 794–801, 2012.

[2] Z. Goraj and P. Zakrzewski, "Aircraft fuel systems and their influence on stability margin," *Prace Instytutu Lotnictwa*, vol. 4, no. 183, pp. 29–40, 2005.

[3] F. Z. Seisan, "Modeling and control of a co-axial helicopter," Ph.D. dissertation, University of Toronto, 2012.

[4] C. Bermes, S. Leutenegger, S. Bouabdallah, D. Schafroth, and R. Siegwart, "New design of the steering mechanism for a mini coaxial helicopter," in *Intelligent Robots and Systems, 2008. IROS 2008. IEEE/RSJ International Conference on.* Nice, France: IEEE, 2008, pp. 1236–1241.

[5] E. W. Beyer, "Design, testing, and performance of a hybrid micro vehicle—the hopping rotochute," Ph.D. dissertation, Georgia Institute of Technology, August 2009.

[6] J. G. Graver, "Underwater gliders: Dynamics, control and design," Ph.D. dissertation, Princeton University, May 2005.

[7] S. S. Vaddi, "Moving mass actuated missile control using convex optimization techniques," in *AIAA Guidance, Navigation, and Control Conference and Exhibit*, Keystone, CO, 2006.

[8] F.-J. Gao and L.-Y. Zhao, "Adaptive sliding mode control with backstepping approach for a moving mass hypersonic spinning missile," *International Confer-*

ence on Applied Science and Engineering Innovation (ASEI 2015), pp. 834–837, 2015.

[9] L. Qin and M. Yang, "Moving mass attitude law based on neural networks," in *Proceedings of the Sixth International Conference on Machine Learning and Cybernetics*, vol. 5, 2007, pp. 2791–2795.

[10] J. Rogers and M. Costello, "A variable stability projectile using an internal moving mass," in *AIAA Atmospheric Flight Mechanics Conference and Exhibit*, Honolulu, HI, 2008.

[11] X.-L. Su, J.-Q. Yu, Y.-F. Wang, and L.-L. Wang, "Moving mass actuated reentry vehicle control based on trajectory linearization," *International Journal Aeronautical and Space Sciences*, vol. 14, no. 3, pp. 247–255, 2013.

[12] R. D. Robinett III, B. R. Sturgis, and S. A. Kerr, "Moving mass trim control for aerospace vehicles," *Journal of Guidance, Control, and Dynamics*, vol. 19, no. 5, pp. 1064–1070, 1996.

[13] C. Gao, W. Jing, and P. Wei, "Research on application of single moving mass in the reentry warhead maneuver," *Aerospace Science and Technology*, vol. 30, no. 1, pp. 108–118, 2013.

[14] J. E. White and R. D. Robinett III, "Principal axis misalignment control for deconing of spinning spacecraft," *Journal of Guidance, Control, and Dynamics*, vol. 17, no. 4, pp. 823–830, 1994.

[15] Y. Yao and Y. Jiang, "Attitude stabilization of spacecraft with two moving-mass via interconnection and damping assignment," in *Chinese Control and Decision Conference (CCDC 2008)*. IEEE, 2008, pp. 5115–5118.

[16] P. K. Menon, S. S. Vaddi, and E. J. Ohlmeyer, "Finite-horizon robust integrated guidance-control of a moving-mass actuated kinetic warhead," in *AIAA Guid-*

ance, Navigation, and Control Conference and Exhibit, Keystone, CO, 2006, pp. 21–24.

[17] B. Wie, D. Murphy, M. Paluszek, and S. Thomas, “Robust attitude control systems design for solar sails, part 1 propellantless primary acs,” in *AIAA Guidance, Navigation, and Control Conference and Exhibit*, Providence, RI, 2004.

[18] C. Scholz, D. Romagnoli, B. Dachwald, and S. Theil, “Performance analysis of an attitude control system for solar sails using sliding masses,” *Advances in Space Research*, vol. 48, no. 11, pp. 1822–1835, 2011.

[19] “Ultra stick 25e arf,” http://www.e-fliterc.com/Products/Default.aspx?ProdID=EFL4025, accessed: 12/22/2015.

[20] Y. C. Paw, “Synthesis and validation of flight control for uav,” Ph.D. dissertation, The University of Minnesota, December 2009.

[21] “Power 25 brushless outrunner motor, 870kv,” http://www.e-fliterc.com/Products/Default.aspx?ProdID=EFLM4025A, accessed: 12/22/2015.

[22] “Thunder power 4400mah 3-cell/3s 11.1v prolite + power 25c lipo,” http://www.thunderpowerrc.com/Products/4400ProlitePlusPower/TP4400-3SP25_2, accessed: 12/22/2015.

[23] “Hs-5085mg premium metal gear micro servo,” http://hitecrcd.com/products/servos/micro-and-mini-servos/digital-micro-and-mini-servos/hs-5085mg-premium-metal-gear-micro-servo/product, accessed: 03/26/2016.

[24] R. E. Roberson and C. Downey, “Torques on a satellite vehicle from internal moving parts,” *J. appl. Mech*, vol. 25, no. 2, pp. 196–200, 1958.

[25] C. Grubin, “Dynamics of a vehicle containing moving parts,” *Journal of Applied Mechanics*, vol. 29, no. 3, pp. 486–488, 1962.

[26] F. L. Janssens and J. C. Van Der Ha, "Stability of spinning satellite under axial thrust and internal mass motion," *Acta Astronautica*, vol. 94, no. 1, pp. 502–514, 2014.

[27] D. Mingori and Y. Yam, "Nutational stability of a spinning spacecraft with internal mass motion and axial thrust," *AIAA paper 86-2271*, pp. 367–375, 1986.

[28] D. L. Mingori, D. M. Halsmer, and Y. Yam, "Stability of spinning rockets with internal mass motion," *Advances in Astronautical Sciences*, vol. 82, pp. 199–209, 1993.

[29] Y. Yam, D. L. Mingori, and D. M. Halsmer, "Stability of a spinning axisymmetric rocket with dissipative internal mass motion," *Journal of Guidance, Control, and Dynamics*, vol. 20, no. 2, pp. 306–312, 1997.

[30] F. L. Charnousko, "On motion of a rigid body having internal masses," *Mechanics of Solids*, vol. 8, pp. 33–44, 1973.

[31] G. R. Salimov, "Motion of a spacecraft containing a moving element in a gravitational field," *Mechanics of Solids*, vol. 9, pp. 30–36, 1974.

[32] D. D. Leshchenko, "Motion of a rigid body with movable point mass," *Mechanics of Solids*, vol. 11, pp. 33–36, 1976.

[33] G. R. Salimov, "Stability of rotating space station containing a moving element," *Mechanics of Solids*, vol. 10, pp. 52–56, 1975.

[34] L. D. Akulenko and D. D. Leshchenko, "Some problems of the motion of a rigid body with a moving mass," *Mechanics of Solids*, vol. 13, pp. 24–28, 1978.

[35] J. Han and G. Hong, "Modeling of aircraft with time-varying inertia properties," in *AIAA SciTech*, Kissimmee, FL, 2015.

[36] D. M. Halsmer and D. L. Mingori, "The passive coning attenuator (pca); internal mass motion and axial thrust combine to produce asymptotic nutational

stability," in *AIAA/AAS Astrodynamics Conference, Hilton Head, SC*, 1992, pp. 1087–1096.

[37] F. L. Janssens and J. C. van der Ha, "Stability of spinning satellite under axial thrust, internal mass motion, and damping," *Journal of Guidance, Control, and Dynamics*, vol. 38, no. 4, pp. 761–771, 2015.

[38] D. M. Halsmer and D. L. Mingori, "Nutational stability and passive control of spinning rockets with internal mass motion," *Journal of Guidance, Control, and Dynamics*, vol. 18, no. 5, pp. 1197–1203, 1995.

[39] Y. T. Ahn, "Attitude dynamics and control of a spacecraft using shifting mass distribution," Ph.D. dissertation, The Pennsylvania State University, December 2012.

[40] P. K. Menon, G. D. Sweriduk, E. J. Ohlmeyer, and D. S. Malyevac, "Integrated guidance and control of moving-mass actuated kinetic warheads," *Journal of Guidance, Control, and Dynamics*, vol. 27, no. 1, pp. 118–126, 2004.

[41] Y. Yi and F. Zhou, "Variable centroid control scheme over hypersonic tactical missile," 2003.

[42] P. Lin and J. Zhou, "Researching variable structure control of moving mass reentry-vehicles," in *Computer Science and Information Technology (ICCSIT), 2010 3rd IEEE International Conference on*, vol. 8, 2010, pp. 126–129.

[43] X.-Y. Zhang, Y.-X. Zhao, D.-X. Xu, and K.-P. He, "Sliding mode control for mass moment aerospace vehicles using dynamic inversion approach," *Mathematical Problems in Engineering*, vol. 2013, 2013.

[44] X. Zhang, P. Li, D. Xu, B. Mao, and K. He, "Nonlinear predictive control of mass moment aerospace vehicles based on ant colony genetic algorithm optimization," *Mathematical Problems in Engineering*, vol. 2013, 2013.

[45] J. Liu, X. Gao, and Y. Ma, "Study on guidance and control technology of mass moment vehicle," in *2009 IEEE International Conference on Control and Automation*, Christchurch, New Zealand, 2009, pp. 679–684.

[46] E. Zhao and B. W. Song, "Modeling and variable structure control of autonomous underwater vehicles with moving mass," in *Applied Mechanics and Materials*, vol. 130, 2012, pp. 1963–1967.

[47] S. Xu, W. Cao, and R. Li, "Research on response characteristic of moving-mass controlled flying vehicle," in *Proceedings of 2014 IEEE Chinese Guidance, Navigation and Control Conference*, Yantai, China, 2014, pp. 2161–2165.

[48] S. Wang, M. Yang, and z. Wang, "Moving-mass trim control system design for spinning vehicles," in *Intelligent Control and Automation, 2006. WCICA 2006. The Sixth World Congress on*, 2006, pp. 1034–1038.

[49] T. R. Kane and D. Sobala, "A new method for attitude stabilization," *AIAA Journal*, vol. 1, no. 6, pp. 1365–1367, 1963.

[50] T. R. Kane and M. P. Scher, "A method of active attitude control based on energy considerations." *Journal of Spacecraft and Rockets*, vol. 6, no. 5, pp. 633–636, 1969.

[51] J. E. Cochran and N. O. Speakman, "Rotational motion of a free body induced by mass redistribution," *Journal of Spacecraft and Rockets*, vol. 12, no. 2, pp. 89–95, 1975.

[52] P. M. Bainum and R. Sellappan, "The use of a movable telescoping end mass system for the time-optimal control of spinning spacecraft," *Acta Astronautica*, vol. 5, no. 10, pp. 781–795, 1978.

[53] K. D. Kumar and A.-M. Zou, "Attitude control of miniature satellites using movable masses," in *SpaceOps 2010 Conference*, Huntsville, AL, 2010.

[54] P. F. Guo and L. Y. Zhao, "Modeling and attitude control of a spinning spacecraft with internal moving mass," in *Proceedings of the 2nd International Conference on Computer Science and Electronics Engineering (ICCSEE 2013)*, 2013, pp. 2938–2941.

[55] D. W. Childs, "A movable-mass attitude-stabilization system for artificial-g space stations," *Journal of Spacecraft and Rockets*, vol. 8, no. 8, pp. 829–834, 1971.

[56] D. W. Childs and T. L. Hardison, "A movable-mass attitude stabilization system for cable-connected artificial-g space stations," *Journal of Spacecraft and Rockets*, vol. 11, no. 3, pp. 165–172, 1974.

[57] A. El-Gohary, "On the control of programmed motion of a rigid body containing moving masses," *International Journal of Non-Linear Mechanics*, vol. 35, no. 1, pp. 27–35, 2000.

[58] V. Krementulo, "About stabilization of equilibrium position of a rigid body with moving masses," *Mechanics of Solids*, vol. 2, pp. 46–50, 1980.

[59] A. El-Gohary, "Global stability of the rotational motion of a rigid body containing moving masses," *International Journal of Non-Linear Mechanics*, vol. 36, no. 4, pp. 663–669, 2001.

[60] N. M. Kachurina and V. V. Krementulo, "Stabilization of rotational motion of a rigid body using movable masses," *Mechanics of Solids*, vol. 16, pp. 96–101, 1981.

[61] A. El-Gohary, "On the orientation of a rigid body using point masses," *Applied mathematics and computation*, vol. 151, no. 1, pp. 163–179, 2004.

[62] J. Shen and N. H. McClamroch, "Translational and rotational maneuvers of an underactuated space robot using prismatic actuators," *The International Journal of Robotics Research*, vol. 21, no. 5-6, pp. 607–618, 2002.

[63] C. Gao, P. Wei, and W. Jing, "Dynamics modeling and control system design for the reentry warhead controlled by single moving mass," in *2013 10th IEEE International Conference on Control and Automation (ICCA).* Hangzhou, China: IEEE, 2013, pp. 1218–1223.

[64] S. Bouabdallah, R. Siegwart, and G. Caprari, "Design and control of an indoor coaxial helicopter," in *Proceedings of the 2006 IEEE/RSJ International Conference on Intelligent Robots and Systems.* Beijing, China: IEEE, 2006, pp. 2930–2935.

[65] C. Bermes, K. Sartori, D. Schafroth, S. Bouabdallah, and R. Siegwart, "Control of a coaxial helicopter with center of gravity steering," in *Proceedings of Intl. Conf. on SIMULATION, MODELING and PROGRAMMING for AUTONOMOUS ROBOTS*, Venice, Italy, 2008, pp. 492–500.

[66] C. A. Woolsey, "Hamiltonian attitude dynamics for a spacecraft with a point mass oscillator," in *In Proceedings of the 15th International Symposium on Mathematical Theory of Networks and Systems*, 2002.

[67] C. A. Woolsey and N. E. Leonard, "Moving mass control for underwater vehicles," in *Proceedings of the American Control Conference.* Anchorage, AK: IEEE, 2002, pp. 2824–2829.

[68] C. A. Woolsey, "Reduced hamiltonian dynamics for a rigid body/mass particle system," *Journal of Guidance, Control, and Dynamics*, vol. 28, no. 1, pp. 131–138, 2005.

[69] N. Mahmoudian, "Efficient motion planning and control for underwater gliders," Ph.D. dissertation, Virginia Polytechnic Institute and State University, September 2009.

[70] P.-X. Wei, C.-S. Gao, and W.-X. Jing, "Roll control problem for the long-range maneuverable warhead," *Aircraft Engineering and Aerospace Technology: An International Journal*, vol. 86, no. 5, pp. 440–446, 2014.

[71] W. Jing, P. Wei, C. Gao, C. Jiang, and X. Zheng, "Roll control analysis for the long-rang reentry vehicle under composite control," in *Proceedings of the 34th Chinese Control Conference*, Hangzhou, China, 2015, pp. 5587–5592.

[72] T. Petsopoulos, F. J. Regan, and J. Barlow, "Moving-mass roll control system for fixed-trim re-entry vehicle," *Journal of Spacecraft and Rockets*, vol. 33, no. 1, pp. 54–60, 1996.

[73] Y. Wang, J. Yu, L. Wang, and Y. Shen, "Roll autopilot design for reentry vehicle with moving-mass control system," in *Proceedings of the 34th Chinese Control Conference*, Hangzhou, China, 2015, pp. 5572–5576.

[74] J. Rogers, "Applications of internal translating mass technologies to smart weapons systems," Ph.D. dissertation, Georgia Institute of Technology, December 2009.

[75] B. G. Kunciw, "Optimal detumbling of a large manned spacecraft using an internal moving mass," Ph.D. dissertation, The Pennsylvania State University, August 1973.

[76] T. L. Edwards and M. H. Kaplan, "Automatic spacecraft detumbling by internal mass motion," *AIAA Journal*, vol. 12, no. 4, pp. 496–502, 1974.

[77] B. G. Kunciw and M. H. Kaplan, "Optimal space station detumbling by internal mass motion," *Automatica*, vol. 12, no. 5, pp. 417–425, 1976.

[78] J.-Z. Hong, "Nutation damping of spinning satellite with viscous annular dampers," *Acta Astronautica*, vol. 19, no. 12, pp. 939–946, 1989.

[79] R. H. Byrne, R. D. Robinett, and B. R. Sturgis, "Moving mass trim control system design," in *AIAA, Guidance, Navigation and Control Conference*, San Diego, CA, 1996, pp. 1–9.

[80] R. H. Byrne, B. R. Sturgis, and R. D. Robinett, "A moving mass trim control system for reentry vehicle guidance," in *Proceedings of the 21st Atmospheric Flight Mechanics Conference*, San Diego, CA, 1996, pp. 644–650.

[81] J. Balaram, "Sherpa moving mass entry descent landing system," in *ASME 2005 International Design Engineering Technical Conferences and Computers and Information in Engineering Conference*, Long Beach, CA, 2005, pp. 63–79.

[82] R. M. Mukherjee and J. Balaram, "Attitude dynamics and control of moving mass multibody aeromaneuver vehicle," in *AIAA Atmospheric Flight Mechanics Conference and Exhibit*, Honolulu, HI, 2008.

[83] B. M. Atkins and E. M. Queen, "Internal moving mass actuator control for mars entry guidance," *Journal of Spacecraft and Rockets*, pp. 1–17, 2015.

[84] S. Thomas, M. Paluszek, B. Wie, and D. Murphy, "Aocs performance and stability validation for large flexible solar sail spacecraft," in *Proceedings of the 41st AIAA/ASME/SAE/ASEE Joint Propulsion Conference* & *Exhibit*, Tucson, AZ, 2005.

[85] B. Wie and D. Murphy, "Solar-sail attitude control design for a sail flight validation mission," *Journal of Spacecraft and Rockets*, vol. 44, no. 4, pp. 809–821, 2007.

[86] K. R. Lorell and B. O. Lange, "An automatic mass-trim system for spinning spacecraft," *AIAA Journal*, vol. 10, no. 8, pp. 1012–1015, 1972.

[87] W. Okolo, A. Dogan, and W. Blake, "Alternate trimming methods for trailing aircraft in formation flight," *Journal of Guidance, Control, and Dynamics*, vol. 38, no. 10, pp. 2018–2024, 2015.

[88] T. Yuhara and K. Rinoie, “Conceptual design study on lh2 supersonic transport for the 2030-2035 time frame,” in *50th AIAA Aerospace Sciences Meeting including the New Horizons Forum and Aerospace Exposition*, Nashville, TN, 2012.

[89] S. Candel, “Concorde and the future of supersonic transport,” *Journal of propulsion and power*, vol. 20, no. 1, pp. 59–68, 2004.

[90] H. G. Turner, “Fuel management for concorde: A brief account of the fuel system and the fuel pumps developed for the aircraft,” *Aircraft Engineering and Aerospace Technology*, vol. 43, no. 3, pp. 36–39, 1971.

[91] D. Collard, “Future supersonic transport studies at aerospatiale,” in *SAE(Society of Automotive Engineers) Transactions*, vol. 99, 1990, pp. 1700–1708.

[92] C. Orlebar, *The Concorde Story.* Osprey Publishing, 1997, p. 39.

[93] D. Collard, “Concorde airframe design and development,” in *SAE(Society of Automotive Engineers) Transactions*, vol. 100, 1991, pp. 2620–2641.

[94] P. Bhatta, “Nonlinear stability and control of gliding vehicles,” Ph.D. dissertation, Princeton University, September 2006.

[95] J. Graver, J. Liu, C. Woolsey, and N. E. Leonard, “Design and analysis of an underwater vehicle for controlled gliding,” in *Proc. 32nd Conference on Information Sciences and Systems*, Princeton, NJ, 1998, pp. 801–806.

[96] N. E. Leonard and J. G. Graver, “Model-based feedback control of autonomous underwater gliders,” *Oceanic Engineering, IEEE Journal of*, vol. 26, no. 4, pp. 633–645, 2001.

[97] F. Zhang, F. Zhang, and X. Tan, “Steady spiraling motion of gliding robotic fish,” in *Intelligent Robots and Systems (IROS), 2012 IEEE/RSJ International Conference on*, Vilamoura, Algarve, Portugal, 2012, pp. 1754–1759.

[98] S. Tangirala and J. Dzielski, "A variable buoyancy control system for a large auv," *IEEE Journal of Oceanic Engineering*, vol. 32, no. 4, pp. 762–771, 2007.

[99] J. Rogers and M. Costello, "Control authority of a projectile equipped with a controllable internal translating mass," *Journal of Guidance, Control, and Dynamics*, vol. 31, no. 5, pp. 1323–1333, 2008.

[100] J.-W. Li, B.-W. Song, and C. Shao, "Tracking control of autonomous underwater vehicles with internal moving mass," *Acta Automatica Sinica*, vol. 34, no. 10, pp. 1319–1323, 2008.

[101] S. Wang, M. Yang, and Z. Wang, "Moving-mass control system for spinning vehicle guidance based on ga," in *Systems and Control in Aerospace and Astronautics, 2006. ISSCAA 2006. 1st International Symposium on*, 2006, pp. 364–367.

[102] I. M. Ross, "Mechanism for precision orbit control with applications to formation keeping," *Journal of Guidance, Control, and Dynamics*, vol. 25, no. 4, pp. 818–820, 2002.

[103] S. R. Vengate, "Development and flight test of moving-mass actuated unmanned aerial vehicle," Master's thesis, The University of Texas at Arlington, Arlington, TX, May 2016.

[104] O. Chanute, *Progress in flying machines.* Courier Corporation, 1997, pp. 93–94.

[105] H. S. Wolko and J. D. Anderson, *The Wright Flyer: an engineering perspective.* Smithsonian, 1983, p. 48.

[106] J. Waishek, A. Dogan, and W. Blake, "Derivation of the dynamics equations of receiver aircraft in aerial refueling," *Journal of Guidance, Control, and Dynamics*, vol. 32, no. 2, 2009.

[107] D. Lundstrm, K. Amadori, and P. Krus, “Validation of models for small scale electric propulsion systems,” in *48th AIAA Aerospace Sciences Meeting Including the New Horizons Forum and Aerospace Exposition*, Orlando, FL, 2010.

[108] J. Schoemann and M. Hornung, “Modeling of hybrid electric propulsion systems for small unmanned aerial vehicles,” in *12th AIAA Aviation Technology, Integration, and Operations (ATIO) Conference and 14th AIAA/ISSMO Multidisciplinary Analysis and Optimization Conference*, Indianapolis, IN, 2012.

[109] R. Papdeja and P. Sankala, “Modelling and simulation of three phase brushless dc motor with using model reference adaptive controller,” *International Journal of Inventions in Computer Science and Engineering*, vol. 1, no. 3, 2014.

[110] A. Kiruthika, A. Rajan, and P. Rajalakshmi, “Mathematical modelling and speed control of a sensored brushless dc motor using intelligent controller,” in *Emerging Trends in Computing, Communication and Nanotechnology (ICE-CCN), 2013 International Conference on*, March 2013, pp. 211–216.

[111] “Servo calculator program,” http://www.irks.org/downloadable-files/downloadable-files.htm, note = Accessed: 03/17/2016,.

[112] “Battery discharge/charge cycling using keithley series 2400 sourcemeter instruments,” http://www.tek.com/sites/tek.com/files/media/document/resources/Battery_Discharge_AN.pdf, accessed: 03/31/2016.

[113] B. W. McCormick, *Aerodynamics, aeronautics, and flight mechanics.* John Wiley & Sons, New York, 1995, vol. 2.

[114] M. S. Selig, “Modeling propeller aerodynamics and slipstream effects on small uavs in realtime,” in *AIAA Atmospheric Flight Mechanics Conference*, Toronto, Ontario Canada, 2010.

[115] B. R. Mullins, "Aircraft equations of motion," February 2016, lecture notes in Flight Dynamics class in the semester of spring 2016 at The University of Texas at Arlington.

[116] D. B. Owens, D. E. Cox, and E. A. Morelli, "Development of a low-cost sub-scale aircraft for flight research: The faser project," in *25th AIAA Aerodynamic Measurement Technology and Ground Testing Conference*, no. 2006-3306, San Francisco, California, 2006.

[117] A. Durai, R. Dodamani, R. Antony, S. Chitlur, R. Gopalan, and S. Ahmed, "Experimental studies on a propelled micro air vehicle," in *29th AIAA Applied Aerodynamics Conference*, Honolulu, HI, 2011.

[118] "Housed brushless dc (bldc) motors, dih18-16-bbna," http://www.beikimco.com/motor-products/brushless-dc/BLDC-brushless-housed-motors, accessed: 02/11/2016.

[119] "12x8e performance data (versus advance ratio and mph)," https://www.apcprop.com/v/PERFILES_WEB/listDatafiles.asp, accessed: 12/22/2015.

[120] S. A. Erturk and A. Dogan, "Trim analysis of a moving-mass actuated airplane in steady turn," in *51st AIAA Aerospace Sciences Meeting including the New Horizons Forum and Aerospace Exposition*, Grapevine, TX, 2013.

[121] ——, "Trimming mass-actuated airplane in turns with zero side slip angle," in *AIAA Atmospheric Flight Mechanics Conference*, National Harbor, MD, 2014.

[122] U. S. Atmosphere, "Noaa, nasa, usaf," *Washington DC*, 1976.

[123] P. C. Müller and H. I. Weber, "Analysis and optimization of certain qualities of controllability and observability for linear dynamical systems," *Automatica*, vol. 8, no. 3, pp. 237–246, 1972.

[124] F. L. Lewis and V. L. Syrmos, *Optimal control.* John Wiley & Sons, 1995.

BIOGRAPHICAL STATEMENT

Sukru Akif Erturk was born in Kayseri, Turkey in 1989. He received his B.S. degree in Aeronautical Engineering from Istanbul Technical University, Turkey, in 2011. He also joined ERASMUS Student Exchange Program for the academic year 2009-2010. Within the scope of this program, he completed his junior year at University of Glasgow, United Kingdom. He had a long term summer internship from Turkish Aerospace Industries (TAI) in Turkey in 2009. After graduating with his B.S. in 2011, he started the B.S. to Ph.D. program in Aerospace Engineering at The University of Texas at Arlington (UTA) in Computer Aided Control System Design (CACSD) Laboratory. He was also affiliated as a Graduate Teaching Assistant (UTA) from 2011 to 2016 at UTA during this period. His current research interests are atmospheric flight mechanics, guidance, navigation and control, and unmanned systems. He is an AIAA member.